

**MODELLING OF SETTLEMENT
INDUCED BUILDING DAMAGE
GIORGIA GIARDINA**

Modelling of Settlement Induced Building Damage

Giorgia Giardina

© 2013, Giorgia Giardina

All rights reserved. No part of this book may be reproduced, stored in a retrieval system, or transmitted, in any form or by any means, without prior permission from the copyright owner.

ISBN 978-94-6191-614-3

Keywords: building damage, masonry, settlement, tunnelling

Printed by Ipskamp Drukkers, Enschede, The Netherlands

Modelling of Settlement Induced Building Damage

Proefschrift

ter verkrijging van de graad van doctor
aan de Technische Universiteit Delft,
op gezag van de Rector Magnificus Prof. ir. K.C.A.M. Luyben,
voorzitter van het College voor Promoties,
in het openbaar te verdedigen
op vrijdag 15 februari 2013 om 10.00 uur door

Giorgia GIARDINA

Environmental Engineer,
University of Brescia, Italy

geboren te Peschiera del Garda, Italië

Dit proefschrift is goedgekeurd door de promotoren:

Prof. dr. ir. J.G. Rots
Dr. ir. M.A.N. Hendriks

Samenstelling promotiecommissie:

Rector Magnificus,	voorzitter
Prof. dr. ir. J.G. Rots,	Technische Universiteit Delft, promotor
Dr. ir. M.A.N. Hendriks,	Technische Universiteit Delft, promotor
Prof. ir. J. Bosch,	Technische Universiteit Delft
Prof. ir. R.P.J. van Hees,	Technische Universiteit Delft
Prof. dr. P.B. Lourenço,	Universidade do Minho
Prof. ir. D.R.W. Martens,	Technische Universiteit Eindhoven
Prof. dr. ing. P. Riva,	Università degli studi di Bergamo

Summary

This thesis focuses on the modelling of settlement induced damage to masonry buildings. In densely populated areas, the need for new space is nowadays producing a rapid increment of underground excavations. Due to the construction of new metro lines, tunnelling activity in urban areas is growing. One of the consequences is a greater attention to the risk of damage on existing structures. Thus, the assessment of potential damage of surface buildings has become an essential stage in the excavation projects in urban areas (Chapter 1). The current damage risk assessment procedure is based on strong simplifications, which not always lead to conservative results. Object of this thesis is the development of an improved damage classification system, which takes into account the parameters influencing the structural response to settlement, like the non-linear behaviour of masonry and the soil-structure interaction.

The methodology used in this research is based on experimental and numerical modelling. The design and execution of an experimental benchmark test representative of the problem allows to identify the principal factors and mechanisms involved. The numerical simulations enable to generalize the results to a broader range of physical scenarios. The methodological choice is based on a critical review of the currently available procedures for the assessment of settlement-induced building damage (Chapter 2).

A new experimental test on a 1/10th masonry façade with a rubber base interface is specifically designed to investigate the effect of soil-structure interaction on the tunnelling-induced damage (Chapter 3). The experimental results are used to validate a 2D semi-coupled finite element model for the simulation of the structural response (Chapter 4). The numerical approach, which includes a continuum cracking model

Summary

for the masonry and a non-linear interface to simulate the soil-structure interaction, is then used to perform a sensitivity study on the effect of openings, material properties, initial damage, initial conditions, normal and shear behaviour of the base interface and applied settlement profile (Chapter 5). The results assess quantitatively the major role played by the normal stiffness of the soil-structure interaction and by the material parameters defining the quasi-brittle masonry behaviour.

The limitation of the 2D modelling approach in simulating the progressive 3D displacement field induced by the excavation and the consequent torsional response of the building are overcome by the development of a 3D coupled model of building, foundation, soil and tunnel (Chapter 6). Following the same method applied to the 2D semi-coupled approach, the 3D model is validated through comparison with the monitoring data of a literature case study. The model is then used to carry out a series of parametric analyses on geometrical factors: the aspect ratio of horizontal building dimensions with respect to the tunnel axis direction, the presence of adjacent structures and the position and alignment of the building with respect to the excavation (Chapter 7). The results show the governing effect of the 3D building response, proving the relevance of 3D modelling.

Finally, the results from the 2D and 3D parametric analyses are used to set the framework of an overall damage model which correlates the analysed structural features with the risk for the building of being damaged by a certain settlement (Chapter 8). This research therefore provides an increased experimental and numerical understanding of the building response to excavation-induced settlements, and sets the basis for an operational tool for the risk assessment of structural damage (Chapter 9).

Samenvatting

Deze dissertatie gaat over het modelleren van de schade die zettingen kunnen veroorzaken bij metselwerk gebouwen. De roep om meer ruimte in dichtbevolkte gebieden zorgt voor een toename van ondergrondse bouwprojecten. Zo worden in steeds meer steden tunnels voor nieuwe metrolijnen aangelegd. Door deze ontwikkelingen groeit ook de aandacht voor het risico op schade aan bestaande panden. Het vooraf inschatten van mogelijke schade aan bovengrondse gebouwen is daarmee een essentieel onderdeel geworden van bouwprojecten met ontgravingen in stedelijke gebieden (Hoofdstuk 1). De huidige procedure om schade te voorspellen maakt gebruik van sterke vereenvoudigingen, die niet altijd tot conservatieve resultaten leiden. Doel van deze dissertatie is om een beter systeem te ontwikkelen om de mate van geïnduceerde schade te voorspellen: een systeem dat de parameters meeneemt die bepalen hoe een constructie op zettingen reageert, zoals het niet-lineaire gedrag van metselwerk en de wisselwerking tussen gebouw en ondergrond.

De methode die in dit onderzoek wordt gebruikt, is zowel op experimenteel als numeriek modelleren gebaseerd. Met een experimentele referentietest, speciaal ontworpen en uitgevoerd om dit probleem te representeren, kunnen de belangrijkste factoren en mechanismen in kaart gebracht worden. De numerieke simulaties maken het vervolgens mogelijk om de resultaten te veralgemeniseren naar een breder spectrum van fysieke scenario's. De keuze voor deze methode is gebaseerd op een kritische beschouwing van de procedures die op dit moment beschikbaar zijn voor het vooraf inschatten van door zettingen veroorzaakte gebouwen (Hoofdstuk 2).

Een nieuwe proefopstelling, schaal 1:10, van een metselwerk gevel op een rubberen tussenlaag is gepresenteerd. Deze test is speciaal ontworpen om het effect van grond-gebouwinteractie op schade door ondertunneling te onderzoeken (Hoofdstuk 3). De

resultaten worden gebruikt voor het valideren van een 2D semi-gekoppeld eindig-elementenmodel voor het simuleren van constructieve respons (Hoofdstuk 4). Deze numerieke aanpak, die bestaat uit een continu scheurmodel voor het metselwerk en een niet-lineaire tussenlaag voor het simuleren van grond-gebouwinteractie, wordt vervolgens gebruikt om te onderzoeken in hoeverre openingen, materiaaleigenschappen, initiële schade, initiële condities, normaal- en schuifgedrag van de tussenlaag en opgelegde zettingsprofielen de gevoeligheid van een gebouw voor schade beïnvloeden (Hoofdstuk 5). De resultaten stellen kwantitatief vast hoe groot de invloed is van de normaalstijfheid in grond-gebouwinteractie en van de materiaalparameters die het quasi-brosse gedrag van metselwerk bepalen.

Met een 2D model kunnen het verschuivende 3D verplaatsingsveld zoals dat bij ontgravingen ontstaat, en de daarmee gepaard gaande torsierespons van een gebouw slechts in beperkte mate beschreven worden. Deze beperkingen worden weggenomen met de ontwikkeling van een 3D gekoppeld model van gebouw, fundering, grond en tunnel (Hoofdstuk 6). Met dezelfde methode die voor de 2D semi-gekoppelde aanpak is gebruikt, wordt het 3D model gevalideerd door het te vergelijken met monitoringgegevens afkomstig van een praktijkgeval beschreven in de literatuur. Het model wordt vervolgens gebruikt voor een parameterstudie naar de invloed van enkele geometrische factoren: de verhouding tussen de horizontale afmetingen van een gebouw ten opzichte van de richting van de tunnelas, de aanwezigheid van aangrenzende constructies en de positie en ligging van het gebouw ten opzichte van de uitgraving (Hoofdstuk 7). De resultaten tonen het overheersende effect van de 3D gebouwrespons, en bewijzen daarmee het belang van 3D modelleren.

Tot slot worden de resultaten van de 2D en 3D parameterstudies gebruikt om een raamwerk op te stellen voor een overkoepelend schademodel dat de geanalyseerde constructieve eigenschappen relateert aan het risico voor een gebouw om schade op te lopen bij een zekere zetting (Hoofdstuk 8). Zo vergroot dit onderzoek zowel het experimenteel als het numeriek inzicht in hoe gebouwen reageren op door ontgravingen veroorzaakte zettingen. Daarmee legt het de basis voor een werkend hulpmiddel voor het inschatten van risico's op constructieve schade (Hoofdstuk 9).

Contents

Summary	i
Samenvatting	iii
1 Introduction	1
1.1 Background	1
1.2 Research questions	4
1.3 Methodology	4
1.4 Contributions of this research	6
1.5 Thesis outline	6
2 Review of modelling methods	9
2.1 Preliminary assessment: current regulations and approximate methods	9
2.1.1 Introductory definitions of ground movements	10
2.1.2 Eurocode 7	14
2.1.3 Dutch regulations	15
2.1.4 Other approximate methods	16
2.2 Limiting Tensile Strain Method: description and accessibility	19
2.2.1 Assumptions	19
2.2.2 Procedures	19
2.2.3 Limitations	27
2.3 Finite Element Analysis	28
2.3.1 Building modelling	29
2.3.2 Soil modelling	29
	v

Contents

2.3.3	Tunnel modelling	30
2.3.4	Foundation and soil-structure interaction modelling	32
2.3.5	Proposed 3D coupled model	32
2.4	Crack modelling for masonry structures	35
2.4.1	Discrete approach	35
2.4.2	Continuum approach	36
2.4.3	Incremental iterative analysis	37
2.4.4	Sequentially linear analysis	37
2.5	From seismic to settlement vulnerability	39
2.5.1	Seismic vulnerability assessment	39
2.5.2	Settlement vulnerability assessment	43
3	Experimental analysis of a masonry façade	45
3.1	Experimental model	45
3.2	Modelling issues	48
3.2.1	Façade scaled model	48
3.2.2	Load amplification	50
3.2.3	Settlement configuration	53
3.2.4	Soil-structure interaction	54
3.3	Material properties	55
3.3.1	Mortar	56
3.3.2	Bricks	56
3.3.3	Reduced scale masonry	56
3.4	Instrument set-up and monitoring system	61
3.5	Experimental results	62
3.6	Mechanical interpretation	68
3.7	Analytical assessment	71
3.8	Conclusions	73
4	2D numerical analysis of a masonry façade	75
4.1	Numerical model	75
4.1.1	Discrete model	77
4.1.2	Continuum model	77
4.2	Numerical results	79
4.2.1	Deformations, crack patterns and bedding reactions	79
4.2.2	Incremental-iterative analysis	79
4.2.3	Damage classes	87
4.2.4	Sequentially linear analysis	88
4.3	Conclusions	95

5	2D sensitivity study	97
5.1	Identification and selection of parameters and variations	97
5.2	Results	102
5.2.1	Amount of openings	103
5.2.2	Material parameters	106
5.2.3	Initial loading and damage conditions	112
5.2.4	Soil-structure interaction	116
5.2.5	Settlement profile	122
5.3	Conclusions	126
6	3D finite element modelling	127
6.1	3D coupled model of building and soil	128
6.2	Tunnel advance modelling	130
6.2.1	Numerical model	130
6.2.2	Results and discussion	130
6.3	3D pile foundation modelling	136
6.3.1	Dutch pile foundation	136
6.3.2	Single element evaluation	140
6.3.3	3D coupled model	143
6.3.4	Results and discussion	143
6.4	Validation case study: the Mansion House in London	149
6.4.1	Numerical model	151
6.4.2	Results and discussion	155
6.5	Conclusions	163
7	3D sensitivity study	165
7.1	Identification and selection of parameters and variations	165
7.2	Results	174
7.2.1	Orientation	175
7.2.2	Grouping	178
7.2.3	Position	179
7.2.4	Alignment	179
7.3	Comparison with Building Risk Assessment	186
7.3.1	Orientation	187
7.3.2	Grouping	189
7.3.3	Position	189
7.3.4	Global comparison	190
7.4	Conclusions	191

Contents

8	Settlement vulnerability system	195
8.1	Damage model	195
8.2	2D damage function	197
8.3	3D damage function	207
8.4	Conclusion	213
9	Conclusions	215
9.1	Returning to the research questions	215
9.2	Scientific contributions	218
9.3	Future research	219
	Bibliography	221
A	LTSM spreadsheet application	231
A.1	User's manual	231
A.2	Examples	243
B	Experimental analysis of a masonry façade: measured displacements	253
C	Results of the 3D sensitivity study	261
	Acknowledgements	275
	Curriculum Vitae	277

Introduction

1

In June and September 2008 two unrelated accidents at the Vijzelgracht station interrupted the construction of the new North-South metro line in Amsterdam. Due to the leakage in a slurry diaphragm wall, a number of houses adjacent to the construction site experienced severe differential settlements and suffered from significant damage (Figure 1.1). As the city centre of Amsterdam has many listed monumental buildings, a clear risk exists of loss of monumental values. The excavation works were suspended for several months, causing a serious financial loss and a considerable loss of credibility of the entire project among the inhabitants. The event highlighted the need for safe subsurface building methods that reduce or prevent settlements, and for a definite and reliable procedure for the vulnerability assessment of settlement-induced building damage.

1.1 Background

The continuous increase in urban density represents a fundamental issue in modern society. One of the strategies adopted to satisfy the request for additional space has been the expansion in the vertical direction. By constructing high-rise buildings, the cities have conquered new residential and working space upwards, with a corresponding downwards growth due to the excavation of deeper foundations. Furthermore, the exploitation of the underground dimension has allowed to construct new space consuming facilities, such as parking garages and transport infrastructures, without affecting the quality of the existing urban space at the surface.

However, a consequence of subsurface building activity is the development of ground settlements. The induced displacements affect the area surrounding the



Figure 1.1: Masonry building damaged by differential settlements, Vijzelgracht, Amsterdam. Temporary supporting structures are visible on the left part.

construction site where, in most cases, existing buildings are present. The consequent risk of structural damage has a considerable economical impact on this kind of projects. First, instant and unplanned mitigating measures have to be taken to limit further ground deformations. Then, if damage still occurs, additional expenses are required for repairing and strengthening the damaged buildings. The need for repairing and mitigating procedures leads to increased financial costs. Moreover, unexpected damages on private or public structures have a large negative impact on public opinion. For these reasons, nowadays the risk of damage to residential buildings or architectural heritage has become a politically relevant issue.

Assuming the necessity of the underground activity development, different strategies can be adopted in order to mitigate the risk of settlement-induced damage to existing buildings:

- an accurate preliminary damage risk assessment in the planning phase, which accounts for most of the possible causes of damage;
- the use of advanced excavation techniques during the execution phase, in order to reduce the magnitude of the ground settlements;
- the adoption of settlement mitigation measures or building strengthening techniques in the areas that are indicated as high risk from the preliminary assessment;

- a constant monitoring of soil and building conditions during and after the excavation activity, in order to recognize unexpected settlements or damage as soon as possible.

This thesis focuses on the analysis and optimization of the first aspect. The preliminary damage assessment currently in use consists of a staged procedure. First, the ground displacements induced by the excavations are calculated neglecting the presence of surface structures. Then, a simple 2D analytical approach called Limiting Tensile Strain Method (LTSM) is applied to those building located in areas where the expected greenfield deformations are larger than defined limit values. The LTSM consists of a fully decoupled soil-structure analysis in which the structure is modelled as a linear elastic beam with corresponding geometrical properties and equivalent stiffness.

As a result of its simplicity, the LTSM has some disadvantages which affect its feasibility:

- it neglects the non-linear response of the structure, so cracking and post-crack redistribution of stresses and stiffness are not considered;
- it does not take into account the effect of the interaction between the building, its foundations and the soil;
- it neglects the influence of the openings (doors and windows) on the initiation and propagation of the cracks;
- it does not include an appropriate method to deal with building types other than masonry structures, like concrete frame structures;
- it can not take into account possible initial loading or existing damage.

Due to the decoupled approach, the LTSM it generally leads to conservative results. However, by assuming a homogeneous distribution of deformations and neglecting the possible pre-existing damage, it could in some cases underestimate the consequences of the predicted settlement.

An attractive solution for the evaluation of the non-linear behaviour of soil, building and soil-structure interaction is represented by numerical models. They allow for the inclusion of these effects in a comprehensive calculation, and they enable performing numerical tests on a wide range of possible scenarios (e.g. different building layouts, material properties, settlement profiles). A major challenge is that the numerical results need to be validated by comparison with experimental measurements and field observations. Furthermore, due to the high computational cost and specialized expertise required to perform the analyses and to process and interpret the results, the indications derived from the finite element analyses should be translated into simplified assessment procedures, in order to be applicable to common projects.

1.2 Research questions

The aim of this project is the development of a reliable and practical modelling approach for the prediction of settlement-induced damage to masonry buildings. The approach requires to consider the non-linear behaviour of structural materials, the mutual influences of building and ground deformations through the foundation and the most relevant factors which play a role in the structural response. The research is limited to masonry buildings and it focuses on the structural aspects of the problem. The reliability of the proposed numerical model has to be guaranteed by its validation through physical models and case studies; the practical value of the approach depends on the possibility to summarize the numerical results into a comprehensive vulnerability classification which relates the effect of specific features of the structure with a certain level of expected damage. Hence, the main research question of this study is:

How to develop and validate an improved modelling approach for the damage assessment of buildings subjected to settlements?

The main question can be decomposed into the following sub-questions:

- What are the most effective indicators to assess the settlement-induced damage?
- What are the most suitable numerical approaches to simulate the problem?
- How to design and perform a laboratory benchmark test to validate the proposed model?
- How can the numerical model evaluate the factors governing the structural response to settlements?
- How to derive an improved classification system from the analysis results?

1.3 Methodology

In this thesis, a 3D finite element approach for the development of an improved classification system of tunnelling-induced damage to buildings is proposed. The system is based on the principles of the seismic vulnerability risk assessment. The idea from which this work originates is that the vulnerability of a building in terms of susceptibility to be damaged by a ground shaking of a given intensity could be transposed to the sensitivity of the structure to be damaged by a given settlement scenario.

A correlation between a certain settlement trough and the most probable level of damage, for a certain building typology, can be defined using finite element models. In this thesis, a 3D fully coupled model of building, soil and tunnelling is presented. The attention of this study is mainly focused on the non-linear behaviour of the building and the soil-structure interaction. An elastic soil with a Young's modulus linearly increasing with the depth is assumed. The settlement profile transverse to the tunnel axis is simulated through a controlled volume loss. A staged analysis is performed to reproduce the 3D tunnel advance and the consequent longitudinal settlement profile. In this way, also the possible torsional effect on the structure is taken into account. The building material is modelled by a smeared crack model with tension softening, which allows to simulate the progressive damage. A non-linear interface is adopted to represent the soil-structure interaction.

Preliminary investigations are conducted on simplified 2D models, to evaluate the material behaviour. For the structure, different material constitutive laws are evaluated, in order to set a reliable relation between the physical description of the damage in terms of crack width and the interpretation of the finite element analysis output.

To analyse the effect of the soil-structure interaction on structural damage, a new experimental laboratory benchmark test is designed and executed: a tunnelling-induced settlement profile is applied to a scaled model of a masonry façade. The façade is assembled using scaled bricks and mortar layers. Amplified vertical loads are applied in order to replicate the prototype stress field. A pre-defined settlement trough is imposed by means of a flexible steel profile connected to the façade base, and the soil-structure interaction is simulated by inserting a layer of rubber between the masonry façade and the steel profile, allowing for an accurate calibration of the interface stiffness.

The experimental measurements in terms of deformation and crack pattern evolution are used to validate the boundary conditions and the material constitutive law of the 2D model in the specific case of tunnelling-induced damage. Standard incremental-iterative and innovative sequentially linear techniques are applied to perform the analysis with quasi-brittle crack propagation. The numerical outcomes are also compared with the damage assessment resulting from the application of the traditional LTSM.

After the evaluation of the specific modelling details (material model, analysis approach, effect of boundary conditions), the potential of the proposed 3D coupled model is tested through a case study, the Mansion House in London, which was affected by tunnelling-induced subsidence. A variational study is then performed in order to evaluate the influence of different parameters on the structural response to settlement. The results of the variational study are compared with the outcomes of

an empirical assessment procedure based on field observations.

Finally, the numerical results are summarized in a comprehensive damage model which correlates the main building characteristics with the risk of being damaged by a certain level of settlement. The proposed damage function describes the global vulnerability of the structure.

1.4 Contributions of this research

- The thesis introduces the framework of a new approach for the preliminary damage risk assessment of buildings subjected to differential settlements, especially induced by tunnel excavations.
- A 2D semi-coupled approach for the simulation of the effect of soil-structure interaction on the building damage is proposed and validated by comparison with experimental results.
- An experimental laboratory test is performed on a scaled masonry façade subjected to a pre-defined settlement trough and including a non-linear soil-structure interface. This test sets a new benchmark for the validation of numerical models.
- A comprehensive 3D finite element model including the coupled effect of soil, tunnel and structure is proposed and validated making use of field measurements.
- The proposed modelling approach is a further step towards the development of numerically based fragility curves for the assessment of settlement-induced damage.

1.5 Thesis outline

Chapter 2 presents the state-of-the-art in preliminary assessment of settlement-induced damage to existing buildings. Current regulations based on simplified procedures, the Limiting Tensile Strain Method, and numerical approaches based on finite element models are described, highlighting their advantages and disadvantages in relation to the practical use.

Chapter 3 describes the design, execution and results of an experimental test performed on a 1/10th masonry façade with well-defined soil-structure interaction subjected to tunnelling-induced settlement.

Chapter 4 deals with the definition of a 2D semi-coupled finite element model including the effect of cracking and soil-structure interaction. The model is validated through comparison with the experimental test results; discrete and continuum crack models, and incremental-iterative and sequential linear analysis approaches are compared.

Chapter 5 presents the results of a sensitivity study performed on the validated 2D model. The study investigates the effect of geometrical, material, initial loading and soil-structure interface behaviour.

Chapter 6 proposes the 3D coupled model. First, the main modelling issues, i.e. soil, tunnelling, building and soil-structure interaction, are addressed and individually analysed. Then the global approach is validated by simulating a real-case of tunnelling-induced damage to a historical building.

Chapter 7 focuses on the performed 3D sensitivity study. The effect of building material, position, orientation and aspect ratio is evaluated and compared with the results of empirical and analytical assessment procedures.

Chapter 8 draws the framework of a vulnerability system derived from the results of the 2D and 3D parametric sensitivity studies.

Chapter 9 summarizes the results and gives final recommendations.

An overview of the thesis outline is given in Figure 1.2.

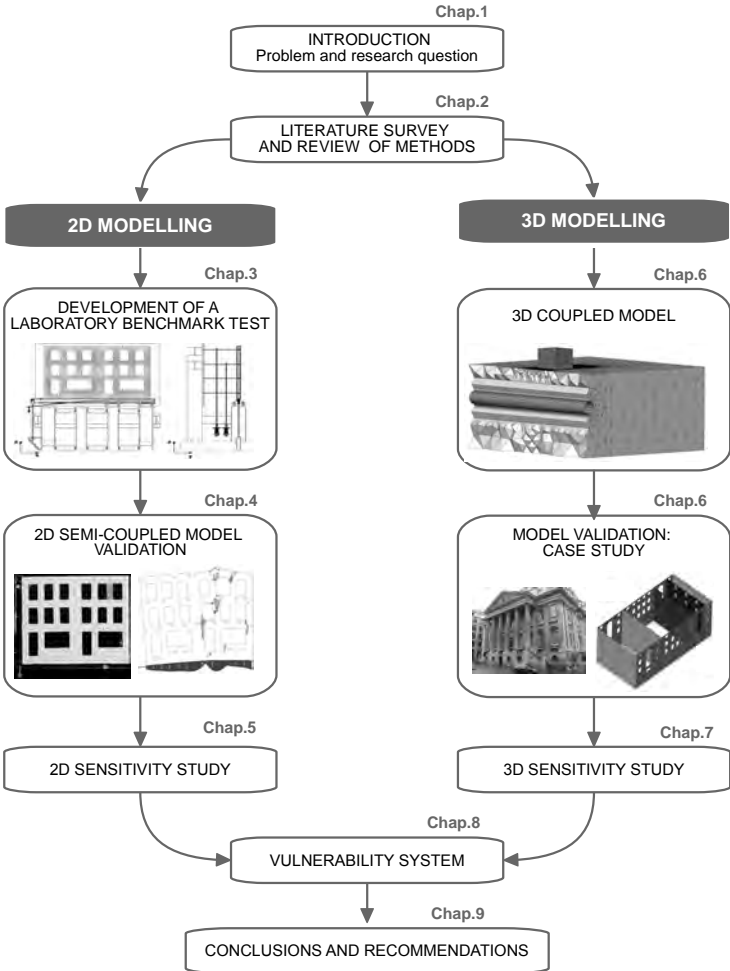


Figure 1.2: Thesis outline overview.

Review of modelling methods 2

In this chapter, an overview of the available methods for the preliminary assessment of settlement-induced damage to buildings is given. The survey includes several European standards and other procedures established in the field practice during major underground projects. The attention is mainly focused on the tunnelling-induced settlements, but most of the described criteria can be generalized to the effect of other excavation works.

The assessment procedures are introduced with increasing level of complexity. First, the pure greenfield approaches based on the expected soil deformation as a consequence of the excavation are presented. Then, empirical-analytical methods taking into account also a simple model of the structure are illustrated. Finally, the main features of more advanced numerical simulations are described. For each method, a critical review in terms of its advantages and disadvantages is offered.

At the end of the chapter, probabilistic approaches for the vulnerability assessment are introduced: the parallel between the different criteria adopted in case of natural hazards and their possible extension to man-induced risks defines the theoretical basis for an improved settlement vulnerability system.

2.1 Preliminary assessment: current regulations and approximate methods

The empirical assessment procedures covered in this section indicate limit values directly applicable to deformations of the ground and the structures.

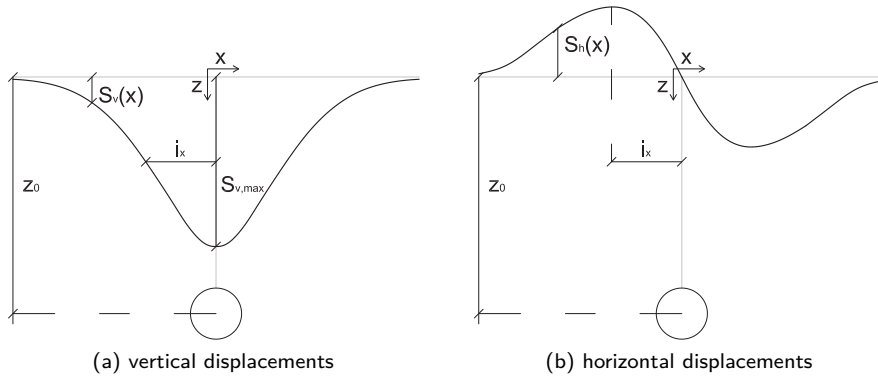


Figure 2.1: Empirical-analytical curves for tunnelling-induced displacements in the transverse direction.

2.1.1 Introductory definitions of ground movements

The so-called greenfield settlements can be predicted with different methods, from simple empirical-analytical models to advanced numerical techniques. Here only the empirical-analytical curves commonly used in the design phase for tunnelling and deep excavations are described.

Ground movements due to tunnelling

Tunnel excavations cause a 3D ground displacement field. In the preliminary assessment, the greenfield deformations are generally decomposed in the transverse and longitudinal direction with respect to the tunnel axis.

Transverse direction According to Peck (1969), the greenfield settlement trough in the transverse direction can be analytically described by a Gaussian error function (Figure 2.1a).

The vertical displacement is calculated as:

$$S_v(x) = S_{v,\max} e^{-\frac{x^2}{2i_x^2}} \quad (2.1)$$

where $S_{v,\max}$ is the maximum settlement measured above the tunnel axis, x is the horizontal distance from the tunnel axis and i_x is the horizontal distance between the vertical axis and the point of inflection.

O'Reilly and New (1982) showed that the trough width parameter i_x can be calculated as:

$$i_x = K(z_0 - z) \quad (2.2)$$

where z_0 is the tunnel depth and K is a dimensionless constant depending on the soil type. For $z=0$, the related i_x represents the distance between the vertical axis and the point of inflection on the ground surface. Several authors derived different values for i_x (Mair et al., 1993; O'Reilly and New, 1982).

The volume of the settlement trough per unit length is given by:

$$V_S = \int_{-\infty}^{\infty} S_v(x) dx = \sqrt{2\pi} i_x S_{v,\max} \quad (2.3)$$

The volume loss ratio V_L is defined as:

$$V_L = \frac{V_S}{\frac{\pi D^2}{4}} \quad (2.4)$$

where D is the initial tunnel diameter.

The greenfield settlement can now be expressed in terms of volume loss ratio:

$$S_v(x) = \sqrt{\frac{\pi}{2}} \frac{V_L D^2}{4 i_x} e^{-\frac{x^2}{2i_x^2}} \quad (2.5)$$

O'Reilly and New (1982) showed, assuming a radial displacement field, that the horizontal greenfield displacement of the soil surface in the transverse direction (Figure 2.1b) can be calculated as:

$$S_h(x) = -\frac{x S_v(x)}{z_0} \quad (2.6)$$

Longitudinal direction According to Attewell and Woodman (1982), the vertical settlement profile in the longitudinal direction (Figure 2.2a) can be described by:

$$S_v(y)_{x=0} = S_{v,\max} \Phi(y) \quad (2.7)$$

In Equation (2.7), $S_{v,\max}$ is the maximum settlement in the transverse direction, y is the horizontal coordinate in the longitudinal direction starting at 50% of the

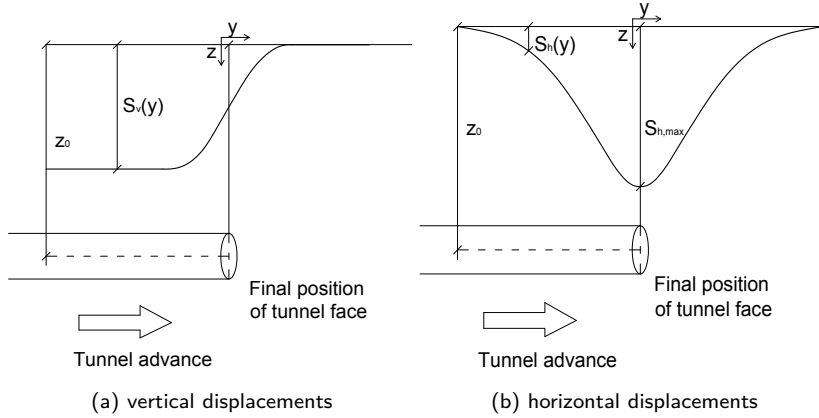


Figure 2.2: Empirical-analytical curves for tunnelling-induced displacements in the longitudinal direction.

longitudinal trough maximum settlement and $\Phi(y)$ is the cumulative probability function, defined as:

$$\Phi(y) = \frac{1}{i_y \sqrt{2\pi}} \int_{-\infty}^y e^{-\frac{y^2}{2i_y^2}} \quad (2.8)$$

where i_y is the trough width parameter of the longitudinal settlement profile, often assumed equal to i_x .

Attewell and Woodman also calculated the horizontal longitudinal movements (Figure 2.2b) as:

$$S_h(y)_{x=0} = \frac{V_L D^2}{8z_0} e^{-\frac{y^2}{2i_y^2}} \quad (2.9)$$

Ground movements due to deep excavation

The vertical displacement calculated in Equation (2.1) can be adapted to ground movements induced by deep excavation, assuming that the vertical wall is located at the inflection point $x = i_x$ (Figure 2.3a).

Therefore, the above equation becomes (Lee et al., 2007):

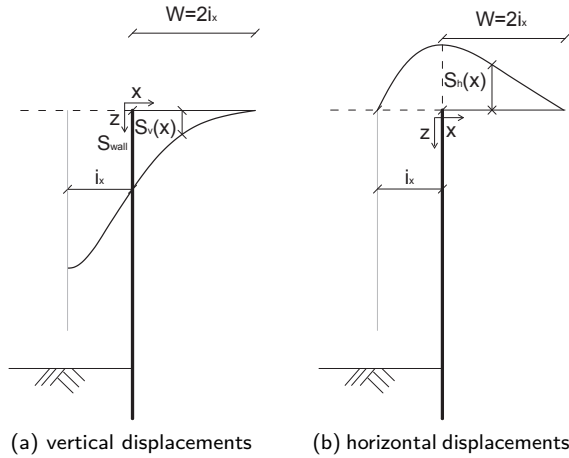


Figure 2.3: Empirical-analytical curves for ground displacements due to deep excavations.

$$S_v(x) = S_{wall} e^{\left[0.5 - 0.5\left(1 + \frac{2x}{W}\right)^2\right]} \quad (2.10)$$

where S_{wall} is the settlement measured at wall location, x is the horizontal distance from the wall and $W = 2i_x$ is the settlement trough width.

Caspe (1966) gave an estimation of the settlement trough width:

$$W = (H_e + H_d) \tan\left(45 - \frac{\phi}{2}\right) \quad (2.11)$$

where H_e is the excavation depth, H_d is the influence depth below the excavation and ϕ is the frictional angle of soil. H_d is assumed to be equal to the excavation width B_e if $\phi = 0$, while $H_d = 0.5B_e \tan\left(45 - \frac{\phi}{2}\right)$ if $\phi > 0$.

The horizontal displacement (Figure 2.3b) can be calculated as:

$$S_h(x) = -\beta \left(1 + \frac{2x}{W}\right) S_v(x) \quad (2.12)$$

where β is the ratio of horizontal movement to settlement, equal to 0.5 for diaphragm walls and 1.0 for sheet pile walls.

In the preliminary assessment, the buildings located in areas characterized by greenfield deformations smaller than defined limit values are considered to be safe. In the other cases, mitigation measures or further analyses are required.

The main deformation parameters adopted in the regulations are illustrated in Figure 2.4 and defined as follows:

- the settlement S is the vertical displacement of a point;
- the differential settlement ΔS is the difference between the settlements of two points;
- the relative deflection Δ is the maximum displacement between the settlement profile of two points and a straight line connecting them;
- the deflection ratio Δ/L is the ratio of the relative deflection between two points to the length between them;
- the rotation θ is the gradient of a straight line connecting two points;
- the tilt ω is the body rotation of the part of the structure defined by two points;
- the angular distortion (or relative rotation) β is the rotation of the straight line connecting two points relative to their tilt.

2.1.2 Eurocode 7

The Eurocode 7, referred next as Eurocode or EC7, establishes limiting values for foundation movements of ordinary and new constructions (CEN, 2007b). For open or infilled frames and load bearing or continuous brick walls, the maximum allowed angular distortion β (Figure 2.4) varies between 1/2000 and 1/300. A limit value of 1/500 is acceptable for many structures, to prevent the occurrence of a serviceability limit state. Considering that the resistance offered by the foundations makes the sagging deformation mode (Figure 2.4a) less sensitive than the hogging one (Figure 2.4b), these values have to be halved for the hogging mode (thus 1/4000, 1/600 and 1/1000, respectively). A limitation of the Eurocode is that it refers to new constructions only, while in case of excavation in urban areas, the damage assessment needs to be performed on the existing surface buildings.

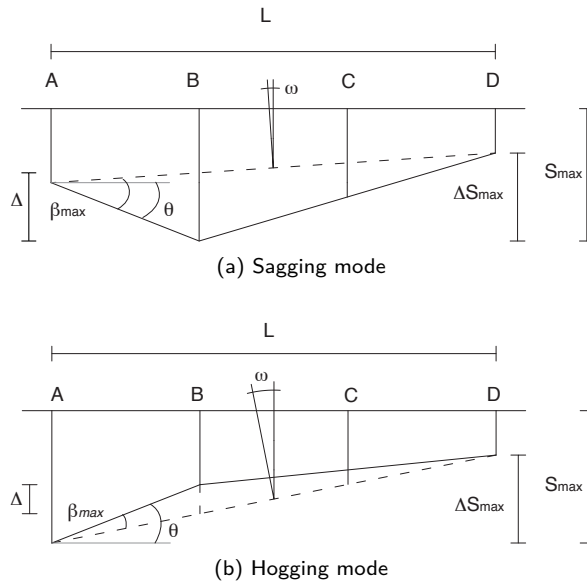


Figure 2.4: Deformation parameters: settlement S , differential settlement ΔS , relative deflection Δ , deflection ratio Δ/L , rotation θ , angular distortion (or relative rotation) β and tilt ω .

2.1.3 Dutch regulations

The Dutch Centre for Civil Engineering Research and Codes (CUR) provided for a damage classification of buildings on shallow foundations based on the maximum allowed rotation θ (CUR, 1996). Table 2.1 shows the different damage classes and their related rotation limits.

Other Dutch reports contain recommendations for buildings on pile foundation (CUR, 2008) and damage classification based on crack width (CUR-COB, 2000), but without references to limit values for ground deformations.

More detailed indications are given by local government regulations. The municipality of Amsterdam adopted a classification of the building quality based on the monitored cracks (SWD, 1998). For each of the classes indicated in Table 2.2, a different renovation level is recommended, from light interventions (class I) to complete demolition (class IV). If the ground deformation exceeds the criteria defined in

Table 2.1: Damage classification according to CUR (1996).

Damage class	Damage level	Rotation θ
0	No damage	$\leq 1/500$
1	Aesthetic damage	$1/500 - 1/300$
2	Structural damage	$1/300 - 1/100$
3	Risk for residents	$\geq 1/100$

Table 2.2: Building quality classification adopted by the Amsterdam municipality (SWD, 1998).

Quality class	Cracking level	Crack width
I	No cracking	0 mm
II	Slight cracks	0 – 2 mm
III	Moderate cracks	2 – 5 mm
IV	Severe cracks	> 5 mm

Table 2.3, the surface buildings fall in quality class IV. Guidelines to assess foundation and masonry conditions are also provided.

In Rotterdam (IGWR, 2009), horizontal and vertical tilt values are used to define building conditions (Table 2.4).

2.1.4 Other approximate methods

Several different empirical methods are internationally recognized in engineering practice for the first level assessment. These criteria neglect the effect of the surface buildings on the differential settlements. On the other hand, they have the advantage of the simplicity, and they can therefore be applied to a large number of structures potentially affected by the excavation. Skempton and MacDonald

Table 2.3: Limit values for the definition of building quality class IV, Amsterdam (SWD, 1998).

Deformation criterion	Limit value
Angular distortion β	1/50
Maximum settlement rate	4 mm/year
Maximum variation of settlement rate	2 mm/year

Table 2.4: Limit values for the definition of building conditions, Rotterdam (IGWR, 2009).

Building conditions	Horizontal tilt ω masonry buildings	Horizontal tilt ω concrete buildings	Vertical tilt ω_v
Good	$< 1/100$	$< 1/300$	$< 1/66$
Acceptable	$1/100 - 1/67$	$1/300 - 1/150$	$1/66 - 1/50$
Poor	$1/67 - 1/50$	$1/150 - 1/100$	$1/50 - 1/33$
Bad	$> 1/50$	$> 1/100$	$> 1/33$

Table 2.5: Angular distortion limits (Skempton and MacDonald, 1956).

Damage description	Limiting angular distortion β
Cracking of structures	$1/500$
Cracking of particularly sensitive brick structures	$1/1000$
Structural damage of façade	$1/150$

(1956) recommended the limit values for the angular distortion β shown in Table 2.5. Meyerhof (1953) introduced stricter criteria, distinguishing between load bearing walls and frame structures. Later he defined different safe limits for unreinforced bearing walls in hogging and sagging zone (Table 2.6). Polshin and Tokar (1957) defined similar limits for bricks walls in terms of deflection ratio Δ/L and they related them to the building length to height ratio (Table 2.7). Bjerrum (1963) estimated limiting values for the angular distortion β , relating them to the expected damage occurring to different types of structures. Table 2.8 summarizes his indications. Rankin (1988) suggested sole values of maximum rotation $\theta = 1/500$ and maximum settlement $S_{v,\max} = 10$ mm to exclude any risk of relevant damage.

Table 2.6: Angular distortion limits (Meyerhof, 1982).

Damage description	Limiting angular distortion β
Cracking of load bearing walls	1/1000
Cracking of infilled frames	1/500
Cracking of frame structures	1/250
Damage of unreinforced load bearing wall:	
hogging zone	1/2000
sagging zone	1/1000

Table 2.7: Deflection ratio limits (Polshin and Tokar, 1957).

Building length to height ratio L/H	Limiting deflection ratio Δ/L
$L/H \leq 2$	1/3333
$L/H = 8$	1/1000

Table 2.8: Angular distortion limits (Bjerrum, 1963).

Type of damage	Limiting angular distortion
Danger to frames with diagonals	1/600
Safe limit for no cracking	1/500
First cracking in panel walls	1/300
Visible tilting of high, rigid buildings	1/250
Danger of structural damage to general buildings	1/150

2.2 Limiting Tensile Strain Method: description and accessibility

The Limiting Tensile Strain Method (LTSM) is an empirical-analytical method used in engineering practice to predict the potential damage of buildings due to ground deformations (Boscardin and Cording, 1989; Burland and Wroth, 1974). The procedure was extensively adopted as second level of assessment for the London Underground Jubilee Line Extension project (Mair et al., 1996).

In the first level of preliminary assessment, simple indicators of the greenfield deformations, calculated neglecting the building on the surface, are compared with limit values, as described in Section 2.1. The buildings subjected to deformations higher than the limit values are evaluated by the LTSM, which includes a simplified model of the building itself.

In this section, assumptions, procedure and limitations of the LTSM are presented and discussed.

2.2.1 Assumptions

The LTSM is based on several simplifications, which allow for its easy and flexible application to the general preliminary assessment.

1. It is a decoupled assessment method: greenfield settlements are initially calculated and subsequently applied to an isolated model of the structure, which does not include the soil.
2. The building is represented as a linear elastic beam with the relevant building dimensions.
3. The analysis is limited to a 2D model of the structure.
4. The greenfield settlements are directly applied to the beam model, and the foundations are not modelled.
5. An equivalent bending and shear stiffness is derived for the beam; doors and windows of the building are not represented explicitly.

2.2.2 Procedures

The LTSM is subdivided in successive steps (Figure 2.5). First of all, the ground movements of the considered site are calculated, neglecting the presence of any structure. These greenfield displacements are then imposed to a simple model of the building. The settlement-induced deformations and strains of the equivalent

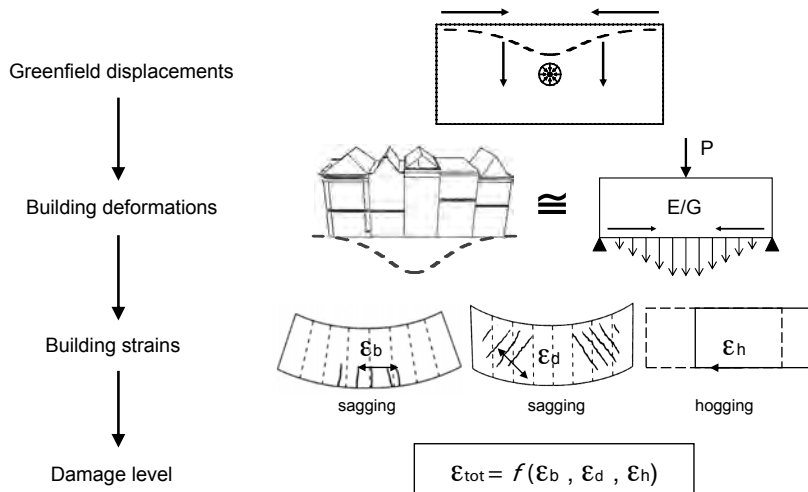


Figure 2.5: Schematization of the LTSM approach (after Boscardin and Cording (1989); Burland and Wroth (1974)).

building are subsequently calculated and related to a possible damage level. In the next section the separate steps of the procedure are illustrated.

Projection of greenfield ground movements on the building

The horizontal and vertical greenfield displacement profiles as described in Section 2.1.1 are applied to the building model as prescribed displacements. According to Mair et al. (1996), the influence area of the greenfield movements is limited by the 1 mm settlement line. In case of a long building extending the influence area, only the part of the building located inside the influence area is considered (Figure 2.6a).

Mair et al. (1996) assume that the building can be split at the point of inflection of the vertical settlement trough. In this way the parts of the structure subjected to convex (hogging) and concave (sagging) profile can be analysed separately (Figure 2.6b).

Determination of differential building deformations

The building is represented as an equivalent isotropic elastic beam (Figure 2.7a), with the same length L and height H of the structure. H is calculated from the

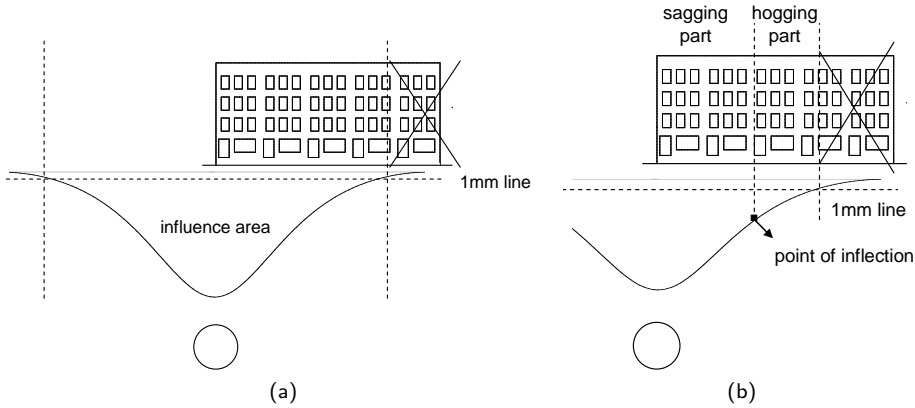


Figure 2.6: (a) Cut off for the building at 1 mm settlement line and (b) building partition at the point of inflection (after Mair et al. (1996)).

foundation level to the top floor, usually neglecting the roof. For each of the parts in which the building is split (hogging and sagging), the L/H ratio is calculated. The ratio between an equivalent flexural stiffness E and shear stiffness G is assigned to the beam. Burland and Wroth (1974) advise for a massive wall a value for E/G of 2.6. According to Burland et al. (2001), a modified E/G ratio of 12.5 should be adopted for frame structures, in order to take into account their flexibility and material ductility. Burland and Wroth (1974) defined various parameters to quantify the building deformation from the greenfield ground displacements (Figure 2.7b).

Calculation of induced building strains

According to Burland and Wroth (1974), based on an analytical beam equation for a simply supported beam in plane strain conditions, the maximum bending strain $\epsilon_{b,\max}$ and the maximum diagonal strain $\epsilon_{d,\max}$ can be derived as:

$$\epsilon_{b,\max} = \frac{\frac{\Delta}{L}}{\frac{L}{12I} + \frac{3I}{2LH} \frac{E}{G}} \quad (2.13)$$

$$\epsilon_{d,\max} = \frac{\frac{\Delta}{L}}{1 + \frac{HL^2}{18I} \frac{G}{E}} \quad (2.14)$$

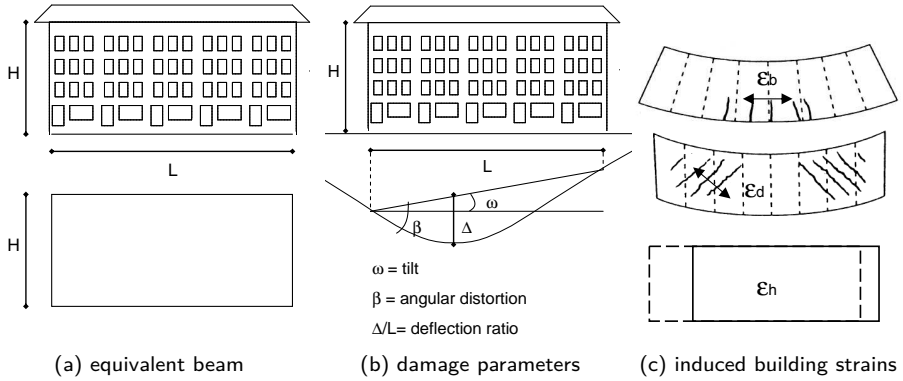


Figure 2.7: LTSM procedure: determination of building deformations and strains.

where I is the moment of inertia of the equivalent beam and t is the distance from the neutral axis to the edge of the beam in tension. For the sagging zone the neutral axis is assumed in the middle of the beam ($t = H/2$), for the hogging zone at the lower edge ($t = H$). The difference in the assumption of the neutral axis position for sagging and hogging zone derives from the empirical observation that a building in the convex part of the settlement profile is generally more susceptible to damage.

The change in length ΔL of the structure due to the applied horizontal displacements results in a horizontal strain:

$$\varepsilon_h = \frac{\Delta L}{L} \quad (2.15)$$

Combination of induced building strains

The bending and diagonal strains, calculated from the vertical settlements, and the horizontal strain, derived from the horizontal settlements, are assumed as uncoupled, and then combined in the total bending strain ε_{bt} and the total shear strain ε_{dt} . ε_{bt} is the combination of the maximum bending strain and the average horizontal strain, determined by simple superposition, while ε_{dt} is the combination of the maximum diagonal strain and the average horizontal strain, calculated using the Mohr's circle of strain:

$$\varepsilon_{bt} = \varepsilon_{b,\max} + \varepsilon_h \quad (2.16)$$

$$\varepsilon_{dt} = \frac{\varepsilon_h}{2} + \sqrt{\left(\frac{\varepsilon_h}{2}\right)^2 + \varepsilon_{d,\max}^2} \quad (2.17)$$

The highest value of these two combinations represents the total strain assumed for the structure.

Classification of building damage

The total strain value is related to a certain level of potential damage, described in terms of crack pattern and ease of repair (Boscardin and Cording, 1989; Burland and Wroth, 1974). The relation between the bandwidths of strain level and the different damage categories is illustrated in Table 2.9.

Additional recommendations

Boscardin and Cording (1989) suggested to use as input parameter the angular distortion β instead of the deflection ratio Δ/L . Netzel (2009) recommended to use the deflection ratio to calculate the bending strains and the angular distortion to calculate the diagonal strain of the equivalent beam. He also modified the shear factor value and he proposed an alternative approach for frame structures. Moreover, based on numerical analysis performed on 2D models of massive walls and masonry façades, he recommended to include the effect of the horizontal movement in the hogging zone and to neglect it in the sagging zone, in order to obtain a conservative damage prediction.

To take into account the beneficial effect of creep and relaxation of the structural material, the Foundation for Building Research gave recommendations about the variation of tolerable strain limits depending on the settlement rate (SBR (1998), Table 2.10). It also provided for indication of the limits reduction depending on the initial building conditions (SBR (1998), Table 2.10).

Differential settlements can occur at the connection of services to buildings, due to different stiffness or foundation of the services and the structures (Figure 2.8a). To avoid damage, the SBR (1998) advises that for Dutch conditions the maximum tolerable differential settlement at the connection of services and building is

$$\Delta z = z_1 - z_2 = 50 \text{ mm} \quad (2.18)$$

Table 2.9: Damage classification system (Boscardin and Cording, 1989; Burland and Wroth, 1974).

Category of damage	Damage class	Description of typical damage and ease of repair	Approx. crack width (mm)	Limit. tensile strain levels
Aesthetic damage	Negligible	Hairline cracks of less than about 0.1 mm width.	up to 0.1 mm	0 - 0.05
	Very slight	Fine cracks which can easily be treated during normal decoration. Perhaps isolated slight fracturing in building. Cracks in external brickwork visible on close inspection.	up to 1 mm	0.05 - 0.075
	Slight	Cracks easily filled. Redecoration probably required. Several slight fractures showing inside of building. Cracks are visible externally and some repainting may be required externally to ensure water tightness. Doors and windows may stick slightly.	up to 5 mm	0.075 - 0.15
Functional damage, affecting serviceability	Moderate	The cracks require some opening up and can be patched by a mason. Recurrent cracks can be masked by suitable linings. Repainting of external brickwork and possibly a small amount of brickwork to be replaced. Doors and windows sticking. Service pipes may fracture. Weather-tightness often impaired.	5 to 15 mm or a number of cracks > 3 mm	0.15 - 0.3
	Severe	Extensive repair work involving breaking out and replacing sections of walls, especially over doors and windows. Windows and door frames distorted, floors sloping noticeably. Walls leaning or bulging noticeably, some loss of bearing in beams. Service pipes disrupted.	15 to 25 mm, but also depends on number of cracks	> 0.3
Structural damage, affecting stability	Very severe	This requires a major repair involving partial or complete rebuilding. Beams loose bearing, walls lean badly and require shoring. Windows broken with distortion. Danger of instability.	usually > 25 mm, but depends on number of cracks	> 0.3

Table 2.10: Implementation in the LTSM of the settlement rate and the building condition (SBR, 1998).

Settlement rate	Increase of the tolerable strain limit	Building condition	Reduction of the tolerable strain limit
Short term	0%	Good	0%
Medium term	20%	Moderate	20 – 30%
Long term	55%	Poor	55 – 75%

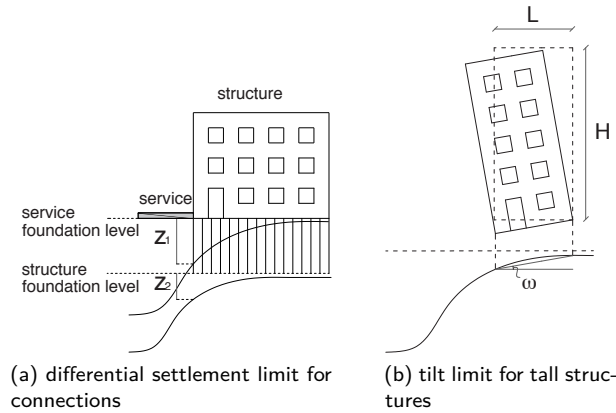


Figure 2.8: LTSM: additional recommendations.

where z_1 is the settlement of the structure foundation level and z_2 is the settlement of the services foundation level (Figure 2.8a). This empirical value represents only a rough indication in case of absence of any special flexible connection.

In order to avoid stability problems, Schultze and Horn (1990) advised to limit the tilt ω for tall structures to the maximum value of:

$$\omega_{max} = 0.005 \frac{L}{H} \quad (2.19)$$

where L is the base width of the building and H is the height of the building (Figure 2.8b).

The basic LTSM procedure with the presented additional recommendations has been summarized and implemented in an interactive spreadsheet (Appendix A). The

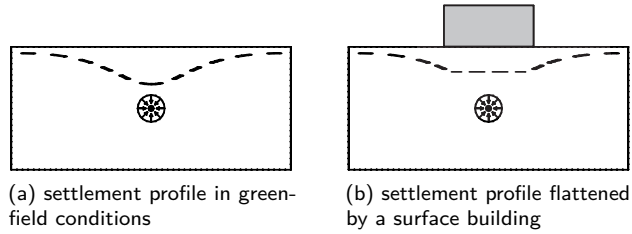


Figure 2.9: Soil-structure interaction effect on the settlement profile.

spreadsheet, included in the COB recommendations for the design of excavation pits in urban environment (Korff and Roggeveld, 2012), can be used as a simplified design tool for the preliminary classification of settlement-induced damage to buildings, according to LTSM.

Relative stiffness method

The original formulation of the LTSM neglects the soil-structure interaction effect on the settlement profile (Figure 2.9) and therefore can lead to damage overestimations. In order to evaluate the effect of building stiffness on the settlement profile, Potts and Addenbrooke (1997) performed a series of plane strain parametric analyses. Based on these numerical results, they suggested to multiply the greenfield deformations for convenient modification factors, according to the equations:

$$\left(\frac{\Delta}{L}\right) = M_{\frac{\Delta}{L}} \left(\frac{\Delta}{L}\right)_{\text{gf}} \quad (2.20)$$

$$\varepsilon_h = M_{\varepsilon_h} \varepsilon_{h,\text{gf}} \quad (2.21)$$

In Equation (2.20) $\frac{\Delta}{L}$ is the actual deflection ratio, $M_{\frac{\Delta}{L}}$ is the deflection ratio modification factor and $\left(\frac{\Delta}{L}\right)_{\text{gf}}$ is the greenfield deflection ratio. In Equation (2.21) ε_h is the actual horizontal strain, M_{ε_h} is the horizontal strain modification factor and $\varepsilon_{h,\text{gf}}$ is the greenfield horizontal strain.

Potts and Addenbrooke (1997) provided design charts to correlate the modification factors with the relative bending and axial stiffness, defined as:

$$\rho^* = \frac{EI}{E_s \left(\frac{L}{2}\right)^4} \quad (2.22)$$

$$\alpha^* = \frac{EA}{E_s \left(\frac{L}{2}\right)} \quad (2.23)$$

where I and A are the moment of inertia and the cross section area of the equivalent beam in plane strain conditions and E_s is the secant stiffness of the soil at 0.01% axial strain obtained from a triaxial compression test on a sample taken at half tunnel depth.

To overcome the disadvantage of ρ^* not being dimensionless in plane strain conditions, Franzius et al. (2006) modified ρ^* and α^* to be dimensionless, either in 2D plane strain and 3D conditions:

$$\rho^* = \frac{EI}{E_s L^2 z_0 B} \quad (2.24)$$

$$\alpha^* = \frac{EA}{E_s LB} \quad (2.25)$$

where z_0 is the depth of the tunnel axis and B is the width of the equivalent beam, corresponding to the building dimension in direction parallel to the tunnel axis.

2.2.3 Limitations

The LTSM is in principle a conservative method of assessment. However, analysing the individual features of the Limiting Tensile Strain Method (Section 2.2.1), it is possible to show that not all of them lead to conservative results.

1. The first simplification is the selection of a decoupled method: pure greenfield displacements are applied to an isolated model of the structure, which does not include the soil. This assumption is conservative, because the effect of building weight and stiffness tends to decrease the differential settlements and deformations Franzius (2003).
2. The representation of the building as a linear elastic element neglects the stress and stiffness redistribution due to the non-linear behaviour of the structural material. The phenomenon is particularly relevant in case of masonry structures,

which are subjected to brittle and localized cracking. The missing damage-induced redistribution can lead to incorrect predictions of damage and structural failure patterns.

3. The reduction of the 3D interaction problem to a 2D representation is one of the non-conservative simplifications. First of all, neglecting the 3D field of soil displacements and the tunnel advance effect can lead to an underestimation of the damage, even on façades in the direction transverse to the tunnel axis. Furthermore, also the effect of transversal walls on the global response and the 3D torsional behaviour of the structure, in particular when the tunnel track is not aligned to the building direction, could be relevant for the global damage (Franzius et al., 2006).
4. Due to the fact that in the limiting tensile strain approach the calculated displacements are applied directly to the beam model, the interaction effect provided by the foundation is neglected. This is in principle a conservative assumption for vertical displacements, but for horizontal displacements it can lead to an underestimation of the damage if the building is located in the sagging zone of the tunnelling-induced trough (Netzel, 2009). Especially the horizontal shear transfer capacity between soil and structure plays a role in this respect.
5. A last possible source of inaccurate assessments is the omission of an explicit representation of doors and windows. In the LTSM, the presence of big openings can be taken into account only in terms of a reduced equivalent stiffness (Pickhaver et al., 2010; Son and Cording, 2007). The fact that corners in openings work as damage localizers is ignored.

For all these reasons, a more detailed research is not only the logical following evaluation step for buildings where the second level of assessment indicates non-negligible damage, but it is also a necessary verification for those cases where the LTSM could result in an underestimation of the damage.

2.3 Finite Element Analysis

With the modern progress of numerical strategies and the parallel development of computational resources, analysis approaches which can satisfy the requirement for the detailed assessment have become more accessible. The Finite Element Method, for example, allows to represent the ground, the tunnel and the structures in a

unified fully-coupled model, which accounts for the interaction between these three components. Advanced constitutive laws enable to simulate all relevant non-linear behaviour of the materials involved. Mesh generation software makes it possible to include structural details. Staged analyses performed on 3D models allow for the evaluation of tunnelling advance effects and 3D response of the building. In the geomechanics research field, different finite element models were proposed using sophisticated soil stress–strain relations and advanced tunnel construction simulations, coupled with relatively simple models of the building (Bloodworth, 2002; Burd et al., 2000; Franzius, 2003).

2.3.1 Building modelling

In the first numerical analysis of soil-structure interaction, the building was represented as an elastic beam with equivalent axial and bending stiffness (Potts and Addenbrooke, 1997). Then, a no-tension criterion for the masonry, keeping the behaviour in compression elastic, was introduced (Augarde, 1997). Liu (1997), Burd et al. (2000) and Bloodworth (2002) adopted for their 2D and 3D analyses relatively simple constitutive models characterized by low tensile strength and high strength in compression. Rots (2000) simulated the masonry tension softening behaviour, which is necessary for a realistic post-peak stress redistribution; Netzel and Kaalberg (2000) applied it to a 3D model of a building with pile foundations, decoupled from the greenfield settlement profile. The same concept was applied to a series of 2D coupled analyses to evaluate the effect of the soil-building interface on the damage pattern (Boonpichetvong et al., 2006; Netzel, 2009). These numerical approaches could also be used to verify the results of operational tools for the diagnosis of structural damage due to soil subsidence (de Vent, 2011).

2.3.2 Soil modelling

The simplest finite element model adopted to simulate the ground displacements due to tunnel excavation in greenfield conditions considers the soil as a linear elastic continuum. It is well known that this constitutive law leads to a settlement trough wider and flatter than the one obtained from monitoring data (Rowe et al., 1983). A subsequent attempt simulated the soil by an elastic perfectly plastic material, but did not significantly improve the output settlement profile. It was shown that a narrower settlement curve can be obtained by adopting an elastic soil with stiffness increasing along the depth (Rowe et al., 1983). Addenbrooke et al. (1997), in their numerical studies on the soil-structure interaction, compared different pre-yield models with a Mohr-Coulomb failure criterion and showed that an improvement of the non-elastic

models could only be obtained by taking into account the non-linear effect at small deformations. The same soil model was adopted by Franzius (2003) for 3D FEM analysis of tunnel excavation effects on buildings. A widely spread constitutive law for the ground, used in 3D simulation of tunnelling, is a multi-surface plasticity model which includes the variation of stiffness at small pre-failure strains (Houlsby et al., 1999). This soil model was applied by various authors to the coupled analysis of tunnelling and structures (Augarde, 1997; Bloodworth, 2002; Liu, 1997). In their studies, the building on the surface was modelled with an increasing level of details, from a simple equivalent elastic beam to interconnected plane stress walls with no-tension behaviour. Despite the advance in soil non-linear constitutive laws, all the numerical models produce a tunnelling-induced settlement profile wider than the analytical gaussian curve proposed by Peck (1969), which is commonly considered as an acceptable simulation of greenfield data (Franzius et al., 2006).

2.3.3 Tunnel modelling

The first numerical models on tunnelling effects were limited to 2D and focused on the transverse settlement profile due to the ground volume loss. To simulate this phenomenon, many different methodologies were developed, to be subdivided in two main categories: stress reduction and displacement methods.

In the stress reduction method, the volume loss is obtained by diminishing the support pressure p_s which balances the ground pressure p_g after the soil excavation and the lining installation (Figure 2.10a). In the displacement method, after the soil removing, the lining is installed at a defined location and with a prescribed shape, smaller than the excavated area, in order to allow the movements of the ground towards the tunnel and to obtain the required volume loss (Figure 2.10b). Due to this procedure, the first formulation of the displacement method was called gap method (Rowe et al., 1983). The gap method was adopted also by Potts and Addenbrooke (1997) to control the volume loss in their numerical evaluation of the building stiffness effect. Other available 2D approaches combine these two basic strategies to obtain mixed methods, like the grout pressure method (Möller and Vermeer, 2008).

Augarde (1997) introduced an approach which allows to simulate not only the transverse volume loss but also the tunnelling advance in 3D. First, the ground initial conditions are calculated applying the weight of the soil elements. Then, a slice of tunnel elements is removed from the soil. Simultaneously, an elastic lining is installed, and out of balance forces are applied to the tunnel to equilibrate the new load conditions. Then, these forces are incrementally removed and a further radial pressure p_r is applied to the lining in order to obtain the desired amount of volume

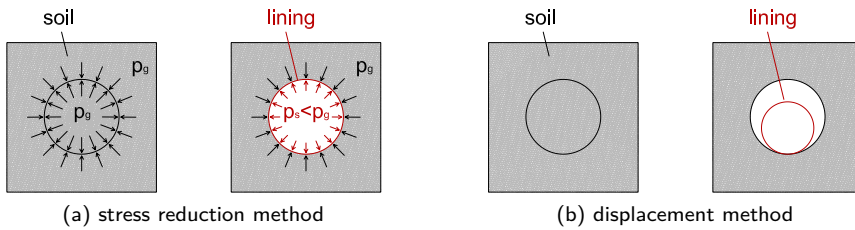


Figure 2.10: Numerical methods for 2D tunnelling simulation.

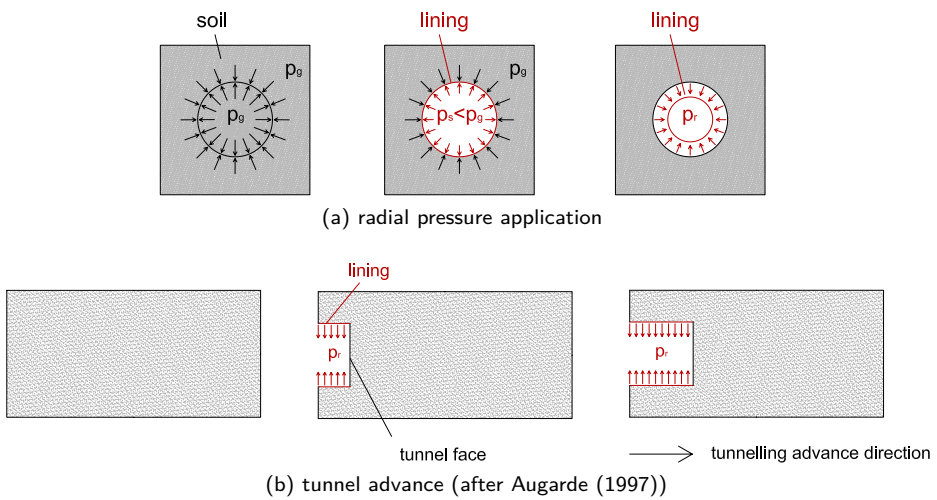


Figure 2.11: Numerical methods for 3D tunnelling simulation.

loss (Figure 2.11a). The procedure is repeated for sequential slices of soil until the tunnel is constructed completely (Figure 2.11b). This modelling strategy makes it possible to simulate the volume loss during the excavation stage.

2.3.4 Foundation and soil-structure interaction modelling

Foundations play a fundamental role in the transmission of the ground deformations to the building. Most coupled numerical models represent the bottom of the structure as fully tied to the soil elements (Augarde, 1997; Bloodworth, 2002). A line interface between 2D elements of structure and soil was introduced in finite element analyses in order to take into account the effect of normal and shear foundation stiffness on the building response (Boonpichetvong et al., 2006; Franzius, 2003; Netzel, 2009).

2.3.5 Proposed 3D coupled model

In this thesis, an improved global modelling approach is presented, which gives particular attention to the simulation of the structural non-linear behaviour. With regard to the analysed limitations of the simplified LTSM approach, the main features of the proposed model are:

1. A fully coupled finite element model, which takes into account the mutual interaction between the surface building and the soil and its tunnelling-induced settlements.
2. A cracking model for the masonry, with a post peak softening behaviour to reproduce the internal stress and stiffness redistribution after damage; this model allows for a realistic representation of the damage in terms of crack width and number.
3. A 3D representation with the simulation of tunnelling advance, to include the torsional behaviour of buildings, the construction phase effect, the combination of longitudinal and transverse trough and the possibility to study aligned as well as non aligned buildings.
4. A non-linear soil-structure interaction simulated by interface elements which transfer part of the horizontal and vertical deformations from the ground to the structure.
5. A detailed representation of the building, including bearing transverse walls and main openings.

The scheme in Figure 2.12 shows how the proposed model is positioned among the available damage assessment modelling approaches, with respect to represented elements and constitutive laws. The main features of the different models are

summarized in Table 2.11. Compared to previous approaches, the proposed model introduces the simulation of both non-linear masonry and soil-structure interaction in a 3D coupled model. The foundation, the soil and the tunnel represent a system of mixed boundary conditions for the building. The two main requirements are reproducing the selected reference settlement trough and simulating the effect of tunnelling advance on the surface. Considering these aims, a simplified linear elastic model is accepted for the soil.

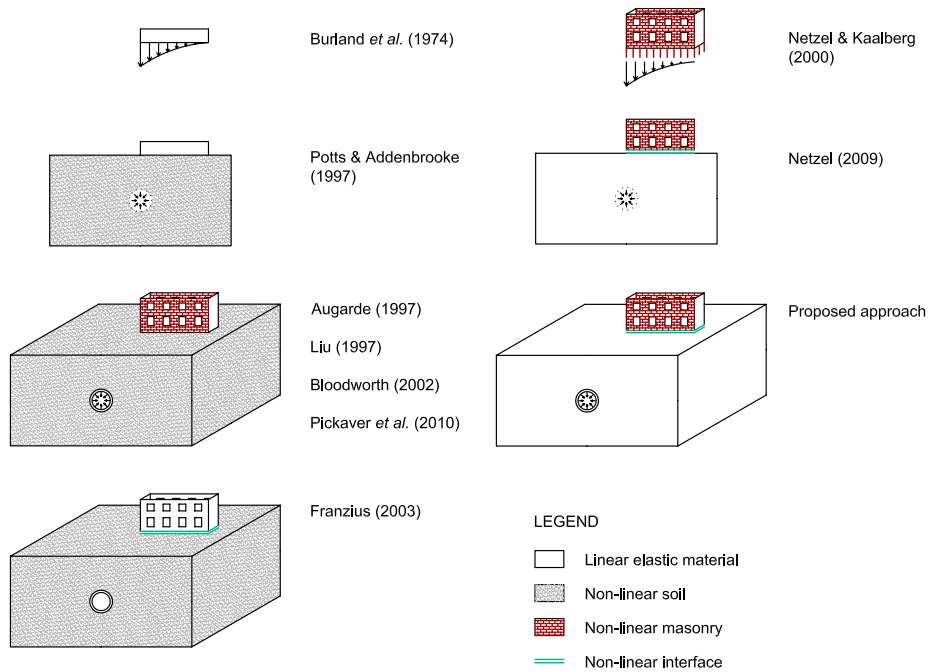


Figure 2.12: Scheme of the main features of the available damage assessment models. (See Table 2.11 for details).

Table 2.11: Overview of the development in modelling for the settlement-induced damage of masonry buildings.

Authors	Coupling	Dim.	Soil	Building	Tunnelling	Soil-structure interface
Burland and Wroth (1974)	Uncoupled model	1D	No	Elastic beam	No	No
Potts and Addenbrooke (1997)	Coupled model	2D	Non-linear elastic plastic	Elastic beam	Solid elements removal, application of radial stresses on tunnel boundary	No
Augarde (1997)	Coupled model	3D	Multi-surface plasticity	No-tension plane stress walls. Openings included	Soil elements removal, lining activation, radial stresses on tunnel boundary	No
Liu (1997)	Coupled model	2D/3D	Multi-surface plasticity	Elastic no-tension with small residual tensile strength. Openings included	Soil elements removal, radial stresses on tunnel boundary	No
Bloodworth (2002)	Coupled model	3D	Multi-surface plasticity	No-tension plane stress walls. Openings included	Soil elements removal, lining activation, radial stresses on tunnel boundary	No
Franzius (2003)	Coupled model	2D/3D	Non-linear elastic plastic	Elastic beam/ shell walls	Soil elements removal, lining activation	Non-linear interface
Netzel and Kaalberg (2000)	Uncoupled model	3D	No	Smearred cracked walls with tension softening. Openings included	No	Pile foundation
Netzel (2009)	Coupled model	2D	Linear elastic, stiffness increasing with depth	Smearred cracked walls with tension softening. Openings included	Contraction of the tunnel area	Non-linear interface

Authors	Coupling	Dim.	Soil	Building	Tunnelling	Soil-structure interface
Pickhaver et al. (2010)	Coupled model	3D	Multi-surface plasticity	Elastic beam/ no-tension plane stress walls. Openings included	Soil elements removal, lining activation and application of radial stresses on tunnel boundary	No
Proposed method	Coupled model	3D	Linear elastic, stiffness increasing with depth	Total strain smeared cracked walls with tension softening. Openings included	Soil elements removal, lining activation and application of radial stresses on tunnel boundary	Non-linear interface

2.4 Crack modelling for masonry structures

The damage classification system for masonry buildings subjected to various settlement profiles refers to the number of cracks and the crack width. The convenience of using numerical analysis in the framework of the existing damage classification system strongly depends on the possibility of relating the finite element output to the required assessment input in terms of cracks. Cracking of quasi-brittle materials can be incorporated in constitutive laws for finite element models by means of two approaches: discrete and smeared modelling.

2.4.1 Discrete approach

In the discrete models for masonry, the brick units and the mortar joints are represented as separate elements. This approach allows for the simulation of the actual texture of the masonry structure and for the localization of the damage in pre-defined planes of weakness, which generally correspond to the mortar joints (Rots, 1997). In the framework of the discrete approach, various computational models have been proposed, accounting for different levels of details. The finite element discretization can vary from the separate representation of brick, mortar and their contact interface (Lourenço, 1996; Rots, 1997) to a simplified approach that unifies the mortar joint and the mortar-brick interfaces in a single discontinuity (Alfaiate et al., 2003; Gambarotta and Lagomarsino, 1997a; Lourenço and Rots, 1997). Analyses of settlement-induced damage on masonry structures with the distinct element method (Son and Cording, 2005) also fall in the category of discrete approaches. Depending on the physical application and the governing failure mode

to be captured by the numerical model (tensile, shear or compressive), differences can be found in the failure mechanisms included in the constitutive relations.

The discrete approach makes possible a direct estimation of the crack width, and therefore allows for an immediate comparison with the actual damage classification for buildings subjected to settlements. An accurate material testing is necessary to provide the model parameters. For actual projects of large structures or complex geometries the mesh generation and analysis effort may be considerable.

2.4.2 Continuum approach

In the continuum models, the masonry is represented as a single material with homogenized properties. The constitutive law describing the material behaviour relates the average stress and strain, and the damage is smeared out in the continuum elements. The continuum modelling approaches implemented in finite element analysis are generally classified in smeared crack-, damage- and plasticity- based models (Calderini and Lagomarsino, 2008; Gambarotta and Lagomarsino, 1997b; Massart et al., 2004; Rots, 2002; Zucchini and Lourenço, 2004).

Considering the different elastic modulus of masonry in the direction parallel and perpendicular to the longitudinal joints, an orthotropic linear-elastic model can be used for the initial stiffness (Rots, 1997). As for the discrete models, failure criteria can be associated with tension, compression and shear modes. In the analysed case of masonry buildings subjected to tunnelling-induced settlements, the damage is mainly due to tensile and shear stresses, and therefore the focus is on the modelling of tension and slipping modes.

In the continuum models, the cracking direction does not necessarily follow the material texture. The models provide crack strains which have to be translated to crack widths via the use of the crack bandwidth h as a finite element discretisation parameter (Rots, 2002). The material homogenization leads to a decreased number of material parameters and to a reduced time and computational effort, making the continuum models more suitable for the analysis of large-scale structures.

More recently, embedded discontinuities have been devised (Jirásek, 2000). Displacement discontinuities within a continuum element could be dealt with by enriching the element. The translation to crack widths is no longer necessary. Crack trajectories could run across the finite element mesh. To the author's knowledge no large scale analysis on masonry structures using embedded discontinuities have been published to date.

2.4.3 Incremental iterative analysis

The non-linear system of equations that arises from the discretisation of a physical model can be solved by adopting an incremental-iterative scheme (e.g. Belytschko et al. (2000)). As long as the evolving cracks grow in a stable manner, this scheme generally works quite well. However, due to the softening behaviour of quasi-brittle materials, convergence problems may arise as soon as microcracks coalesce into macrocracks which in turn results in unloading of the material at either side of the crack. Similarly, at structural level, a sudden release of the elastic energy, stored in uncracked parts of the façade and in the bedding, produces snap-throughs and snap-backs in the load–displacement response, which complicates the convergence behaviour in incremental-iterative procedures.

Starting from the 80s of the last century, researchers have attempted to find a successful and comprehensive solution for the convergence difficulties (Crisfield and Wills, 1988; de Borst, 1987). Although significant progress has been made in arc-length methods (Gutiérrez, 2004), it takes considerable knowledge, experience and effort to be able to work with these methods. Consequently, even nowadays, researchers may be confronted with the challenges posed by complex non-linear finite element analyses (Alfaiate et al., 2003). The difficulties involved when trying to solve the convergence problems, motivated the development of a non-iterative solution technique called sequentially linear analysis.

2.4.4 Sequentially linear analysis

This alternative solution procedure for non-linear finite element analysis, which was first proposed by Rots (2001), can be described as an event-by-event strategy (Rots et al., 2008). The basic idea is to capture the structural response through a series of scaled linear analyses, in which the scaling of the linear analyses is fully determined by “events”. In the present work, two types of event are considered: crack initiation and crack propagation. For each linear analysis, first the smallest load multiplier that leads to a critical stress state at some integration point is computed. Subsequently, the stiffness and strength are instantaneously reduced at the most critically loaded integration point according to a saw-tooth law. A saw-tooth law is a stepwise secant approximation of the continuous stress–strain relation (Figure 2.13). The pattern of identifying the minimum critical load factor and locally reducing the stiffness and strength properties is continuously repeated throughout the numerical simulation. The primary advantage of this approach is its numerical robustness since no iterative procedure is required to follow the global equilibrium path, even in case of sharp snap-back and brittle cracking.

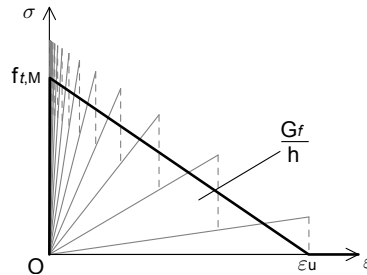


Figure 2.13: Continuous stress–strain relation (thick line) and the corresponding saw-tooth law (in grey).

An extension of the sequentially linear analysis (SLA) concept towards non-proportional loading was first proposed by DeJong et al. (2008, 2009). In their work, they assumed two types of loads: initial loads (which are constant and act permanently at the structure) and reference loads (which are scaled throughout the analysis). They demonstrated that it might not always be possible to select a critical load multiplier such that at all integration points a constitutively admissible stress state arises. That is, at some integration points the governing stress may grow larger than the actual material strength, regardless of the value of the load scale factor.

In Chapter 4 of this thesis, when constitutively inadmissible stresses are imminent, the last “successful” combination of initial and reference loads is scaled down proportionally, which implies that the initial loads are temporarily not fully present (Hendriks and Rots, 2013; Lekkerkerker, 2011). A possible explanation for the described problem is that per analysis step only one damage increment at only one integration point is applied, whereas in reality multiple damage increments may be required to obtain a new equilibrium state. Physically speaking, with the adopted strategy the structure is temporarily unloaded to allow for a stress redistribution, while new cracks arise or existing cracks propagate. In this way, the governing material law is always respected. To summarize, when no load multiplier exists such that at all integration points the material law is obeyed, the initial loads as well as the reference loads are temporarily scaled down proportionally. However, the initial loads may be recovered later on in the analysis.

2.5 From seismic to settlement vulnerability

The traditional approach to the assessment of excavation-induced damage on buildings is a deterministic correlation between ground deformation and expected level of structural damage, as described in the previous sections of this chapter. Recently, probabilistic approaches based on the same simplified analytical models have been presented (Juang et al., 2011), in order to include parametric variations and uncertainty effects. These probabilistic methods have already been extensively developed for predictions involving natural hazards, like the seismic (Calvi et al., 2006) and the flood (NRC, 2000) risk assessment. They can be applied to the geotechnical practice for the risk of man-induced damage. More specifically, the concept of risk as a potential that a certain event leads to a loss can be directly extended to the potential of structural damage due to an excavation-induced subsidence.

2.5.1 Seismic vulnerability assessment

The seismic vulnerability of a building represents its potential to be damaged by a ground shaking of a given magnitude. The vulnerability-based classification of structures is used to define a correlation between a given earthquake scenario and the most probable level of damage, for a certain building typology. The correlation between structural demand and expected level of damage can be generally derived using different types of data: empirical observations from field or experimental measurements, analytical or numerical results obtained by physical models, and expert judgements (Calvi et al., 2006).

Empirical vulnerability curves are based on data collected during post-earthquake surveys; analytical relations are obtained by the results of numerical analysis performed on structural models, while judgement-based empirical curves are derived from the personal evaluations of experts. All correlations are obtained by a statistical treatment of the data sets. A preliminary classification of the buildings is necessary in order to identify similar expected damage mechanisms on the basis of the structural parameters which have the strongest influences on the seismic response, like the building geometry, the material mechanical quality, the type of resistant system and the efficiency of the connections.

Judgemental vulnerability systems

A method to derive the vulnerability functions is the statistical elaboration of expert opinions. For the ATC-13, for example, a team of earthquake engineers provided an estimation of the average damage level related to different seismic intensity values

Table 2.12: Vulnerability classes according to building types by ATC (1985).

Material	Type of structure
Wood	
Light metal	
Unreinforced masonry	Bearing wall Load bearing frame
Reinforced masonry	Shear wall without moment-resisting frame Shear wall with moment-resisting frame
Reinforced concrete	Shear wall without moment-resisting frame Shear wall with moment-resisting frame Non ductile moment-resisting frame Ductile moment-resisting frame
Steel	Braced frame Moment resisting frame

for various building types (ATC, 1985). The classification of ATC-13 is based on the predominant structural material (wood, steel, masonry, concrete) and the vertical and horizontal structural organization (shear wall or moment resisting frame, see Table 2.12).

Empirical vulnerability systems

One of the empirical vulnerability approaches is based on the calculation of the probability to obtain a certain damage level due to a given seismic input, for an assigned class of building. This relation between ground motion and expected damage is expressed by the Damage Probability Matrices (DPM) (Braga et al., 1982; Whitman et al., 1973). The first DPMs were based on the MSK intensity scale (Medvedev, 1977), which is widely used in Europe starting in 1964. With regard to the classifications of buildings in vulnerability classes, the MSK considered three categories of structures, based on the vertical structural type. Later versions of DPMs (Giovinazzi and Lagomarsino, 2004), based the definition of damage probability functions on the European Macroseismic Scale (EMS) (Grünthal, 1998). In the EMS, six vulnerability classes are considered, taking into account the building material, the type of resistant system and the influence of the level of earthquake design of the structure (Table 2.13).

The assignment of a basic vulnerability class for a certain building is based on the combination of the type of structure (frame, walls) and the prevalent construction material (masonry, concrete, steel or wood). The transition to a weaker or a more

Table 2.13: Vulnerability classes according to building types (after Grünthal (1998)).

Type of structure		Vulnerability Class					
		1	2	3	4	5	6
Masonry	Rubble stone, natural stone	O					
	Adobe (earth brick)	O—					
	Simple stone	..O					
	Massive stone	—O..					
	Unreinforced, with manufactured stone units	..O..					
	Unreinforced, with RC floors	—O..					
	Reinforced or confined	..O—					
Reinforced concrete	Frame without Earthquake-Resistant Design (ERD)	...—O..					
	Frame with moderate level of ERD	...—O—					
	Frame with high level of ERD	...—O—					
	Walls without ERD	..O—					
	Walls with moderate level of ERD	..O—					
	Walls with high level of ERD	..O—					
Steel	Steel structures	...—O—					
Wood	Timber structures	...—O—					

resistant level depends on the influence of some factors which can affect the overall vulnerability, like the regularity, the ductility, the proximity to other buildings, the workmanship quality, the state of preservation, the already applied retrofits.

Another example of an empirical approach is represented by the Vulnerability Index Method (Benedetti and Petrini, 1984; CNR-GNDT, 1993). In this method, the susceptibility of a building to damage by an earthquake is indicated by a global score:

$$I_V = \sum_{i=1}^{10} k_i Q_i \quad (2.26)$$

which takes into account not only the general structural typology, but also the influence of characteristics like the plan and elevation configuration, the location, the type of foundations, the state of conservation. Each of the 10 parameters listed in Table 2.14 is identified by a qualification coefficient Q , depending on the building class (from A to D in Table 2.14) and assigned through an inspection; the weight k defines the relative importance of that particular feature on the seismic response.

In Japan, a common procedure to assess the vulnerability of a reinforced concrete building is the screening approach. In the Japanese Seismic Index Method, for example, a seismic performance index of the analysed structure is calculated,

Table 2.14: Vulnerability factors considered in the Vulnerability Index Method (Benedetti and Petrini, 1984).

Parameter	Class				Weight k
	A	B	C	D	
1. Organization of vertical structures	0	5	20	45	1.00
2. Nature of vertical structures	0	5	25	45	0.25
3. Location of the building and type of foundation	0	5	25	45	0.75
4. Distribution of resistant elements	0	5	25	45	1.50
5. Plan configuration: regularity	0	5	25	45	0.50
6. Vertical configuration: regularity	0	5	25	45	var.
7. Horizontal structures	0	5	15	45	var.
8. Roofing	0	15	25	45	var.
9. Details	0	0	25	45	0.25
10. Physical conditions	0	5	25	45	1.00

accounting for the basic building type, the structural details and the possible deterioration and cracking (JBDPA, 1990). Different versions of screening methods are also applied in Turkey, considering the type of resistant system (Hassan and Sozen, 1997), the material properties, the quality of workmanship and the architectural characteristics (Yakut, 2004).

Analytical vulnerability systems

The analytical methods are based on the evaluation of the seismic response through structural models (Bernardini et al., 1990; Singhal and Kiremidjian, 1996). They can cover the lack of post-earthquake data for particular building typologies. For this reason, they are often used in combination with the empirical methods, in the so-called hybrid approaches (Kappos et al., 1998).

In US, the HAZUS project FEMA (1999), is an example of application of a mechanical vulnerability model. The definition of building typologies is based on the classification system of BSSC (1992). A modification of the mechanical spectrum-based method adopted by HAZUS is used in the RISK-UE (2004) project, in combination with the macroseismic method (Giovinazzi and Lagomarsino, 2004).

The macro-modelling approach is a numerical method for the seismic assessment of un-reinforced masonry buildings, and it has been implemented in commercial software (Brencich et al., 1998; Magenes and Della Fontana, 1998). Based on the

subdivision of each building wall into linear macro-elements connected by rigid nodes, it enables to evaluate the structural response by identifying the main failure modes.

2.5.2 Settlement vulnerability assessment

Given the above description, it is worth considering the construction of an improved classification system for settlement-induced damage based on the same principles of the seismic vulnerability assessment. In both situations, the aim is to obtain a reliable prediction of the expected structural damage for a given input scenario: the ground motion due to an earthquake or the ground settlement due to an excavation. The vulnerability of a building in terms of susceptibility to damage by a ground shake of a given magnitude is transferred to the sensitivity of the structure to be damaged by a given settlement scenario. A preliminary evaluation of the building vulnerability can be done through an inspection based on the same idea of the Vulnerability Index Method. The structural features which are relevant for the settlement-induced damage will be different from the characteristics which influence the seismic behaviour, but a similar attribution of weights and qualification coefficients to the involved parameters can be done. In Chapter 9, an improved classification system, based on finite element analyses and considering the intrinsic vulnerability of the structure, is suggested.

Experimental analysis of a masonry façade

3

Laboratory tests performed in a controlled environment provide a better insight of the parameters governing the structural response to tunnelling and can be used as validation of computational models. This chapter presents an experiment carried out on a 1/10th scaled masonry façade subjected to tunnel-induced settlement. The results demonstrate the significant effects of soil structure interaction, presence of openings and brittle masonry cracking on the final damage.

3.1 Experimental model

To prove their reliability, numerical models require accurate comparison with real parameters and results. A possibility for the validation is offered by the comparison with field measurements from actual projects. To be used as validation of numerical models, a case study should include:

- a significant settlement-induced damage on the structure and a clearly recognizable damage mechanism, up to the structural failure;
- accurate field measurements of the settlement profile and its progress in time;
- the description of the soil-structure interaction, in terms of normal and tangential behaviour of the ground-foundation-building system;
- a detailed survey of significant structural damage, in terms of building deformation, crack pattern and crack width. The correlation between this information and the data related to the settlement development is particularly important

This chapter is based on Giardina et al. (2012)

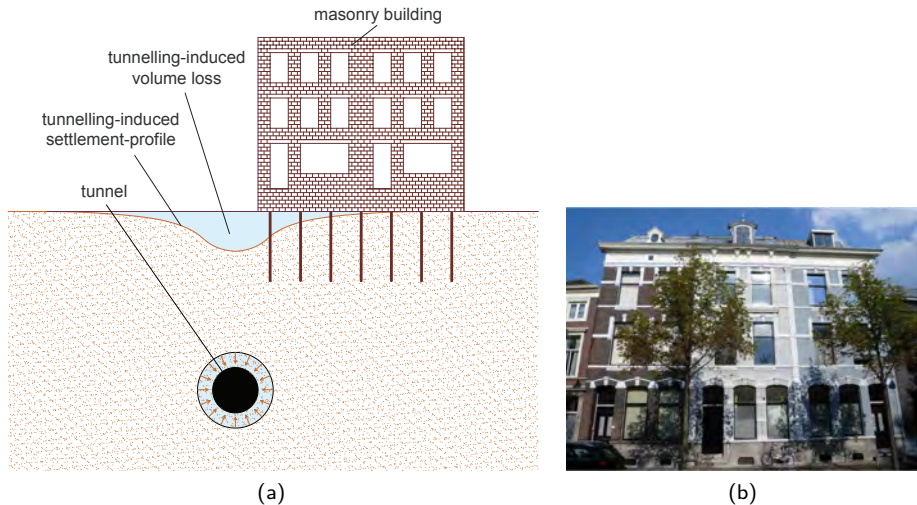


Figure 3.1: (a) Physical situation reproduced by the model and (b) historic Dutch house (prototype).

to verify the potential of the model to predict the damage progression, from crack initiation to complete failure;

- the mechanical characterization of all the involved components (soil parameters, properties of the building materials).

However, with the exception of a few cases (Burland et al., 2001), the literature in the field does not offer well-documented case studies which satisfy these requirements.

A solution to the lack of complete real data is given by performing laboratory tests. Pre-defined settlement troughs can be applied to scaled building models. In this way, the problem is modelled under experimentally known conditions, and monitored throughout the entire test. Only very few experiments have been published on complex masonry structures subjected to ground displacements (Laefer et al., 2011; Marini et al., 2006; Son and Cording, 2005). Moreover, the lack of accurate crack measurements makes difficult the validation of numerical models simulating the material damage.

This chapter presents the results of a laboratory test carried out on a scaled masonry façade subjected to tunnel-induced settlements. Specific attention was paid to the soil-structure interaction modelling. The coupled effect of building weight and stiffness, soil characteristics and type of foundations plays a fundamental

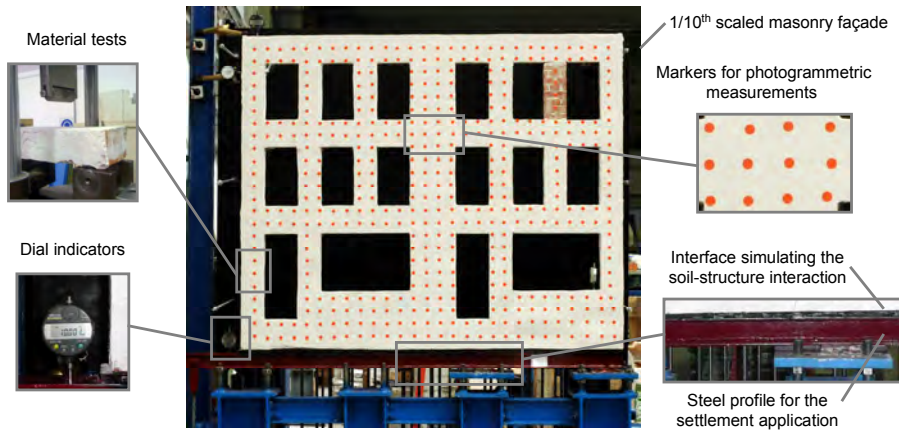


Figure 3.2: Main features of the experimental test.

role in the structural response, affecting the settlement profile and the resulting building damage. In this experiment, the coupling effect was included by means of an interface, with known normal stiffness, in order to clearly identify its effect on the structural response.

The experiment reproduces the situation illustrated in Figure 3.1a. A circular tunnel is excavated in soft soil under a masonry structure on a wooden pile foundation. The structure is situated outside the inflection point of the tunnel-induced settlement profile, in the hogging zone. The geometry of the building consists of a block of two house units and it is representative of typical historic Dutch houses (Figure 3.1b). The main features of the experiment are illustrated in Figure 3.2 and consist of:

- the construction of a 1/10th scaled masonry façade by the assemblage of scaled bricks and thin mortar joints. Compared to previous works (Laefer et al., 2011; Son and Cording, 2005) the different modelling solution represented here is the application of amplified vertical loads in order to replicate the prototype stress field (Marini et al., 2006);
- the controlled application of a pre-defined settlement trough by means of a flexible steel profile connected with the façade base;
- the simulation of the soil-structure interaction by inserting a layer of rubber between the masonry façade and the steel profile. This allows for an accurate

calibration of the interface stiffness, which plays a fundamental role in the building response;

- a continuous monitoring of the façade movements during the test execution. Deformations of specific points of the building are measured by dial indicators; furthermore, a photogrammetric system is used for displacement field monitoring and crack detection;
- a series of companion tests performed on the materials in order to measure their mechanical properties.

The main objective of this study is to make available accurate and reliable experimental data to be used as validation of numerical results. After describing the modelling choices and the experimental results, a mechanical interpretation and an analytical assessment are given.

3.2 Modelling issues

In this section, the transition from the real situation to the laboratory model is conceptually and practically described. The discussion concerns four main modelling issues: the geometrical scaling, the consequent amplification of loads, the settlements configuration and the soil-structure interaction. The modelling solutions were determined with relation to the main objective of the presented work. The priority guiding the different choices was therefore the generation of experimental data to be used for the validation of possible numerical models (Table 3.1). In this respect, more attention was paid to the definition of known and reproducible conditions (loads, constraints, material parameters) than to the accurate representation of the prototype.

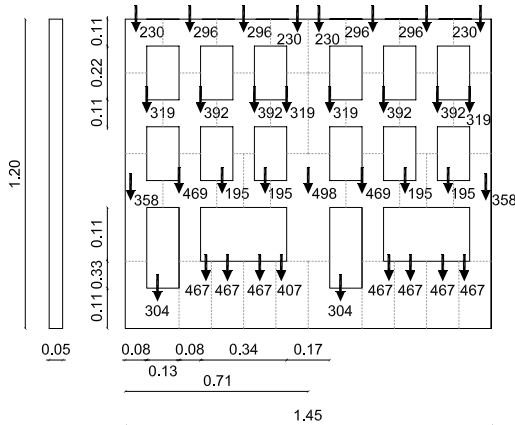
3.2.1 Façade scaled model

For practical reasons, the prototype shown in Figure 3.1a was scaled to 1/10 of the original size. Assuming that the façade represents the structural element most sensitive to settlement-induced damage, the 3D building was reduced to the 2D model shown in Figure 3.3, following a modelling approach commonly adopted in practice. The effect of transverse walls was not taken into account.

The masonry façade described in Figure 3.3a was built using 1010 scaled solid bricks and 2 mm thick layers of low strength lime mortar. The bricks were obtained by cutting solid bricks of $55 \times 120 \times 250 \text{ mm}^3$ (UNI 5628-65) in 30 parts. The

Table 3.1: Main features of the experimental model in relation to the prototype and the validation of a numerical model.

Prototype	Experimental model	Numerical model
3D building with brittle material	2D façade with brittle material	2D façade with a damage model
True scale	Scaled	Scaled
Tunnel-induced settlement profile	Simulated settlement profile	Simulated settlement profile
Soil-structure interaction depending on soil, building and foundation	No-tension interface with known normal stiffness	Non-linear interface or contact model



(a)



(b)

Figure 3.3: (a) Geometry of the scaled model, tributary areas and location of the amplification loads (dimensions in m, forces in N); (b) front view of the experimental set-up.

resulting bricks have dimensions of $25 \times 40 \times 50 \text{ mm}^3$. The choice of the mortar joint thickness was based on practical reasons. Wooden lintels were inserted above the openings. The actual properties of brick units, mortar prisms and masonry samples were evaluated through the material tests described in Section 3.3.

The test set-up has been re-adapted from an existing one. The original system was realized for a settlement test performed on a scaled model of the Loggia Palace, in Brescia (Marini et al., 2006). The experimental set-up consists of the 3D steel frame shown in Figure 3.3b.

3.2.2 Load amplification

The quantities involved in the experiment follow the equations of the dimensional analysis (Buckingham, 1914) applied to problems of stress and strain:

$$K_F = K_E K_L^2 = K_\sigma K_L^2 = K_\gamma K_L^3 = K_k K_L^3 \quad (3.1)$$

where K_F is the point load scale factor, K_E is the Young's modulus scale factor, K_L is the length scale factor, K_σ is the stress scale factor, K_γ is the specific weight scale factor and K_k is the bedding stiffness scale factor. The bedding stiffness relates the stress with the displacement, and typically has the units of N/m^3 .

Unlike in previous works (Laefer et al., 2011; Son and Cording, 2005), where the strength and the stiffness of the materials were reduced, the aim of the experiment is to keep the material strength and the stress conditions as close as possible to the prototype ones. This leads to the condition $K_\sigma = 1$. Since the material of the model and the real building is the same, $K_E = 1$, and since the geometrical scale factor is $K_L = 1/10$, Equation (3.1) accordingly yields $K_F = 1/100$, $K_\gamma = 10$ and $K_k = 10$. Therefore, to reproduce the same stress field, the material specific weight of the model should be 10 times larger than the one of the prototype material. If the prototype masonry is adopted instead ($K_\gamma = 1$), there are two possible strategies to overcome the problem: performing a centrifuge test, which induces an amplified acceleration on the structure (Farrell, 2010), or introducing extra loads in the vertical direction, to reproduce the real stress gradient. Due to the difficulty to replicate such a large and complex structure in a centrifuge, the latter solution was adopted in this work.

The sum of the amplification loads F_M was dimensioned such that the stress level at the model base $\sigma_{M,\text{base}}$ was equal to the stress level at the prototype base $\sigma_{P,\text{base}}$.

$$\sigma_{P,\text{base}} = \frac{W_P}{A_P} \quad (3.2)$$

$$\sigma_{M,\text{base}} = \frac{W_M + F_M}{A_M} \quad (3.3)$$

where W_p and W_M are the prototype and the model weight, and A_p and A_M are the cross-sectional areas at the base of the wall for the prototype and the model, respectively.

Equation (3.1) gives:

$$\sigma_{M,\text{base}} = \sigma_{p,\text{base}} K_\sigma = \sigma_{p,\text{base}} \quad (3.4)$$

$$W_M = W_p K_L^3 \quad (3.5)$$

$$A_M = A_p K_L^2 \quad (3.6)$$

Substituting Equation (3.5) and Equation (3.6) in Equation (3.2) and Equation (3.3) and subsequently in Equation (3.4) yields:

$$F_M = W_p K_L^2 - W_p K_L^3 = 0.009 W_p = 9.0 W_M$$

The prototype weight W_p includes the façade self weight and part of the floor loads, based on a tributary length of 1 m. To reproduce the vertical gradient of stress along the façade height, the extra load was applied at 35 discrete points, as indicated in Figure 3.3a. The façade was then subdivided in tributary areas, and the single values were calculated considering the tributary area of each point load.

As shown in Figure 3.4a, 35 horizontal bars transfer the vertical amplification loads to the model. They were loaded in the mid-span through vertical bars and supported at their ends on the fixed frame and on the façade. The connection with the frame was realized by means of the system illustrated in Figure 3.4b, to avoid the bar slipping off. On the façade side, a segment of a rubber o-ring was inserted between the bar and the masonry, to create a hinge and to align the load along the mid-plane of the wall. This solution allows for small rotations of the load bar system, which follows the applied differential settlement. Moreover, the o-ring allows for the diffusion of the stresses on a wider portion of masonry. The bars system also provides the bracing action to the structure in the out-of-plane direction.

The vertical bars were connected to the horizontal bars through ringbolts (Figure 3.4b). A series of conical spring washers were interposed between each bar and its connection to the fixed frame, to significantly reduce the bar axial stiffness. The springs are characterized by a known non-linear load–displacement diagram, which allows to measure the applied force through the springs shortening. During the application of the vertical settlement, the spring displacements were regularly monitored and their load was recovered if necessary, in order to avoid variations in

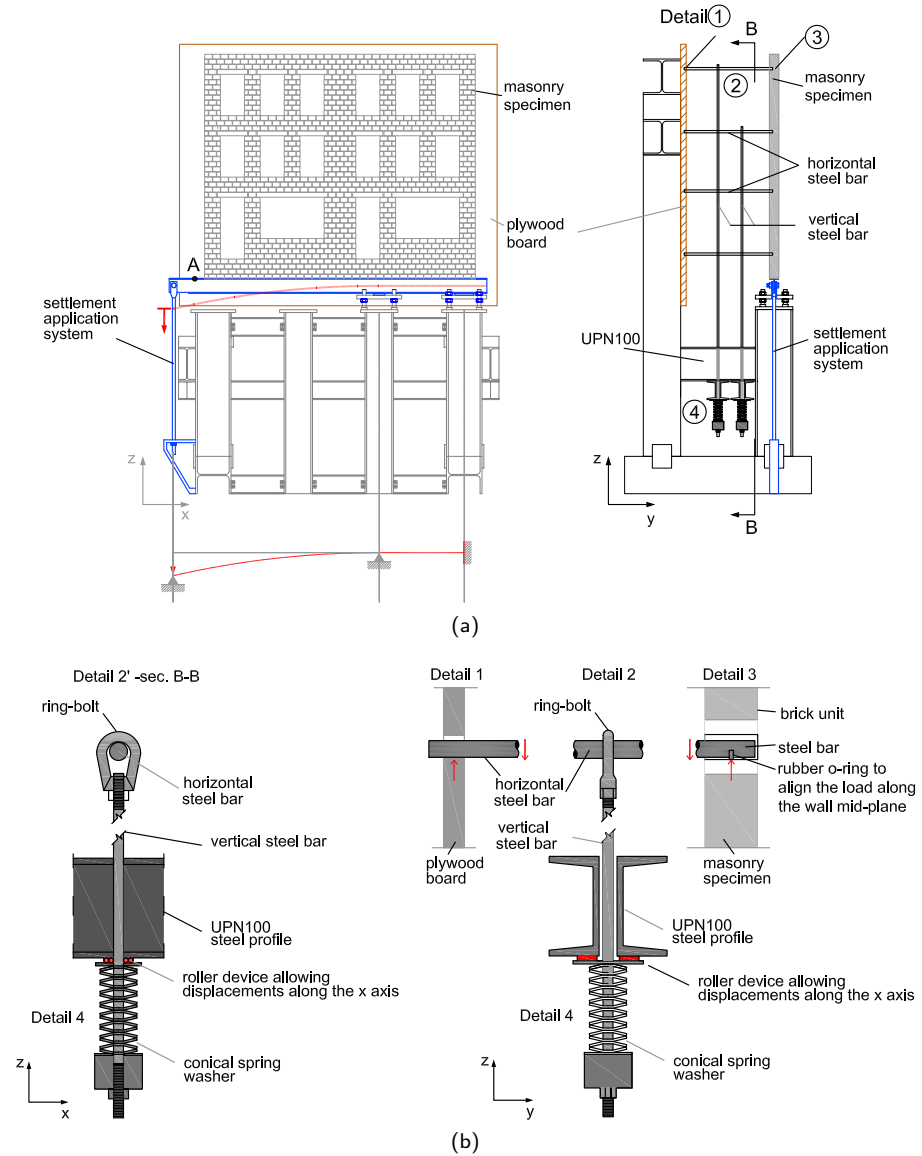


Figure 3.4: (a) Front and lateral view of the experimental set-up and (b) details of the system for the application of the amplified vertical loads.

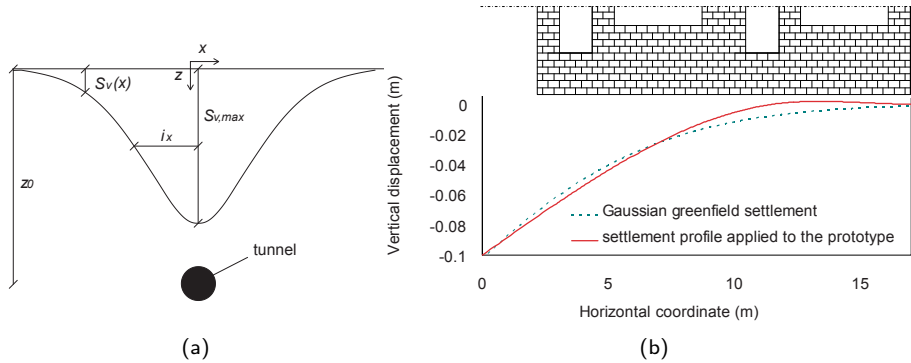


Figure 3.5: (a) Gaussian curve to describe the vertical displacements due to tunnelling, in the transverse direction (Peck, 1969); (b) settlement profile applied to the model prototype.

the façade pre-compression. Roller devices were inserted between the load system and the supporting beam connected to the fixed frame, in order to allow for the horizontal shifting (Marini et al., 2006).

3.2.3 Settlement configuration

The analytical curve proposed by Peck (1969) (Equation (2.1) and Figure 3.5a) produces a settlement profile wider than the one obtained from field data, but the Gaussian curve is still commonly accepted for the preliminary assessment. The settlement trough applied to the prototype represents a pure hogging deformation, which is considered the most dangerous for the surface building (Burland et al., 2001). The graph in Figure 3.5b shows that the selected profile is comparable to the greenfield settlement-induced by a 20 m deep tunnel driven in stiff clay ($K=0.4$ in Equation (2.2)). The settlement profile applied to the model was derived using a linear elastic numerical analysis and then verified by applying the designed maximum displacement to the steel profile before the façade construction.

The model was supported by a H-shaped steel profile. This beam was connected to the fixed frame through a hinge and a fixed constraint, as shown in Figure 3.4a. Once the left end of the steel profile was pulled downwards, the resulting scheme led to the pre-defined hogging deformation. The progression of the test was controlled by the maximum displacement applied to the beam and measured under the bottom

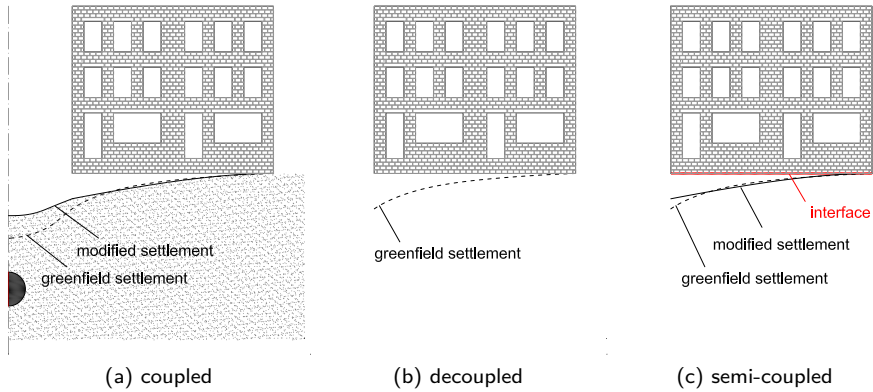


Figure 3.6: Modelling approaches.

left corner of the model (point A in Figure 3.4a). The settlement was applied in 23 steps of 0.5 mm, reaching a final displacement of 11.5 mm on the scaled model. This value corresponds to a final settlement of 115 mm on the prototype. During the test, the tension of the vertical bars was verified and re-adjusted through the shortening of the conical spring washers, every 5 steps, in order to keep the vertical loads constant. Due to the high stiffness of the steel profile, the maximum displacement caused by vertical loads on the profile was 0.6 mm, thus more than one order of magnitude smaller than the one caused by the applied displacement (11.5 mm).

3.2.4 Soil-structure interaction

The interaction between the soil, the building and its foundation plays a fundamental role in the structural response to tunnelling. Field measurements showed that the greenfield settlement profile is modified by the weight and the stiffness of the building-foundation system (Burland et al., 2001). Therefore, the most realistic approach to predict the building damage is a coupled numerical analysis (Figure 3.6a). Due to the complex mesh generation and to the computational expenses required by the fully coupled model, in actual engineering practice the preliminary damage prediction is based on an empirical-analytical decoupled approach, where the greenfield settlements are directly applied to a simplified model of the structure (Figure 3.6b). A compromise solution can be represented by the the semi-coupled model (Rots, 2000) (Figure 3.6c). In this approach, the greenfield settlements are applied to a non-linear interface

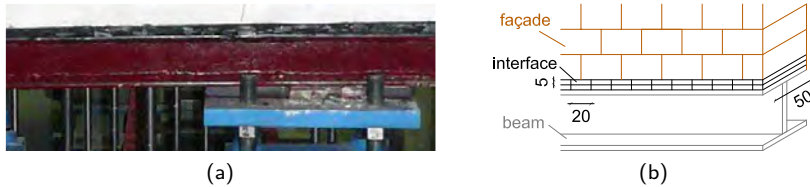


Figure 3.7: Rubber interface simulating the soil-structure interaction (dimensions in mm).

accounting for the soil and foundation stiffness. The model localizes the non-linear behaviour of different types of soil and foundation in a single numerical element, and therefore an accurate calibration of the interface parameters is required.

In order to allow for further validation of the last mentioned numerical approach, the effect of soil-structure interaction is modelled in this experiment by including a rubber interface of known compressive stiffness and no-tension behaviour between the façade and the H-shaped beam (Figure 3.7a). To simplify the number of parameters involved, and considering that field measurements show that the soil generally does not transmit horizontal strains to the structure (Burland et al., 2004), the interface does not provide shear strength. The interface design follows the simplified procedure adopted by Rots (2000) for the calculation of the equivalent interface stiffness of a pile foundation. For a typical Dutch historic house with the prototype dimensions, the resulting bedding stiffness is $k_{n,P} = 0.07 \text{ N/mm}^3$ (see Rots (2000) for further details). Applying the bedding stiffness scale factor $K_k = 10$, the equivalent bedding stiffness of the model interface becomes $k_{n,M} = 0.7 \text{ N/mm}^3$.

The interface was made by two layers of rubber strips with geometry illustrated in Figure 3.7b. The actual normal stiffness of the interface was measured through a preliminary compressive test and the design value of $k_{n,M} = 0.7 \text{ N/mm}^3$ was verified. The two horizontal layers were not connected to each other, simulating a no-tension behaviour in the normal direction, and the rubber layers were sliced to reduce the interface shear stiffness.

3.3 Material properties

Material mechanical characteristics were investigated by means of experimental tests carried out on the masonry components, i.e. lime mortar and clay brick units, and on scaled masonry samples (Figure 3.12). The material testing results are summarized

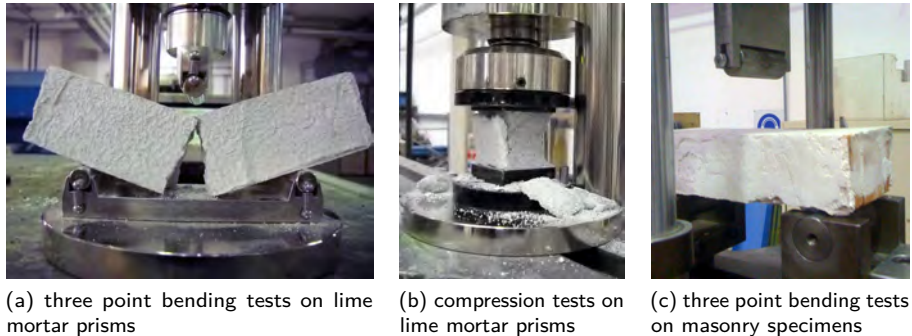


Figure 3.8: Material testing.

in Table 3.2. Some combination of material parameters, resulting from the tests, was not consistent with literature results. A reassessment would be desirable, but for practical reasons it was not performed during this research.

3.3.1 Mortar

The mortar was composed by hydrated lime and 0.1 mm sand aggregate. The lime mortar mechanical properties were investigated with reference to specific standards for lime based materials (CEN, 2007a). Flexural strength was measured through three point bending tests, performed on lime mortar prisms (Figure 3.8a). At failure, the prism breaks into halves, and the two prism portions are tested in compression (Figure 3.8b). Tests were performed after 35 day curing in controlled environmental conditions. The average lime mortar flexural strength is $f_{f,m} = 0.31 \text{ N/mm}^2$, whereas the average compressive strength is $f_{c,m} = 0.62 \text{ N/mm}^2$.

3.3.2 Bricks

The compressive strength of the solid clay bricks was measured by loading up to collapse a pile of 8 brick units. Collapse occurred at $f_{c,u} = 14 \text{ N/mm}^2$.

3.3.3 Reduced scale masonry

Three small masonry specimens were taken from the model upon completion of the settlement test (5 brick layers, $84 \times 50 \times 133 \text{ mm}^3$, Figure 3.9a). Pier samples

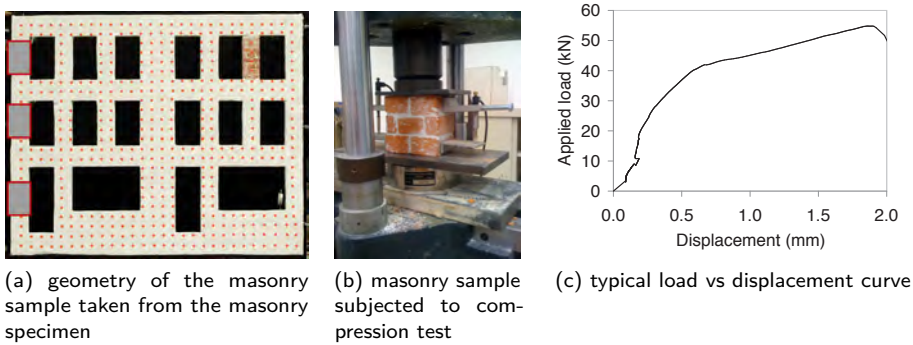


Figure 3.9: Masonry compression testing.

were tested in compression (Figure 3.9b). The average scaled masonry compressive strength $f_{c,M}$ was measured as equal to 11.4 N/mm^2 (Figure 3.9c). The result is quite unusual, as traditional masonry usually exhibits smaller strength. However, the data can be the result of the reduced thickness of the joints.

Other specimens ($84 \times 50 \times 160 \text{ mm}^3$) were tested in three point bending (Figure 3.8c) and in pure tension. The latter test results were disregarded, as all specimens failed at negligible load levels. During three point bending tests particular precautions were taken to prevent friction at the supports to avoid that friction would interfere with the flexural resistance. The average flexural strength based on 3 specimens was $f_{f,M} = 0.29 \text{ N/mm}^2$ and failure always occurred at the mortar to brick interface.

Shear tests were performed for varying vertical confinement, thus simulating masonry shear behaviour under different compression levels. Compressive stress levels were selected to reproduce the masonry stress magnitude at the first floor level (0.2 N/mm^2) and at the masonry wall base (0.3 N/mm^2). Further tests were carried out at a high confinement level of 0.4 N/mm^2 . For each pre-compression stress level, three masonry specimens were tested.

The masonry specimens are brick couplets bonded by thin 2 mm lime mortar joint. Figure 3.10a,b shows the special testing equipment designed for scaled masonry shear testing (Giuriani et al., 2007). The tests were carried out in displacement control. By tightening bolt A, a relative displacement is applied to steel profiles B and C, which are glued to the bottom and top brick respectively. The alignment of the steel components B and C allows applying the shear load along the mortar

bed-joint mid plane. A roller support is interposed between the masonry couplet top face and the transverse steel plate to avoid any friction during the test. Vertical rebar pretension allows applying the confinement stress distribution to the specimen. In order to keep the vertical stress level constant throughout the test, the vertical rebar stiffness is significantly reduced by means of a series of conical spring washers. This way no significant variation in the applied vertical load is induced by the bar deformation caused by the joint slip. Figure 3.11a shows average shear stress vs displacement curves for varying vertical confinement levels. All curves show an initial linear elastic branch until the shear peak strength is reached, when a crack develops and propagates along the brick to mortar joint interface. Peak shear strength increases for increasing vertical confinement. The post peak shows a softening trend until pure friction resistance is reached. For increasing applied displacement a slight reduction in the friction resistance follows the wearing of the fracture asperities. As expected, the failure behaviour of masonry joints under shear actions for varying moderate vertical confinement levels, can be described by the Mohr Coulomb friction law (Figure 3.11b):

$$\tau_u = c - \sigma \tan \phi = 0.03 + 0.27\sigma$$

where c is the initial shear strength, $\tan \phi$ is the tangent of the friction angle of the interface between brick unit and mortar joint and σ is the vertical confinement. For higher normal compressive stresses, the validity of the Coulomb law is lost and crushing/shearing of the units is observed.

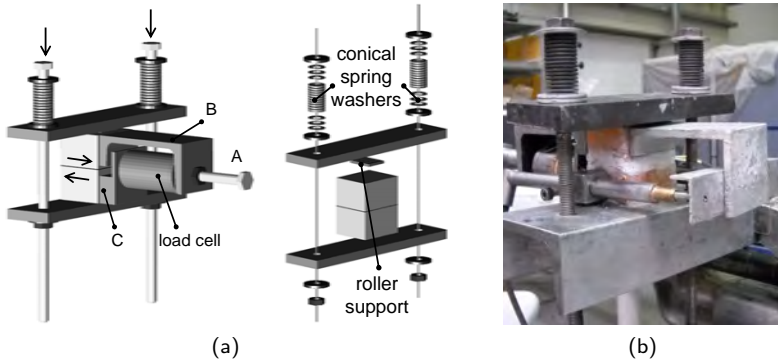


Figure 3.10: a) Shear test set-up (Giuriani et al., 2007); b) masonry couplet subjected to shear test.

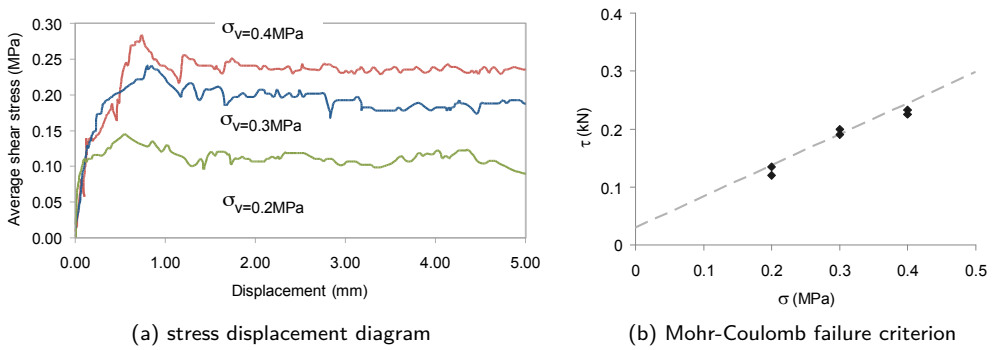


Figure 3.11: Shear test results.

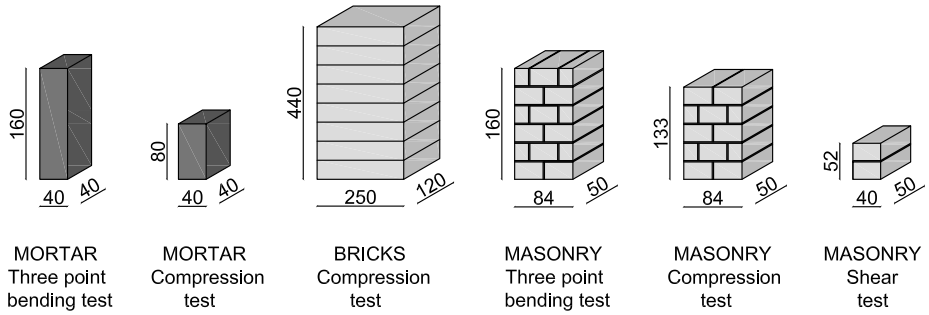


Figure 3.12: Specimens for the material characterization tests.

Table 3.2: Material characterization.

Material	Dimension (mm)	Number of specimens	Type of test	Measured parameter	Average value
Mortar	40×40×160	3	Three point bending	Flexural strength	$f_{f,m}=0.31$ N/mm ²
	40×40×80	3	Compression	Compressive strength	$f_{c,m}=0.62$ N/mm ²
Brick	250×120×440 (8 units)	3	Compression	Compressive strength	$f_{c,u}=14$ N/mm ²
Masonry	84×50×160	3	Three point bending	Flexural strength	$f_{f,M}=0.29$ N/mm ²
	84×50×133 (5 layers)	3	Compression	Compressive strength	$f_{c,M}=11.4$ N/mm ²
	40×50×52	3	Shear	Cohesion Friction angle	$c=0.03$ N/mm ² $\tan \phi=0.27$

3.4 Instrument set-up and monitoring system

Different measurement techniques were applied to monitor the model response in terms of displacements, deformations, damage pattern and crack width growth. The accurate recording of these data as a function of the applied settlement is essential to understand the model behaviour and to allow for further validation.

Before the activation of the vertical load the façade was covered with a 1 mm layer of white gypsum to facilitate the damage monitoring (Figure 3.13a). Bending tests were performed on masonry specimens, to verify that the gypsum layer was not influencing the façade stiffness. The width opening of the individual cracks which were identified as most relevant to the failure mechanism was monitored through the application of Whittemore strain gauges (Figure 3.13b). The location of the main cracks will be described later in Section 3.5.

Dial indicators measured the vertical and horizontal displacements of the façade upper corner (points B and C in Figure 3.13b). The relation between these movements and the vertical displacement measured at the supporting beam level (point A in Figure 3.13b) gives an indication of the global response. In particular, the horizontal displacement of point C allows for the interpretation of the model rotation during and after cracking.

Moreover, photogrammetric measurements were taken in order to monitor the displacement field variation. A grid of 12 mm circular markers with a spacing of 50 mm was glued on the model surface before the beginning of the test (Figure 3.13b). Two fixed grids of markers were placed at each side of the model and used as reference system for the image post-processing (Figure 3.13a). Pictures of the façade and the reference grid were taken at each settlement application step using a high resolution digital camera with a fixed 50 mm lens. In the post-processing of the pictures (Yang, 2009) the pixels of the red markers were isolated from the white background. For each marker, the position of the geometric centre of its pixels was defined in x and y coordinates. The matrices of the marker position at the different steps allowed for the calculation of their relative horizontal and vertical displacements. If the markers are used as nodes of a structural mesh of the model, this technique makes it possible to derive the strain evolution. Furthermore, discontinuities in the monitored displacement field enable to verify the crack position and progression of the cracks.

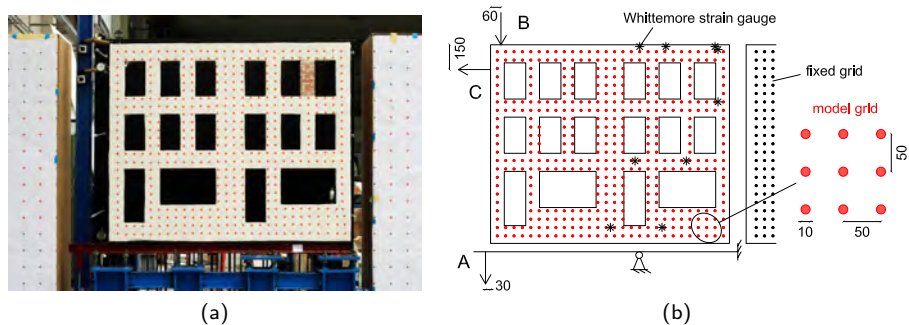


Figure 3.13: a) Monitoring set-up; b) position of dial indicators A, B and C for displacement monitoring, Whittemore strain gauges for crack width monitoring and grid of markers for the photogrammetric measurements (dimensions in mm).

3.5 Experimental results

This section illustrates the results of the test in terms of displacements, strains, crack pattern and damage evolution. No damage was detected as a consequence of the pre-compression.

Figure 3.14 shows the vertical and horizontal displacements of the model top left corner for increasing vertical displacement A. Figure 3.15 shows the modification of the vertical displacements transmitted from the steel profile to the façade as a consequence of the interface. The results are derived from photogrammetric measurements at different levels of maximum applied settlement.

The horizontal displacement measured by the dial displacement C (Figure 3.14a) reflects the crack pattern development (Figure 3.14b). Due to the negligible movement of the right end of the building, this measure represents the relative horizontal displacement of the façade top. The curve shows a first change in slope after 2 mm of settlement, at the onset of the first just visible cracks (hairline cracks), mainly located at the corners of the openings. The resulting crack pattern, the kinematic mechanisms and the vector plots of the incremental displacements of the markers at 2.5 mm, 5 mm, 7.5 mm and 10 mm of maximum applied settlement are illustrated in Figure 3.16. The initial damage affects the right part of the model, in the area located between the hinge and the fixed supports of the beam. The façade shows a crack pattern typical of a structure subjected to bending moment, with a vertical crack arising at the top, near the hinge section. The exact location of the cracks is

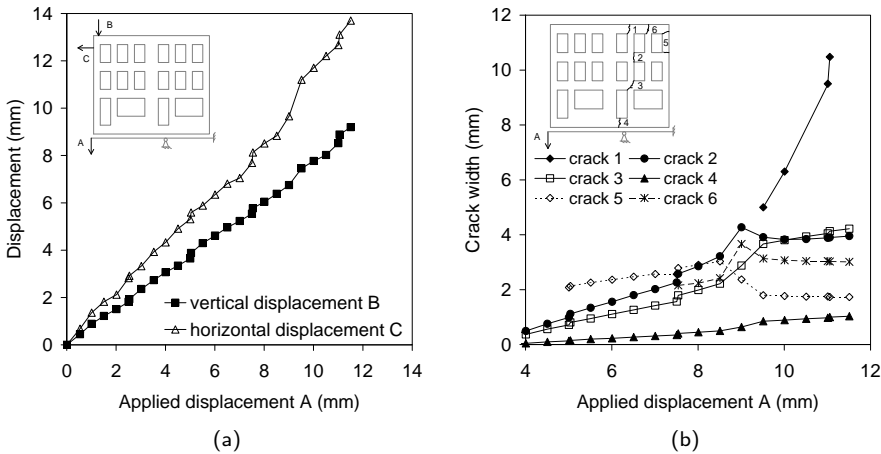


Figure 3.14: a) relation between the applied settlement and the vertical and horizontal displacements of dial indicators B and C, respectively; b) relation between the applied settlement and the width of the monitored cracks.

strongly dependent on the position of the windows, which induce stress localization at their corners and define the weakest cross sections (Figure 3.16a).

After the onset of hairline cracks, the trend of the horizontal displacement curve is essentially linear up to 7 mm of settlement. The initial cracks grow and propagate from one side to the other of the architraves and the piers between the windows, following the mortar joints. This tendency demonstrates that the structure is subjected to a rigid body motion of the portions of masonry defined by the initial cracks. In particular, the entire block at the left of the hinge support rotates following the imposed settlement trough (block I in Figure 3.16b). This mechanism causes the horizontal pulling of blocks II and III; as a consequence, piers IV and V start rotating (Figure 3.16b).

An increase of the slope can be seen between 7 and 7.7 mm of settlement, when 3 of the 4 cracks delimiting the rotating block I (Figure 3.16b) open significantly (crack 6, 2 and 3). Another sensitive change of slope occurs between 9 and 9.5 mm of maximum applied displacement. This corresponds to a very sudden increment of crack width of the first upper crack (crack 1). Consequently, the main rigid rotation shifts from block I to block VI, which is defined by cracks 1 and 4. This second mechanism continues to develop for increasing settlements, until the end of the test.

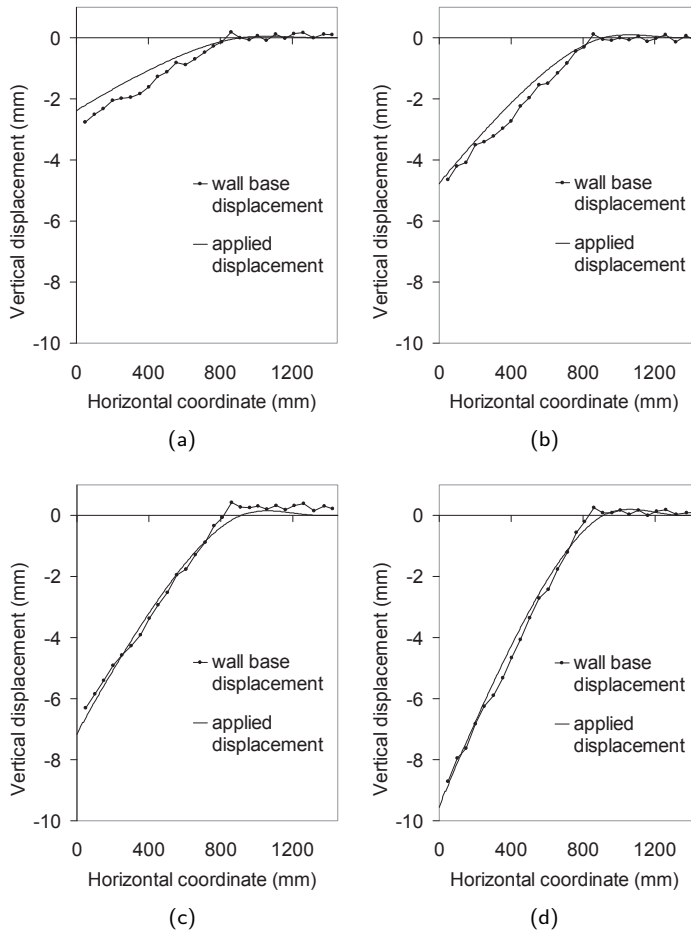
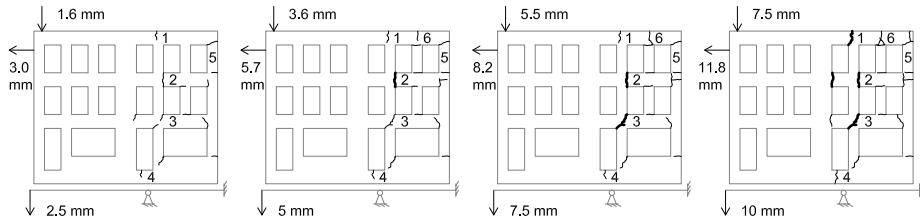
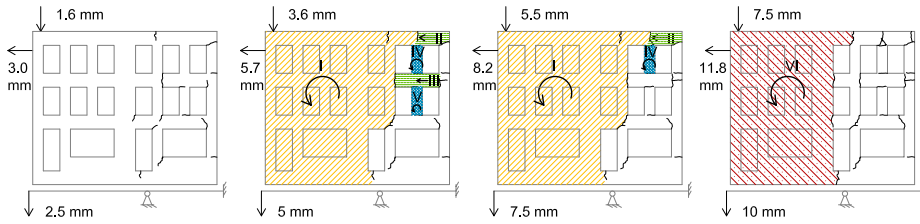


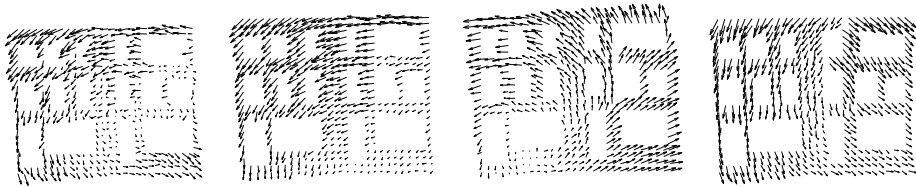
Figure 3.15: Interface effect on the transmission of the applied settlement profile of the façade at 2.5 mm (a), 5 mm (b), 7.5 mm (c) and 10 mm (d) of maximum applied vertical displacement.



(a) crack pattern evolution



(b) kinematic mechanism development and identification of the main rigid blocks (from I to VI)



(c) vector plots of the incremental displacement of the markers

Figure 3.16: Experimental results at increasing level of maximum applied displacements (from left to right).

Table 3.3: Crack width at increasing values of applied maximum settlement from Whittemore strain gauges measurements.

Maximum applied settlement (mm)	Crack 1 (mm)	Crack 2 (mm)	Crack 3 (mm)	Crack 4 (mm)	Crack 5 (mm)	Crack 6 (mm)
3.0						
3.5		0.261	0.630			
4.0		0.492	0.367	0.044		
4.5		0.757	0.561	0.097		
5.0		0.986	0.714	0.134	2.080	
* 5.0		1.118	0.804	0.150	2.133	
5.5		1.339	0.945	0.197	2.255	
6.0		1.556	1.107	0.227	2.360	
6.5		1.800	1.261	0.269	2.471	
7.0		2.019	1.419	0.312	2.570	
7.5		2.261	1.565	0.348	2.566	
* 7.5		2.577	1.790	0.404	2.788	2.154
8.0		2.852	1.985	0.448	2.904	2.235
8.5		3.215	2.217	0.499	3.030	2.418
9.0		4.269	2.875	0.641	2.370	3.664
9.5	5.000	3.909	3.665	0.851	1.796	3.134
10.0	6.300	3.826	3.803	0.891	1.766	3.069
10.5		3.842	3.935	0.939	1.743	3.042
11.0	9.500	3.888	4.048	0.975	1.750	3.041
* 11.0	10.480	3.897	4.128	0.998	1.733	3.024
11.5		3.950	4.219	1.032	1.731	3.014

* indicates a spring load recovering step

More detailed information can be derived from the analysis of the individual cracks monitored by the Whittemore strain gages. Numerical values are reported in Table 3.3. Figure 3.14b illustrates the relation between the maximum applied settlement and the crack width of six relevant cracks. For crack 1 the crack width was measured only in the final steps of the test. As for the global horizontal displacement curves (Figure 3.14a), also in this graph a linear trend can be observed up to 7.5 mm of settlement, proving the onset and progression of a rigid body motion. Thereafter, all the cracks show a bigger width increment, which indicates a rapid development of the initial rotating mechanism. The situation changes at 8.5 mm of settlement. Cracks 2, 6 and 3 grow significantly between 8.5 and 9 mm of vertical displacement, and then they tend to unload and partially close. The reason for this unloading is the brittle development of crack 1. As a consequence, the main kinematic mechanism moves from one block to another, as described above. An overview of the kinematic

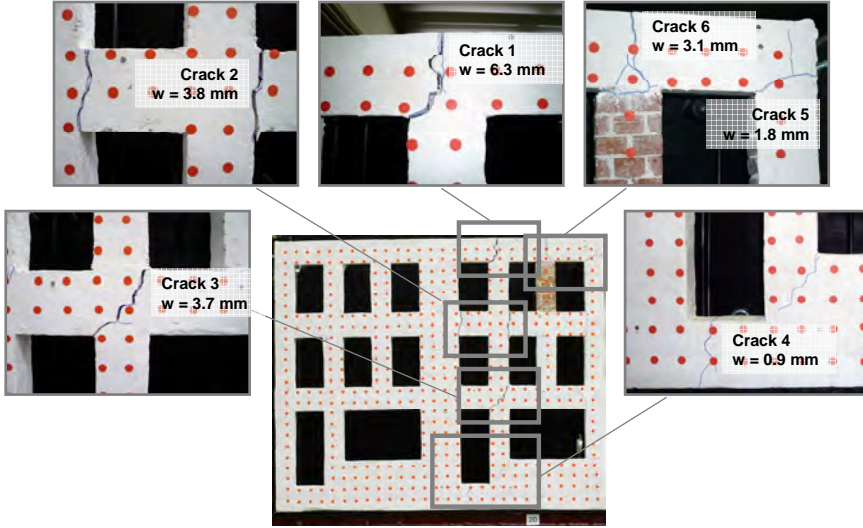


Figure 3.17: Crack pattern at 10 mm of settlement applied to the scaled model.

motions is offered by Figure 3.16, where the vector plots of each marker incremental displacements are shown. The displacements of all markers are also tabulated in Appendix B.

For a maximum vertical displacement of 10 mm the façade shows a very severe damage, with a maximum crack width of 6.3 mm and several cracks larger than 1 mm (Figure 3.17). The displacement of the façade base with respect to the applied settlement is presented in Figure 3.15d. Detailed pictures of the main cracks are shown in Figure 3.17. In the real scale prototype this would correspond to a maximum crack width of 63 mm for 100 mm of soil subsidence. The interpretation of the damage level based on the actual damage classification system for structures subjected to tunnel-induced settlement is discussed in Section 3.7.

For a correct use of these results as validation of numerical models, it is worth to mention that the scale effect on fracture energy has to be taken into account. The material fracture energy G_f is defined as the amount of dissipated energy necessary to create a unit area of a crack. Typical units for G_f are N/m. With reference to Equation (3.1), the fracture energy scale factor K_{Gf} can be related to the Young's modulus scale factor through the equivalence:

$$K_E K_L^2 = K_{Gf} K_L \quad (3.7)$$

which yields $K_{Gf} = 1/10$. In the presented experiment, the prototype material was chosen and $K_{Gf} = 1$ was used instead. Therefore, when applying computational models for quasi-brittle materials based on fracture energy to simulate the test results, $K_{Gf} = 1$ has to be applied.

3.6 Mechanical interpretation

The analysis of the monitored displacements and the principal crack progression allows for a mechanical interpretation of the model response. Figure 3.16a shows the crack pattern development, with initial hairline cracks evolving in macro cracks. For increasing values of the applied displacement, the rotation of the left part becomes clearly visible (Figure 3.16b), leading to complete separation.

The evolution of internal and interface stresses caused by the imposed settlement can be schematised by simplifying the façade as a wall without openings (Figure 3.18) (Mastrodicasa, 1993). In the initial stage, before the vertical load activation, the wall is subjected to self weight only. This produces a uniformly distributed pressure p_0 on the interface (Figure 3.18, diagram a); the interface reacts with an equal and opposite pressure r_0 (Figure 3.18, diagram b). As soon as the vertical loads are applied, the pressure and the reaction proportionally increase, reaching the values p_1 and r_1 , respectively. The application of the settlement profile causes a vertical dragging motion of the affected wall portion, from the left end to the hinge support. In case of a relatively stiff structure, or a settlement affecting only a small portion of the wall base, a gap arises between the no-tension interface and the wall, and the interface reaction vanishes. As a consequence of the hogging trough, the wall is subjected to bending and shear deformations. The interface stresses concentrate and increase around the support, while the wall part on the right end tends to uplift and unload the interface (Figure 3.18, diagram c).

The shear and bending moment qualitative diagrams can be derived by subsequent integration of the stress diagram (Figure 3.18, diagram e). The maximum shear is acting at the hinge support, while the section subjected to maximum bending moment is located between the hinge and the fixed supports. As a matter of fact, the first crack arises vertically on the upper side of the section subjected to the highest tensile stress (crack 1 in Figure 3.17).

The initial bending damage was also predictable from the type of applied settlement (Mastrodicasa, 1993). Considering a settlement on a relatively long portion of the wall base, the maximum bending stress σ_{\max} and the maximum shear stress τ_{\max} acting on the wall without openings as a consequence of the settlement can be evaluated as:

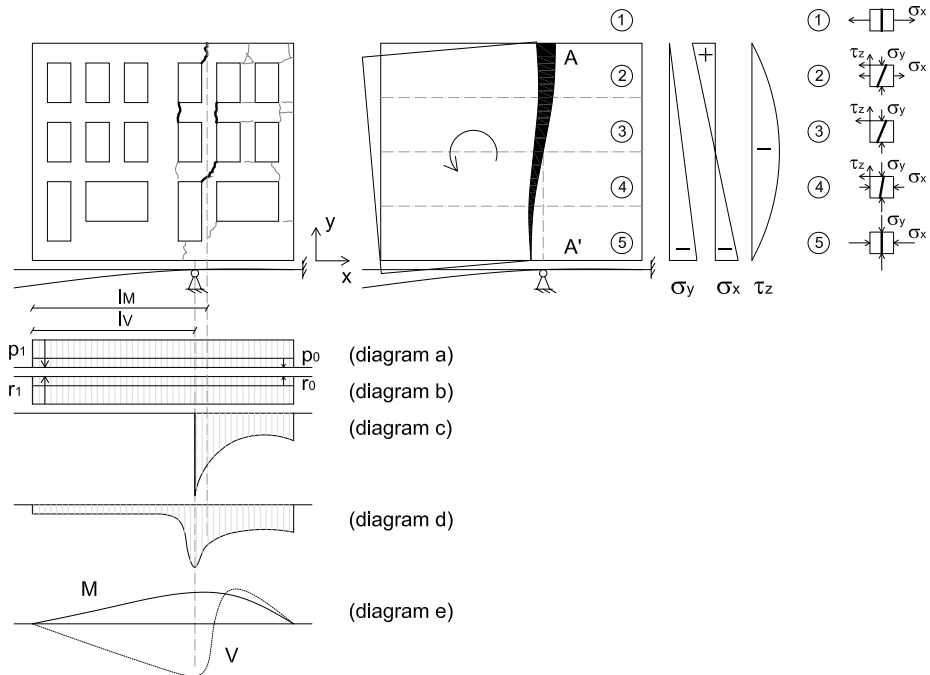


Figure 3.18: Mechanical interpretation of the experimental results. All the diagrams, with the exception of diagram d, refer to the simplified model of the façade as a wall without openings.

$$\sigma_{\max} = \frac{M_{\max} \frac{1}{2} h}{I} \quad (3.8)$$

$$\tau_{\max} = \frac{3}{2} \frac{V_{\max}}{A} \quad (3.9)$$

where h is the wall height, I is the wall moment of inertia and A is the wall cross section. The maximum moment M_{\max} and the maximum shear V_{\max} are:

$$M_{\max} = \frac{1}{2} \gamma h t l_M^2 \quad (3.10)$$

$$V_{\max} = \gamma h t l_V \quad (3.11)$$

where γ is the wall mass per unit volume (including the amplified vertical loads), t is the wall thickness and l_M and l_V are the distances between the wall left end and the sections subjected to maximum moment and maximum shear, respectively. Being $I = \frac{1}{12} t h^3$ and $A = t h$, σ_{\max} and τ_{\max} become $\sigma_{\max} = 3 \frac{\gamma l_M^2}{h}$ and $\tau_{\max} = \frac{3}{2} \gamma l_V$. Since $l_M > l_V$ (Figure 3.18) and $l_V > h/2$, $\sigma_{\max} > \tau_{\max}$, and therefore the initial damage is expected to be caused by bending.

The analysis of the simplified stress diagrams makes it also possible to predict the cracking direction. Figure 3.18 qualitatively shows the stresses acting on the wall section. On the portion of wall between the hinge and the fixed support, the wall weight and the vertical loads cause a linear distribution of normal stresses σ_y . The diagram of the moment-induced normal stresses σ_x and the shear-induced tangential stresses τ_z are assumed linear and parabolic, respectively. Figure 3.18 also qualitatively shows the stresses acting on infinitesimal material elements located at 5 different levels of the transverse section A-A'. For each element, the preferential crack orientation can be derived from the resulting principal stress direction. The damage arising in section A-A' is consistent with the high ratio between the portion of the building subjected to settlement and its entire length (Mastrodicasa, 1993), and it can be recognized in the rotation mechanism of the façade (Figure 3.16d).

Although useful to identify the main motion components affecting the façade response, these interpretations are limited by the initial simplified assumptions. In the first instance, the idealization of the façade model as a simple massive wall neglects the effect of the openings on the crack pattern localization, initiation and development. The actual openings also affect the façade stress field, and therefore the interface reaction, which in reality is not uniformly distributed. In the second place, the interaction between the actual stiffness of the structure and the interface causes a stress redistribution which differs from the one idealized in diagram c of Figure 3.18. In particular, due to the low strength mortar and the large amounts of

openings, the tested façade is not stiff enough to allow for gapping with the interface, during the settlement application. Therefore, the interface reaction does not vanish, but assumes a distribution more similar to the one qualitatively represented in Figure 3.18, diagram d. More specifically, up to an applied vertical displacement of about 2 mm the interface compressive stresses are due to the sum of the model self-weight and the amplified vertical loads. For increasing values of settlement, the combination of tensile stresses induced to the façade and low material tensile strength caused the masonry damage. The effect of the progressive cracking is a significant reduction of the façade stiffness. As a consequence, the structure follows the applied hogging profile, keeping the interface in compression. This effect is also confirmed by Figure 3.15, where the vertical displacements of both sides of the interface are compared. The effect of complex geometries, non-linear behaviour of the material and interface stiffness can be successfully estimated through advanced numerical analysis, which will be presented later in this chapter.

3.7 Analytical assessment

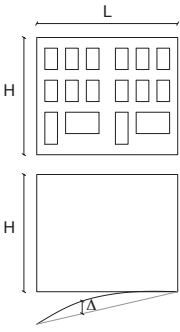
The results of the experimental test in terms of final damage have been compared with the assessment derived from the application of the Limiting Tensile Strain Method (LTSM) to the prototype (Section 2.2).

According to the analytical procedure, the vertical greenfield displacements as calculated in Section 3.2.3 have been imposed on a simplified model of the façade prototype. The model consists of an equivalent isotropic elastic beam, with the same length L and height H of the structure (Table 3.4).

Depending on the structural typology, an equivalent stiffness E and a shear stiffness G are assigned to the beam. Limit values for the ratio E/G are available in literature (Burland and Wroth, 1974; Son and Cording, 2007). For a masonry wall without openings, a value of E/G equal to 2.6 is indicated (Burland and Wroth, 1974). For a percentage of window openings of 30%, like in the analysed case, a minimum value of 11 is suggested (Son and Cording, 2007). Based on analytical beam equations for a simply supported beam, the maximum bending strain $\varepsilon_{b,\max}$ and the maximum diagonal strain $\varepsilon_{d,\max}$ of a structure subjected to hogging deformation (Burland and Wroth, 1974) can be derived from Equation (2.13) and Equation (2.14):

$$\varepsilon_{b,\max} = \frac{3\left(\frac{L}{H}\right)\left(\frac{\Delta}{L}\right)}{\frac{1}{4}\left(\frac{L}{H}\right)^2 + 1.5\left(\frac{E}{G}\right)} \quad (3.12)$$

Table 3.4: Data and results of the LTSM application to the prototype façade.

	Height	H	12 m
	Length	L	14.5 m
	Applied settlement	S	0.1 m
	Applied deflection ratio	Δ/L	2.6×10^{-3}
	Bending and shear stiffness ratio	E/G	11
	Maximum bending strain	$\epsilon_{b,\max}$	0.06%
	Maximum diagonal strain	$\epsilon_{d,\max}$	0.25%
	Total tensile strain	ϵ_t	0.25%

$$\epsilon_{d,\max} = \frac{3\left(\frac{E}{G}\right)\left(\frac{\Delta}{L}\right)}{\frac{1}{2}\left(\frac{L}{H}\right)^2 + 3\left(\frac{E}{G}\right)} \quad (3.13)$$

where Δ is the equivalent beam deflection (Table 3.4).

The highest value of the bending and diagonal strain represents the total tensile strain of the structure, and it is compared with the limiting values listed in Table 2.9. The ranges defined by the limiting tensile strain values are related to a certain level of potential structural damage, and they define six different damage categories. For each category an indication of the expected damage in terms of crack width and number of cracks is provided.

Table 3.4 reports the input data and the intermediate results of the LTSM application to the prototype façade. According to the LTSM, a moderate damage is expected for the prototype, with a maximum crack width up to 15 mm. The results clearly underestimate the final damage. One reason for this can be seen in the very low mortar strength. According to the Dutch Building Research Foundation (SBR, 1986), the tolerable strain limits of Table 2.9 should be reduced in order to take into account the initial building conditions. Considering the low quality of the mortar, a reduction up to 75% of the tolerable strain limits could be applied in this case, leading to a very severe damage classification. Another possible explanation for the non-conservative assessment performed by the LTSM is the presence of many large openings. This feature allows to increase the ratio between the equivalent beam bending and shear stiffness, but it also leads to significant damage localization, which is not taken into account in the analytical evaluation.

3.8 Conclusions

For the practice of damage assessment, laboratory tests are essential to validate numerical and analytical procedures under controlled conditions. In this chapter the tunnelling-induced damage on masonry structures was analysed through an experimental test on a 1/10th scaled façade model. Particular focus was placed on the load amplification, necessary to reproduce the prototype stress field, and on the soil-structure interaction, modelled by an interface with known normal stiffness. Displacements, deformations, damage pattern and crack width evolution resulting from the incremental application of an hogging settlement profile were monitored throughout the test.

The results showed that the soil-structure interaction plays an essential role in the structural response. The interface reduces the vertical displacements applied to the model. Furthermore, depending on the relative stiffness between the façade and the interface, stress redistribution is occurring within the façade. This proves the need of an accurate soil-structure interaction modelling to predict the settlement-induced damage. Further research based on field data is necessary to assign realistic values to the interface parameters.

The final damage strongly depends also on the presence of openings. Doors and windows lead to concentration of stresses at their corners, and therefore affect the crack localization. The damage development causes an additional redistribution of the façade internal stresses and further modifications of the final crack pattern.

The comparison with the damage assessment performed by applying the LTSM showed that in this case the analytical method underestimates the observed damage. Possible reasons for this non-conservative result can be found in the low mortar quality and the large amount of openings, which are not explicitly included in the LTSM. However, additional experimental and numerical tests, and comparison with analytical results are required to determine a clear tendency.

2D numerical analysis of a masonry façade

4

The results of the experimental test described in the previous chapter have been used to validate a semi-coupled approach for the modelling of the response of masonry buildings subjected to tunnelling-induced settlements. The 2D finite element model includes a continuum cracking model for the masonry material and a non-linear interface accounting for the soil and foundation stiffness. Continuum and discrete approaches for the masonry modelling have been evaluated, and incremental iterative and sequentially linear solution schemes have been compared. The results proved the capability of the continuum model to accurately reproduce the crack pattern and the deformation of the tested structures.

4.1 Numerical model

In the laboratory test described in Chapter 3, the 1/10th scaled masonry façade was subjected to self-weight and to a vertical load of 12.2 kN distributed in 35 application points. Single bricks were removed at the location of the applied loads, and wooden lintels were inserted above the openings. The façade was supported by a H-shaped steel profile with a hinge and a fixed constraint. A controlled hogging deformation was applied to the structure by pulling downwards the left end of the steel profile. A rubber layer simulating the soil-structure interaction was inserted between the façade and the steel beam. The 2D finite element model reproducing the experimental test is illustrated in Figure 4.1. Geometrical dimensions and applied load values are reported in Table 4.1.

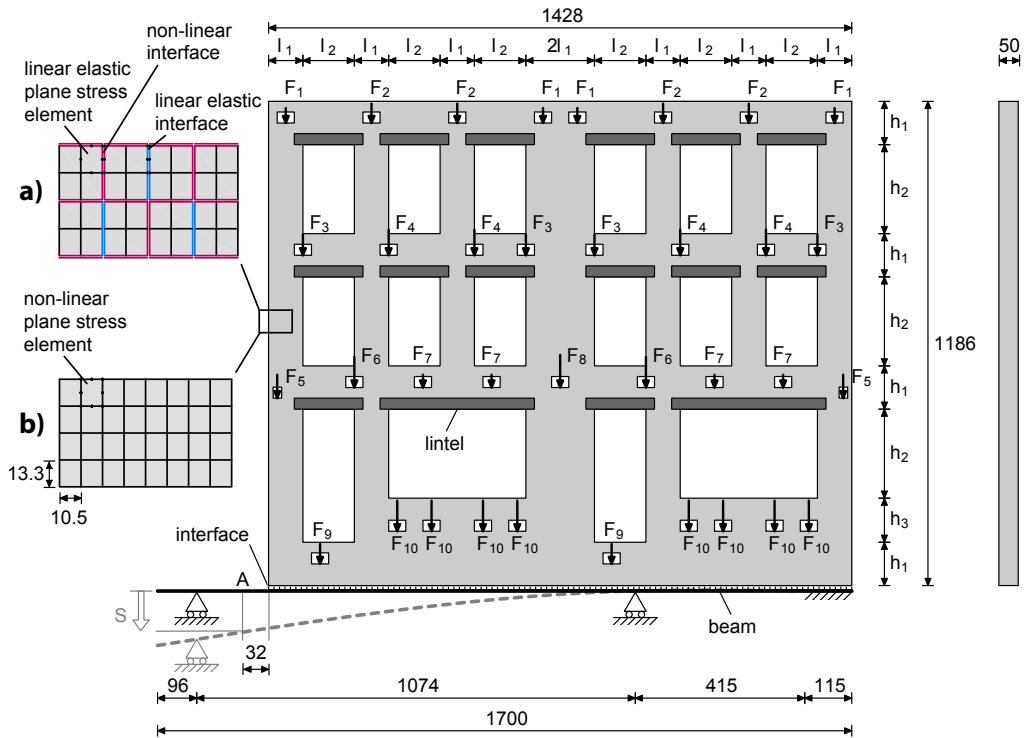


Figure 4.1: Model of the scaled masonry façade.

Table 4.1: Model geometrical dimensions and applied load values

Dimension	Value (mm)	Force	Value (N)	Force	Value (N)
l_1	84	F_1	230	F_6	469
l_2	126	F_2	296	F_7	195
h_1	106	F_3	319	F_8	498
h_2	218	F_4	392	F_9	304
h_3	108	F_5	358	F_{10}	467

4.1.1 Discrete model

In the discrete model, the bricks were represented by 8-node plane stress elements (Figure 4.1, insert (a)). The mortar joints and mortar-brick contact surfaces were lumped into 6-node line interface elements with zero-thickness. Vertical 6-node line interface elements with zero-thickness were inserted in the mid-axis of each brick.

Among all possible failure mechanisms, only the cracking and the sliding of the joints were observed in the experiment and included in the numerical model. The continuum units were modelled as linear elastic, as the vertical interfaces in the brick mid-axis, while a non-linear relation was assumed for the head and bed interfaces, both in tension and shear. The tension behaviour after cracking is governed by a tension softening law defined by tensile strength and fracture energy values. A Coulomb friction criterion was adopted in shear.

The material parameters were obtained from the experimental tests and they are listed in Table 4.2. The Young's modulus of the units and the mortar were derived from the related compressive strength. The normal and shear stiffness of the interfaces were calculated as (Lourenço and Rots, 1997):

$$k_{n,i} = \frac{E_u E_m}{t_m (E_u - E_m)} \quad (4.1)$$

$$k_{t,i} = \frac{G_u G_m}{t_m (G_u - G_m)} \quad (4.2)$$

where E_u and E_m are the Young's modulus of the unit brick and mortar joint respectively, G_u and G_m are the related shear modulus and t_m is the thickness of the mortar joint (Lourenço and Rots, 1997). The adopted parameters are indicated in Table 4.2. The tensile strength of the head and bed interfaces was estimated from the flexural tensile strength of masonry samples, where failure always occurred at the mortar-brick contact surface. Coulomb friction parameters were provided by shear tests on masonry couplets (Section 3.3).

6-node line interface elements were inserted between the façade base and the steel profile (Figure 4.1). This interface was characterized by no tension, assigned stiffness in compression and negligible stiffness in shear (Table 4.2).

4.1.2 Continuum model

In the continuum approach, the façade was modelled by 8-node plane stress elements with 3×3 and 2×2 points Gaussian integration schemes for the incremental-iterative analysis and the sequentially linear analysis, respectively (Figure 4.1, insert (b)). A coaxial rotating crack model was applied to the masonry for the incremental-iterative analysis, whereas for the sequentially linear analysis a fixed crack model was adopted

Table 4.2: Material parameters for discrete and continuum model

Model	Material	Parameter	Value
Discrete	Brick unit	Young's modulus	$E_u = 8 \times 10^3 \text{ N/mm}^2$
		Density	$\rho_u = 1.9 \times 10^{-6} \text{ kg/mm}^3$
		Poisson's ratio	$\nu_u = 0.2$
	Brick and lintel interface	Normal stiffness	$k_{n,u} = 5.5 \times 10^3 \text{ N/mm}^3$
		Tangent stiffness	$k_{t,u} = 2.1 \times 10^3 \text{ N/mm}^3$
	Mortar	Young's modulus	$E_m = 1 \times 10^3 \text{ N/mm}^2$
		Thickness	$t_m = 2 \text{ mm}$
		Poisson's ratio	$\nu_m = 0.2$
	Head and bed interface	Normal stiffness	$k_{n,i} = 0.55 \times 10^3 \text{ N/mm}^3$
		Tangent stiffness	$k_{t,i} = 0.21 \times 10^3 \text{ N/mm}^3$
		Tensile strength	$f_{t,i} = 0.1 \text{ N/mm}^2$
		Fracture energy	$G_{f,i} = 0.01 \text{ N/mm}$
		Cohesion	$c_i = 0.03 \text{ N/mm}^2$
Friction angle		$\tan \phi_i = 0.27$	
Continuum	Masonry	Dilatancy angle	$\tan \psi_i = 0$
		Young's modulus	$E_M = 3 \times 10^3 \text{ N/mm}^2$
		Density	$\rho_M = 1.9 \times 10^{-6} \text{ kg/mm}^3$
		Poisson's ratio	$\nu_M = 0.2$
		Tensile strength	$f_{t,M} = 0.1 \text{ N/mm}^2$
		Fracture energy	$G_{f,M} = 0.01 \text{ N/mm}$
Discrete and continuum	Lintel wood	Young's modulus	$E_w = 11 \times 10^3 \text{ N/mm}^2$
		Density	$\rho_w = 0.5 \times 10^{-6} \text{ kg/mm}^3$
		Poisson's ratio	$\nu_w = 0.15$
	Beam steel	Young's modulus	$E_s = 2.1 \times 10^5 \text{ N/mm}^2$
		Density	$\rho_s = 7.5 \times 10^{-6} \text{ kg/mm}^3$
		Poisson's ratio	$\nu_s = 0.3$
	Base interface	Normal stiffness	$k_{n,b} = 0.7 \text{ N/mm}^3$
Tangent stiffness		$k_{t,b} = 1 \times 10^{-9} \text{ N/mm}^3$	
		Tensile strength	$f_{t,b} = 0 \text{ N/mm}^2$

with a step-wisely reducing shear stiffness (DeJong et al., 2008). For both crack models, a linear tension softening relation was assumed after cracking. The tension softening law (Figure 2.13) was defined by the tensile strength f_t , the fracture energy G_f and the crack bandwidth h , which is related to the element size and equal to 11.8 mm. The material parameters are listed in Table 4.2. For the simulation with SLA, the non-linear stress-total strain relation was approximated by a saw-tooth law consisting of 15 saw-teeth (Figure 2.13). By using these crack models, the façade is modelled as a homogeneous isotropic linear elastic continuum before cracking; after the crack onset, it behaves as a non-linear orthotropic continuum. Note that for the incremental-iterative analysis the axes of orthotropy are always aligned with the principal stresses, whereas for sequentially linear analysis those axes are fixed upon crack initiation. As for the discrete model, no damage criterion was assumed in compression. 6-node line interface elements were inserted between the façade and the steel profile.

4.2 Numerical results

First the numerical results are presented and discussed in terms of deformations, crack pattern and bedding reactions. After that, damage classes are defined based on the numerical results. By doing so, the numerical results can be compared not only with the experimental results but also with the Limiting Tensile Strength Method (LTSM), currently used in engineering practice.

4.2.1 Deformations, crack patterns and bedding reactions

The non-linear numerical incremental iterative analysis was performed by means of three subsequent loading phases. First the model self-weight was activated, then the vertical pre-compression loads were applied, and finally a maximum settlement of 11.5 mm was applied in 23 steps of 0.5 mm, as done in the experiment. The displacements were reset to zero after the application of vertical loads. Results from the discrete and continuum numerical model were compared in term of deformation, cracks pattern and crack width.

4.2.2 Incremental-iterative analysis

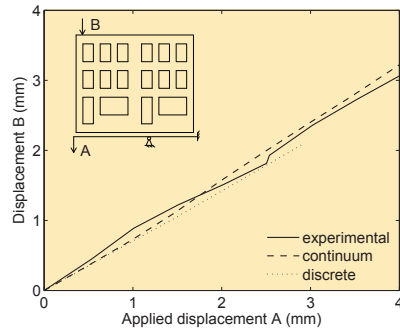
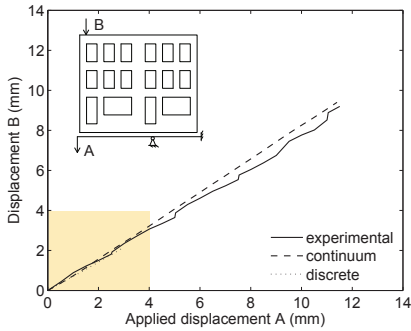
Figure 4.2a shows the vertical displacement of the façade (point B, located at 60 mm from the façade corner) as a function of the applied settlement (measured at point A, at 30 mm from the façade corner on the steel profile). The discrete model curve

exhibits a good agreement with the experimental curve, up to an applied settlement of 3 mm. After that, convergence could not be reached. A thorough study of the reasons has not been performed. The continuum model and experimental curves match well throughout the entire simulation, proving the model ability to capture the settlement reduction due to the interface effect. Figure 4.2b illustrates the relation between the horizontal displacement of point C, located at 150 mm from the façade corner, and the applied displacement. Also in this case, the discrete model reproduces the experimental behaviour up to 3 mm of applied displacement. In the continuum case the structural response is well simulated up to the end of the test.

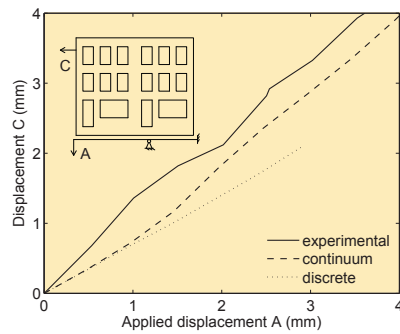
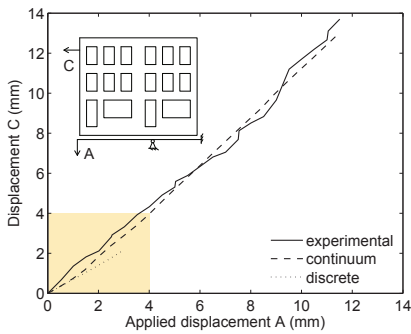
In Figure 4.3 the performance of the numerical analysis is evaluated in terms of resulting crack patterns. Both models are able to reproduce all the main cracks leading to the failure mechanism. For the discrete model, the numerical convergence can be reached only up to the micro-crack pattern onset, while in the continuum model the global crack pattern growth matches the one experimentally observed up to the end of the test. This allows to capture the main kinematic mechanisms as described in Section 3.5 (Figure 4.3, Experimental model, and Figure 4.5). In particular, the model reproduces the localization and propagation of bending cracks 1, 2 and 3, which define the rotating block I. The comparison between the crack width, experimentally measured by the Whittemore strain gauges, and the relative displacements between the same points of the numerical models demonstrates a good prediction of the crack width growth also in quantitative terms (Figure 4.4). The continuum model exhibits an earlier localization of crack 1 and a slight overestimation of crack 2. Crack 3 and 4 are well simulated throughout the entire test, and also the development of crack 6 is in good agreement with the monitored data, while the width of crack 5 is significant underestimated.

Figure 4.3 shows the distribution of stresses normal to the base interface. The interface remains in compression throughout the entire analysis. Initially, the compression stresses are due to the vertical loads, with a non-uniform stress distribution depending on the opening locations. For increasing values of settlement, the combination of tensile stresses induced to the façade and the low material strength causes the masonry damage, as previously described. This reduces the façade stiffness. As a consequence, the structure follows the applied hogging profile and the compression is reduced, but no tension and thus no gap arises. Figure 4.3 also highlights the interaction between the distribution of interface stresses and the redistribution of the façade stresses due to masonry cracking. A clear reduction of compressive interface stresses occurs at the cracked section which defines the rotation mechanism (block I and VI in Figure 4.3, Experimental model).

The comparison with the experimental measurements makes it also possible to evaluate the capability of the numerical model in simulating the modification



(a)



(b)

Figure 4.2: (a) Vertical displacement of point B and (b) horizontal displacement of point C as a function of applied settlement: comparison between numerical and experimental results. The graphs on the left show the displacements of point B and C throughout the entire test, while the graphs on the right show the same displacements up to 4 mm of applied settlement.

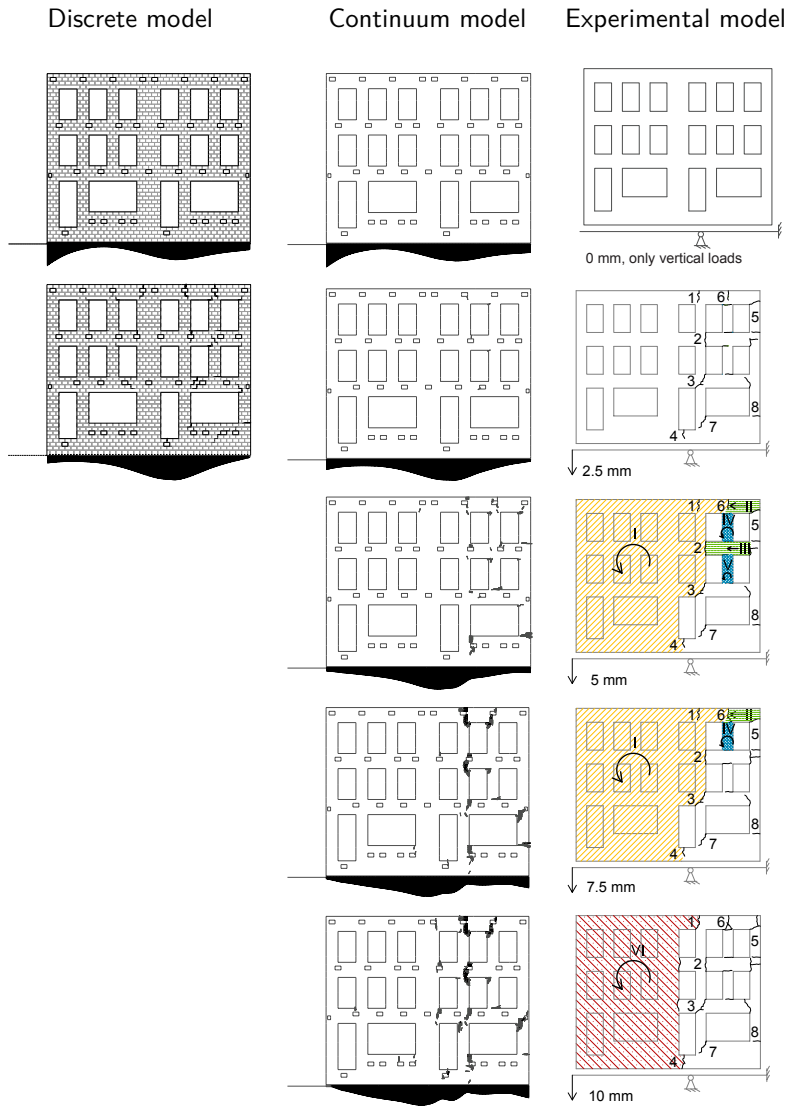
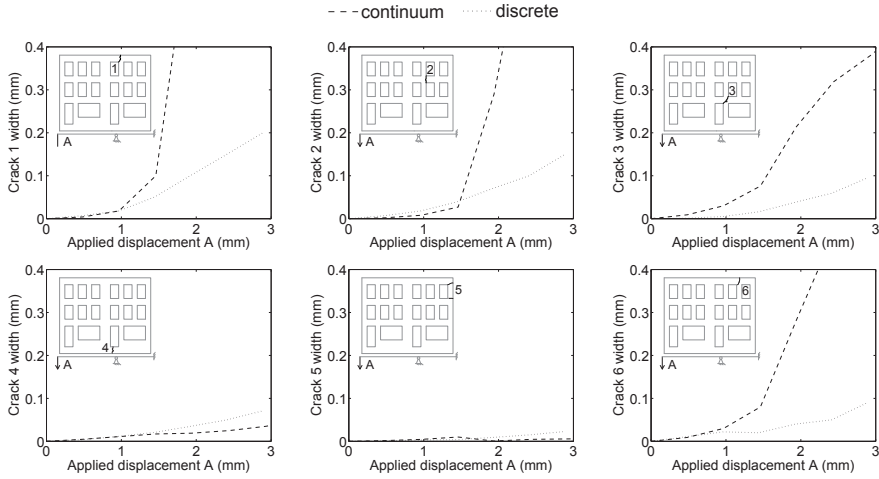
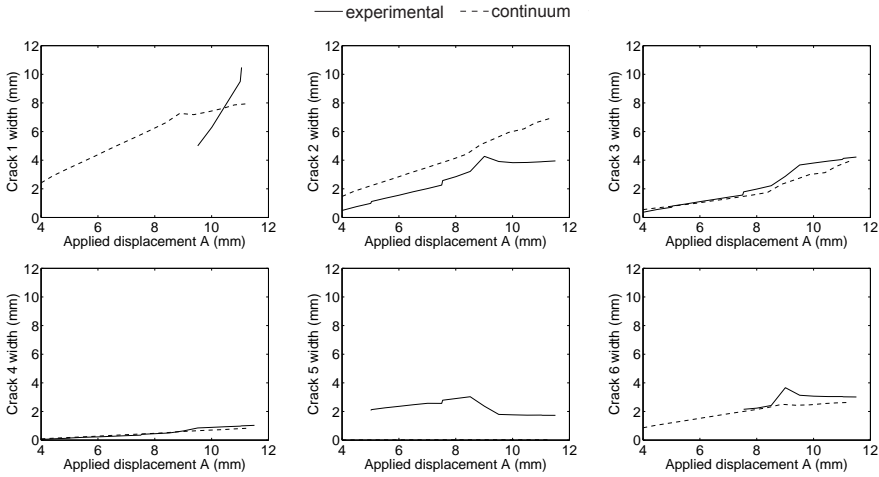


Figure 4.3: Crack pattern development and normal stresses of the base interface at different level of applied settlement: comparison between numerical and experimental results.



(a) comparison between discrete and continuum model



(b) comparison between continuum model and experimental results, available from 4 mm of applied settlement

Figure 4.4: Crack width growth of significant cracks as a function of applied settlement.

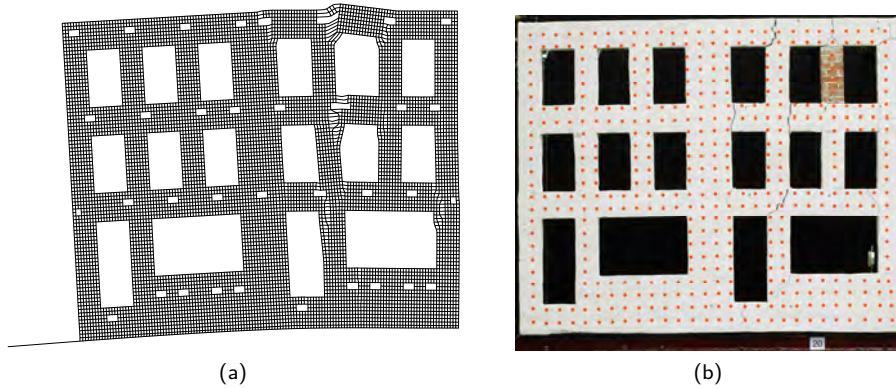


Figure 4.5: Continuum model: comparison between deformed mesh (a) and experimental results (b) at 10 mm of applied vertical displacement.

of the applied settlement profile due to the base interface stiffness. In Figure 4.6 the experimental and numerical base wall displacements are compared with the applied settlement profile, showing the façade splitting, the rotation of blocks and the settlement profile flattening due to the relative stiffness between the interface and the structure.

Mesh and step size dependency

To evaluate the influence of the model discretization on the response, a mesh refinement study was performed. The reference mesh, made by 8-node plane stress elements with dimensions $10.5 \times 13.3 \text{ mm}^2$ (Figure 4.1, insert (b)) was compared with a finer mesh of 8-node elements with dimensions $5.25 \times 6.65 \text{ mm}^2$ and a mesh of 4-node elements with dimensions $10.5 \times 13.3 \text{ mm}^2$. Figure 4.7 shows the displacements of the points B and C for the three different models, while Figure 4.8 compares the maximum principal strain distributions. No significant differences can be detected in the façade response, proving that the original mesh refinement was sufficient.

A critical aspect of the incremental-iterative scheme applied to cracking models is represented by convergence difficulties, which especially arise in case of large-scale structures of very brittle material (low G_f and substantial amount of elastic energy storage). In the reference case, assuming a convergence criterion based on internal energy with a tolerance of 1×10^{-4} and a maximum of 1×10^3 iterations, the convergence is reached in 22 out of 23 loading steps. In order to investigate

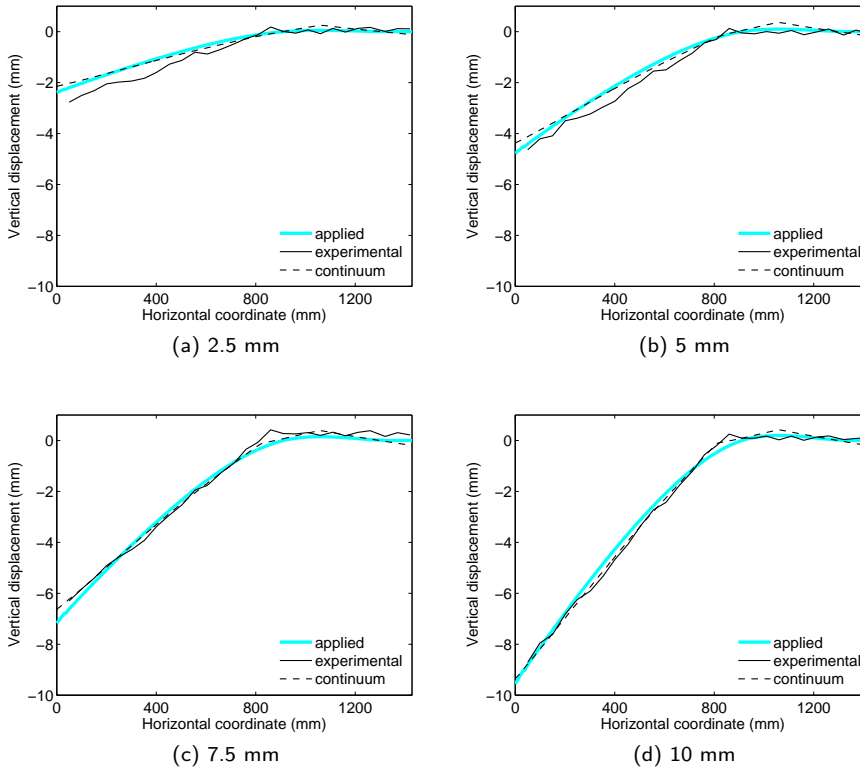


Figure 4.6: Comparison between numerical and experimental settlement at the façade base for applied vertical displacement of (a) 2.5 mm, (b) 5 mm, (c) 7.5 mm and (d) 10 mm.

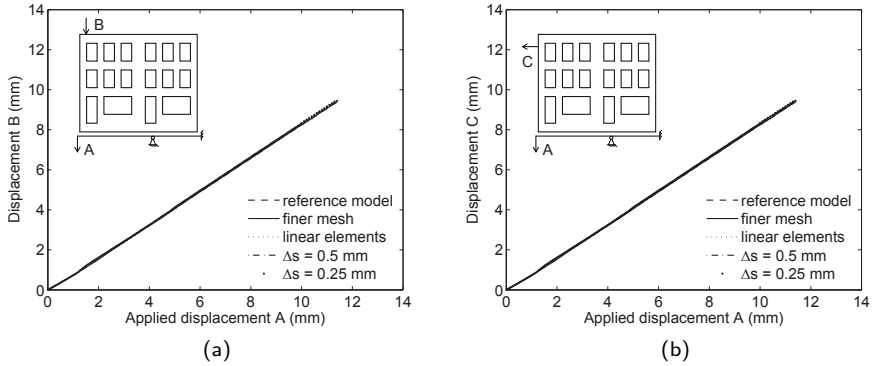


Figure 4.7: (a) Vertical displacement of point B and (b) horizontal displacement of point C as a function of applied settlement: influence of the mesh and step size.

the influence of load step size, the displacement was first applied in 23 steps of 0.5 mm and then in 46 steps of 0.25 mm; no load step size dependency was observed (Figure 4.7).

Scale effect

To verify the possibility to extend to real buildings the numerical results derived from the scaled model, the same analysis was performed on a real-scaled model of the tested façade. The outcomes in terms of displacements of control points and

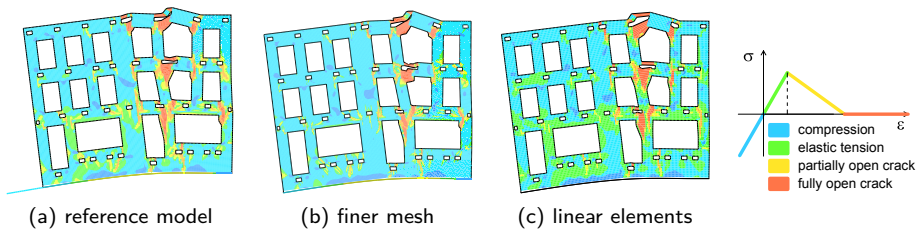


Figure 4.8: Maximum principal strain distribution and deformed configuration at 11.5 mm of applied displacement, for different mesh sizes.

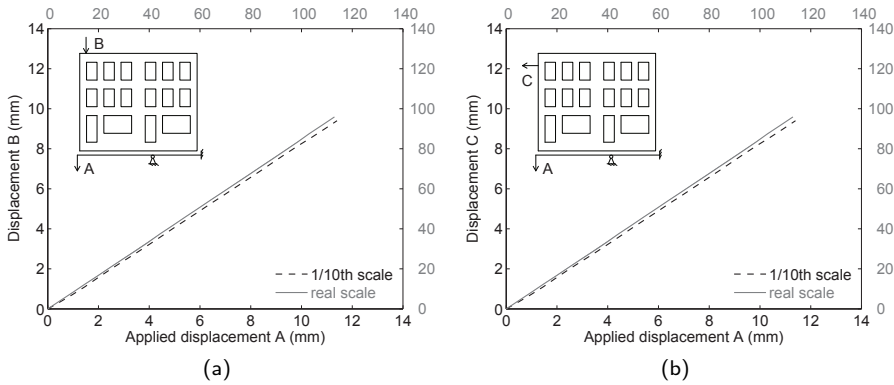


Figure 4.9: (a) Vertical displacement of point B and (b) horizontal displacement of point C as a function of applied settlement: scale effect.

maximum principal strains show a substantial agreement between the two models (Figure 4.9 and Figure 4.10).

4.2.3 Damage classes

Burland and Wroth (1974) introduced a damage classification based on the admissible tensile strain for an elastic beam equivalent to the structure. This damage classification includes also an indication of the expected crack width (Figure 4.11a). Here the computationally derived crack width was used to present the numerical

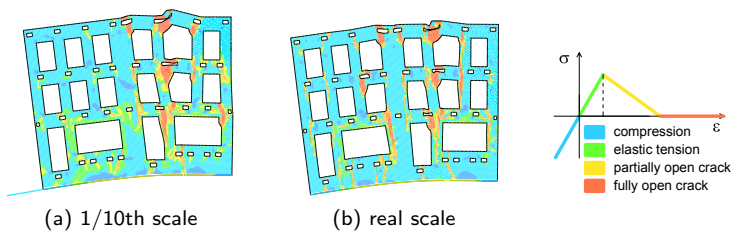


Figure 4.10: Maximum principal strain distribution and deformed configuration at 11.5 mm of applied displacement: scale effect.

results according to the same classification system. Figure 4.11b compares the numerically calculated and the experimentally monitored maximum crack width. As indicator of the applied deformation, the deflection ratio Δ/L is assumed, where Δ is the maximum displacement between the settlement profile and the straight line connecting the two ends of the façade base, and L is the façade length (Figure 4.11b). Figure 4.11c illustrates the experimental and numerical damage levels obtained by comparing the maximum crack width with the values indicated by Burland and Wroth (1974). The limiting crack width values corresponding to the six damage classes were reduced by a factor of 10, according to the model geometrical scale factor. The similar tendency of the experimental and numerical curves corresponds to the development of the mechanism illustrated in Figure 4.3. The results show an overestimation of the damage level in the numerical model, with respect to the experimental test. This is due to the earlier localization and propagation of crack 1 (Figure 4.4), which in both the numerical and experimental model determines the dominant failure mechanism.

Figure 4.11c and Figure 4.11d emphasizes the difference between the classification system based on the numerically derived crack width and the classification system based on the analytically calculated strain of the equivalent beam (LTSM). A value of $E/G = 11$ is assumed, to take into account the decreased shear stiffness in a façade with 30% of openings (Son and Cording, 2007). Results show that the LTSM predicts lower levels of damage, with respect to the crack width-based classification. A reason can be seen in the fact that the E/G ratio takes into account the decreased global shear stiffness induced by the openings, but it neglects their significant effect in terms of stress concentration and consequent damage localization.

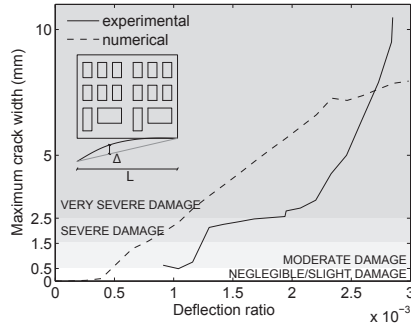
In actual buildings the maximum crack width could be partially reduced by the restraint offered by roof and transverse walls, which are not included in the experimental model nor in the numerical model. However, the results prove the need to perform extended sensitivity studies on numerical models accounting for masonry cracking, in order to refine the available damage assessment design curves (Franzius, 2003; Potts and Addenbrooke, 1997).

4.2.4 Sequentially linear analysis

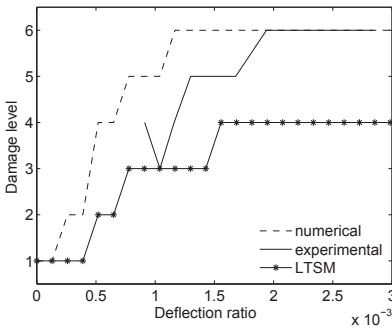
The numerical simulation with SLA showed a considerable number of microcracks at the end of the initial loading phase. In fact, 2478 linear analyses were required to fully apply the initial loads which consist of the dead weight plus the nodal forces accounting for the increased gravity load due to the downsizing of the façade. In other words, 2478 damage increments had to be applied to the model to attain a load multiplier λ_{ini} of 1.0. Note that so far no settlement S (see Figure 4.1) was

Dam. level	Damage class	Crack width (mm)	Tensile strain (%)
1	Negligible	up to 0.1	0-0.05
2	Very slight	up to 1	0.05-0.075
3	Slight	up to 5	0.075-0.15
4	Moderate	5 to 15	0.15-0.3
5	Severe	15 to 25	> 0.3
6	Very severe	> 25	> 0.3

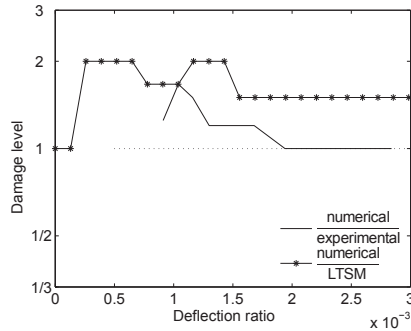
(a)



(b)



(c)



(d)

Figure 4.11: a) Crack width- and strain-based damage classification and its relation with the damage levels assumed in this work; b) maximum crack width vs. applied deflection ratio: experimental and numerical results; c) damage classification as a function of the applied deflection ratio: comparison between experimental, numerical and LTSM results; d) ratio between numerical crack width- and analytical strain-based damage levels as a function of the applied deflection ratio.

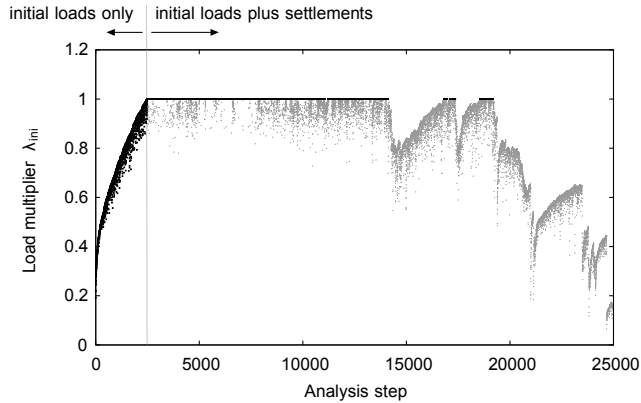


Figure 4.12: Evolution of the initial load multiplier λ_{ini} throughout the simulation with SLA. Light grey dots indicate linear analyses in which the initial loads could not be fully applied.

imposed yet. The dark grey points to the left of the grey line in Figure 4.12 illustrate the gradual application of the initial loads. The relatively large number of damage increments in the initial loading phase may be attributed to the fineness of the mesh and the number of saw-teeth per integration point. Figure 4.13a shows the resulting crack pattern at the end of the initial loading phase. Despite the large number of damage increments, the maximum crack width is still very small (less than 4×10^{-2} mm). The microcrack pattern matches the one obtained with the incremental-iterative analysis.

In the next phase of the simulation, consisting of 22522 linear analyses, the imposed settlements were added to the initial loads, leading to new cracks primarily located at the right hand side of the façade (Figure 4.13b). The computed crack pattern matches the experimental one reasonably well. Furthermore, up to a certain settlement the computed evolution of the displacement components B and C is in line with the experimentally obtained curves (Figure 4.14). Throughout the simulation, which consists of 25000 linear analyses, for a relatively large number of steps (13550) it was not possible to fully apply the initial loads and some scalar multiple of the settlements without temporarily violating the material law at at least one integration point. That is, for those steps no combination of load multipliers $\lambda_{ini} = 1.0$ and λ_{crit} exists without attaining constitutively inadmissible stresses. Consequently, for those steps the last successful load combination was proportionally scaled, which means that the initial loads were not fully applied. Those steps have been marked with

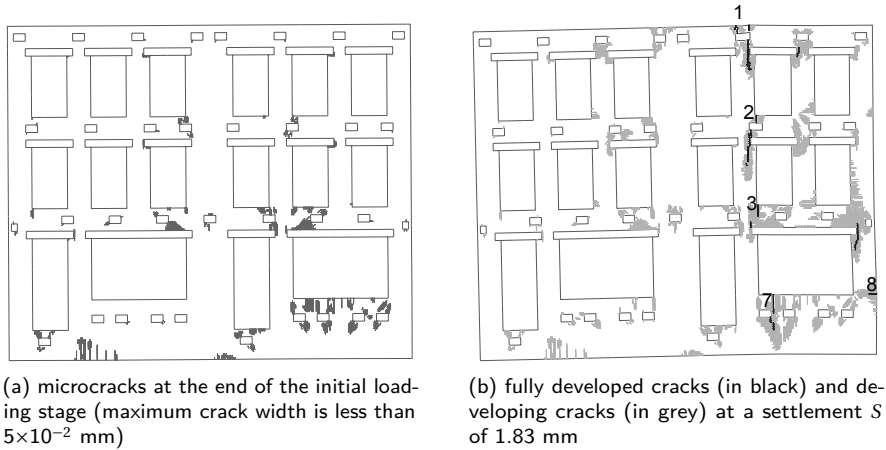


Figure 4.13: Crack patterns computed with SLA.

light grey dots in Figure 4.12 and Figure 4.14.

Figure 4.15a shows the crack width evolution at five different locations in the structure which have been labeled 1, 2, 3, 7 and 8 in Figure 4.13b. The crack width along the vertical axis was computed as the product of the mean crack strain (averaged over all cracked integration points of the element at the given location) and the element's crack band width. The settlement along the horizontal axis was monitored at dial A which has been corrected for the deflection immediately after the initial loading phase. For clarity, each line in the plot has been constructed using only a few points from the obtained response. As an illustration, all points of the crack at location 1 together with its line from Figure 4.15a were plotted in Figure 4.15b. The dots show the typical snap-type behaviour associated with SLA. Again, a dark grey dot indicates a step with a proper load combination (i.e. fully applied initial loads and a certain settlement) whereas a light grey dot marks a step in which such a load combination does not exist. The lines in Figure 4.15a reveal a behaviour which is typical of unreinforced masonry buildings subjected to imposed settlements. Initially, the crack widths grow at a fairly low rate. Suddenly, some cracks start to open up rapidly.

The crack at location 8 behaves differently compared to the other cracks. When the other cracks start to open up rapidly, crack 8 actually starts to close. This suggests that the upper right piece of the façade starts to break apart from the rest

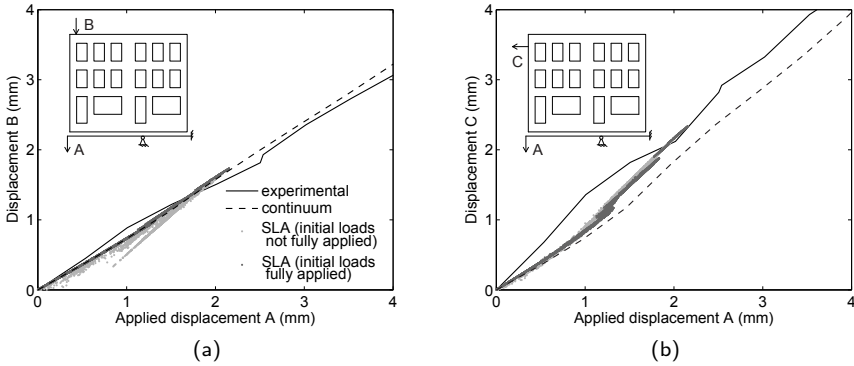


Figure 4.14: Displacements B and C as a function of displacement A.

of the façade. The issue here is that the crack is not just closing but the loading is reversed as well (from tension to compression). To investigate in detail what is happening, the evolution of the vertical stress σ_{yy} , the vertical total strain ϵ_{yy} , and damage variable d along a cross section at location 8 have been plotted in Figure 4.16. The damage variable d is defined as

$$d = 1 - \frac{E_{red}}{E_0} \quad (4.3)$$

with E_{red} and E_0 the reduced and initial Young's moduli of the masonry, respectively. The three pictures in the top row of Figure 4.16 show these variables after full application of the initial loads (step 2478), revealing no damage at all. After 14000 linear analyses the damage has progressed quite far along the cross section and the crack has opened up. However, after the major valley in Figure 4.12 (step 16971) a smaller total strain ϵ_{yy} indicates that the crack starts to close. In fact, after 19163 linear analyses, a negative total strain is observed, which means that part should be in compression. However, due to the earlier arisen damage, the stiffness in this area has almost vanished. In other words, there is hardly any resistance against this deformation. The reason is that currently a proper crack closing algorithm has not been included in the SLA formulation. Consequently, the initial loads which act at the part of the façade that came loose can no longer be carried. This explains why load multiplier λ_{ini} can no longer be maintained at a value of 1. In fact, it is successively being reduced (from step 19163 in Figure 4.12).

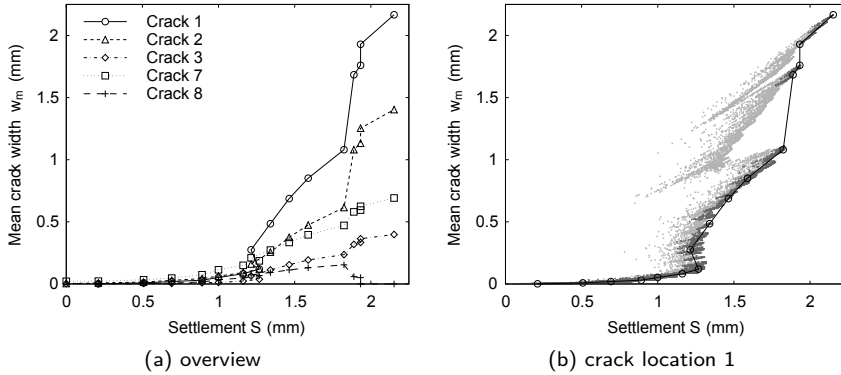


Figure 4.15: Crack width development as a function of the applied settlement computed with SLA.

Figure 4.17 supports the same conclusion, however presented in a different way. It shows the stress–strain history of the rightmost integration point along the considered cross section at crack location 8. Dark grey dots indicate analysis steps in which the initial loads could be fully applied, whereas light grey dots mark analysis steps in which the initial loads were only partially applied. Note that, due to the development of the crack, virtually all stiffness has been lost at this integration point before the crack closes. However, upon load reversal the stiffness is not recovered, as indicated by the dots which have a negative total strain ϵ_{yy} . In case a crack closing algorithm would be included, a kink should be visible at the origin of the stress–strain relation.

The presented results look promising with respect to analyses of large-scale masonry buildings, which are typically characterized by a brittle response that is difficult to trace using incremental-iterative techniques. Nevertheless, in order to properly follow crack closure and load reversal, the SLA formulation needs to be extended with a crack closing algorithm, e.g. following the lines devised by Graça e Costa et al. (2011).

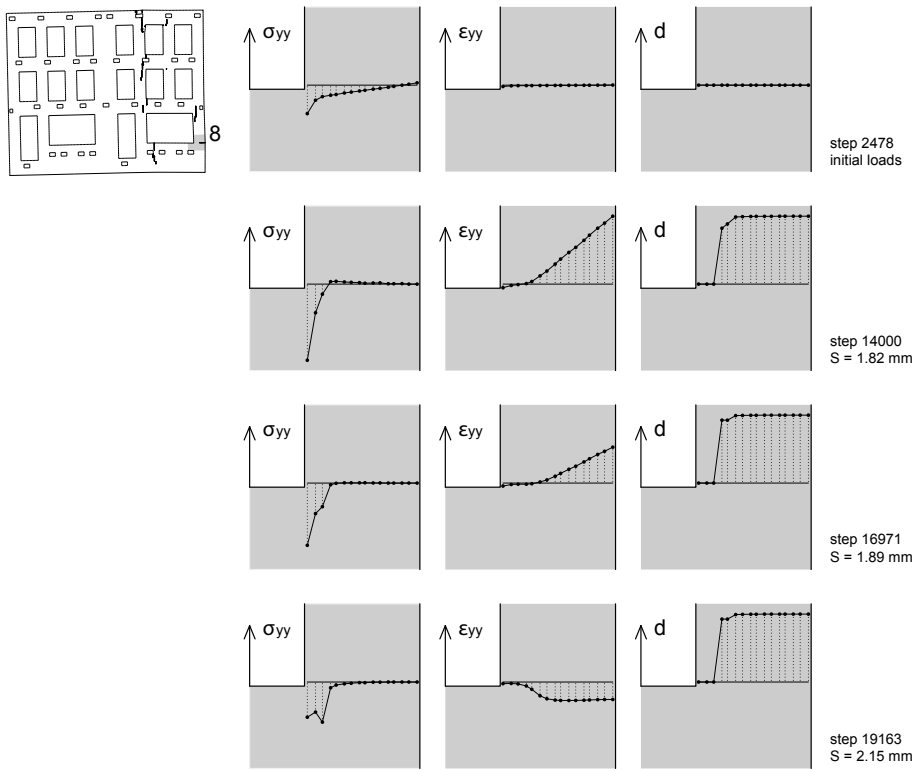


Figure 4.16: Evolution of stress σ_{yy} , strain ϵ_{yy} and damage d along the crack at location 8.

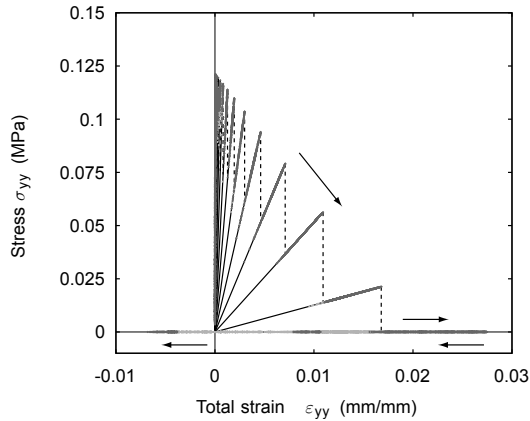


Figure 4.17: Stress–strain history of the rightmost integration point along the cross section at crack location 8.

4.3 Conclusions

In this chapter, a semi-coupled approach was proposed for the numerical evaluation of the settlement-induced damage to masonry structures. As a case-study, a tunnelling-induced settlement was applied to a 2D model of a masonry façade, through a no-tension interface accounting for the soil-structure interaction. The model included the simulation of masonry cracking; continuum and discrete approaches were evaluated, and incremental-iterative and sequentially linear solution schemes were applied.

The simulation of experimental results proved the suitability of the continuum model with incremental iterative scheme to capture the crack pattern development and the crack growth until very severe damage levels. The modelling approach has now also been validated for large applied deformations, leading to extensive cracking. Traditionally, for such extensive cracking there was a lack of validation of numerical models against experiments. Convergence problems, which require further study, have been encountered during the analysis performed on the discrete model. Compared to discrete modelling approaches, the continuum model has the advantage of being applicable to the simulation of large structures and complex geometries.

The application of the sequentially linear analysis scheme to the continuum model showed promising results in terms of crack pattern simulation, although the validation was limited to small applied settlements. The proposed SLA for

non-proportional loads represents a numerically robust alternative for the simulation of brittle material, but a proper crack closing algorithm needs to be included, to allow for the structural response modelling up to large values of deformation.

In conclusion, the continuum model represents an effective, and now validated, tool to be used in parametric analyses, in order to improve the current design curves for the damage assessment.

2D sensitivity study

5

The scaled 2D semi-coupled model of the masonry façade validated by comparison with experimental data in Chapter 4 allows to extend the experimental observations to a broader range of numerically analysed scenarios. The continuum model has been therefore used to perform a sensitivity study on the effect of geometrical, material and loading aspects and of initial and boundary conditions on the façade response to settlements.

5.1 Identification and selection of parameters and variations

This section describes the parameters analysed in the 2D sensitivity study.

Amount of openings The amount of openings was experimentally recognized as influencing the final damage and therefore varied in the numerical tests. Three values of percentage of openings with respect to the wall surface were considered, as shown in Figure 5.1: 0%, 10% and 30%. The last one is in agreement with the experiment described in Chapter 3 (reference case).

Material parameters To simulate the different types of masonry, a range of realistic values was assumed for the parameters defining the material properties: Young's modulus, tensile strength and fracture energy. The combinations under analysis are summarized in Figure 5.2. When varying E and f_t , G_f was varied accordingly (Figure 5.2b,c), in order to keep constant the slope of the softening

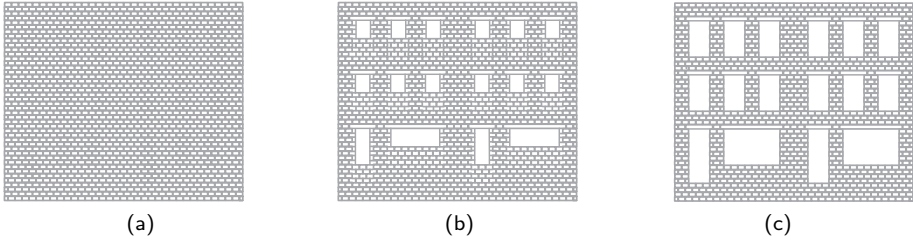


Figure 5.1: Variations of amount of openings: (a) 0%, (b) 10% and (c) 30% (reference case).

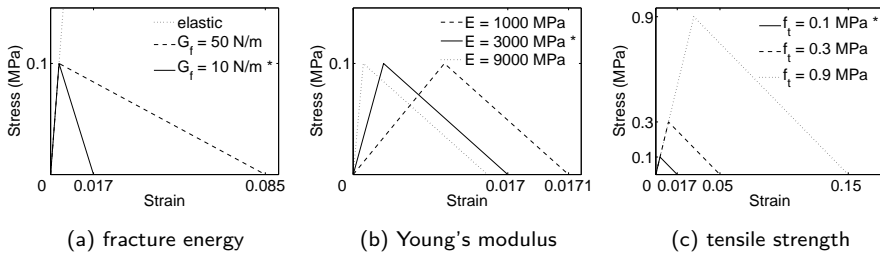


Figure 5.2: Assumed stress–strain relationships for the variations of masonry parameters (* indicates the reference case).

branch. The background is that the slope of the softening branch modifies the strain localization rate. In this way, the effect of changing E and f_t is corrected for this influence.

Initial loading and damage conditions In the reference tested case, vertical amplified loads were applied to the façade before imposing the hogging settlement profiles. In order to take into account the effect of initial loading on the settlement-induced damage, two sets of variations were performed. In the first set of analyses, visualized in Figure 5.3, only the vertical load amplification was varied: the reference case (self-weight plus vertical loads, Figure 5.3c) was compared to the situation where no load was applied before the settlement (Figure 5.3a) and to the case with self-weight only (Figure 5.3b). As for the reference case, the initial loads were kept constant during the settlement application.

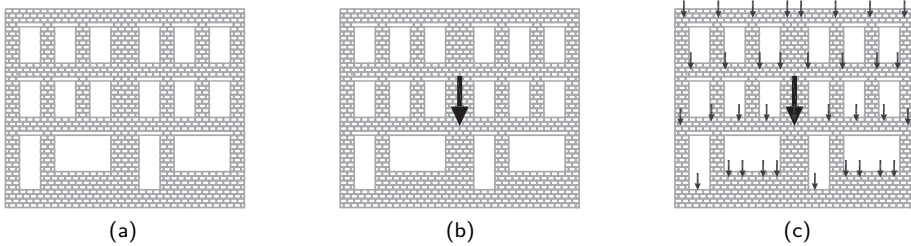


Figure 5.3: Initial loading variations: (a) no initial load, (b) self-weight only and (c) self-weight plus vertical amplified loads (reference case).

The second set of variations was focused on the effect of possible initial damage of the structure: the reference hogging profile was applied to the façade model which was preliminary damaged by doubled vertical loads (Figure 5.4b) or by a sagging settlement profile (Figure 5.4c). The assumed sagging profile is illustrated in Figure 5.5a (sagging curve).

Soil-structure interaction One of the main conclusions derived from the experimental test was the significant influence of soil-structure interaction. The sensitivity study investigated how the normal and shear behaviour of the interface affect the results, as a function of the foundation and soil type and conditions. In particular, first the effect of the interface normal stiffness was investigated. With reference to the stiffness assumed in the experimental model, three different values were considered: $k_n = 0.7 \times 10^7 \text{ N/m}^3$, $k_n = 0.7 \times 10^8 \text{ N/m}^3$ and $k_n = 0.7 \times 10^9 \text{ N/m}^3$ (reference case). The reference value corresponds to the normal stiffness equivalent to a Dutch wooden pile foundation (Rots, 2000), as described in Section 3.2.4.

The influence of the interface behaviour in the tangential direction was also analysed. For this purpose, the reference case with no horizontal displacements applied was compared with two other cases where the model was subjected to the horizontal displacement profile shown in Figure 5.5b (hogging curve). The curve was calculated using Equation (2.6), considering the greenfield settlement profile illustrated in Figure 3.5. Two different values of tangential stiffness were assumed for the interface: $k_t = 0.7 \times 10^8 \text{ N/m}^3$ and $k_t = 0.7 \times 10^9 \text{ N/m}^3$; in both cases a Coulomb friction criterion was adopted, with cohesion $c = 0 \text{ MPa}$, friction angle $\phi = 30^\circ$ and dilatancy angle $\psi = 0^\circ$ (non-associated plasticity).

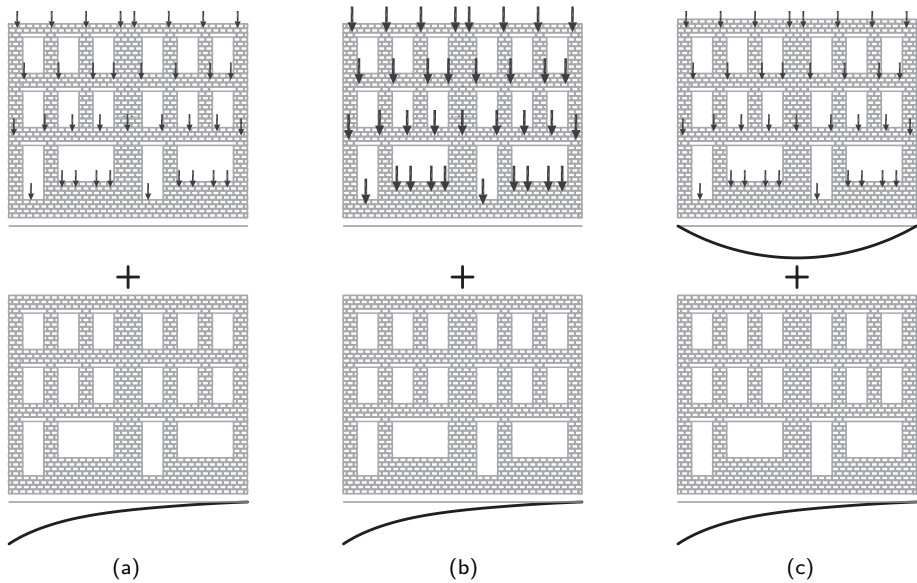


Figure 5.4: Initial damage variation: (a) reference case, (b) doubled initial loading and (c) initial sagging settlement profile.

Settlement profile Finally, the sensitivity study was extended to different types of settlement profiles; this simulates the tunnelling-induced settlement troughs that affect structures in different locations with respect to the tunnel (Figure 5.5 and Figure 5.6). For the two additional settlement troughs, the same variations of interface horizontal behaviour previously applied to the hogging profile were considered: $k_t = 0 \text{ N/m}^3$ (no horizontal displacements), $k_t = 0.7 \times 10^8 \text{ N/m}^3$ and $k_t = 0.7 \times 10^9 \text{ N/m}^3$.

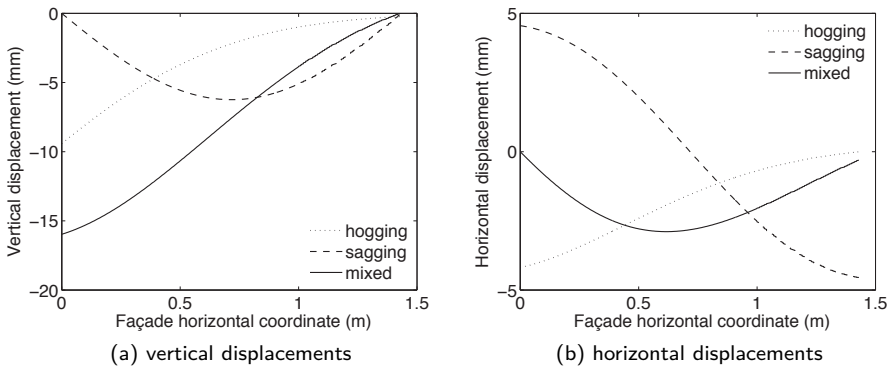


Figure 5.5: Hogging, sagging and mixed hogging-sagging displacement profiles applied to the façade in the sensitivity study.

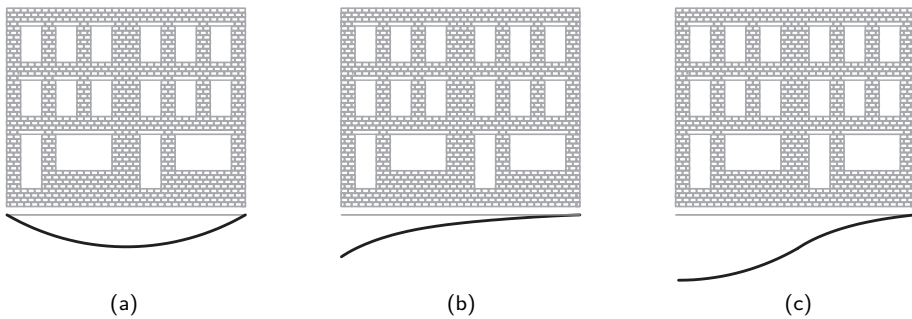


Figure 5.6: Settlement profile variations: (a) sagging, (b) hogging (reference case) and (c) mixed hogging-sagging settlement profile.

5.2 Results

For all the examined variations, the settlement-induced structural response was evaluated by comparing the global deformations and the crack patterns resulting from the parametric analysis. The horizontal strain, angular distortion and maximum crack width as a function of the progressive applied deflection ratio Δ/L were used to quantify the structural damage. The definition of each damage indicator is reported below, and illustrated in Figure 5.7 (Son and Cording, 2005).

Top horizontal strain:

$$\varepsilon_{h,\text{top}} = \frac{\Delta x_D - \Delta x_C}{L} \quad (5.1)$$

Base horizontal strain:

$$\varepsilon_{h,\text{base}} = \frac{\Delta x_A - \Delta x_B}{L} \quad (5.2)$$

Slope:

$$s = \frac{\Delta y_A - \Delta y_B}{L} \quad (5.3)$$

Tilt:

$$\theta = \frac{\Delta x_C - \Delta x_B}{H} \quad (5.4)$$

Angular distortion:

$$\beta = s - \theta \quad (5.5)$$

Note that the deflection ratio Δ/L refers to the settlement profile applied to the lower side of the base interface, while the angular distortion β indicates the consequent structural deformation, measured on the façade.

The maximum crack width was derived from the relative displacements between two nodes located outside the opposite margins of the most cracked localized area. Furthermore, the final damage in terms of maximum crack width was translated into the corresponding damage class, according to Burland and Wroth (1974) (Figure 4.11a). This allowed for a direct comparison of the final assessment with the result of the application of the Limiting Tensile Strength Method (LTSM) to each single variation. The comparison is visualized as the ratio between the numerical and LTSM damage levels (damage level ratio). For values of damage level ratio < 1 the LTSM is less conservative than the numerical analysis. For the calculation of the LTSM damage levels, the procedure described in Section 2.2 was adopted. Horizontal strains, as calculated in Equation (2.15), were included only in hogging cases with horizontal displacements applied to the structure. Different values for the

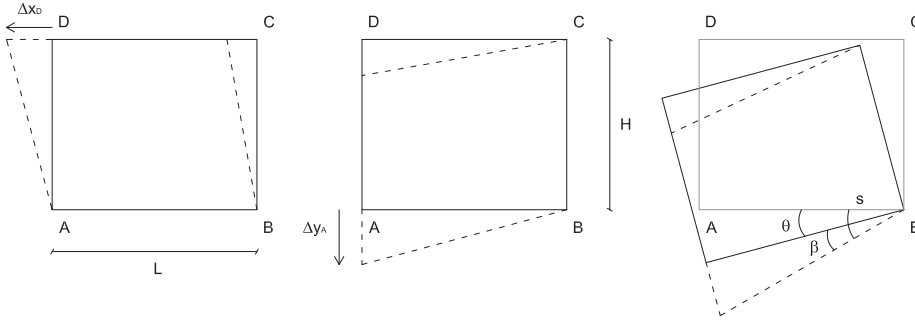


Figure 5.7: Damage indicators used to compare the numerical results.

equivalent stiffness ratio E/G were assumed in the variations of opening percentage (Son and Cording, 2007):

- $E/G = 2.6$ for the wall with 0% of openings;
- $E/G = 8$ for the façade with 10% of openings;
- $E/G = 11$ for the façade with 30% of openings.

5.2.1 Amount of openings

Figure 5.8 shows the maximum principal strain distribution and the deformed configuration at the maximum applied displacement of 11.5 mm (end of the experimental test) for the considered values of opening percentage. For consistency with the reference case, the plane stress elements taken out to represent the missing bricks for the load application were not counted as openings; they can be seen as wall imperfections. The contour plots indicate a strong localization of the damage at the corner of the openings or at the imperfections, where the cracks which define the failure mechanism are concentrated. In the reference case, the first bending crack arises at the top of the façade, and progressively crosses the entire section in the vertical direction (Figure 5.8c). Conversely, in the blind wall the increased stiffness does not allow the structure to bend, and the main crack develops horizontally, near the base (Figure 5.8a). In the intermediate case, the failure mechanism presents both the horizontal and vertical cracks, but limited to the area around the largest window at the ground floor (Figure 5.8b).

The damage indicators increase with the increase of openings (Figure 5.9). In particular, the top horizontal strain (Figure 5.9a) is the deformation parameter which clearly indicates the bending failure mechanism in a hogging area, and it reflects

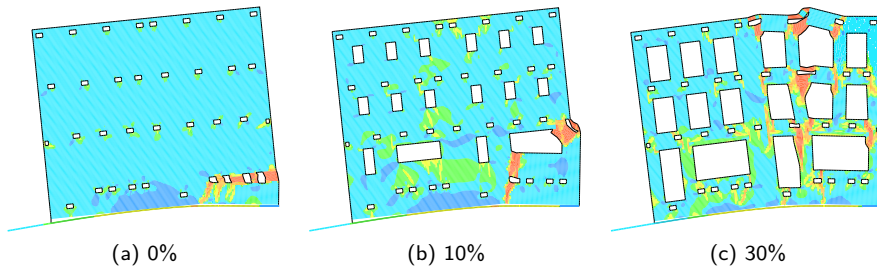


Figure 5.8: Maximum principal strain distribution and deformed configuration at 11.5 mm of applied displacement, for different values of opening percentage.

the maximum crack width evolution (Figure 5.9d). Figure 5.9c shows that for the reference case also the angular distortion β is larger than in the other two models; the structure adapts to the imposed deformation due to the initial flexibility induced by the larger amount of openings and to a further reduction of stiffness after the crack initiation. The evolution of the angular distortion β in the other two cases makes it possible to identify the brittle crack initiation (compare with Figure 5.9d). Around $\Delta/L = 10^{-3}$ for the 10% façade opening ratio and $\Delta/L = 2 \times 10^{-3}$ for the blind wall, a main horizontal crack arises, leading to an accelerated anticlockwise rotation of the façade upper part, and to a simultaneous lowering of the right-bottom corner part of the façade (Figure 5.7). This explains the rapid variation of angular distortion in the two curves (Figure 5.9c).

Figure 5.8 shows how the relatively high stiffness of the blind wall and the wall with the small openings leads to gapping in the no-tension interface, while in the reference case the façade follows more closely the applied settlement trough. The damage level corresponding to the maximum crack width growth (Figure 5.9e) confirms that for the analyzed situation a façade with a larger amount of openings is more prone to the damage induced by the hogging settlement. The increased structural vulnerability due to the crack localization and the reduced shear section has a much stronger effect than the increased bending flexibility given by more openings. As shown in Figure 5.9f, the LTSM only takes into account the latter effect, leading to a substantially higher damage level prediction based on the numerical results compared to the LTSM prediction.

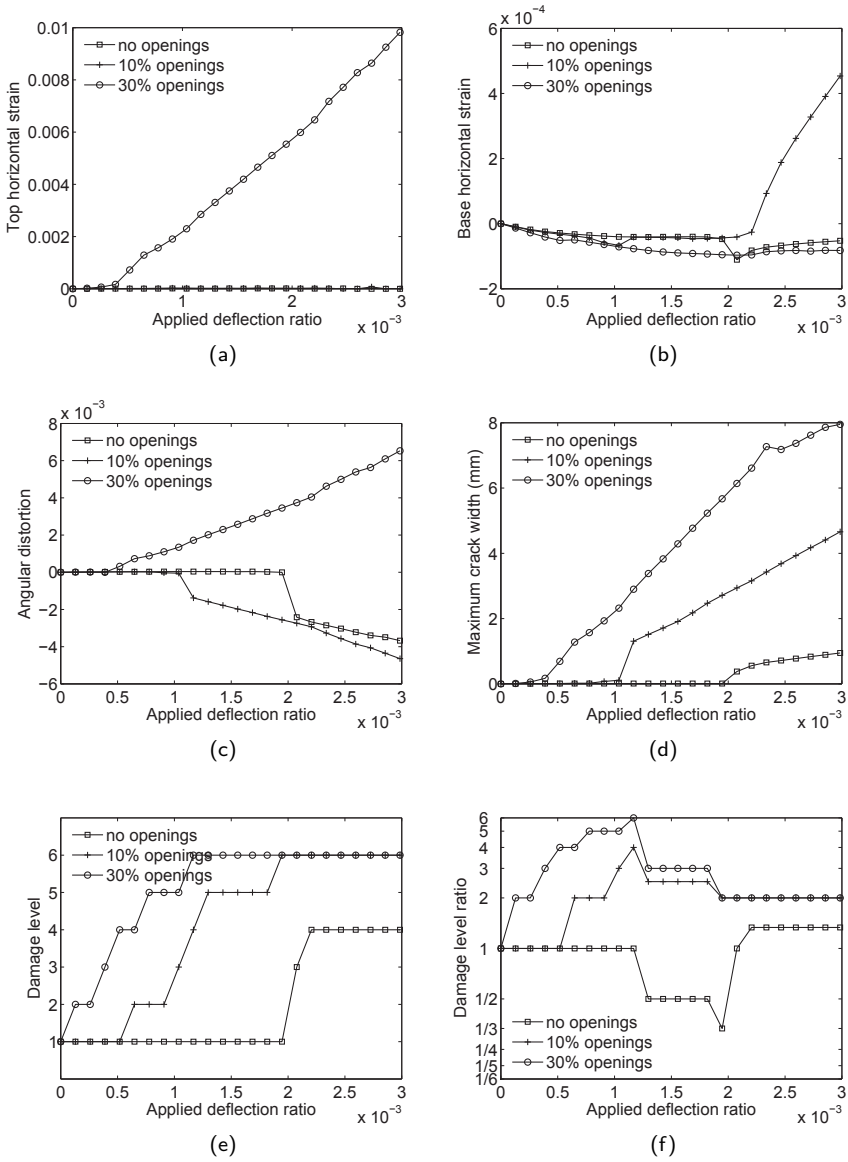


Figure 5.9: Variation of opening percentage: damage indicators as a function of the applied deflection ratio.

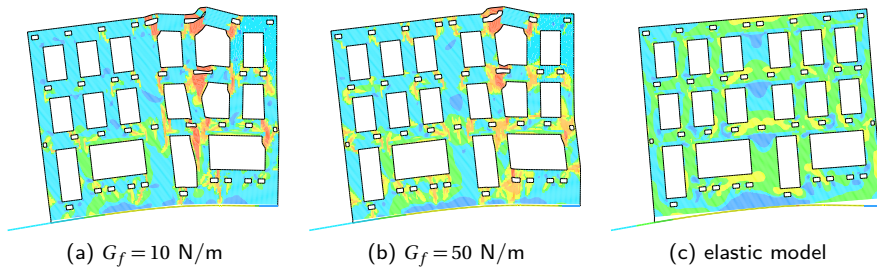


Figure 5.10: Maximum principal strain distribution and deformed configuration at 11.5 mm of applied displacement, for different values of fracture energy G_f .

5.2.2 Material parameters

In the adopted continuum model, the tension behaviour after cracking is defined by the Young's modulus E , the tensile strength f_t , the fracture energy G_f and the crack bandwidth h (Figure 2.13).

Fracture energy Figure 5.10 compares the deformations of the reference model, characterized by a rotating crack model for masonry with $G_f = 10 \text{ N/m}$, with two other cases: a rotating crack model with $G_f = 50 \text{ N/m}$, i.e. higher material ductility, and a linear elastic model. In the non-linear models, the increased value of G_f leads to a slight reduction of the maximum crack width, but it does not alter the failure mechanism (Figure 5.10a,b). On the contrary, the elastic model exhibits a significantly stiffer behaviour, causing a tension-induced gap at the base interface and suggesting a dissimilar failure mechanism, with a different distribution of the maximum principal strain (Figure 5.10c). As a consequence, in the elastic model, the localization of the maximum tensile strains, which indicates the expected location of cracks, differs from the actual crack location observed in the experiment. This result emphasizes the need to use a non-linear model accounting for the post-crack stress redistribution.

The maximum damage induced by a hogging deformation (Figure 5.11d) is well represented by the top lateral strain (Figure 5.11a). As expected, the angular distortion β of the elastic model is not increasing with the applied deflection ratio (Figure 5.11c), while for the cracking model the curve slope increases in correspondence with the main crack opening (see Figure 5.11d). The higher vulnerability of more brittle structures is shown by the increase of β for reduced G_f (Figure 5.11c)

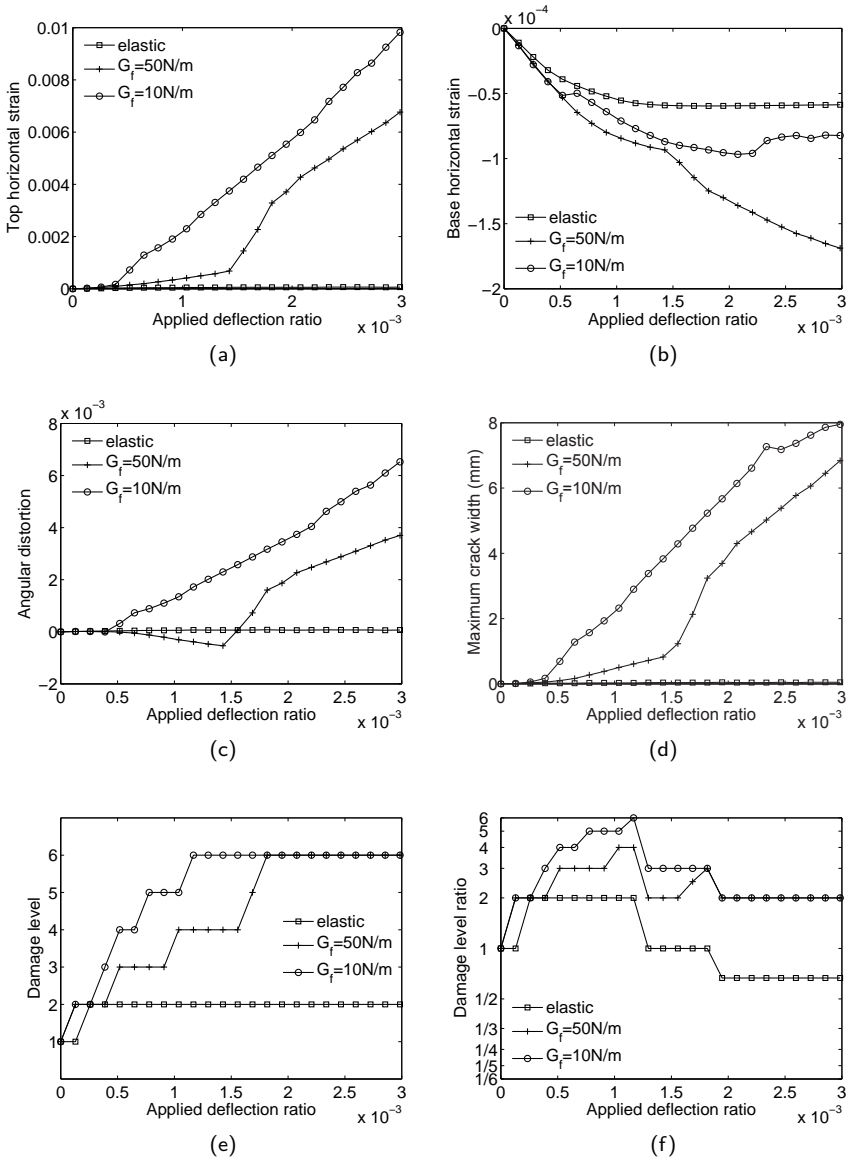


Figure 5.11: Variation of masonry fracture energy: damage indicators as a function of the applied deflection ratio.

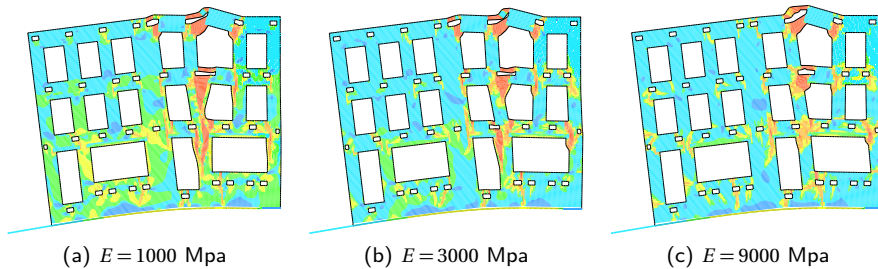


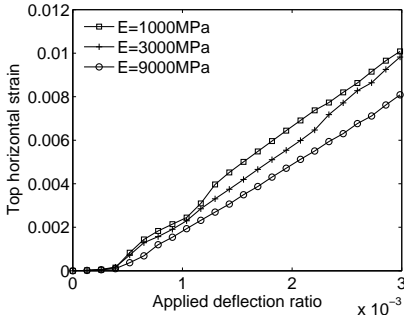
Figure 5.12: Maximum principal strain distribution and deformed configuration at 11.5 mm of applied displacement, for different values of masonry Young's modulus E .

and it is confirmed by the damage level comparison plotted in Figure 5.11e.

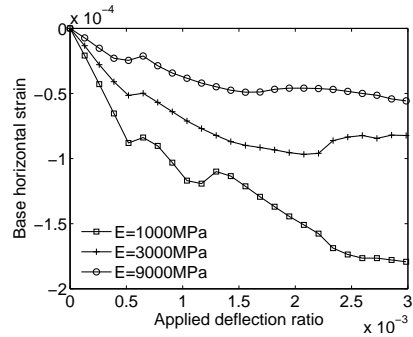
Figure 5.11f shows that the use of the the LTSM would predict a less severe structural damage, if compared to the cracking model (damage level ratio > 1). Due to the basic assumption of the LTSM (linear elastic model strain compared with limiting strain) the analytical procedure cannot consider the redistribution and reserve by slow cracking propagation. The results of numerical analyses could be used to adapt the tensile limiting strain values indicated by the LTSM to include the effect of material cracking parameters on quasi-brittle structural response.

Young's modulus Figure 5.12 and Figure 5.13 show that the model is not particularly sensitive to the variation of E , in terms neither of failure mechanism nor of global damage. The development of top lateral strain (Figure 5.13a), angular distortion (Figure 5.13c) and maximum crack width (Figure 5.13d) as a function of the applied settlement consistently indicates a higher vulnerability of the less stiff structure, which is more prone to follow the imposed deformation. Figure 5.13b shows the corresponding development of compressive strain at the façade base, increasing with a decreasing Young's modulus.

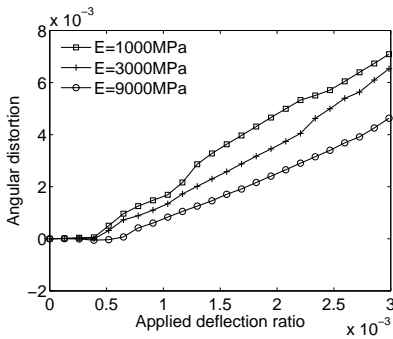
Theoretically, the reduced Young's modulus should lead to crack initiation at higher values of deformation (Figure 5.2b); however, for the assumed range of E values, this effect does not compensate the larger angular distortion. The difference in terms of global damage induced by the tensile strain is not significant, and it does not considerably affect the final damage classification (Figure 5.13e). The relatively little effect of the Young's modulus variation can be explained by the assumption of elastic-softening behaviour for the masonry. The influence of a lower Young's



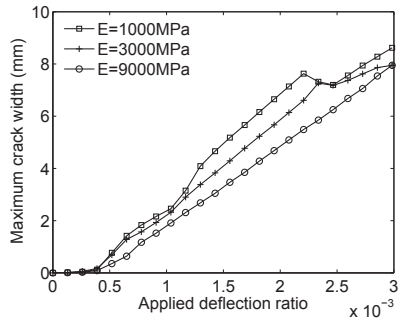
(a)



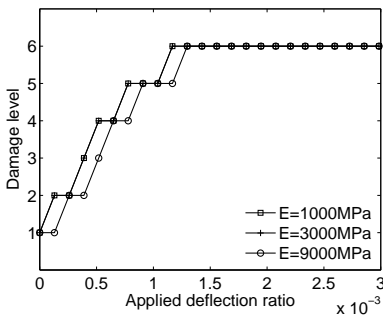
(b)



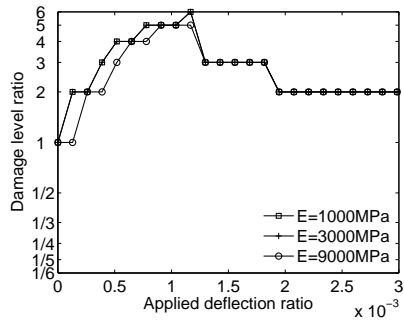
(c)



(d)



(e)



(f)

Figure 5.13: Variation of masonry Young's modulus: damage indicators as a function of the applied deflection ratio.

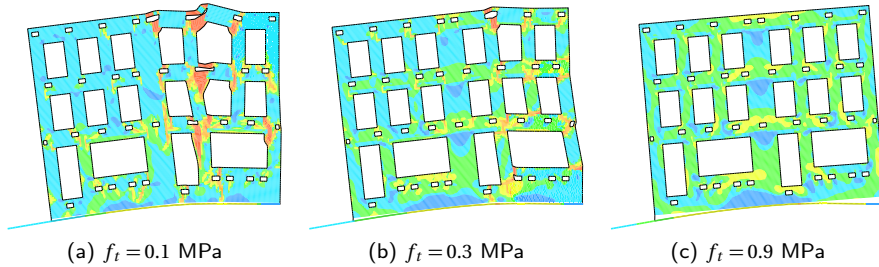


Figure 5.14: Maximum principal strain distribution and deformed configuration at 11.5 mm of applied displacement, for different values of masonry tensile strength f_t .

modulus is in fact negligible, if compared with the global stiffness reduction induced by the cracking. These results are in agreement with the assumptions of the LTSM, which does not contemplate different values for the equivalent beam E/G ratio depending on the type of masonry, but only takes into account different structural types (e.g. façades, bearing walls and frame structures).

Tensile strength The sensitivity analysis performed by varying the masonry tensile strength indicates that f_t has a strong influence on the final damage. An increased strength leads to a structural response similar to the one of an elastic façade (Figure 5.14). This is confirmed by the graphs in Figure 5.15. As for the reference case ($f_t = 0.1$ MPa), the evolution of the horizontal strains $\epsilon_{h,top}$, $\epsilon_{h,base}$ and the maximum crack width w_{max} for $f_t = 0.3$ MPa evidences a strong discontinuity at the crack initiation (Figure 5.15a,b,d). This change of slope occurs at higher values of applied Δ/L . In the extreme case of $f_t = 0.9$ MPa, there is no angular distortion β (Figure 5.15c). The structure is not affected by tensile strain nor damage (Figure 5.15a,d) and the compressive deformation (Figure 5.15b) reaches an asymptotic value which corresponds to the beginning of the interface gapping.

The damage classification is strongly dependent on the f_t variation (Figure 5.15e). As for the fracture energy, the LTSM takes one limiting strain value for all masonry types. For poor quality masonry, characterized by low values of f_t , the analytical method is much less conservative than the numerical model (Figure 5.15f). The difference decreases for materials with higher strength, where the structural response approximates the elastic one. In the same way as for the G_f variations, these results confirm the need to include a crack model when evaluating the structural damage.

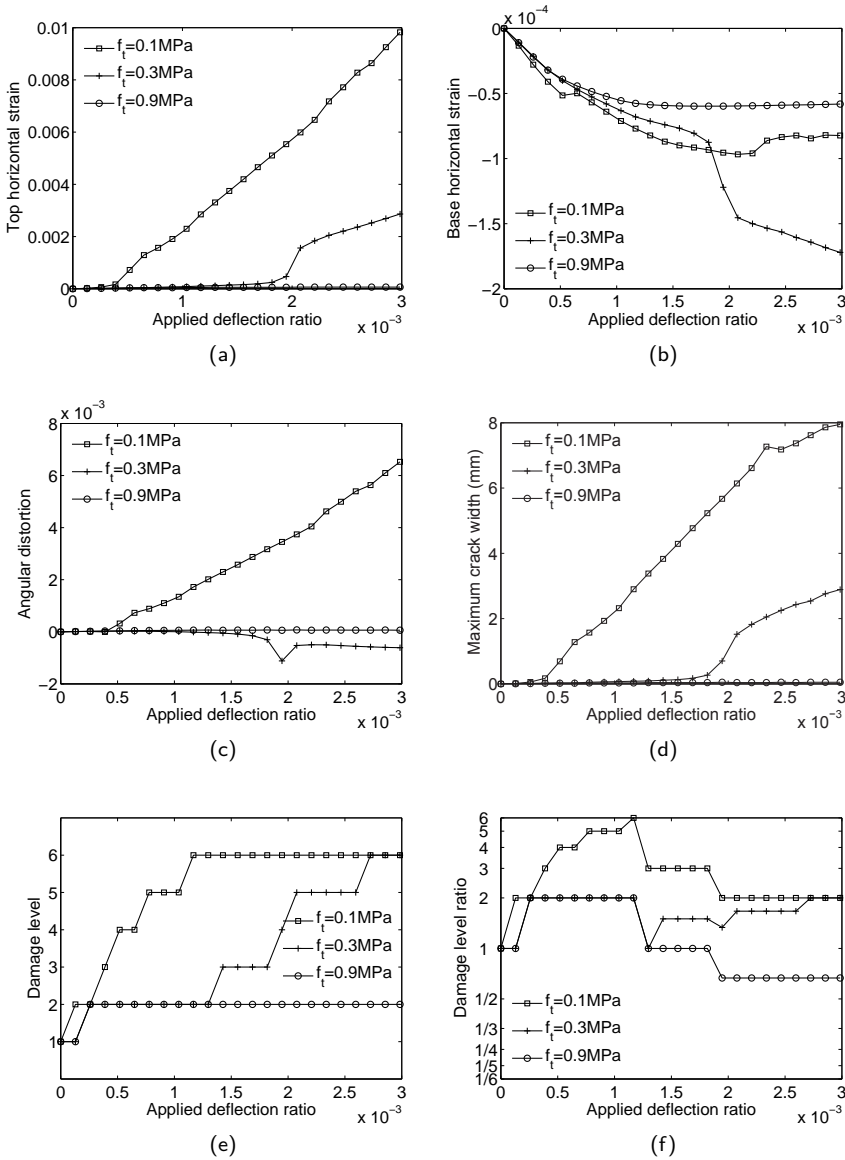


Figure 5.15: Variation of masonry tensile strength: damage indicators as a function of the applied deflection ratio.

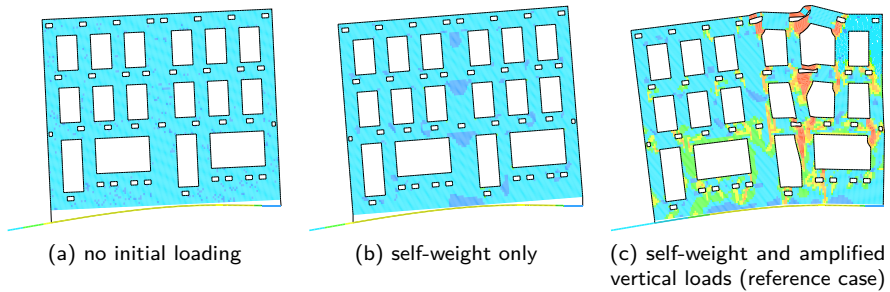


Figure 5.16: Maximum principal strain distribution and deformed configuration at 11.5 mm of applied displacement, for different initial loading.

5.2.3 Initial loading and damage conditions

This section describes the dependency of the structural damage on the building initial state.

Initial loading Figure 5.16 highlights how the initial loading conditions influence the final damage. The response of the model with no initial load applied (Figure 5.16a) and the façade with self-weight only (Figure 5.16b) are compared with the reference case, which includes both the self-weight and the amplified vertical loads (Figure 5.16c).

If no amplified loads are applied, the imposed settlement leads to an extensive gap from both ends of the no-tension interface (Figure 5.16a,b). In absence of any vertical load, the façade is subjected to a rotation about a point at the hogging support beam (Figure 5.16a), while if the structure is subjected to self-weight the contact area is extended, due to the redistribution of interface stresses (Figure 5.16b). In this latter case, the maximum tensile strain localization in the façade occurs at the central section located above the contact area. In both cases, the structure tilts without being affected by internal distortion (Figure 5.17a,c) and no damage arises (Figure 5.17d).

The two variations of initial loading do not represent realistic cases, and therefore the comparison with the LTSM assessment (Figure 5.17f) does not give indications usable in practice. Note that the amplified vertical loads comprise 90% of the total vertical loads. However, it emphasizes the need for a proper evaluation of the initial conditions to obtain an accurate settlement-induced damage prediction.

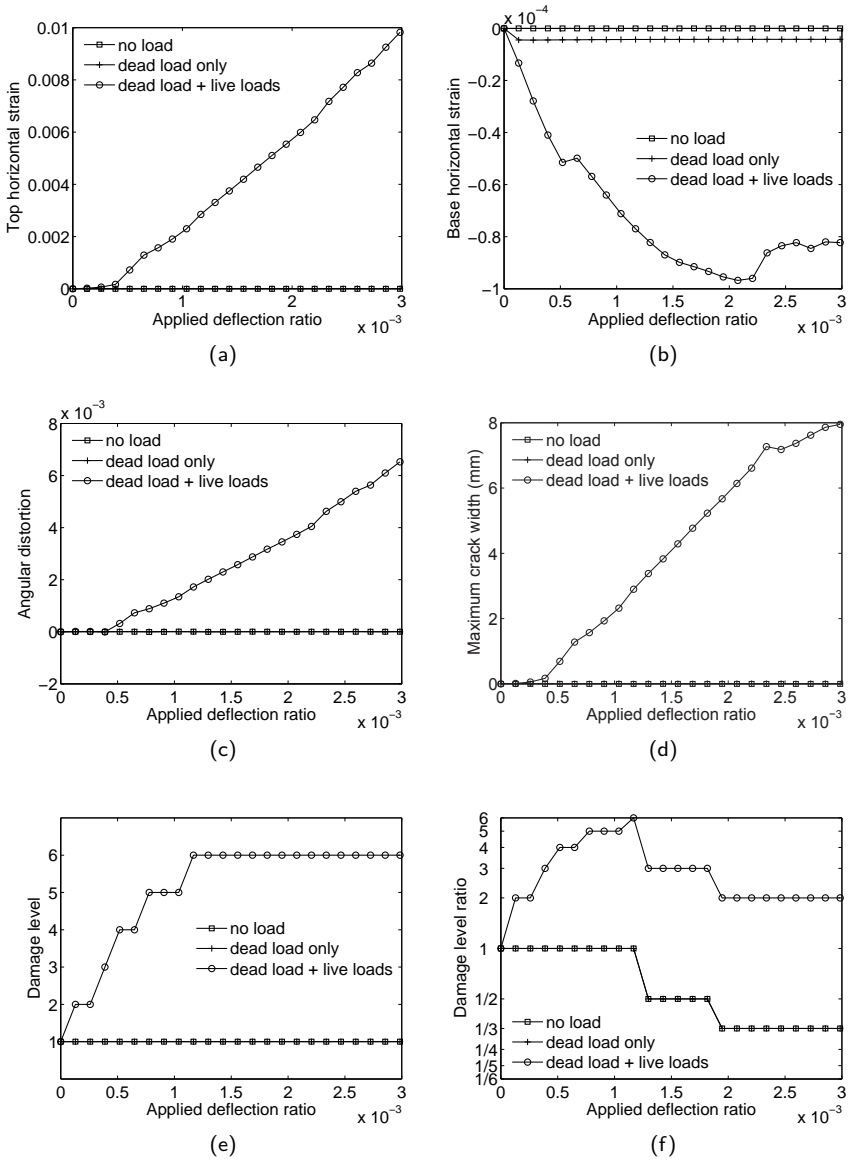


Figure 5.17: Initial loading variation: damage indicators as a function of the applied deflection ratio.

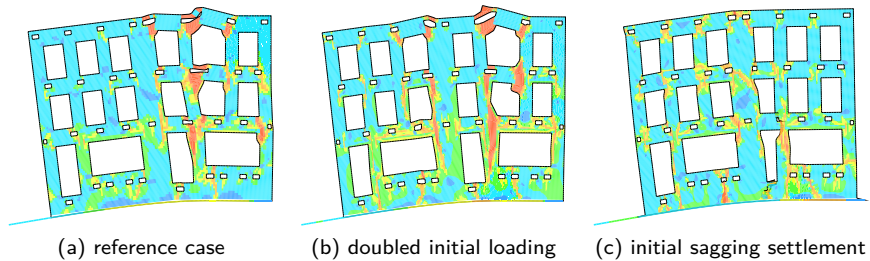


Figure 5.18: Maximum principal strain distribution and deformed configuration at 11.5 mm of applied displacement, for different initial damage.

It also emphasizes the need for establishing a proper load amplification in scaled experiments.

Initial damage In order to deepen this aspect, two other cases were investigated where actions prior to the settlement application caused significant damage to the structure. Figure 5.18 presents the failure mechanisms as a consequence of the reference hogging settlement for a façade subjected to extra initial loading (Figure 5.18b) or to initial sagging settlement trough (Figure 5.18c). The results show the significant influence of the initial damage. The doubled initial loading, induced by the same type of vertical loads with respect to the reference case, makes the structure more vulnerable, causing an earlier damage localization, without altering the failure mechanism. Conversely, the initial sagging profile changes the façade sensitivity to the subsequent hogging displacement. The sagging deformation induces compressive stresses in areas which subsequently are subjected to tension, and therefore delays the hogging type failure mechanism (Figure 5.19a). The maximum crack width (Figure 5.19d), which defines the damage level (Figure 5.19e) is significantly reduced. In this case, the activation of a different failure mechanism makes the initially applied settlement beneficial to the structure, under the assumption of neglecting stress relaxation. However, it is easily deducible that if the building experiences in its history a differential settlement similar to the one induced by tunnelling, an increased vulnerability can be expected.

The initial conditions of the building, both in terms of loading and damage, are not explicitly included in the LTSM. Consequently, in the comparison of Figure 5.17f and Figure 5.19f, only the numerator of the damage level ratio varies with the variation of the initial conditions. This parameter could therefore be usefully included

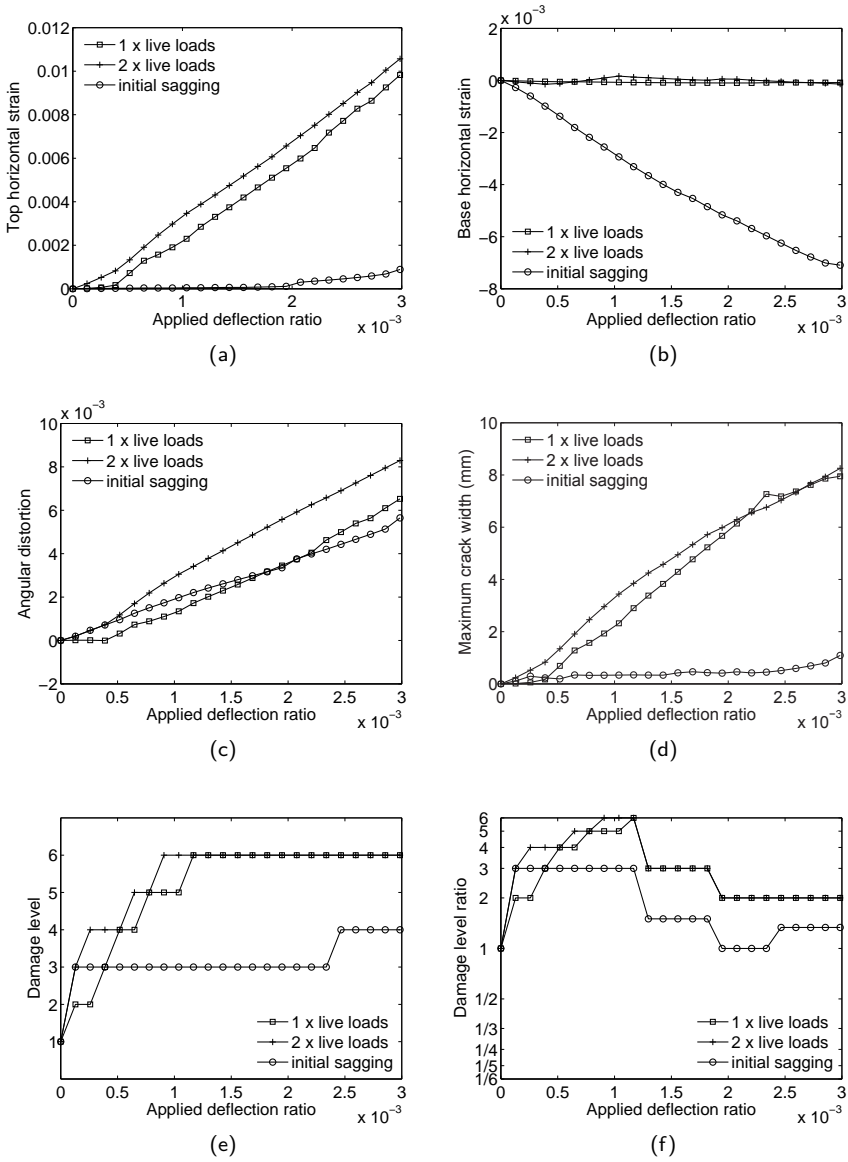


Figure 5.19: Initial damage variation: damage indicators as a function of the applied deflection ratio.

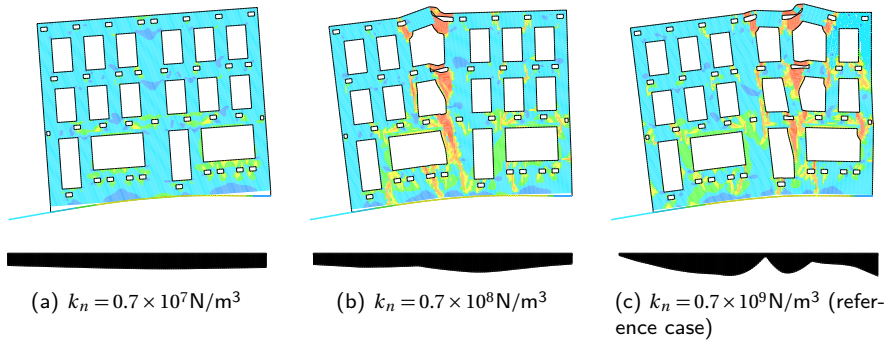


Figure 5.20: Maximum principal strain distribution, deformed configuration and base stress distribution at 11.5 mm of applied displacement, for different values of interface normal stiffness k_n .

in a further refinement of the preliminary assessment, as suggested by the Dutch Foundation for Building Research (SBR 1998, Table 2.10).

5.2.4 Soil-structure interaction

The availability of experimental data corresponding to a specific value of the base interface normal stiffness, which accounts for the interaction between the building, the soil and the foundation, allowed for the validation of the semi-coupled numerical model. Therefore, the reference continuum model represents a solid base for the evaluation of the interface effect on the structural response.

Bedding stiffness For $k_n = 0.7 \times 10^7 \text{ N/m}^3$, thus two orders of magnitude smaller than the reference stiffness, the interface leads to a strong redistribution of the base displacements, and therefore the façade stresses are significantly smaller than the applied ones (Figure 5.20). In this extreme case, the maximum principal strains are everywhere lower than the masonry tensile strength, and no damage arises. For a stiffness of $0.7 \times 10^8 \text{ N/m}^3$, the initial deformations are similar to those in the lower interface stiffness case (Figure 5.21a). However, at $\Delta/L = 2.5 \times 10^{-3}$ the reduced distribution of displacements leads to the façade cracking (Figure 5.21d), which develops according to a failure mechanism different from the reference one (Figure 5.20c). At this level of applied deformation, the façade displacements start to follow the ones related to the reference value with $k_n = 0.7 \times 10^9 \text{ N/m}^3$, and the

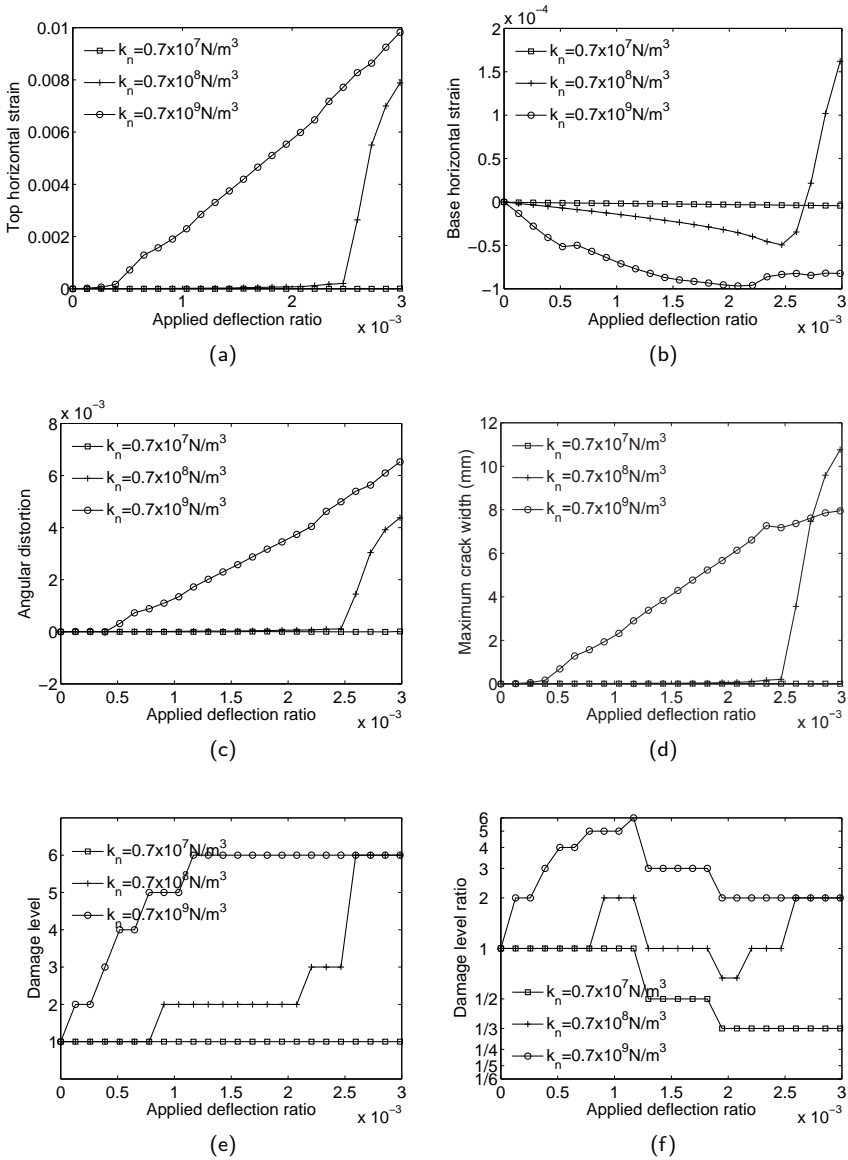


Figure 5.21: Variation of interface normal stiffness: damage indicators as a function of the applied deflection ratio.

amount of damage of the two cases becomes comparable. This tendency is confirmed by the comparison between the applied and resulting settlements at the façade base for difference values of k_n (Figure 5.22).

Figure 5.21e shows the effect of the interface stiffness variation on the final classification. At the same level of applied deflection ratio, the difference between the assumed value of interface stiffness can lead to a difference of up to five damage levels. When comparing the numerically derived damage level with the result of the analytical assessment, the original formulation of the LTSM is adopted, with no evaluation of the soil-structure interaction effect. Therefore, the difference between the three curves in Figure 5.21f is proportional to the damage reduction due to the decreasing interface stiffness. The modification factors introduced by Potts and Addenbrooke (1997) and modified by Franzius (2003) would lead to a less conservative analytical assessment, depending on the ratio between the soil and the structure stiffness. In the analysed cases, the use of the modification factors would reduce the discrepancy between cracking model and LTSM damage levels for $k_n = 0.7 \times 10^7 \text{N/m}^3$, where the LTSM predicts a higher damage level (Figure 5.21f).

The vector plots of the interface normal stresses for the three analysed cases (Figure 5.20) confirm a strong interdependency between the soil-structure interaction stiffness and the final damage, not only in terms of maximum deformation and crack width, but also in type of failure mechanism. The relation is also affected by the amount and location of openings. Note that the façade deformed configurations in (Figure 5.20) refers to the deformations starting at the beginning of the settlement application, when the displacements are reset to zero. Therefore the distance between the supporting beam and the interface base in Figure 5.20a and Figure 5.20b only indicate a relative displacement; no gap is arising in the interface, as proven by the corresponding vector plots of the interface normal stresses.

Horizontal displacements In the reference case, corresponding to the experimental conditions, no horizontal displacements are considered. When applying to the reference model the horizontal component of the hogging profile shown in Figure 5.5b, neither the failure mechanism nor the final damage is significantly modified. The horizontal displacements lead to an earlier crack initiation due to the horizontal strain (Figure 5.24d,e). For increasing values of applied deflection ratio, the horizontal strains at the façade base act as a restraint of the hogging failure mechanism, which is typically characterized by a bending crack developing from the wall top. Finally, the two rotating blocks defined by the vertical crack are sufficiently disconnected to overrule this effect, and the horizontal dragging contributes to a further separation. This conclusion is supported by the evolution of

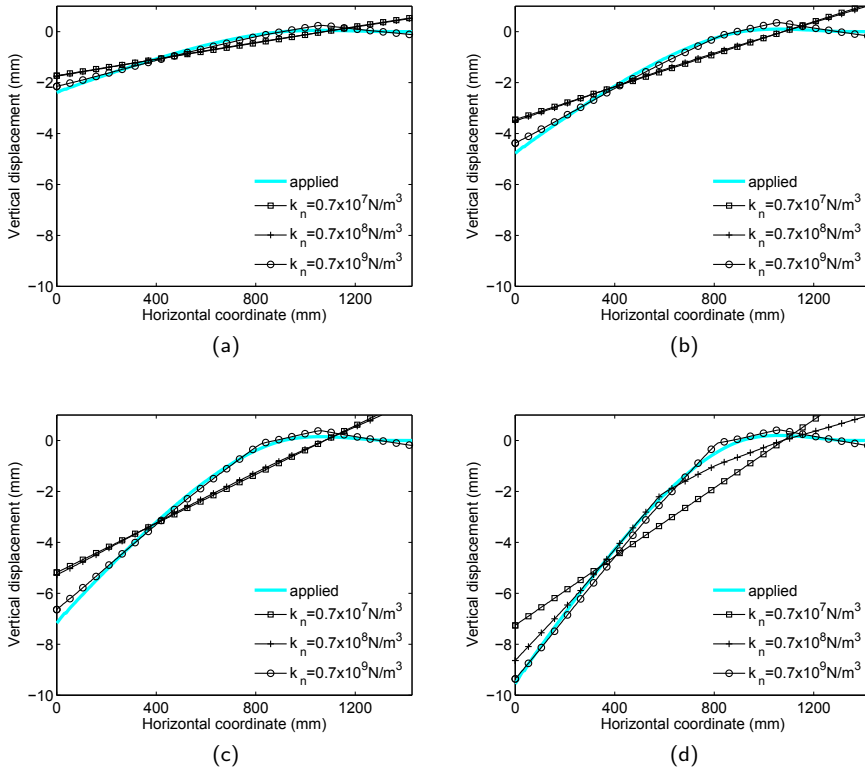


Figure 5.22: Comparison between numerical and experimental settlements at the façade base for for different values of k_n at applied vertical displacement of (a) 2.5 mm, (b) 5 mm, (c) 7.5 mm and (d) 10 mm.

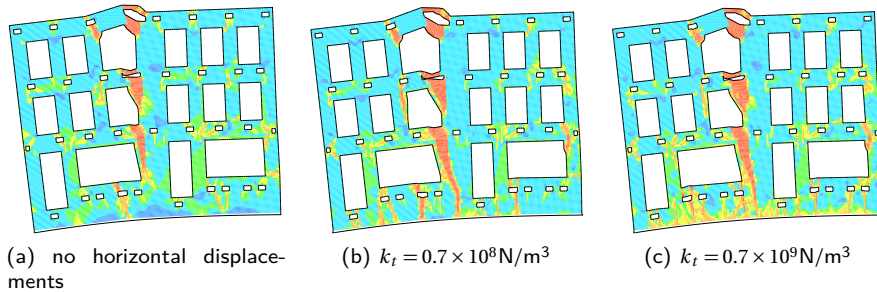


Figure 5.23: Maximum principal strain distribution and deformed configuration at 11.5 mm of applied displacement, for the variation of the interface shear behaviour.

the top horizontal strain $\varepsilon_{h,\text{top}}$ and the maximum crack width w_{max} (Figure 5.24a,d). The horizontal displacements reduce the façade deformation for $\Delta/L > 0.6 \times 10^{-3}$ and $\Delta/L < 1.5 \times 10^{-3}$. Up to the latter value, the model without horizontal strain acting on the base becomes the most damaged (Figure 5.24a,d). Among the two models with horizontal displacements applied, the most vulnerable is the one with the lowest interface shear stiffness.

Figure 5.24e points out the higher vulnerability induced by the horizontal component of tunnelling-induced displacements in a hogging zone. In this graph only the effect of earlier crack initiation is visible, because for $\Delta/L > 1.5 \times 10^{-3}$ all the three cases fall in the highest damage level. For this variation, the damage level ratio in Figure 5.24f it is not proportional to the damage level in Figure 5.24e. The reason is that for buildings in a hogging zone also the LTSM takes into account the increased vulnerability due to horizontal strains. In the analytical evaluation, the horizontal displacement is assumed to be transmitted fully to the structure, and therefore the increase in damage level is conservative. This leads to a reduced difference between the numerical and the analytical outputs. The results of these analyses confirm the conclusions from Netzel (2009): horizontal ground movements in a hogging zone have a negative effect on surface structures. However, for practical use of this recommendation, it has to be taken into account that field observations revealed little transmission of horizontal deformations through continuous footings (Burland et al., 2004).

In this case and in the following variations, the horizontal and vertical displacements were directly applied to the nodes of the interface lower side, without modelling the supporting beam. The applied hogging profile (Figure 5.5) is slightly different

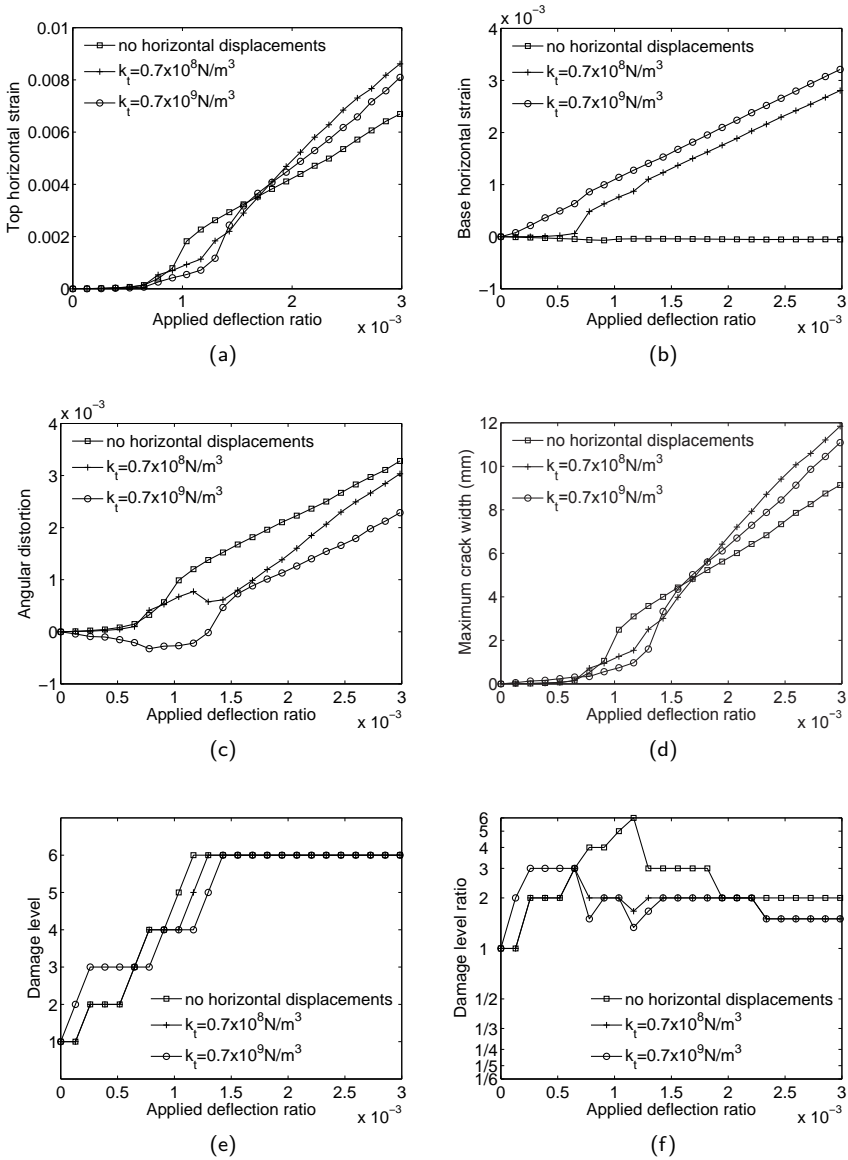


Figure 5.24: Variation of interface shear behaviour: damage indicators as a function of the applied deflection ratio.

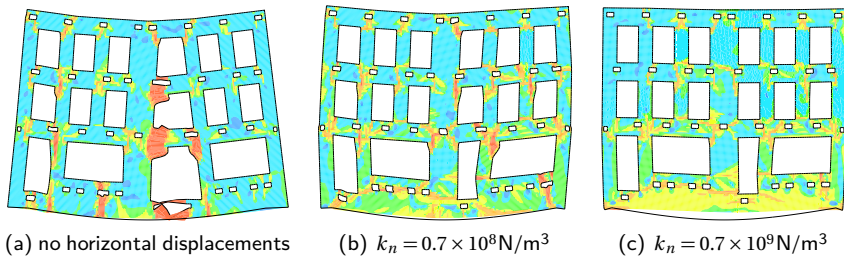


Figure 5.25: Maximum principal strain distribution and deformed configuration at 11.5 mm of applied displacement, sagging profile.

from the previous one (Figure 3.5). This explains the different deformation between the hogging case with no horizontal displacements shown in Figure 5.23a and the reference case.

5.2.5 Settlement profile

In case of buildings subjected to sagging deformation (Figure 5.5a), the horizontal component of ground displacements has a converse effect on the structural response, with respect to the hogging case. If no horizontal displacements are applied, the façade develops a typical failure mechanism with a main central crack initiating from the base (Figure 5.25a). The base horizontal displacements point towards the middle of the façade (Figure 5.5b), resisting the global deformation caused by the vertical displacements. Therefore, they are consistently beneficial for the structure, preventing the main crack development (Figure 5.25b). In the non-realistic case of a very high shear stiffness, the induced stiffening of the façade would lead to the base interface gapping (Figure 5.25c).

In case of sagging, the deformation parameters which reflect best the failure mechanism and the maximum crack growth (Figure 5.26d) are the base lateral strain and the angular distortion (Figure 5.26b,c). The damage level and the damage level ratio (Figure 5.26e,f) show a consistent progression with the increase of the applied deformation, because in the LTSM calculation the effect of horizontal strain is not taken into account. This assumption, commonly adopted in practice, is conservative, because it excludes the beneficial effect of the restraint.

Contrary to what is reported in literature (Burland et al., 2001), at the same level of applied deflection ratio the façade in a sagging area without horizontal

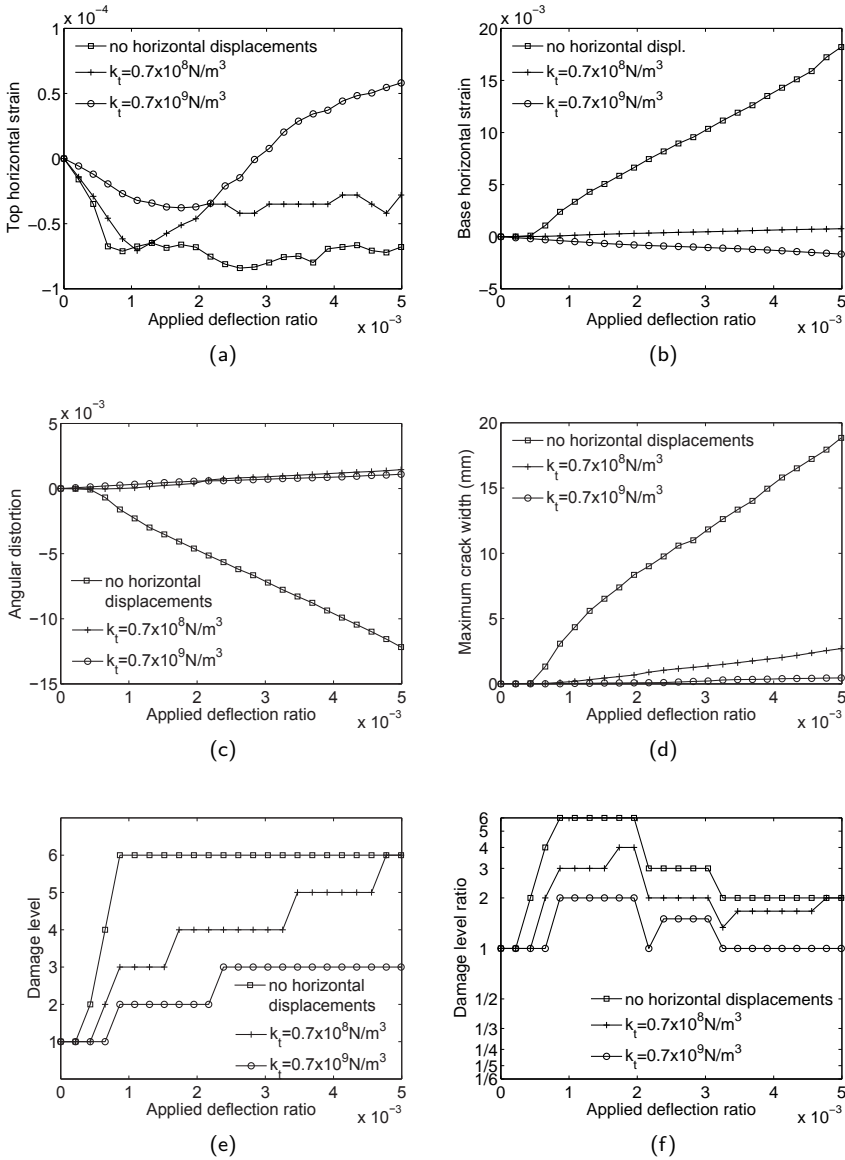


Figure 5.26: Sagging profile: damage indicators as a function of the applied deflection ratio.

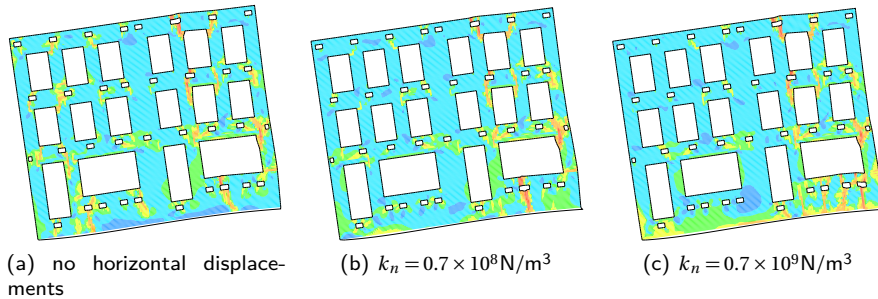
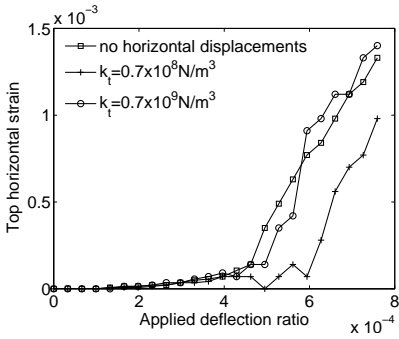


Figure 5.27: Maximum principal strain distribution and deformed configuration at 11.5 mm of applied displacement, hogging-sagging mixed profile.

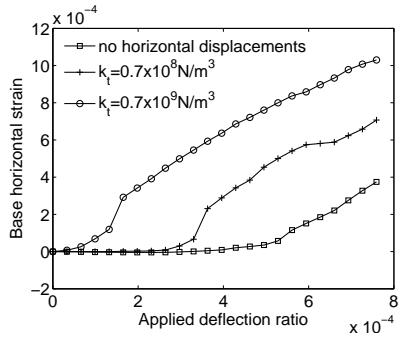
displacements applied exhibits more damage than the one subjected to hogging deformation. A possible explanation lies in the choice for the symmetric sagging deformation, which corresponds to a building located above the tunnel axis, and therefore does not represent a statistically widespread situation in reality. Furthermore, the specific location of openings significantly reduces the cross section in the building area subjected to the larger sagging deformation, facilitating the crack initiation and brittle growth. Lastly, in real buildings a small part of horizontal strains is transmitted from the ground to the structure, acting in a sagging zone as a restraint of the failure mechanism, as described above.

In addition to the pure hogging and pure sagging deformations, a mixed situation, where the middle point of the façade is located above the inflection point of the tunnelling-induced settlement trough, is considered (Figure 5.5). In this case, the first crack develops from the top of the façade in the section subjected to the hogging-induced maximum bending strain (Figure 5.27a).

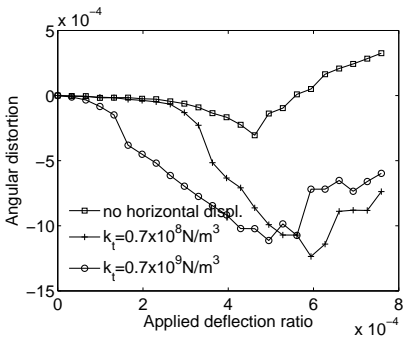
The horizontal displacements increase the structural vulnerability, leading to cracks in the lower part of the façade subjected to hogging deformations. The final damage increases with the increase of the interface shear stiffness (Figure 5.28b,d). With respect to the previous cases in pure hogging and sagging area, the structure is subjected to an applied deflection ratio of almost one order of magnitude smaller. This explains the reduced value of maximum crack width (Figure 5.28d) and the corresponding lower damage level (Figure 5.28e,f).



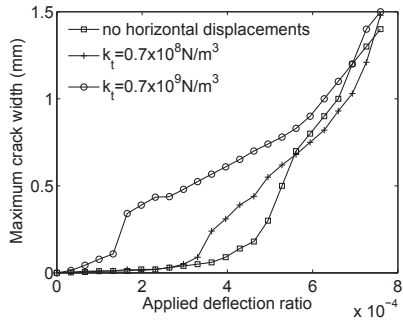
(a)



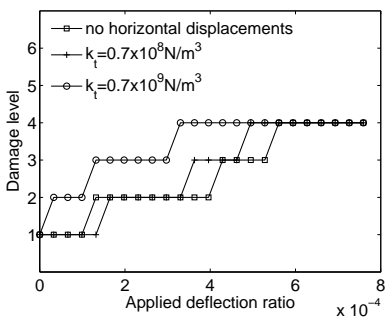
(b)



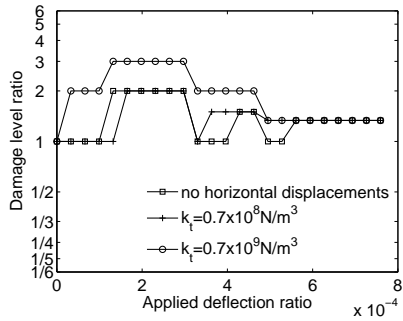
(c)



(d)



(e)



(f)

Figure 5.28: Hogging-sagging mixed profile: damage indicators as a function of the applied deflection ratio.

5.3 Conclusions

In this chapter, the 1/10th scaled 2D finite element semi-coupled model validated in Chapter 4 was used to perform a sensitivity analysis of different factors on the response of a masonry façade due to tunnelling. Geometrical characteristics, material parameters, boundary conditions and initial loading and damage were included in the parametric study. The outputs were used to form a solid framework of evaluation and comparison with the LTSM.

The results underlined the high dependency of the final damage on the material cracking and the soil-structure interaction, which should therefore be included in the structural response evaluation. Due to the great influence of stress redistribution, the use of an elastic constitutive model or an inaccurate evaluation of the soil-structure interaction can lead to the prediction of an incorrect failure mechanism.

The conclusion was confirmed by the comparison between damage classifications based on analytically calculated tensile strain and numerically derived crack width; the comparison also emphasized the need to explicitly take into account the crack localization induced by the openings. These parameters are the ones causing a strong discrepancy between the numerical and the analytical damage classification in the reference case, i.e. the model of the laboratory test. The higher vulnerability of the experimentally validated case is mainly due to the poor quality of the masonry and the large amount of openings which induce crack localization.

Initial loading and initial cracking also strongly influence the structural vulnerability, especially if they damage the structure with the same mechanism subsequently leading to failure. The effect of horizontal displacements, although not always found in real cases, was detected as beneficial for sagging deformations and detrimental for the hogging type.

The quantitative results of the 2D variational study will be used in Chapter 8 to set the framework of an alternative damage classification system.

3D finite element modelling

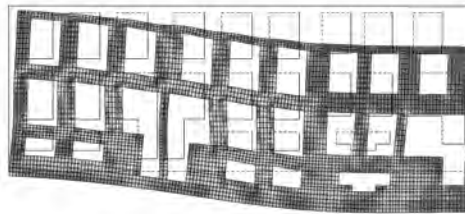
6

In this chapter, a global approach to evaluate the building response to tunnelling-induced settlement is presented. The method is based on a 3D finite element analysis, performed on a fully coupled model of building, foundation, soil and tunnelling. Compared to the 3D models currently available in literature and summarized in Chapter 2, the main improvement of the presented approach consists in the introduction of a crack constitutive law with tension softening to simulate the progressive building damage on a masonry building. Coupling the different components allows reproducing the reciprocal influence between the building and the settlement profile. The 3D simulation of the structure and the tunnelling advance makes it possible to include the longitudinal settlement profile effect and the torsional building response. Two different approaches for the modelling of pile foundations are evaluated: the use of 3D embedded beam elements with interface slip and the use of horizontal interface elements with equivalent non-linear behaviour. To increase the damage assessment accuracy, structural details like openings and transverse walls are included.

The first three sections of the chapter describe the modelling aspects of the building, soil, tunnel excavation and foundations. Section 6.1 gives a synopsis of the model and emphasizes the relevance of the 3D modelling for the structure. Section 6.2 underlines the importance of a proper tunnelling advance method by means of a numerical example. Section 6.3 focuses on representing pile foundations in a 3D model, also by means of a numerical example. The potential of the proposed approach is validated in Section 6.4 through the simulation of a literature case study, the tunnelling-induced damage to the Mansion House in London.



(a) building in Vijzelgracht, Amsterdam



(b) 2D finite element model

Figure 6.1: Numerical analysis of a masonry building damaged by differential settlement (van Abeelen, 2009).

6.1 3D coupled model of building and soil

In the proposed approach the building is modelled in 3D. With respect to the 2D model of a single façade, the 3D representation of the building has the major advantage of including the torsional response to the 3D settlement profile. The numerical analysis of real buildings affected by differential settlements demonstrated that 2D models cannot accurately reproduce the building deformation, unless the stiffening effect of the transverse wall is artificially added to the model, e.g. by means of spring elements (van Abeelen (2009), Figure 6.1).

Consistently with the 2D model illustrated in Chapter 3 and Chapter 4, also the 3D model reproduces the geometry of a typical historic Dutch house (Figure 6.2a). The structure consists of two units separated by an internal wall; the external façades contain door and window openings. The external façades and the internal walls of the house were modelled by shell elements. The roof and the wooden floor diaphragms were not represented because their stiffness is considered negligible with respect to the global stiffness of the building; their weight was included in the building weight. The building was subjected to dead loads and live loads. The rotating crack model experimentally validated in Chapter 4 was adopted for the masonry. The material is

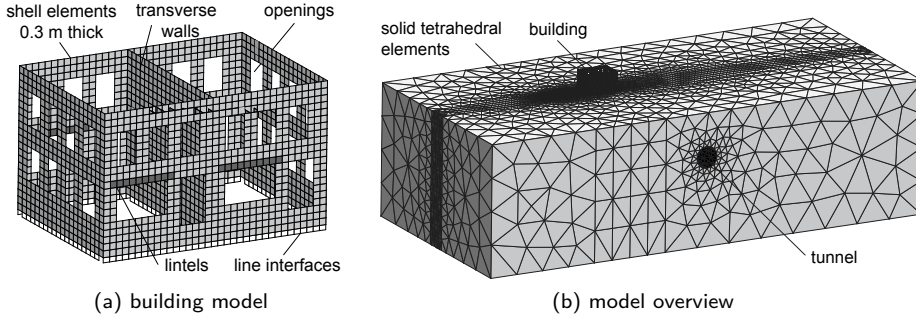


Figure 6.2: Finite element model.

considered elastic in compression and having a linear softening behaviour in tension.

To simulate the transmission of vertical and horizontal deformations from the ground to the structure through the shallow strip foundations, line interface elements were adopted, with a non-linear relation between the normal and shear stresses and the relative displacements across the interface. A no-tension criterion in the normal direction and a Coulomb friction criterion in the tangential direction were assumed.

The soil block was modelled by solid tetrahedral elements (Figure 6.2b). The nodes of the vertical exterior faces of the soil domain were constrained in the normal horizontal direction, while the nodes in the bottom plane were fixed in horizontal and vertical direction. The large size of the soil model, with respect to the tunnel and building dimensions, leaves the area around the building free from boundary effects.

In the proposed model, the focus is placed on the simulation of the 3D structural behaviour of the building, with particular attention to its brittle response. The foundation, the soil and the tunnel represent a system of mixed boundary conditions for the building, with the aim of reproducing the selected reference settlement trough and the effect of tunnelling advance on the surface. Against this background, an elastic constitutive behaviour with the Young's modulus E linearly increasing with the depth z was assumed for the ground:

$$E = E_0 + m z \quad (6.1)$$

where E_0 is the Young's modulus at the surface and m is a constant gradient. In spite of the strong simplification, a preliminary analysis performed on a greenfield model gives a settlement profile comparable with the Gaussian curve and the case

study presented in Section 6.4 shows a good simulation of the ground displacement trough modified by the soil-structure interaction (Figure 6.33).

6.2 Tunnel advance modelling

For the simulation of the tunnel advance, the staged approach proposed by Augarde (1997) and described in Section 2.3.3 was adopted. In order to verify the influence of the staged modelling, the damage due to the tunnel advance was analysed and compared with a simplified analysis where the tunnel advance is ignored and the tunnel volume losses are applied simultaneously over the full length of the tunnel.

6.2.1 Numerical model

The situation illustrated in Figure 6.3 was considered. A tunnel with a diameter of 10 m is excavated in soft soil under a masonry building on shallow strip foundations. Two locations of the building were studied: directly above the centreline of the tunnel and with an eccentricity of 27 meters between the tunnel and the building centrelines.

The tunnelling process was simulated by a sequence of discrete steps. First, the initial state of the model without the tunnel is evaluated (stage 1). The self-weight and the floor loads are applied to the building at this stage. In the next six stages (from 2 to 7 in Figure 6.4), successive circular slices of tunnel elements are removed and a corresponding part of the lining is activated. At each step, the stresses calculated from the previous stage are applied, and the equilibrium state of the new model is obtained through an incremental adaptation to the actual loading. The lining was modelled by curved shell elements with linear elastic behaviour. The building and the soil were modelled according to the criteria illustrated in the previous section. The specific values adopted for the material parameters are listed in Table 6.1.

6.2.2 Results and discussion

The maximum principal strain contour plots and the magnified deformed shapes shown in Figure 6.7 visualize the cracked areas and highlight the different failure mechanisms. The graphs in Figure 6.8 give a representation of the total amount of relevant cracks in terms of the lengthening of the façade, as shown in Figure 6.6 for typical failure mechanisms in hogging and sagging zone. Two different models are compared: the solid line represents the results of the analysis performed including

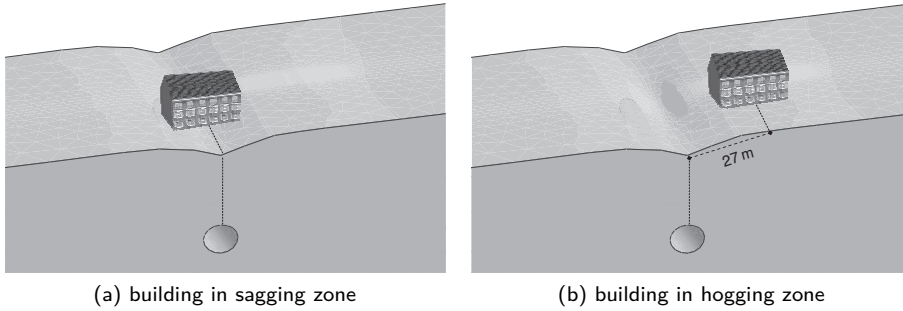


Figure 6.3: Geometry of the problem.

Table 6.1: Parameters for the numerical model.

Material	Parameter	Value
Masonry	Young's modulus	$E_M = 6 \times 10^3 \text{ N/mm}^2$
	Density	$\rho_M = 2.4 \times 10^{-6} \text{ kg/mm}^3$
	Poisson's ratio	$\nu_M = 0.2$
	Tensile strength	$f_{t,M} = 0.3 \text{ N/mm}^2$
	Fracture energy	$G_{f,M} = 0.05 \text{ N/mm}$
Soil	Young's modulus	$E_s = 50 \text{ N/mm}^2$
	Gradient	$m = 1 \times 10^{-2} \text{ N/mm}^3$
	Density	$\rho_s = 2 \times 10^{-6} \text{ kg/mm}^3$
	Poisson's ratio	$\nu_s = 0.3$
Base interface	Normal stiffness	$k_{n,b} = 0.2 \times 10^3 \text{ N/mm}^3$
	Tangent stiffness	$k_{t,b} = 0.1 \times 10^3 \text{ N/mm}^3$
	Tensile strength	$f_{t,b} = 0 \text{ N/mm}^2$
	Cohesion	$c_i = 0 \text{ N/mm}^2$
	Friction angle	$\tan \phi_i = 0.57$
	Dilatancy angle	$\tan \psi_i = 0$

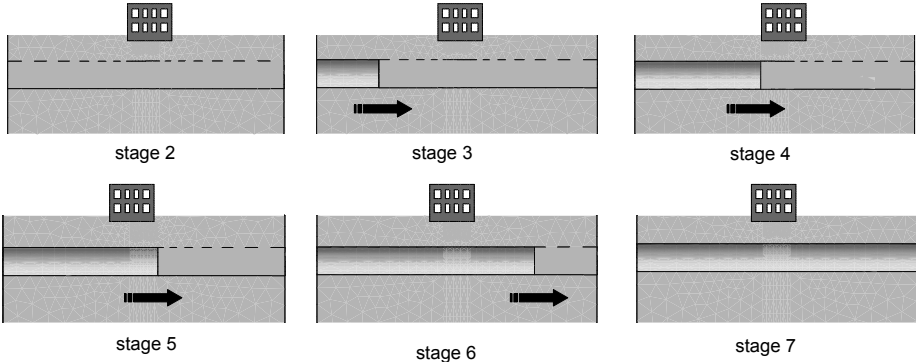


Figure 6.4: Staged analysis.

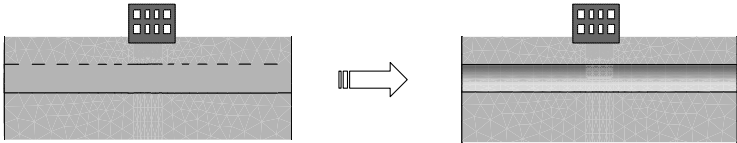


Figure 6.5: Non-staged analysis.

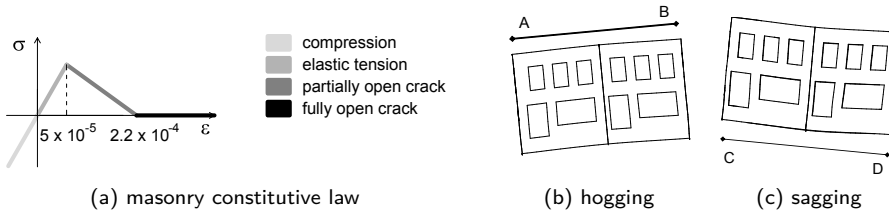


Figure 6.6: Masonry stress–strain relation and distances used to represent the global damage.

the tunnelling progress in time (Figure 6.4), while the dotted line is the output of the model in which the tunnel advance is ignored and the tunnel volume losses (Equation (2.4)) are applied simultaneously over the full length of tunnel (Figure 6.5).

The graphs in Figure 6.8a,c,e show a general increasing of the distance AB (Figure 6.8b), as a consequence of the tunnelling-induced volume loss. Differences can be observed between the damage resulting from the staged analysis and the non-staged ones. Due to the progression of the tunnel, the transverse façade and the interfaces experience a certain amount of inelastic deformation, which is not completely recovered after the tunnel passage. Therefore, the final crack pattern for the structure in the staged analysis is more pronounced than the one obtained by neglecting the tunnel advance. In reality, this effect would be amplified in case of structures previously damaged or with foundations in poor conditions, like in the case of historic buildings. For high values of volume loss, this difference in terms of crack width can lead to a different classification of the building in the traditional damage assessment method. The simplifying assumption of neglecting the time variable influences also the failure mechanism. In fact, if the same volume loss is applied at the same time, then the horizontal deformation of the ground is less gradually redistributed to the structure through the interface, and a certain level of tensile strain is observed in the lower side of the façade (Figure 6.7d-f). In the sagging zone, the settlement profile causes a different failure mechanism (Figure 6.6c), with cracks arising in the lower part of the façade and propagating to the top (Figure 6.7g-i). The role of the soil-structure interaction in the transmission of the deformations to the building is illustrated in Figure 6.8b,d,f. For low values of volume loss, the horizontal restraint represented by the friction reduces significantly the tension due to the vertical settlement, causing an initial slight compression of the façade base (Figure 6.8b). This effect tends to vanish when the vertical settlement becomes dominant (Figure 6.8d,f). For some values of volume loss, also in the sagging zone

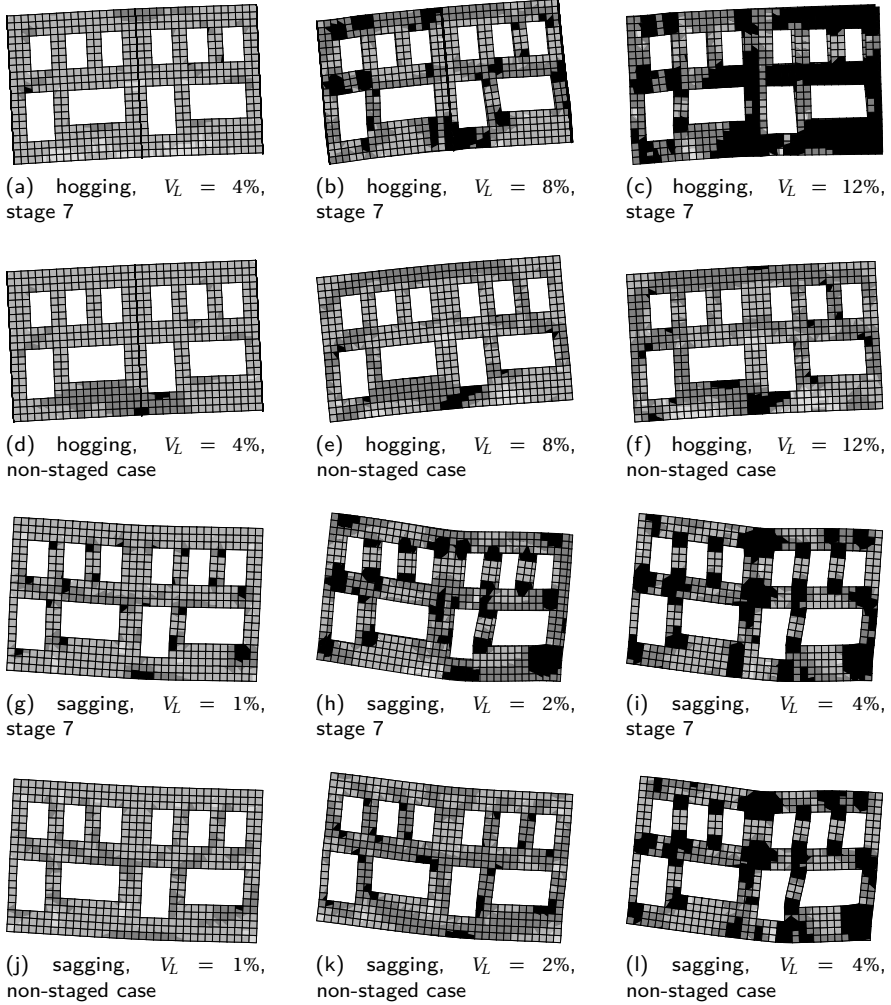
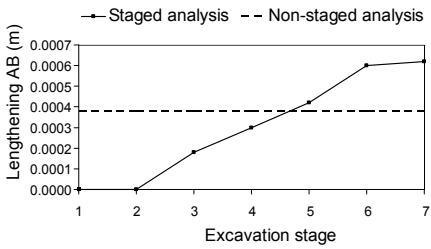
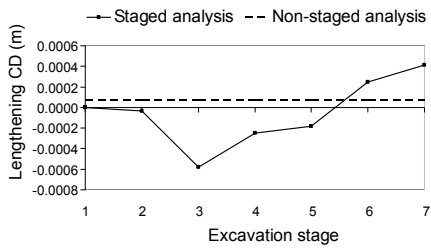


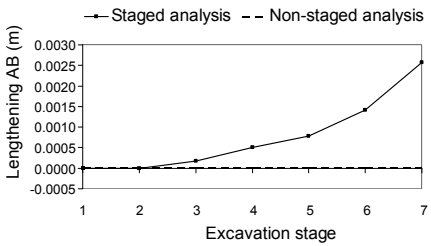
Figure 6.7: Maximum principal strain plots for different building location and volume loss values: comparison between staged and non-staged analysis.



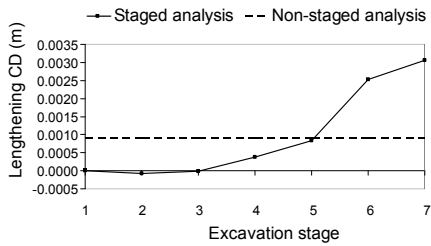
(a) hogging, volume loss = 4%



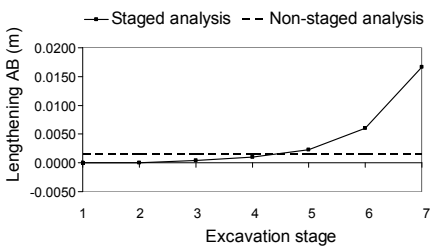
(b) sagging, volume loss = 1%



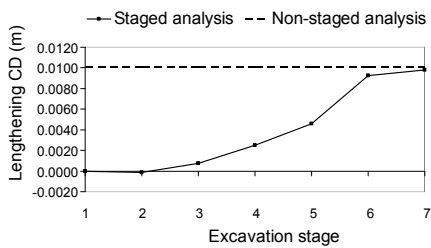
(c) hogging, volume loss = 8%



(d) sagging, volume loss = 2%



(e) hogging, volume loss = 12%



(f) sagging, volume loss = 4%

Figure 6.8: Lengthening of the distances used to indicate the global damage (Figure 6.6b,c) for different building location and volume loss values: comparison between staged and non-staged analysis.

the non-linear deformation accumulated during the tunnelling advance results in a crack pattern which is more severe than the one resulting from the non-staged analysis (Figure 6.8b,d and Figure 6.7g,j,h,k).

6.3 3D pile foundation modelling

An essential role is played by the interaction between the building and the tunnelling-induced settlement trough. In the 2D semi-coupled approach validated in Chapter 4, this interaction was simulated by means of a base interface. The same approach could be used to simulate the foundation response in 3D models. The interface element (Figure 6.9c) behaviour, defined in terms of a relation between the normal and shear stresses and the normal and shear relative displacements across the interface, can be relatively easily adapted to the shallow foundations response (Figure 6.9b). In this section, the specific feasibility of such interface to model pile foundation (Figure 6.9a) is investigated.

Pile foundations can be modelled in detail by means of solid elements with plane interfaces connected to the soil solid elements. The disadvantage of this approach is the complex and fine mesh generation that is required to match the nodes of the pile and the soil elements (Figure 6.10a). This results in a time consuming analysis, both in terms of pre-processing and calculation. The use of 3D embedded beam elements with interface slip represents a valid alternative to this approach (Engin et al., 2009), because the piles can be added to an existing soil mesh with arbitrary mesh lines (Figure 6.10b). The present study aims to a further simplification, by including the non-linear pile foundation response in the properties of an horizontal interface (Figure 6.10c).

6.3.1 Dutch pile foundation

The specific case of an historical Dutch house (Figure 6.9a) with wood foundation driven in the first sand layer to a depth of 10 m (Figure 6.11) was analysed. First, load–displacement curves in vertical and horizontal directions for a single pile were analytically derived. Then, the performance of a single embedded beam and an equivalent horizontal interface was evaluated in terms of displacements. Finally, the two different approaches were applied to a 3D analysis of a masonry building subjected to tunnelling-induced settlements, both in terms of displacement and final structural damage.

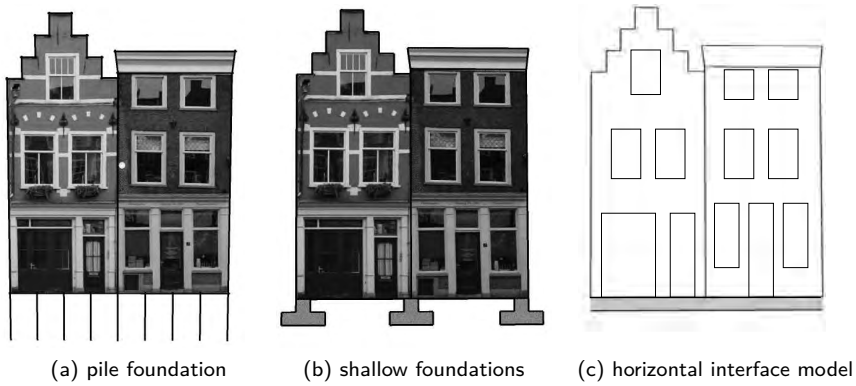


Figure 6.9: Modelling of soil-structure interaction through interface elements.

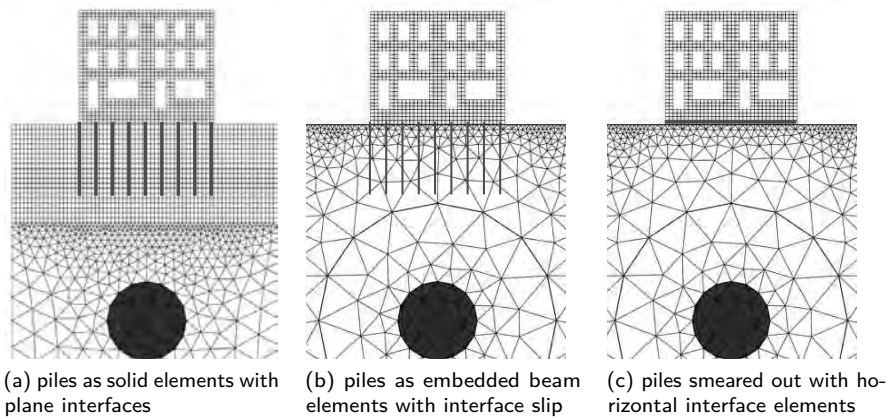


Figure 6.10: Pile foundation modelling approaches: 3D model sections.

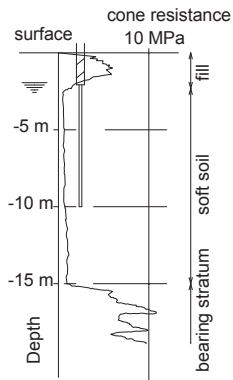


Figure 6.11: Soil stratigraphy and cone penetration test (van Tol, 1999).

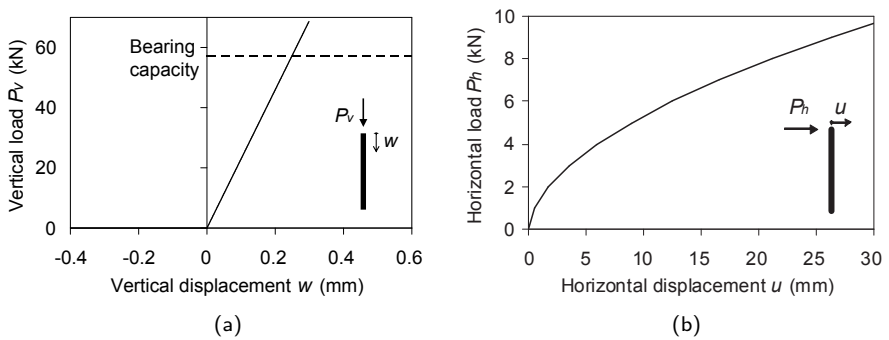


Figure 6.12: Load–displacement curves for vertical (a) and horizontal (b) loads.

Vertical loads

The ultimate bearing capacity Q_u of a single pile is generally calculated as sum of the toe resistance Q_t and the shaft resistance Q_s . Q_t and Q_s are derived from the undrained shear strength c_u of the soil, using the total stress method (Tomlinson, 1980). The toe resistance is given by:

$$Q_t = A_p N_c c_u = 23.4 \text{ kPa} \quad (6.2)$$

where $A_p = 0.26 \text{ m}^2$ is the pile cross section area, N_c is the bearing capacity factor, usually taken as 9 for deep foundations, and c_u is determined using the cone penetration test data:

$$c_u = \frac{q_c - \sigma_{v0}}{N} = 10 \text{ kPa} \quad (6.3)$$

In Equation (6.3), q_c is the minimum cone end resistance profile value (Figure 6.11), σ_{v0} is the total vertical stress and $N=20$ is an empirical coefficient. The shaft resistance is:

$$Q_s = \pi D L \alpha c_u = 57.1 \text{ kN} \quad (6.4)$$

where $D = 0.182 \text{ m}$ is the pile diameter, $L = 10 \text{ m}$ is the pile length, α is the empirical adhesion factor, equal to 1 for the calculated value of c_u (Tomlinson, 1980). Due to the fact that the shaft and toe resistance does not simultaneously coexist, because they are mobilized at different order of displacement magnitude, and that the analysed pile does not reach the consistent base layer, it was assumed that in this case the pile-load bearing capacity depends entirely on the shaft resistance. The load–displacement curve under vertical load was calculated using the approximate analytic method (Randolph and Wroth, 1978). The displacement of the pile shaft is given by:

$$w = \frac{Q_s}{2 \pi L \rho G_s} \ln \left(\frac{r_m}{r_0} \right) \quad (6.5)$$

where r_0 is the pile radius, $G_s = 1.92 \times 10^4 \text{ kPa}$ is the soil shear modulus, $r_m = 2.5 L \rho (1 - \nu)$, $\nu = 0.3$ is the Poisson's ratio of the soil and $\rho = 1$. Figure 6.12a shows the vertical load–displacement curve. The curve gradient represents the pile stiffness k_v , equal to $2.29 \times 10^5 \text{ kPa}$. The dotted line represents the ultimate bearing capacity $Q_u = Q_s$. A no-tension criterion was assumed.

Horizontal loads

The characteristic method (Duncan et al., 1994) was applied to estimate the lateral deflections in single fixed-head piles under lateral loads. The characteristic load is defined as:

$$P_c = F D^2 (E R_1) \left(\frac{\sigma_p}{E R_1} \right)^m (\epsilon_{50})^n = 55.78 \text{ kN} \quad (6.6)$$

where $F = 1$, $E = 1.5 \times 10^7 \text{ kPa}$ is the Young's modulus of the pile, $R_1 = 1$, $\sigma_p = 4.2 c_u$, $\epsilon_{50} = 0.004$, $m = 0.683$ and $n = -0.22$ for clay. The displacement u for different levels of load P_h was derived using the equation:

$$\frac{u}{D} = a \left(\frac{P_h}{P_c} \right)^b \quad (6.7)$$

where $a = 14$ and $b = 1.846$ for clay (Brettmann and Duncan, 1996). The horizontal load–displacement curve is shown in Figure 6.12b.

6.3.2 Single element evaluation

Embedded beam elements are incorporated in the soil elements (Figure 6.13a) and they interact with the soil through normal and shear behaviour of an interface along the beam (Figure 6.13b,c). Using as reference the load–displacement curves derived for a single pile, the performance of a 3D embedded beam element with interface was evaluated. A decoupled analysis was performed: the finite element model of a single embedded beam under vertical load was used to evaluate the equivalent stiffness of the element, while from the same model subjected to horizontal load the normal stiffness was obtained. The vertical displacements w are related to the shear stresses τ_p in the interface along the pile. The horizontal displacements u are related to the normal stresses σ_p in the interface along the pile.

Also the behaviour of the horizontal interface elements is described in terms of relations between the normal and tangential stresses and the relative vertical and horizontal displacements across the interface (Figure 6.14b,c). Due to the element topology (Figure 6.14a), in this case a vertical load was applied to evaluate the normal interface behaviour, while the horizontal load was used to calibrate the shear stress transfer. In fact, for the horizontal interface elements, the vertical displacements w are related to the normal stresses σ_i , while the shear stresses τ_i are associated to the horizontal displacements u .

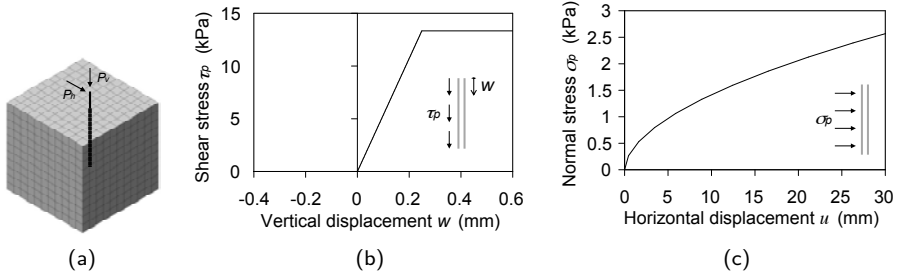


Figure 6.13: Single embedded beam element with an interface along the beam: (a) finite element model and (b,c) constitutive laws.

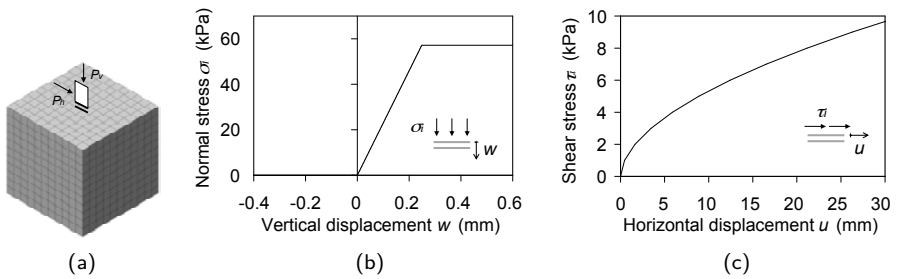


Figure 6.14: Single horizontal interface element: (a) finite element model and (b,c) constitutive laws.

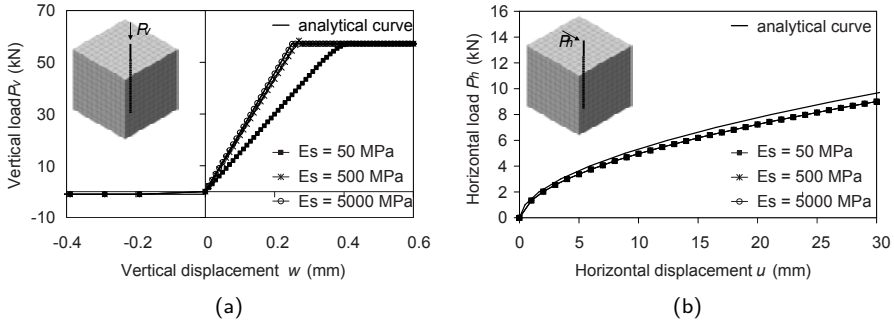


Figure 6.15: Single embedded beam element with an interface along the beam: load–displacement curves for vertical (a) and horizontal (b) loads.

Vertical loads

Figure 6.15a shows the load–displacement curves in vertical direction for the single embedded beam, calibrating the shear stiffness

$$k_{s,p} = \frac{k_v}{(\pi D L)} = 5.36 \times 10^4 \text{ kN/m}^3 \quad (6.8)$$

The analytically derived value includes the soil stiffness influence, while in the FEM the soil is modelled explicitly. Therefore, a sensitivity analysis was performed to evaluate the effect of soil stiffness variation. Results show that for low interface/soil stiffness ratios the interaction can be entirely represented by the interface constitutive law. The same conclusion can be drawn from the analysis of the vertical load–displacement curve for the single interface element with unit area A_i (Figure 6.16a), where the equivalent normal stiffness of the element was calibrated:

$$k_{n,i} = \frac{k_v}{A_i} = 2.29 \times 10^5 \text{ kN/m}^3 \quad (6.9)$$

Horizontal loads

Using a similar approach, the equivalence in terms of global stiffness for both the embedded pile and the interface elements can be derived in the horizontal direction (Figure 6.15b, Figure 6.16b). In this case, the lowest value of soil stiffness assumed in the sensitivity analysis is high enough not to affect the results.

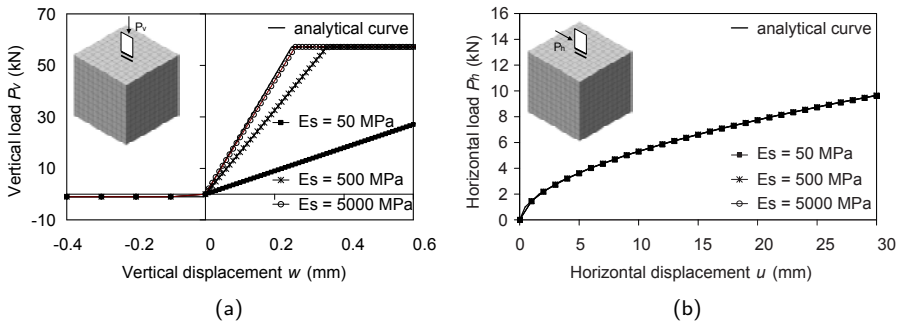


Figure 6.16: Single horizontal interface element: load–displacement curves for vertical (a) and horizontal (b) loads.

6.3.3 3D coupled model

The two pile foundation modelling approaches were then applied to a fully coupled finite element analysis of a tunnel excavation in soft soil. The modelling assumptions for the building, the soil and the tunnel advance are the same illustrated in Section 6.1 and Section 6.2. In this case, the tunnel excavation process was simulated in 20 stages (Figure 6.17b). The model dimensions are shown in Figure 6.17 and Figure 6.18.

Figure 6.19 shows the comparison between the global behaviour of the model with embedded beams and the model with interface elements. The verified equivalence in terms of vertical and horizontal load–displacement curves at the structure base is the required assumption for the further evaluation of the building response to tunnelling. The aim of the comparison between the tunnelling-induced deformation and the final damage of the two models is getting a better insight into the effect of foundation modelling. In particular, the difference in terms of settlement profile transmitted from the soil to the structure was evaluated. By assuming the relatively high value of soil stiffness required to localize the soil–structure interaction at the interface level (Figure 6.16a), the group effect of pile foundations is neglected.

6.3.4 Results and discussion

Figure 6.20a shows the greenfield horizontal and vertical displacements obtained at the surface level as a consequence of the tunnel excavation and without any surface buildings, as a function of the horizontal distance to the tunnel axis. Figure 6.20b

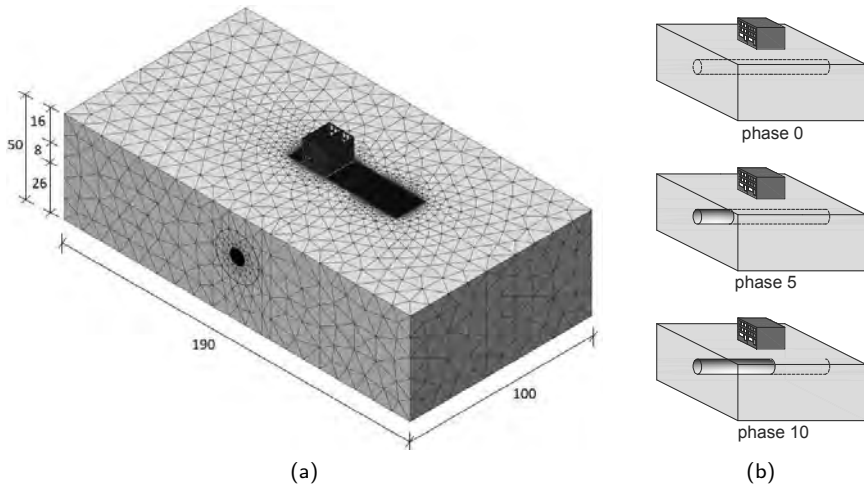


Figure 6.17: (a) Geometry of the 3D finite element model and (b) staged analysis of tunnel advance (Boldrini, 2011). Dimensions in m.

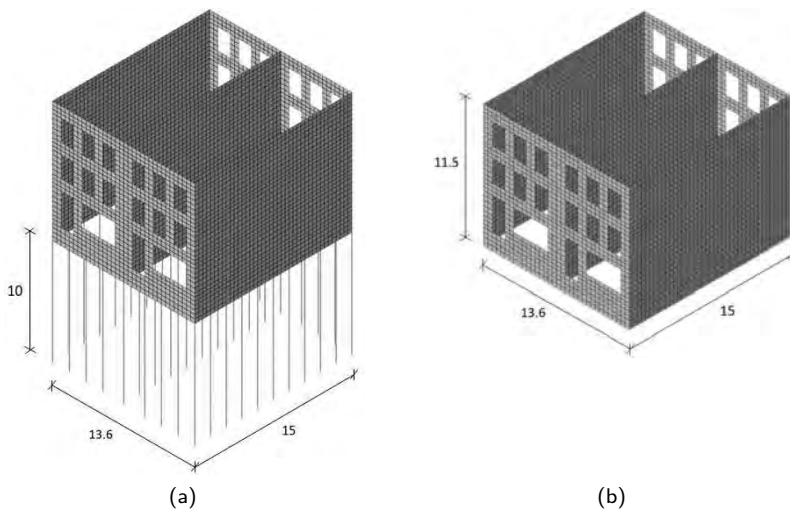


Figure 6.18: Building model with (a) embedded pile beam and (b) interface elements (Boldrini, 2011). Dimensions in m.

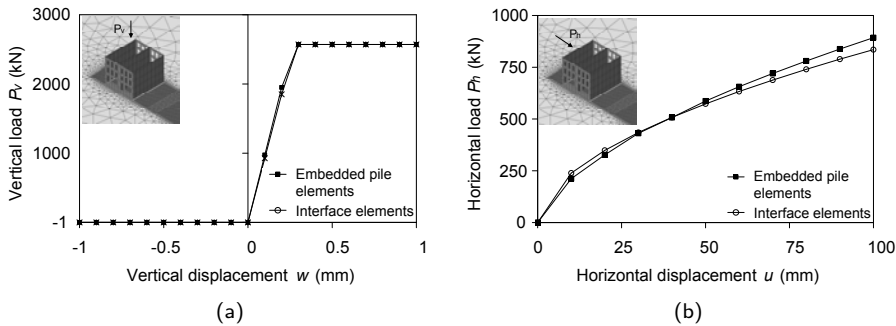


Figure 6.19: Load–displacement curves for the compared models in vertical (a) and horizontal (b) direction.

illustrates the settlement profile of the tunnel advance in the longitudinal direction; the reference section is in the sagging zone at ± 13.6 m from the tunnel axis.

In Figure 6.23 the results of the coupled analysis for the model with the horizontal interface elements are presented. The maximum principal strains and the crack pattern of the front façade highlight the damage mechanism developing during and after the tunnel construction. In the assumed sagging zone, the façade is subjected to a downwards deflection with development of tensile strains at the base. Thus, the cracks start at the lower part of the structure and then propagate to the upper part. A certain amount of diffuse damage is due to the interface shear stiffness, acting as horizontal restraint (Figure 6.21b). The latter effect is governing the response when the pile foundation is modelled by embedded beam elements (Figure 6.21a, Figure 6.22). These elements transfer to the structure a settlement profile located at deeper level, where the magnitude of both vertical and horizontal displacements in the transverse direction is higher. In this sagging case, the lateral restraint provides a compression at the façade base; the compressive strains overrule the tensile strains generated by the building deflection, significantly reducing the extension of the damage. The impact of this effect becomes clearer if the same analysis is performed on a building model with interface elements characterized by negligible shear stiffness (smooth interface, Figure 6.21c, Figure 6.24). In this case, there is no restraint at the bottom and the crack in the middle is free to open up and propagate to the top.

Figure 6.25a shows a quantitative comparison between the three analysed cases in terms of maximum crack width, which is an indicator of the global damage. This value increases significantly from the maximum level of horizontal restraint

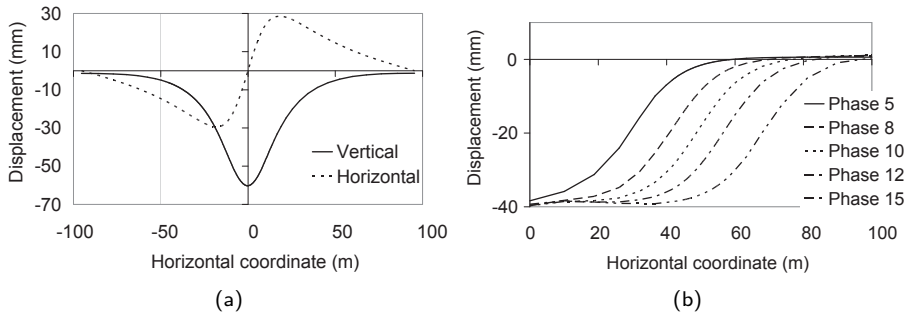


Figure 6.20: Tunnelling-induced greenfield movements at surface level: (a) transverse vertical and horizontal displacement; (b) development of longitudinal settlement with the tunnel advance.

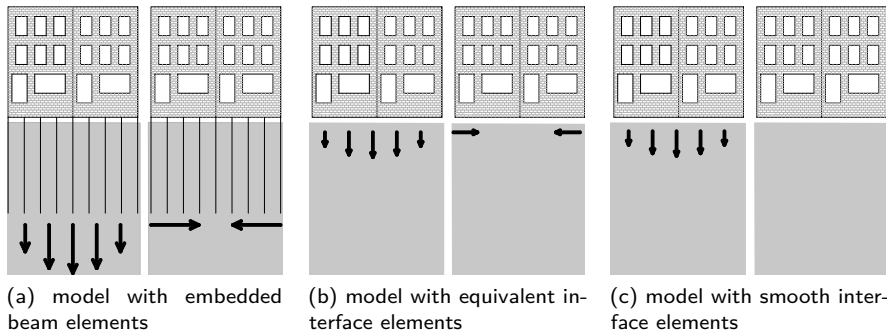


Figure 6.21: Scheme of the vertical and horizontal ground displacement transferred to the building, for sagging situation.

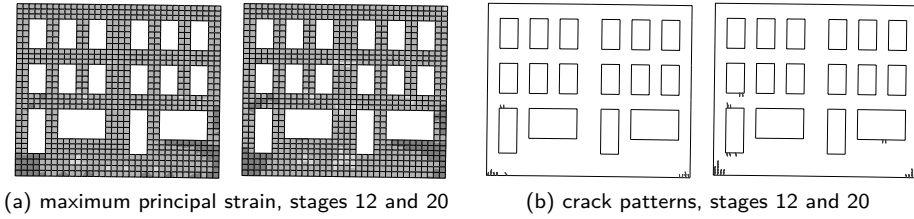


Figure 6.22: Model with embedded beam elements.

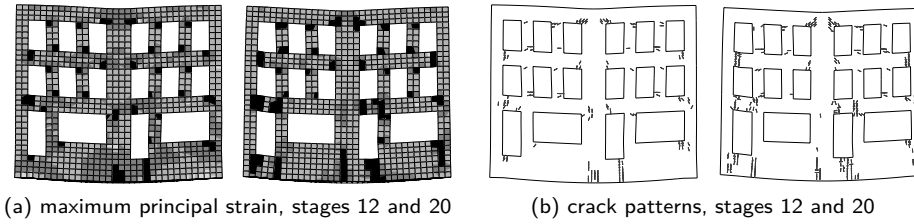


Figure 6.23: Model with equivalent interface elements.

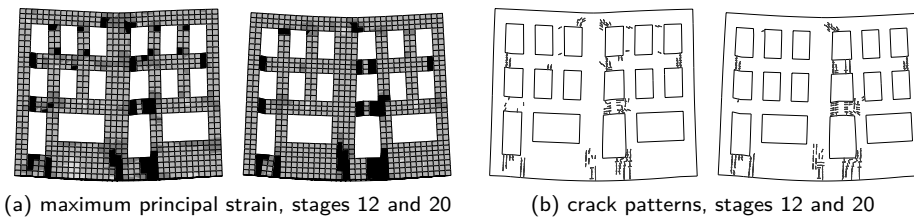


Figure 6.24: Model with smooth interface elements.

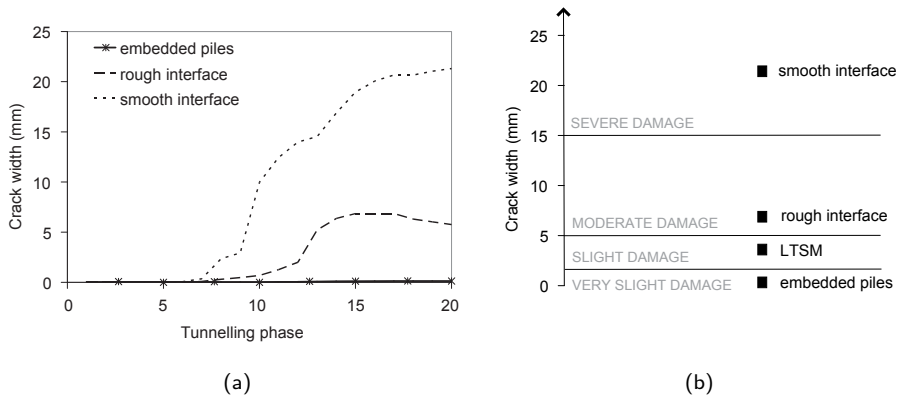


Figure 6.25: (a) Maximum crack width as a function of the tunnel advance: comparison between the different modelling approaches; (b) damage classification: comparison between LTSM and numerical results.

(embedded beams) to the negligible transfer of horizontal strain (smooth interface). The results of the numerical analysis are then compared with the damage assessment according to the Limiting Tensile Strain Method (Boscardin and Cording, 1989; Burland and Wroth, 1974). Input data and results are listed in Table 6.2. For the analysed situation, the LTSM predicts a slight damage level. On the other hand, the numerical analysis shows a larger range of possible results, depending on the modelling approach and the interface parameters adopted to simulate the soil-structure interaction (Figure 6.25b). The results proved the high flexibility of the interface modelling solution, which makes it suitable to represent different types of foundation. Field measurements showed that, in case of continuous footings, the horizontal strains transmitted to the structure are significantly lower than the greenfield ones (Burland et al., 2004). However, considering the strong effect of foundation modelling on the final damage assessment and the general lack of empirical data about the shear behaviour of actual foundations, further field and experimental investigations are required, especially on pile foundation.

Table 6.2: LTSM input data and results.

Height	H	11.5 m
Length	L	13.6 m
Deflection	Δ/L	1.24×10^{-2} m
Bending and shear stiffness ratio	$(E/G)_1$	2.6
	$(E/G)_2$	11
Maximum bending strain, $(E/G)_1$	$\varepsilon_{b,max}$	0.114%
Maximum bending strain, $(E/G)_2$	$\varepsilon_{b,max}$	0.036%
Maximum diagonal strain, $(E/G)_1$	$\varepsilon_{d,max}$	0.065%
Maximum diagonal strain, $(E/G)_2$	$\varepsilon_{d,max}$	0.084%
Total tensile strain, $(E/G)_1$	ε_t	0.114%
Total tensile strain, $(E/G)_2$	ε_t	0.084%
Damage class		Slight

6.4 Validation case study: the Mansion House in London

The potential of the proposed modelling approach was tested through the simulation of a case study, the Mansion House in London, which was affected by the extension of the Docklands Light Railway, between 1988 and 1991.

The damage occurred to the Mansion House due to the construction of the first tunnel of the project, a pedestrian link between Waterloo and City Line. It represents an ideal source of data for different reasons:

- No severe damage was found on the building prior to the tunnel construction (Frischmann et al., 1994). The assumption of neglecting previous localized loss of stiffness in the building model is therefore justified.
- No protective measures need to be included in the model, because they were adopted only after the first tunnel excavation.
- The tunnelling effects in terms of settlement profile and internal wall crack patterns have been well documented (Frischmann et al., 1994).

The Mansion House is a historical masonry building with high heritage value (Figure 6.26a,b). Its dimensions in plan are 65×30 m², it is 25 m high and it has five storeys with wooden floors and three main internal bearing cross walls with thickness decreasing with height. The external façades and the internal walls are characterized



Figure 6.26: Mansion House, London.

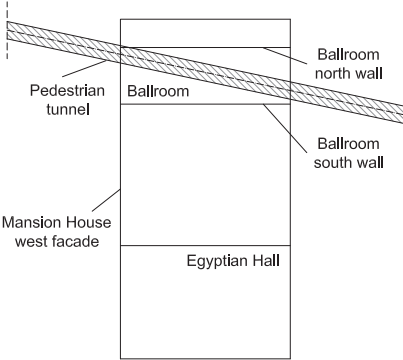


Figure 6.27: Mansion House: location in relation to the tunnel (Frischmann et al., 1994).

by large openings. The palace was built on London clay soil; the original wooden pile foundations were substituted by shallow foundations during repairs.

The construction of the Waterloo and City line link tunnel under the building (Figure 6.27) caused a maximum settlement of about 5 mm; a maximum settlement of 8 mm was measured one year after the tunnel excavation (Frischmann et al., 1994). The ground displacements caused the development of a visible crack set in the top floors of the north internal walls. The crack location and evolution were monitored and protective measures were adopted before the construction of the successive tunnels of the same project (Frischmann et al., 1994).

6.4.1 Numerical model

This section describes the main features of the adopted numerical model.

Soil model For the finite element analysis, a portion of $450 \times 400 \times 100 \text{ m}^3$ of ground was modelled (Figure 6.28a and Figure 6.29). The soil mesh consists of 100.000 solid tetrahedral elements. According to Möller (2006), the minimum transverse and longitudinal mesh dimensions required to avoid boundary effects on the transverse and longitudinal settlement profile are related to the tunnel diameter and the cover to diameter ratio. In this specific case, the minimum values are 30 m and 82 m, respectively. Therefore, the model satisfies the size requirements. The soil parameters are listed in Table 6.3, and they refer to the typical values for London clay (Liu, 1997).

Tunnel model A 3.05 m diameter tunnel was introduced in the middle of the mesh, at 13 m under the surface. A structured mesh of 7200 solid wedge elements allowed to model the incremental excavation by removing successive soil elements at the tunnel face (Figure 6.30), as described in Section 6.2.

The lining was modelled by curved shell elements with elastic parameters (Table 6.3). A radial pressure was applied to the lining towards the tunnel axis; the pressure was incrementally increased in order to reach a volume loss V_L of 1.5%, which corresponds to the ground loss due to the settlements monitored in 1988. At this point, an adjacent slice of soil was removed. The process was repeated until the tunnel excavation was completed, causing the typical transverse and longitudinal settlement profile. A further radial pressure was then uniformly applied all over the tunnel lining in order to obtain the settlement profile measured in 1989, which corresponds to a volume loss of 3.3% (Bloodworth, 2002).

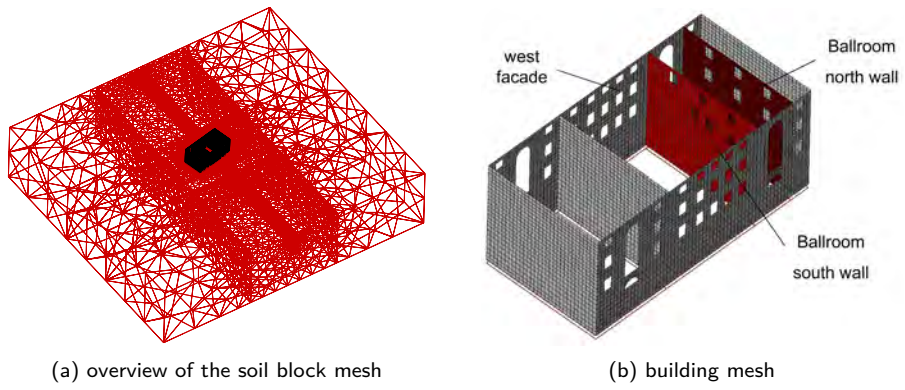


Figure 6.28: Numerical model.

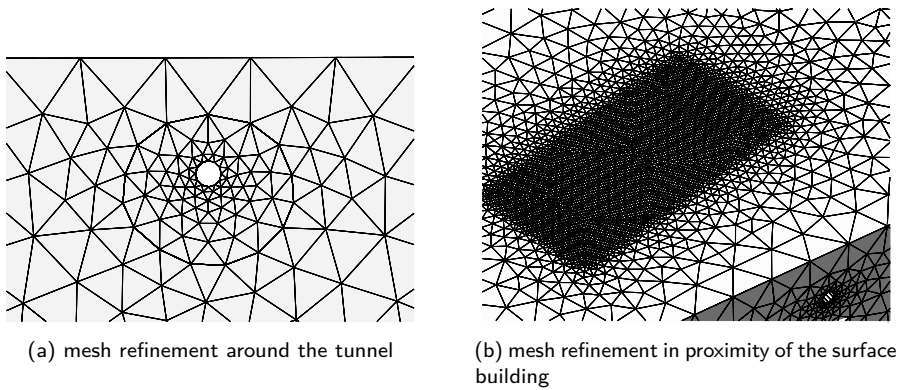


Figure 6.29: Soil mesh refinement.

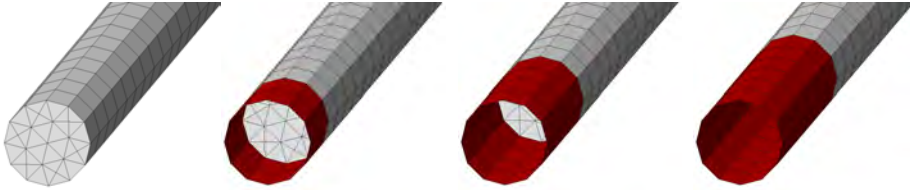


Figure 6.30: Soil removal and lining activation in the consecutive stages of the tunnelling advance process.

Building model The Mansion House was represented with a relatively high level of detail. The external façades and the internal bearing cross walls (Ballroom north and south walls in Figure 6.28b) were modelled by a structured mesh of shell elements, taking into account the thickness reduction with height. In comparison with previous works (Bloodworth, 2002), in this case the inclusion of the Ballroom north and south walls allows for the comparison of the numerically predicted crack pattern with the monitored ones. The most relevant openings were included, while the wooden floors and roof were omitted, because their stiffness was considered to be negligible with respect to the global stiffness of the building. The structure was subjected to dead and live loads.

For the masonry, a rotating crack model was adopted, based on the damage localization over a certain crack bandwidth h , related to the mesh size (Figure 6.31a). The material is elastic in compression; cracks arise if the tensile stress exceeds the tensile strength $f_{t,M}$; the post-peak behaviour is described by a linear tension softening diagram governed by the fracture energy G_f (Figure 6.31b). The Young's modulus E_M and the tensile strength of the masonry depend on the angle between the principal tensile stress direction and the alignment of the bed joints, and therefore so does the fracture energy. Here, a simplified approach was adopted, taking average E_M , $f_{t,M}$ and G_f as if the material were isotropic. The total strain rotating crack model has been proven to be able to represent the crack localization and propagation by comparison with experimental data for the specific case of settlement-induced damage to masonry structures (Chapter 4). The material parameters are given in Table 6.3, and they are derived from material tests (Frischmann et al., 1994) and previous numerical studies conducted on the Mansion House (Bloodworth, 2002).

Soil-structure interface The shell elements used to model the building were connected to the soil via non-linear interface elements (Figure 6.32a). For the interface, a Coulomb friction model with tension cut-of was adopted (Figure 6.32b-

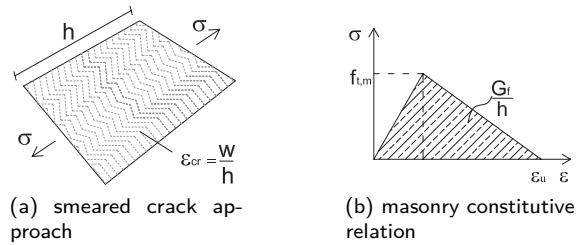


Figure 6.31: Constitutive model for masonry.

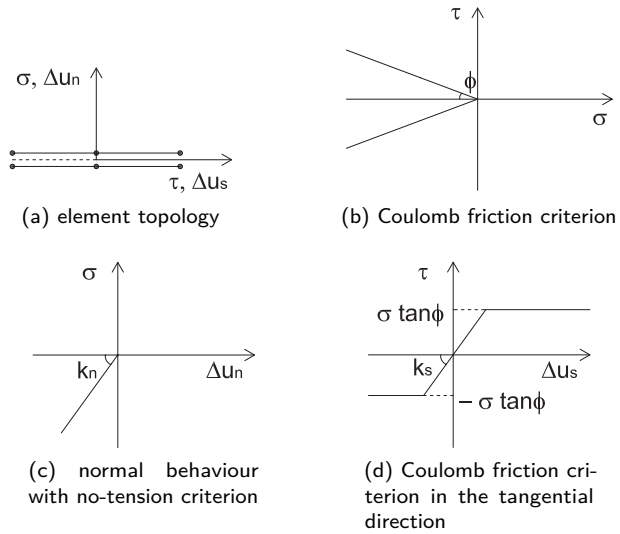


Figure 6.32: Soil-structure interface model.

Table 6.3: Material parameters.

Masonry (Bloodworth, 2002; Frischmann et al., 1994)	Young's modulus	E_M	1×10^3	N/mm ²
	Poisson's ratio	ν_M	0.2	
	Density	ρ_M	2×10^{-6}	kg/mm ³
	Tensile strength	$f_{t,M}$	0.1	N/mm ²
	Fracture energy	$G_{f,M}$	5×10^{-2}	N/mm
Soil (Liu, 1997)	Young's modulus	E_s	1.14×10^2	N/mm ²
	Poisson's ratio	ν_s	0.3	
	Density	ρ_s	2×10^{-6}	kg/mm ³
	Gradient	m	7.8×10^{-3}	N/mm ²
Interface (Netzel, 2009)	Normal stiffness	$k_{n,b}$	0.2	N/mm ³
	Shear stiffness	$k_{t,b}$	0.2×10^{-4}	N/mm ³
	Tensile strength	$f_{t,b}$	0	N/mm ²
	Cohesion	c	0	N/mm ²
	Friction angle	$\tan\phi$	0.57	
	Dilatancy angle	$\tan\psi$	0	
Lining	Young's modulus	E_c	2×10^4	N/mm ²
	Poisson's ratio	ν_c	0.15	
	Density	ρ_c	2.5×10^{-6}	kg/mm ³

d), where interface parameters were selected according to previous studies (Netzel, 2009) and shown in Table 6.3.

6.4.2 Results and discussion

In order to validate the model, the results of the numerical simulation were compared with the available monitoring data. First, the prediction in term of settlement profile under the west façade was evaluated in 2 different excavation stages:

- tunnel excavation completed, $V_L = 1.5\%$;
- tunnel excavation completed, $V_L = 3.3\%$.

Then, the crack pattern and crack widths were analysed for 3 different steps of the process:

- 50% of tunnel excavation, $V_L = 1.5\%$;
- tunnel excavation completed, $V_L = 1.5\%$;
- tunnel excavation completed, $V_L = 3.3\%$.

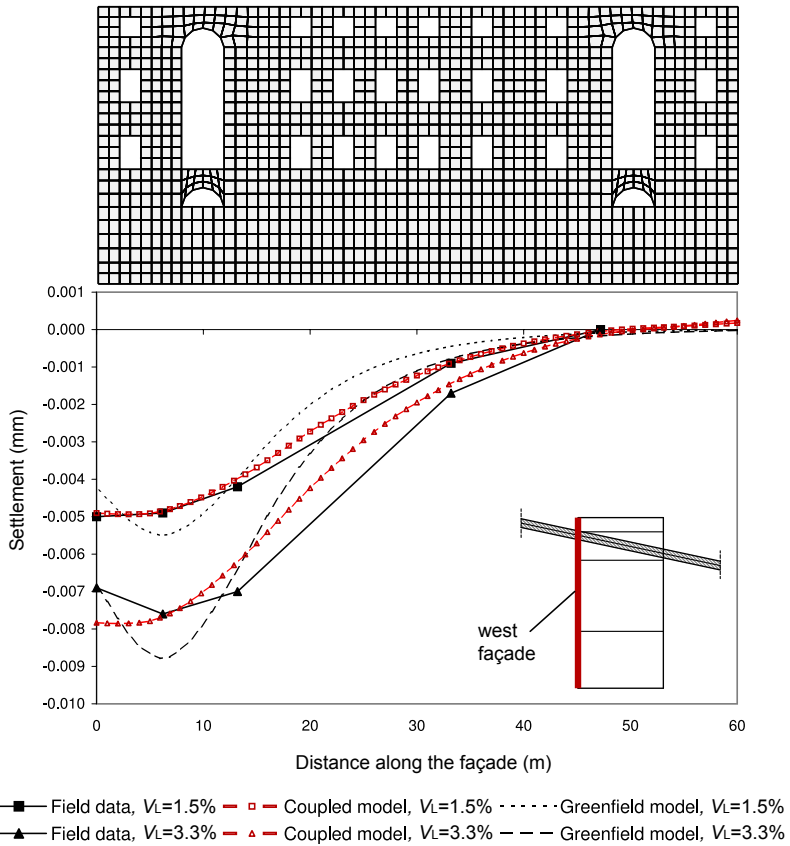
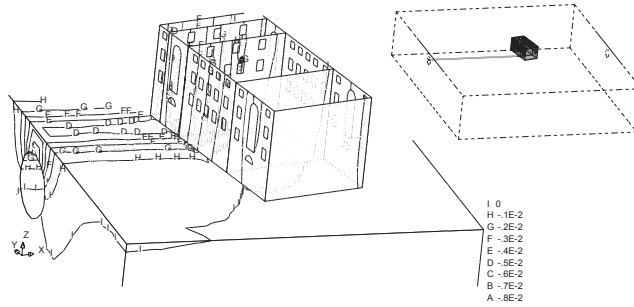
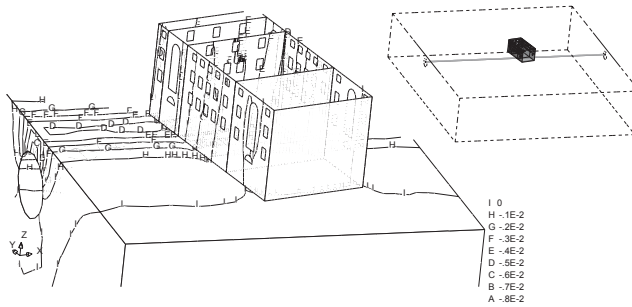


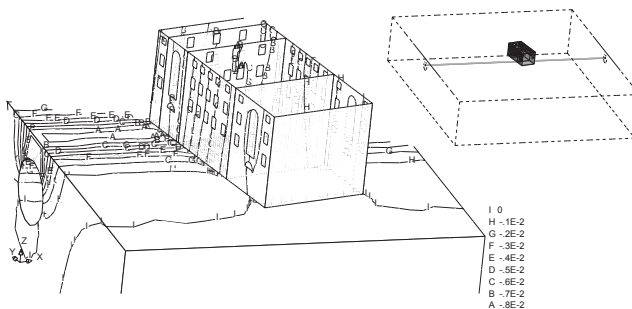
Figure 6.33: Settlement curves under the west façade: comparison between the field measurements and the model results.



(a) 50% of tunnel excavation, $V_L = 1.5\%$



(b) tunnel excavation completed, $V_L = 1.5\%$



(c) tunnel excavation completed, $V_L = 3.3\%$

Figure 6.34: Settlement contour plot for selected analysis staged.

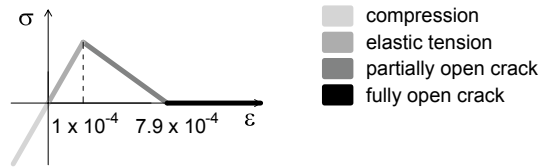


Figure 6.35: Range subdivision of strain contours with reference to the masonry constitutive law.

The interaction effect due to the coupling is underlined by the comparison with the settlement profiles of the corresponding greenfield model, where the staged analysis is carried out in absence of the building (Figure 6.33). The curves derived from the coupled model show a wide and flatter settlement profile, which is clearly induced by the building presence.

Field measurements of the Mansion House external walls were recorded during the construction of the pedestrian tunnel and thereafter. Figure 6.33 shows the comparison between the finite element prediction and the monitored data of the settlements relative to the west façade. The lines indicated as 'coupled model' show that the combination of 3D modelling and tunnel advance simulation can accurately represent the effect of the building weight and stiffness on the tunnelling-induced ground movements. With 2D modelling, this could only be achieved by using special expedients like extra springs to simulate the influence of the transverse walls.

The match with the actual displacements is more accurate for the ground movements obtained at the end of the excavation process, in 1988 ($V_L = 1.5\%$). For the settlements measured after one year, the numerical curve reproduces the real trough with the exception of the north end façade. The difference could be due to the omission, in the model, of the colonnaded pronaos: in the model, the north façade does not represent the extreme transverse element of the real structure, and the west façade settlement profile could be seen as shifted by the pronaos length.

Figure 6.34 shows the settlement distribution on the Mansion House for consecutive analysis stages. The main deformations occur in the Ballroom, which is located directly above the tunnel track, and therefore it constitutes the building part most prone to settlement-induced damage. In Figure 6.34a, the effect of the longitudinal profile is emphasized by showing the vertical ground displacements occurring when the tunnel face reaches the central zone under the building. At this step, the Ballroom north and south walls are subjected to a hogging type deformation. The situation at the end of the tunnel construction and after the application of the

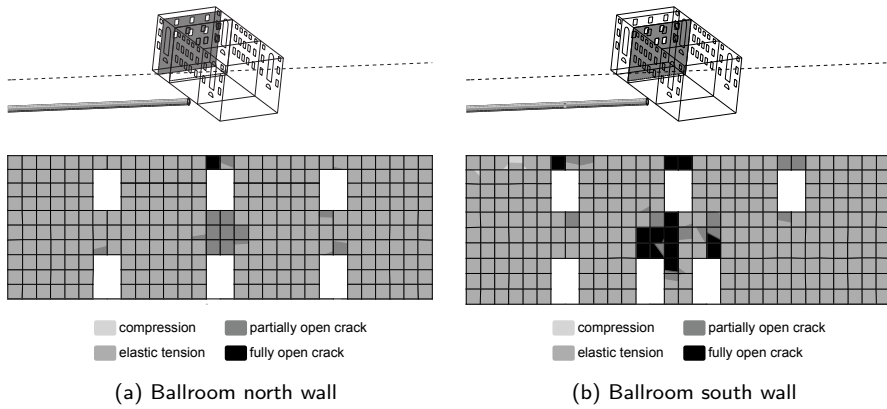


Figure 6.36: Maximum principal strain contour plot, 50% of the tunnel excavation, $V_L = 1.5\%$, upper floors.

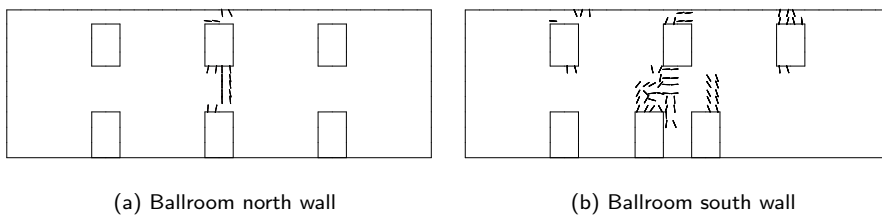


Figure 6.37: Model crack pattern, 50% of the tunnel excavation, $V_L = 1.5\%$, upper floors.

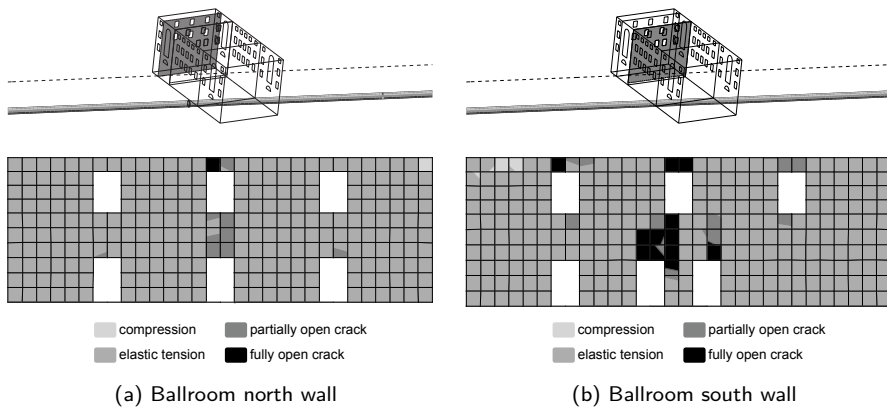


Figure 6.38: Maximum principal strain contour plot, tunnel excavation completed, $V_L = 1.5\%$, upper floors.

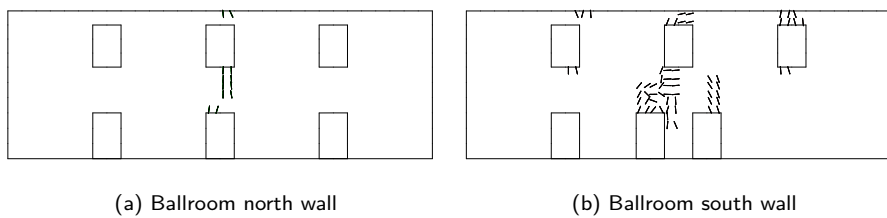


Figure 6.39: Model crack pattern, tunnel excavation completed, $V_L = 1.5\%$, upper floors.

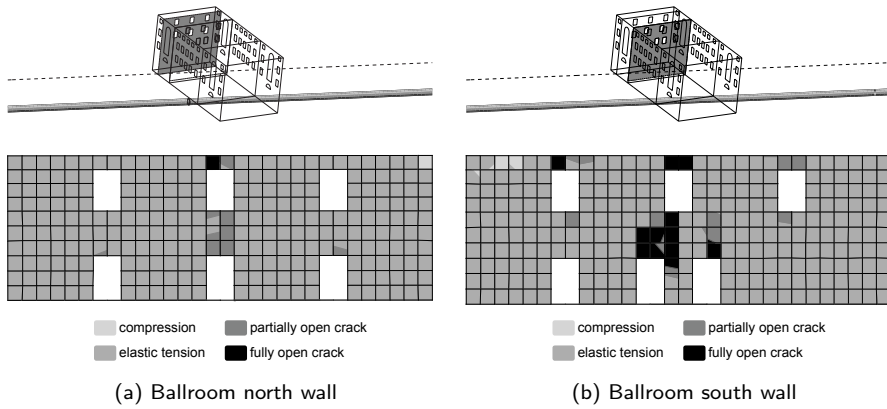


Figure 6.40: Maximum principal strain contour plot, tunnel excavation completed, $V_L = 3.3\%$, upper floors.

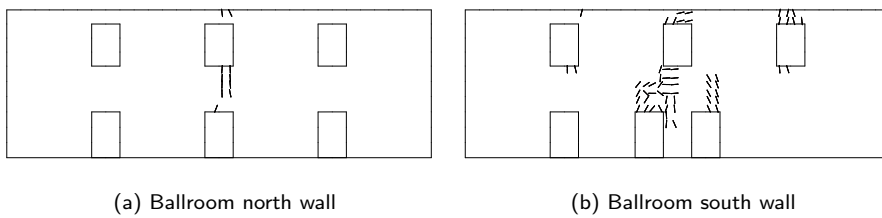


Figure 6.41: Model crack pattern, tunnel excavation completed, $V_L = 3.3\%$, upper floors.

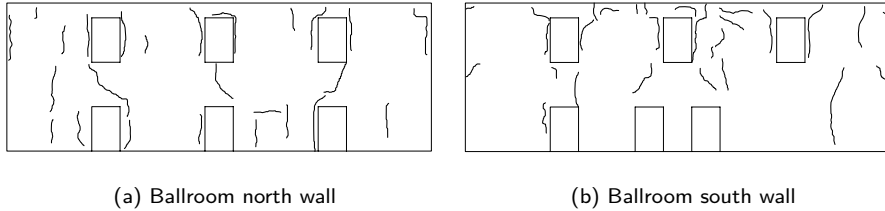


Figure 6.42: Monitored crack pattern, tunnel excavation completed, $V_L = 3.3\%$, upper floors (Frischmann et al., 1994).

radial pressure simulating the further volume loss is presented in Figure 6.34b and Figure 6.34c, respectively.

Figure 6.36 to Figure 6.41 illustrate the maximum principal strain contour plots and the relative crack patterns on the upper floors of the north and south Ballroom walls. In comparison with previous works (Bloodworth, 2002), in this study the inclusion of tension softening allows for a representation of the tunnelling-induced crack pattern comparable with the actual one. The visualised contour ranges refer to the masonry constitutive law shown in Figure 6.35. This allows to distinguish the façade areas in compression, in elastic tension, partially cracked or fully cracked. All the results refer to the three analysis stages mentioned above.

The first cracks arise as a consequence of the longitudinal trough induced deformation in the central part of the walls, starting from the window frames (Figure 6.37). The tunnel advance, and therefore the development of the typical transverse settlement profile, causes the propagation of the damage between the openings (Figure 6.39). The resulting crack pattern is kept unaltered during the next increment of volume loss, with a constant transverse trough along the tunnel (Figure 6.41).

A crack survey carried out one year after the tunnel construction showed the consequences of the displacements on the upper floors of the Ballroom walls (Figure 6.42). The final numerical results show a damage localization around the weak structural points represented by the windows. The surveyed long cracks, visible around the openings, are probably due to an extra stress concentration along the window wooden frames, which have not been included in the finite element model. This suggests the importance of modelling structural details often considered of secondary relevance, like doors and windows, for a realistic prediction of the damage

pattern.

The strain outputs for the masonry allows for the estimation of the crack width. Multiplying the value of the maximum crack strain by the crack bandwidth, a maximum crack width of 0.6 mm and 9 mm is calculated for the north and south Ballroom wall, respectively. This prediction reflects the magnitude order of the monitored crack widths: the survey mentions the presence of cracks wider than 4 mm in the Ballroom, for a maximum settlement of about 8 mm, one year after the tunnel excavation (Frischmann et al., 1994).

6.5 Conclusions

This section presented a global approach to evaluate the building response to tunnelling-induced settlements. The method consists of a staged finite element analysis performed on a 3D coupled model.

The importance of 3D modelling in the damage assessment has been demonstrated by the analysis of the results in terms of crack patterns and failure mechanisms. Neglecting the 3D tunnelling advance leads to an underestimation of the damage; the value of this underestimation depends on different factors, like the expected volume loss and the position of the tunnel with respect to the building, which governs the type of settlement trough. Non-linear modelling of the soil-structure interface is also a relevant issue, because the shear behaviour of the soil-foundation system affects the failure mechanism in a way which is more or less conservative, depending on the considered settlement profile.

The problem of modelling pile foundations in 3D finite element analysis of tunnelling-induced damage to building was addressed. Two different modelling approaches were analysed: use of embedded beam elements with non-linear interfaces and use of non-linear horizontal interfaces with equivalent properties. Results have shown that both the solutions are able to represent the non-linear load–displacement curves at the surface level, in vertical and horizontal directions. The two models were then applied to a 3D staged analysis of a tunnel excavation in soft soil under a masonry building. A total strain rotating crack model was assumed for the building, and the effects of tunnelling-induced settlements were compared in terms of progressive structural damage. The different settlement profiles transferred from the soil to the structure by the embedded beams and the interface elements play a fundamental role in the building response: while the models give similar results for applied test loads at the pile heads, they give significantly different results for the actual loading condition of distributed soils settlements. Results has shown that

field data about the actual behaviour of the foundation are essential to calibrate the parameters of both approaches for numerical modelling.

The application of the proposed 3D model to the Mansion House case study showed that coupling the building and the bored tunnel in a single analysis makes it possible to represent the soil-structure interaction; not only the effect of differential settlements on the structure, but also the influence of the building on the settlement profile is captured. Adopting a smeared crack tension softening model for the masonry permits to reproduce the relation between the tunnelling advance and the volume loss increase, and the crack initiation and propagation; this gives a reasonable crack pattern prediction and a good indication of the crack width order of magnitude. Modelling in three dimensions allows for including the effect of the settlement trough longitudinal component on the building damage and for the contribution of the cross bearing walls to the ground displacements. Representing the soil-structure interaction via interface elements gives the opportunity to modify the foundation parameters without modelling the actual foundation geometry (e.g. by changing the normal and tangential interface stiffness). The shear behaviour of the interface, which models the transmission of the horizontal deformations from the soil to the structure, was proven to affect the damage mechanism significantly. This aspect should be further investigated by means of parametric studies.

The proposed approach overcomes the limitations of the current damage assessment procedure, but due to its required level of refinement and time expenses it cannot be considered as a full substitute for the Limiting Tensile Strain Method. However, the presented validation proves that this analysis method is a useful tool for specific case studies, like sensitive structures or historical heritage. This work also shows the potential of 3D coupled finite element analysis as base for variational studies, performed to evaluate the parameters governing the building response to tunnelling and the effect of their variation on the structural damage.

3D sensitivity study

7

Compared to the 2D semi-coupled model presented in Chapter 4, the 3D modelling approach proposed and validated in Chapter 6 allows to take into account several additional factors influencing the building response to tunnelling:

- the excavation process and the consequent progressive settlement profile along the tunnel axis;
- the global torsional response of the structure due to the 3D displacement field of the ground;
- the local effect of structural elements transverse to the façade.

The 3D model was therefore used to perform a new series of parametric analyses; with respect to the sensitivity study carried out on the 2D model in Chapter 5, the focus was now on the effect of the orientation and the position of the structure with respect to the tunnel. The results in terms of damage were compared with an empirically based risk assessment procedure.

7.1 Identification and selection of parameters and variations

In the numerical analysis, the geometry of the model was varied to take into account the effect of several characteristics which affect the 3D building response (Figure 7.1): the ratio between the horizontal building dimensions with respect to the tunnel axis direction (O), the presence of isolated or grouped buildings (G), the distance from the tunnel axis (P) and the alignment of the building with respect to the tunnel

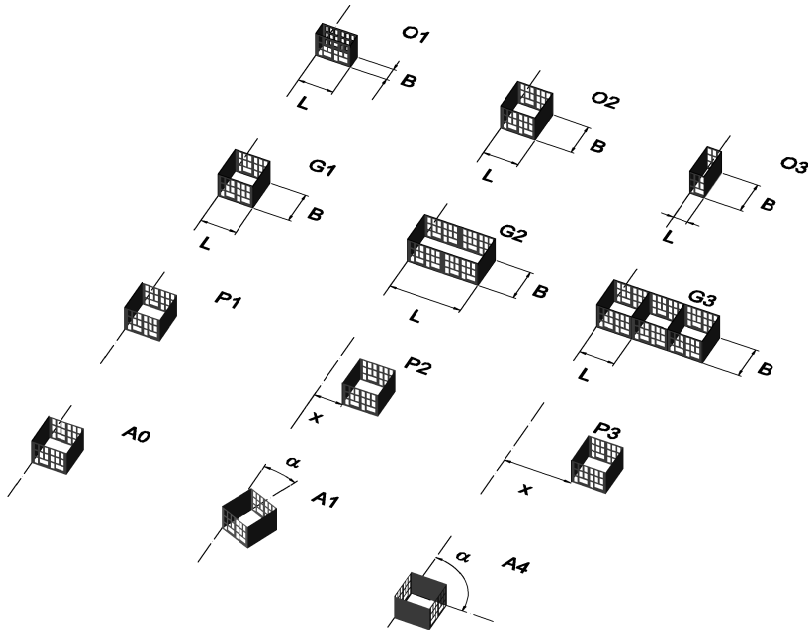


Figure 7.1: Overview of the parameters which were varied in the 3D sensitivity study: orientation O, grouping G, position P and alignment A.

axis (A). The definition of the first three parameters and the reference ranges in the sensitivity study were derived from the Building Risk Assessment (BRA) procedure (Guglielmetti et al., 2008). The BRA is based on empirical observations derived from building monitoring and it was applied during the construction of different metro lines in urban environment.

Orientation As illustrated in Chapter 4 and Section 5.2.1, a masonry façade with a large amount of openings is a structural element particularly vulnerable to settlement-induced damage. Considering a building or a series of adjacent buildings with their façades perpendicular to the tunnel axis, the aspect ratio between the building dimensions in the direction parallel and perpendicular to the tunnel axis affects the global stiffness of the structure in relation with the transverse settlement profile. Furthermore, this aspect ratio, which is here indicated as orientation parameter O,

Identification and selection of parameters and variations 7.1

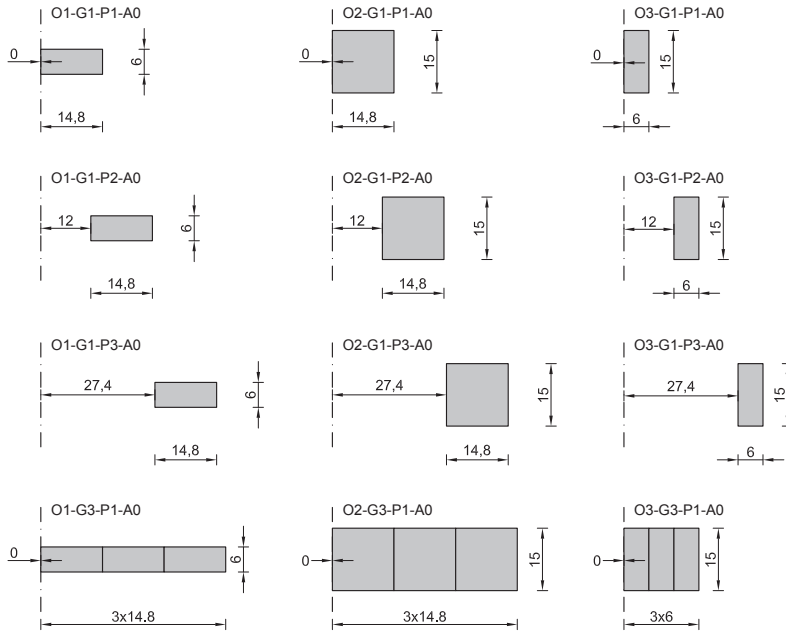


Figure 7.2: Variations of orientation for three different sizes of the basic building unit (Kappen, 2012). Dimensions in m.

varies the specific contribution of the transverse walls to the global stiffness. These two combined effects influence the final façade damage, both during the tunnel advance, as a consequence of the temporary longitudinal settlement profile, and in the final stage, with the permanent transverse settlement profile.

In the parametric study, three different conditions for the B/L ratio were analysed:

- O1: $B/L < 0.5$
- O2: $0.5 < B/L < 2$
- O3: $B/L > 2$

where B and L are the building dimensions in direction parallel and perpendicular to the tunnel axis, respectively (Figure 7.1). The performed variations are listed in Figure 7.2.

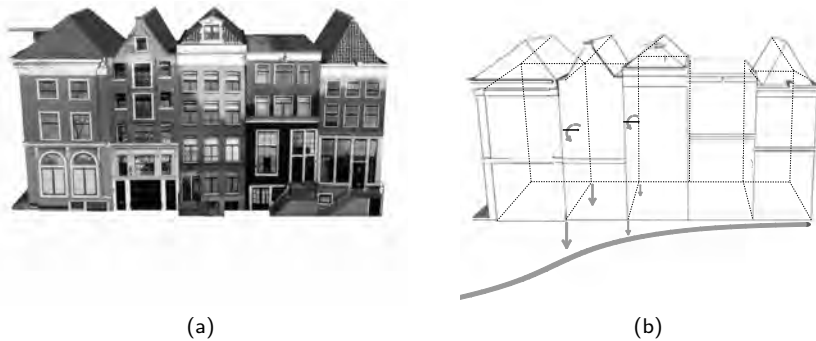


Figure 7.3: (a) Canal-houses in Amsterdam; (b) tunnelling-induced settlement profile and additional differential settlements transmitted by the two common transverse walls to the façade.

Grouping The modified lateral boundary conditions imposed by the presence of adjacent buildings can significantly affect the settlement vulnerability of a masonry façade. Depending on the level of their connections, the structural continuity created by a group of buildings alters the ratio between their bending and shear stiffness, leading to different failure mechanisms. Extending the modelling from the single structure to be assessed to the group of adjacent buildings, allows for a more realistic definition of the lateral boundary conditions; in this way, the analysis can include the differential settlements transmitted by the side buildings through the shared foundations and transverse walls (Figure 7.3). Furthermore, the contribution of the tunnelling-induced settlement is extended to a bigger influence area, giving a combined sagging and hogging deformation to the building group. A real example of such a situation is offered by the so called canal-houses in Amsterdam (Figure 7.3).

The numerical study included variations of the grouping effect G as listed in Figure 7.4:

- G1: isolated building (no interior walls) with dimensions B and $L < 2D$
- G2: isolated building (no interior walls) with $B < 2L$ and $L > 2D$
- G3: grouped building (two interior walls) perpendicular to the tunnel axis

where D indicates the tunnel diameter. Throughout this study the tunnel diameter is 8 m. Note that the condition G2 represents a purely academic case, and that each

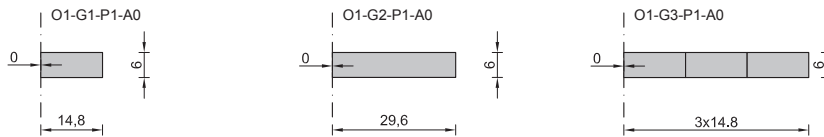


Figure 7.4: Variations of grouping (Kappen, 2012). Dimensions in m.

of the assumed variations implies a different location with respect to the sagging or hogging part of the settlement trough.

Position The location of the tunnel with respect to the surface structures affects the type and magnitude of induced settlement troughs. Assuming a fixed value of volume loss as a consequence of the tunnel excavation, buildings at increasing distances from the tunnel axis are subjected to smaller absolute settlements and to settlements troughs changing from sagging to hogging type.

To include the evaluation of this combined effect, three different values for the ratio between the tunnel-building distance x and the tunnel diameter D were assumed:

- P1: $x/D < 1$
- P2: $1 < x/D < 3$
- P3: $x/D > 3$

The performed variations of position are listed in Figure 7.5.

Alignment Analytical and numerical investigations of the structural response to tunnelling-induced settlement traditionally assume surface structures with the main geometrical directions aligned or perpendicular to the tunnel axis. Although this represents a statistically relevant situation if the tunnel is excavated under the main urban roads, a certain degree of rotation between the tunnel axis and the reference system of the building plant is also a realistic case scenario. Therefore, the investigation of the effect of the alignment parameter A (Figure 7.1) can give a better insight of the torsional response of the structure in relation with the 3D settlement profile caused by the excavation.

For this reason, the parametric analyses listed in Figure 7.6 (Kappen, 2012) were performed. For each of the 9 alignment variations, the three positions P1, P2 and P3 were included.

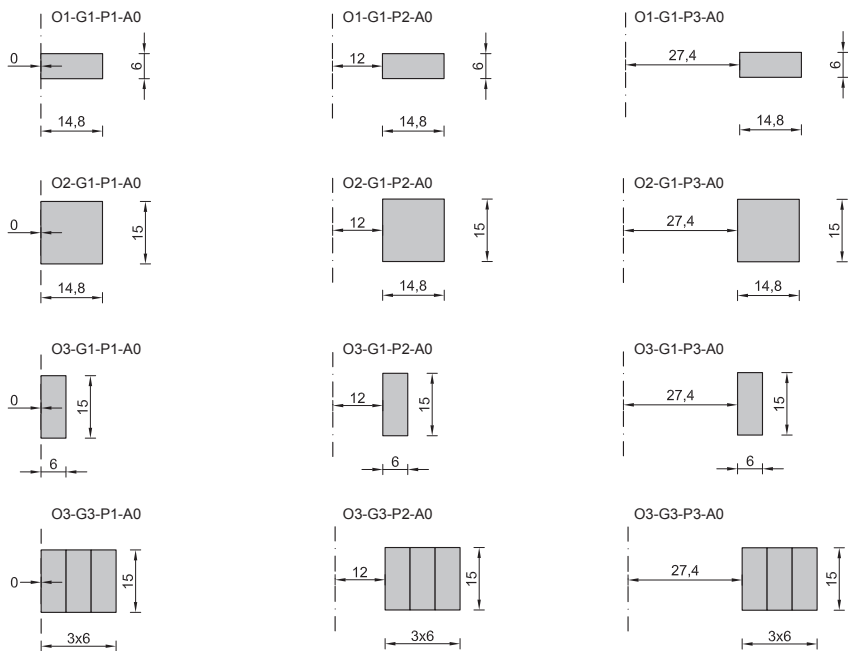


Figure 7.5: Variations of position for different orientation and grouping conditions (Kappen, 2012). Dimensions in m.

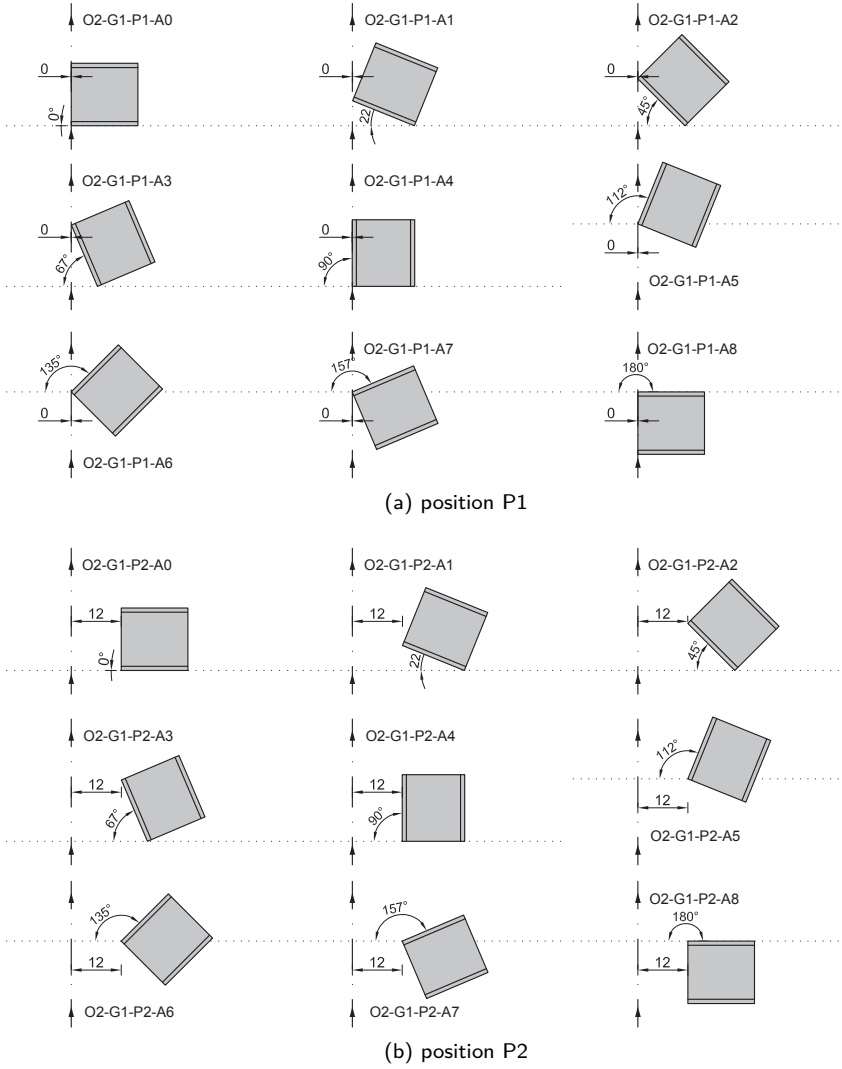


Figure 7.6: Variation of alignment (Kappen, 2012). Dimensions in m.

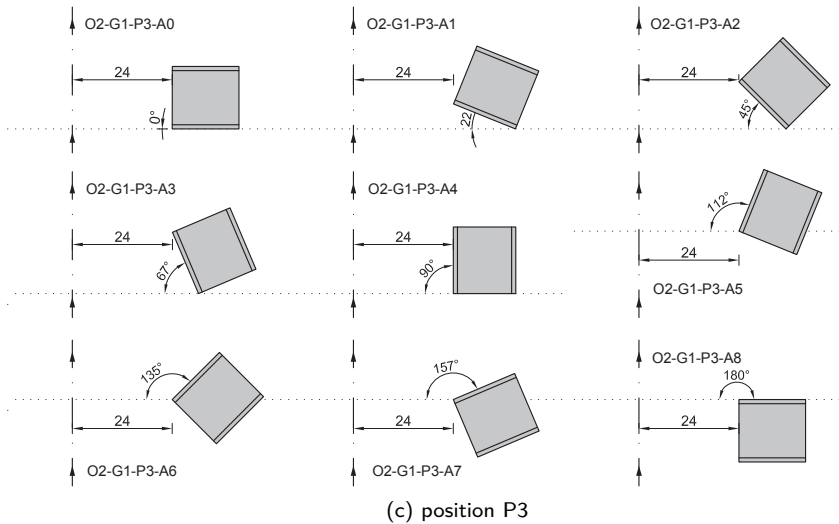


Figure 7.6: (continued) Variation of alignment (Kappen, 2012). Dimensions in m.

Interface shear behaviour As illustrated in Section 5.2.4 and Section 5.2.5, the transmission of horizontal deformations from the ground to the structure can significantly affect the final damage, either in a beneficial or in a unfavourable way, depending on the type of settlement trough, i.e. sagging or hogging. In this study, two extreme conditions for the shear behaviour of the soil-structure interface were considered: a smooth interface, with very low shear stiffness, neglecting any type of shear stress transfer between soil and structure, and a rough interface, with higher stiffness and a Coulomb friction criterion to transmit horizontal shear stresses between soil and structure, depending on the vertical loads. All the cases shown from Figure 7.4 to Figure 7.6 were analyzed for both the rough and smooth interface cases, resulting in 108 numerical analyses. The material parameters for the entire finite element model are summarized in Table 7.1.

Table 7.1: Parameters for the numerical model.

Material	Parameter	Value
Masonry	Young's modulus	$E_M = 6 \times 10^3 \text{ N/mm}^2$
	Density	$\rho_M = 2.4 \times 10^{-6} \text{ kg/mm}^3$
	Poisson's ratio	$\nu_M = 0.2$
	Tensile strength	$f_{t,M} = 0.3 \text{ N/mm}^2$
	Fracture energy	$G_{f,M} = 0.05 \text{ N/mm}$
Soil	Young's modulus	$E_s = 50 \text{ N/mm}^2$
	Gradient	$m = 1 \times 10^{-2} \text{ N/mm}^3$
	Density	$\rho_s = 2 \times 10^{-6} \text{ kg/mm}^3$
	Poisson's ratio	$\nu_s = 0.3$
Lining	Young's modulus	$E_M = 3 \times 10^4 \text{ N/mm}^2$
	Density	$\rho_c = 2.5 \times 10^{-6} \text{ kg/mm}^3$
	Poisson's ratio	$\nu_c = 0.2$
Base interface	Normal stiffness	$k_{n,b} = 0.2 \text{ N/mm}^3$
	Tangent stiffness	$k_{t,b} = 1 \times 10^{-5} \text{ N/mm}^3$ (smooth)
		$k_{t,b} = 5 \times 10^{-2} \text{ N/mm}^3$ (rough)
	Tensile strength	$f_{t,b} = 0 \text{ N/mm}^2$
	Cohesion	$c_i = 0 \text{ N/mm}^2$ (rough)
	Friction angle	$\tan \phi_i = 0.57$ (rough)
Dilatancy angle	$\tan \psi_i = 0$ (rough)	

7.2 Results

As for the sensitivity study carried out on the 2D model in Chapter 5, the results of the 3D parametric analyses are presented in terms of top and base horizontal deformation $\varepsilon_{h,top}$ and $\varepsilon_{h,base}$, angular distortion β , maximum crack width w_{max} and damage classification according to Burland and Wroth (1974) (Section 5.2).

All the results refer to a volume loss $V_L = 2\%$; for the variation of each parameter (orientation, grouping, position, alignment), the deformation and damage indicators are shown as a function of the parameter value. The deformation indicators $\varepsilon_{h,top}$, $\varepsilon_{h,base}$ and β refer to the conditions of the most deformed façade after the complete tunnel excavation, while w_{max} is the maximum crack width of the entire building, considering all the 20 excavation phases. This allows to take into account the possibly not recovered inelastic damage caused by the intermediate tunnelling stages, as illustrated in Section 6.2.

The maximum crack width is calculated as:

$$w_{max} = \varepsilon_{cr,max} h \quad (7.1)$$

where $\varepsilon_{cr,max}$ is the maximum crack strain and h is the crack bandwidth. The value of h is related to the average size of the building finite elements, and it is equal to 566 mm. With respect to the derivation of the maximum crack width from the relative displacements of two nodes located outside the crack (Section 4.2.1), this procedure allows for a more efficient data processing, which is especially convenient in case of 3D modelling. Local verifications were performed to assure the comparability of the results.

Considering that the available field data demonstrated a limited transmission of horizontal deformations from the soil to the structure (Burland et al., 2004), the main focus is on the results obtained by assuming a smooth soil-structure interface. However, the effect of taking into account an increased interface tangential stiffness is illustrated by the comparison between the final damage classifications for the rough and the smooth cases.

In order to highlight the correlation between the damage and deformation results and the failure mechanisms, for each parameter the crack strain contour plot, the 3D deformed shape and the interface normal stresses of a significant variation are presented. Exemplary combinations for an intermediate and the final excavation phase are shown, for both a smooth and a rough interface. For completeness, the figures related to all the analysed combinations are inserted in Appendix C.

7.2.1 Orientation

The effect of building orientation was examined for different alignment, position and grouping conditions. For each of the combination sets shown in Figure 7.2, only the orientation parameter was varied, while the other conditions were kept constant. Figure 7.7 illustrates the case of three grouped buildings (G3), adjacent (P1) and aligned (A0) to the tunnel axis. In Figure 7.8 the damage indicators for this variation are compared with the ones resulting from the other analysed combinations, i.e. single buildings (G1) located at different positions with respect to the tunnel axis (P1, P2, P3). The graphs show that for the selected case (G3-P1-A0) the global damage is moderate for all the assumed values of B/L .

For the orientation O1 and O2, the ratio B/L is modified by varying the dimension B of the transverse walls: the two buildings have the same dimension L in the direction perpendicular to the tunnel axis, and they are subjected to both sagging and hogging type of settlements. Consistently with field observations (Burland et al., 2001), the structure is more vulnerable to the hogging deformation, and therefore the failure mechanism corresponds to the typical hogging-induced damage, with two main vertical crack starting from the façade top. This damage pattern is confirmed by the relatively high values of top lateral strain and angular distortion (Figure 7.8a,c). The response is magnified by the modelling assumption of neglecting the roof representation.

For the O3 case the increased B/L ratio is obtained by reducing the L dimension, and therefore the building falls entirely into the sagging area of the settlement profile. As a consequence, its failure mechanism is characterised by a vertical crack at the façade base, worsen by the rotation of the load bearing transverse walls, during the excavation phases under the building (phase 9 in Figure 7.7). The dominance of a horizontal base strain (Figure 7.8b) reflects this damage pattern.

Figure 7.7 includes the visualization of the base interface normal stresses. The vector plots reveal that the building weight and live loads keep the interface compressed; local unloading is visible below the main cracks.

In case of a single building (G1), for equal dimension L , the damage tends to increase when increasing the longitudinal dimension B (orientation O1 and O2 of the curves G1-P2-A0 and G1-P3-A0 in Figure 7.8e). This happens because the connection between the two façades offered by the transverse walls becomes more flexible, and therefore the stiffening effects against the deformation induced by the transverse settlement profile is reduced. When the B/L ratio increases by decreasing L , the most vulnerable structural elements, i.e. the façades with openings, become smaller, and the risk of damage is reduced.

With reference to the building position, a general decrease in damage for in-

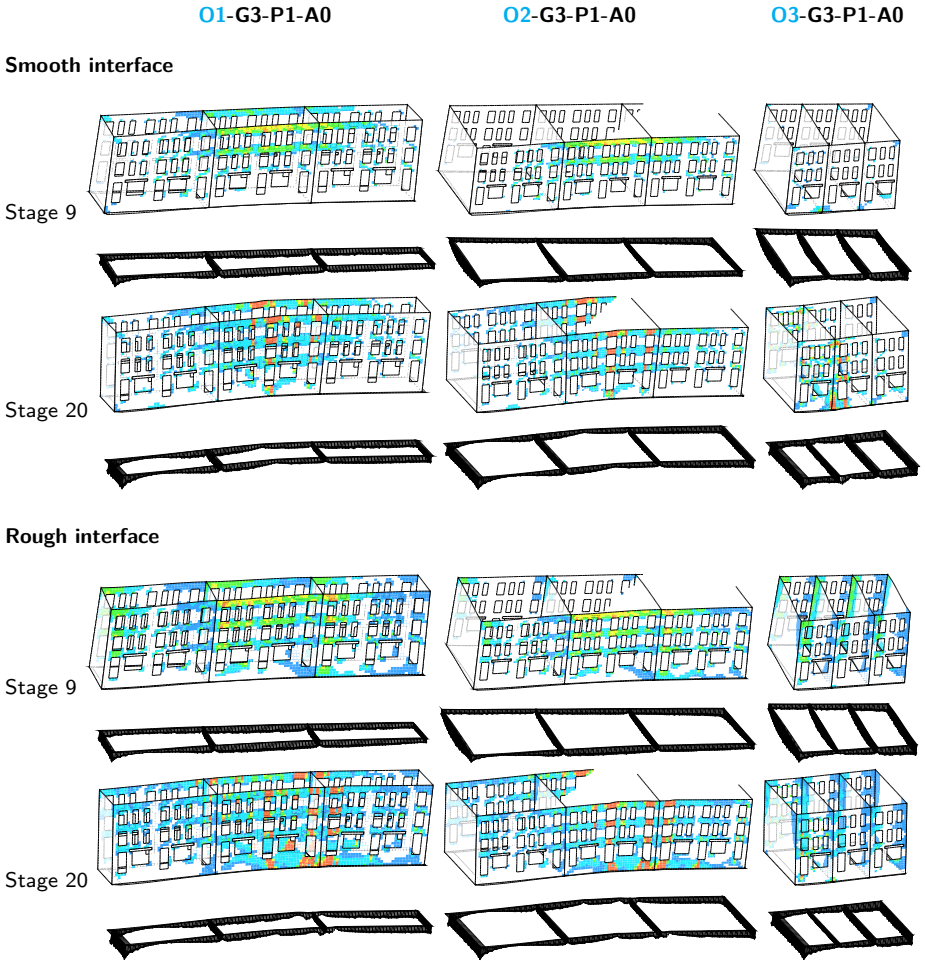


Figure 7.7: Crack strain distribution, deformed configuration and soil-structure interface normal stresses: orientation variation for the G3-P1-A0 cases.

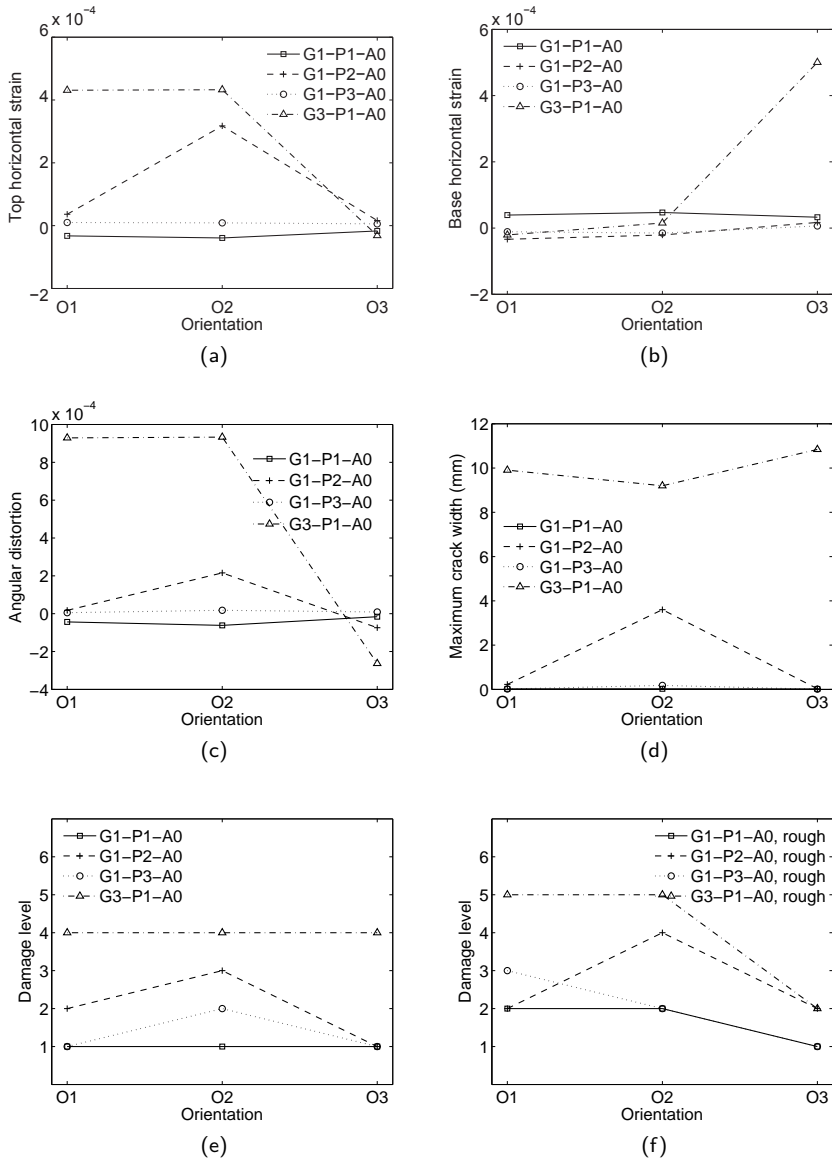


Figure 7.8: Damage indicators as a function of the orientation variations.

creasing distance between the building and the tunnel is observed. In fact, for the positions P2 and P3, the farther the location, the smaller the differential settlement affecting the structure. An exception is represented by the single building in a pure sagging area (P1), which shows a governing tilt deformation with no relevant damage. Failure mechanisms and interface normal stresses for all the variations presented in Figure 7.8 are reported in Appendix C.

As observed in Section 5.2.4, when the horizontal component of tunnelling-induced hogging displacement is transmitted from the ground to the structure, the consequent damage tends to increase. Figure 7.7 shows that for the rough interface properties the hogging cracks propagate all over the façade height (case O1 and O2). When the rough interface is applied to the sagging case (O3), the damage is reduced by the horizontal restraint. The results are confirmed by the global damage assessment based on the maximum crack width (Figure 7.8f). The curves referring to the isolated buildings show a different tendency: the damage in the sagging area is smaller for a smooth than for a rough interface. In fact, due to their reduced geometrical dimensions and flexibility, the isolated buildings do not exhibit the typical hogging and sagging deformations, neither with nor without transmission of ground horizontal displacements (curves G1-P2-A0 in Figure 7.8e,f).

7.2.2 Grouping

Figure 7.9 compares the failure mechanism of three different conditions for a building with ratio $B/L < 0.5$ (O1), adjacent (P1) and aligned (A0) to the tunnel axis. The isolated building with dimensions B and $L < 2D$ (G1) shows a dominant tilt deformation, with a very slight damage of the façade next to the window corners at the connection with the transverse walls. In condition G2, obtained by increasing L , the severe damage is caused by the hogging deformation, showing cracks propagating from the top, recognizable by the larger top lateral strain and angular distortion (Figure 7.10a,c). If more buildings are aligned and connected via common transverse walls, as in the third case illustrated in Figure 7.9 (G3), the coupling effect increases the façade stiffness, and therefore the building is subjected to less severe damage (Figure 7.10d,e).

As previously described, when a building in a sagging zone does not exhibit the typical sagging damage, i.e. a main vertical crack starting from the façade base, the rough interface type does not have any restraint effect on the failure mechanism, and therefore the damage is not reduced but accelerated instead (Figure 7.10e, point G1). In this case, the interface shear behaviour mainly affects the torsional response of the building, because of the deformation induced by the transverse walls during the tunnel excavation (Figure 7.9, rough interface, stage 9).

Conversely, the expected increase of damage caused by the horizontal displacements to the hogging deformation is recognizable in point G3 of Figure 7.10e, and it reflects the extension of the vertical hogging cracks from the top all over the height of the façade (Figure 7.9, rough interface, stage 20). The grouping condition G2 in case of rough interface illustrates the intermediate case already observed in the 2D model (Section 5.2.4), where the horizontal displacements, inducing horizontal tensile strains at the façade base, resist the growth of the vertical crack from the façade top. The final damage is therefore reduced (Figure 7.10f compared to Figure 7.10e, point G2).

7.2.3 Position

Figure 7.11 shows the expected failure mechanism for a single building with $L = B$ (O2-G1), aligned with the tunnel axis (A0), when varying the distance between the building and the tunnel. The graphs in Figure 7.12 demonstrate a damage increment if the building moves from sagging (P1) to a mixed sagging-hogging zone (P2), followed by a significant vulnerability reduction for further increase of the building-tunnel distance, i.e. positioning in the tail of the trough (P3). The tendency is generalized to all the examined cases, with the exception of the grouped building O3-G3-P2-A0. In this case, the extended length of the façade in the direction parallel to the transverse settlement profile does not allow the structure to rigidly tilt as in the other cases (Appendix C). Furthermore, the effect of the settlement profile concavity is intensified by the presence of the transverse walls.

Buildings with smooth and rough interfaces exhibit a different response in all the positions. As described before, the larger sagging deformation occurs in smooth interface conditions, while the buildings in hogging areas are more vulnerable if affected by horizontal displacements (rough interface).

7.2.4 Alignment

Figure 7.13 summarizes the effect of the variation of the angle α (Figure 7.1) between the tunnel and the building axes for an isolated building (G1) with aspect ratio $B/L = 1$ (O2), located in the mixed sagging-hogging zone of the settlement profile (P2). Note that the geometry of the building is slightly different from the corresponding case previously analysed. The damage is more severe for a rough than for a smooth interface, but it does not exceed the slight level (Figure 7.14e,f), due to the compact shape and thus relatively short length in the trough.

However, the relative influence of the alignment parameter is significant, as illustrated by the graphs in Figure 7.14. For the O2-G1-P2 case, the global damage

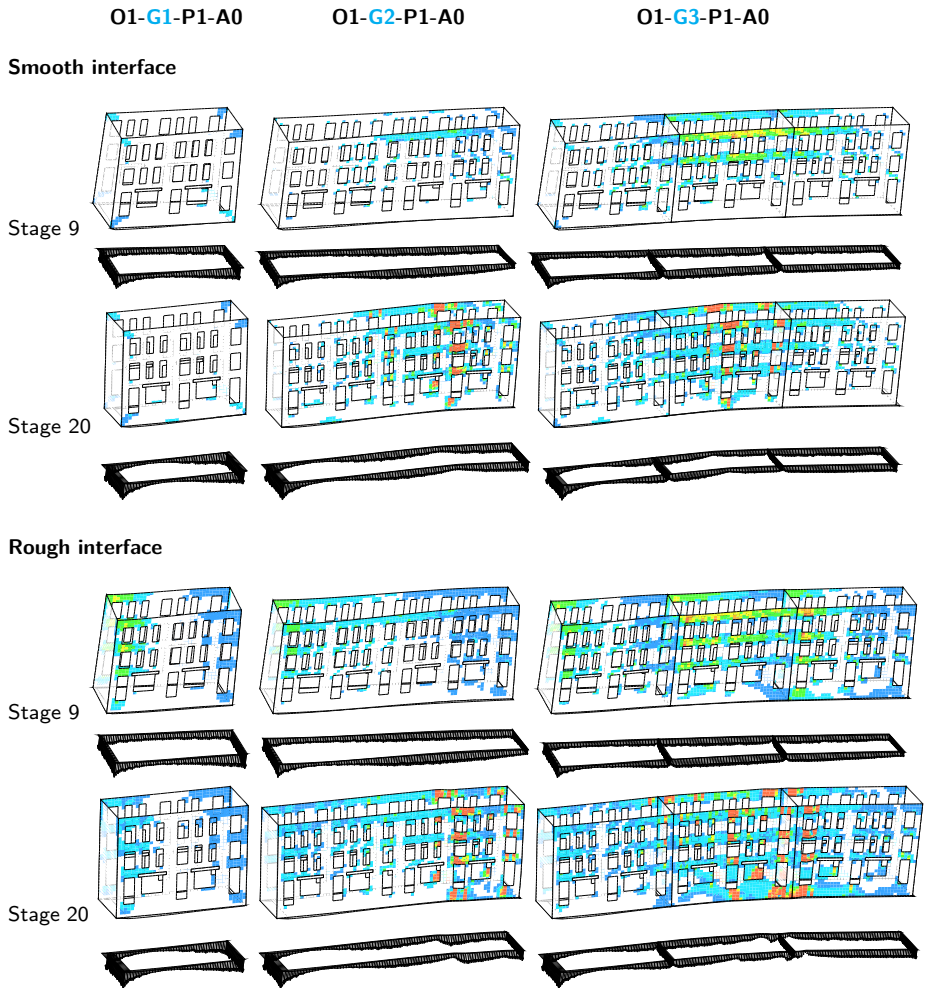


Figure 7.9: Crack strain distribution, deformed configuration and soil-structure interface normal stresses: grouping variation for the O1-P1-A0 case.

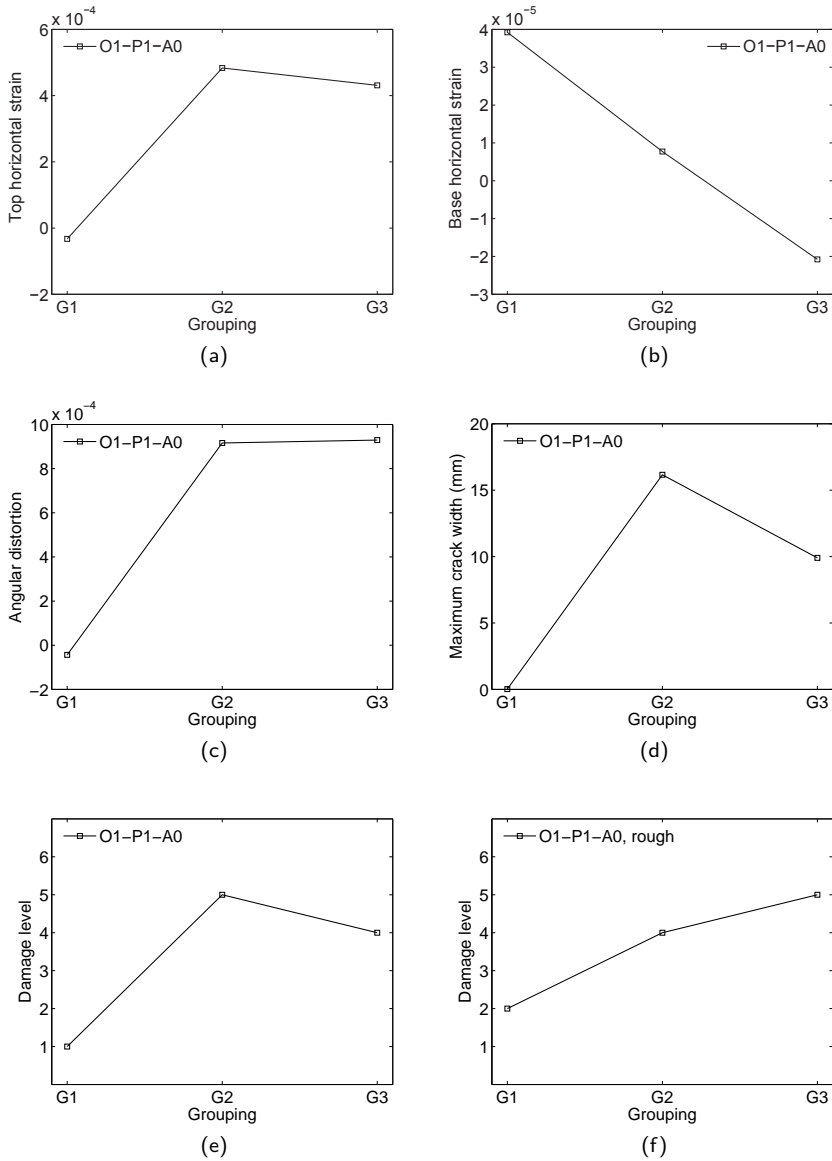


Figure 7.10: Damage indicators as a function of the grouping variations.

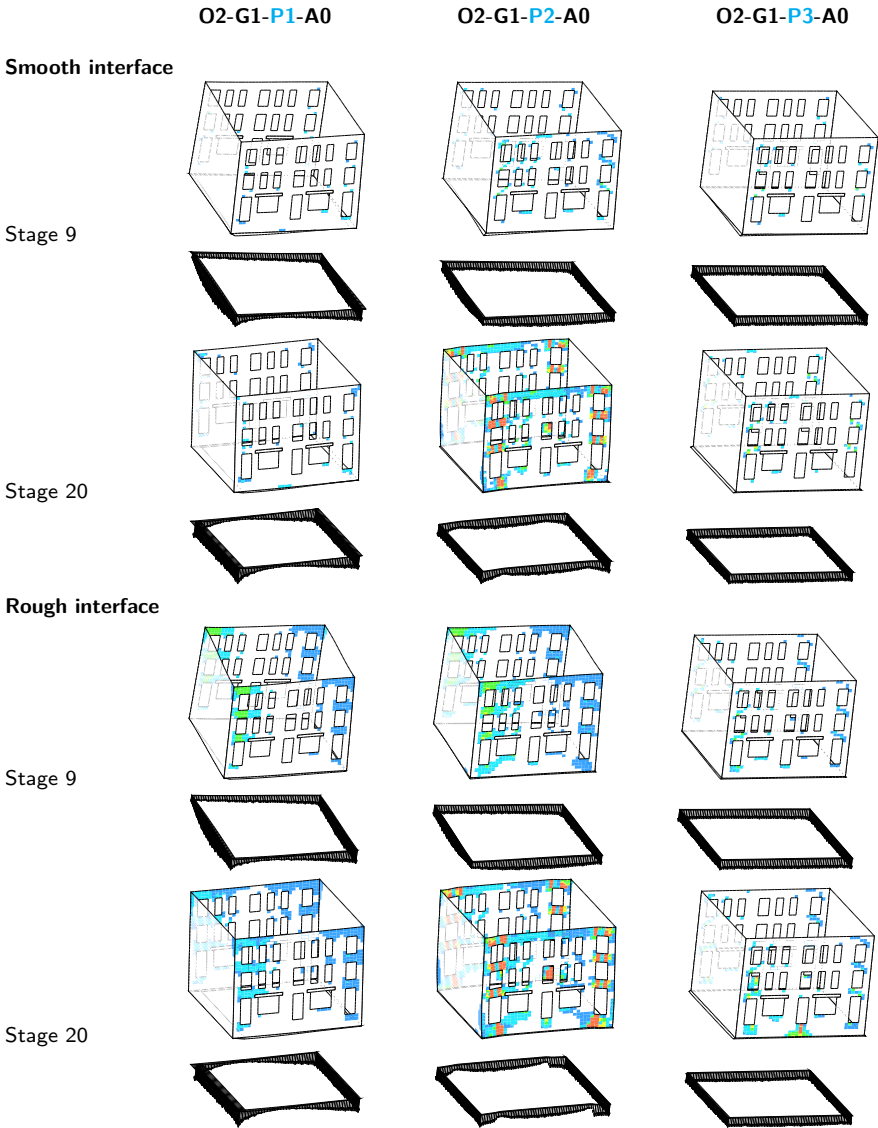


Figure 7.11: Crack strain distribution, deformed configuration and soil-structure interface normal stresses: position variation for the O2-G1-A0 cases.

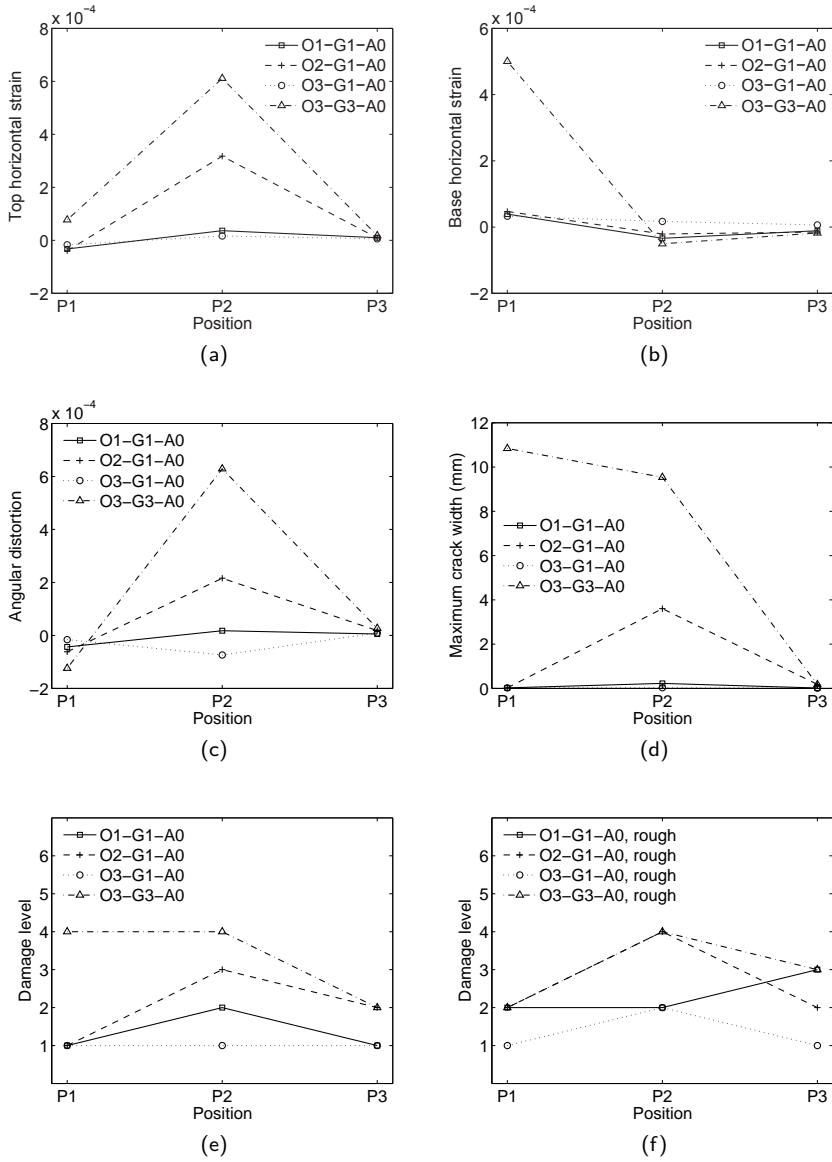


Figure 7.12: Damage indicators as a function of the position variations.

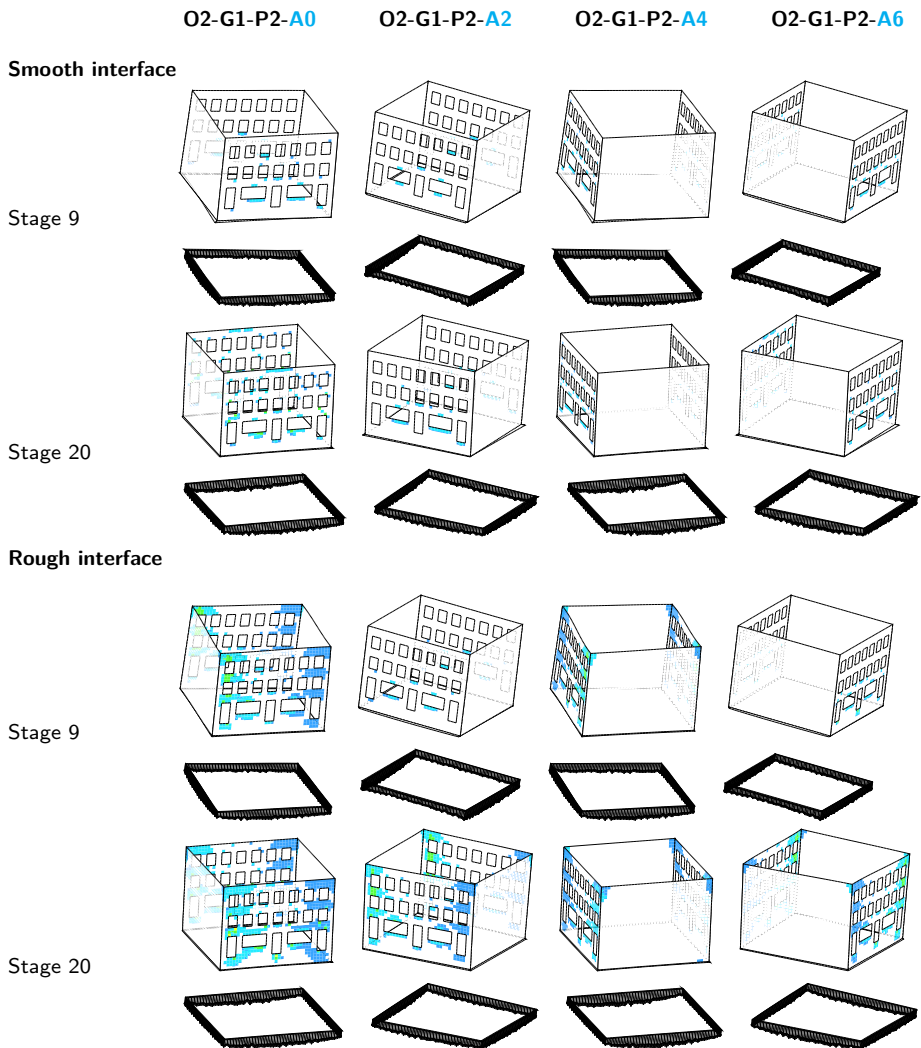


Figure 7.13: Crack strain distribution, deformed configuration and soil-structure interface normal stresses: alignment variation for the O2-G1-P2 case.

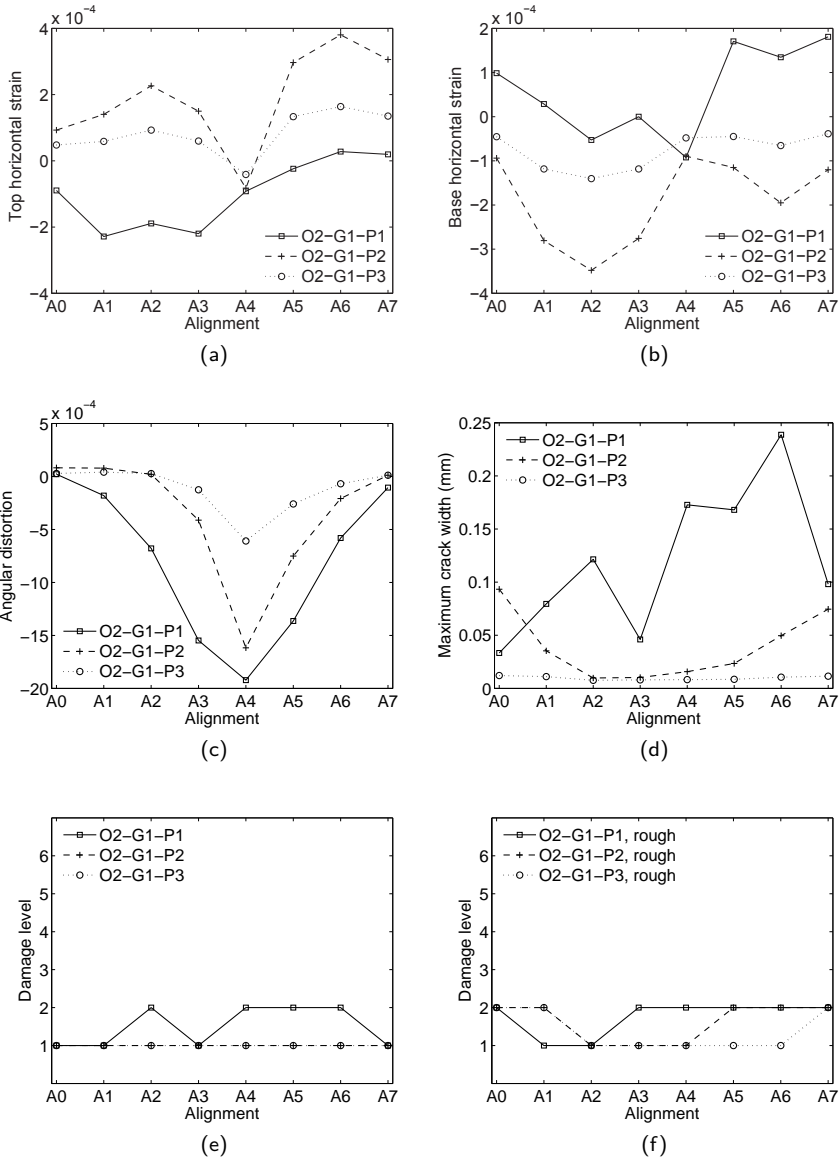


Figure 7.14: Damage indicators as a function of the alignment variations.

decreases with the increase of α from 0° to 90° , and increases afterwards, until $\alpha = 180^\circ$, which corresponds to the initial situation with $\alpha = 0^\circ$. This means that the maximum vulnerability occurs when the façade is parallel to the transverse settlement profile ($\alpha = 0^\circ$ and $\alpha = 180^\circ$). The same effect, although softened by the increased distance from the tunnel, and therefore by the decreased maximum settlement, can be observed for the building in position P3. It can be deduced that in position P2 and P3 the building is far enough from the tunnel centreline not to be significantly affected by the longitudinal settlement profile. This conclusion is supported by the fact that the maximum crack width is observed at stage 20, after the complete tunnel excavation.

Conversely, in a sagging area, rather than in a mixed hogging-sagging area, the combination of different factors with comparable influence prevents from the identification of a univocal trend (Figure 7.14d). The structural response depends more significantly on the longitudinal tunnelling-induced profile. As a consequence, an important role is played in this case by the inclination of the blind walls with respect to the tunnel axis, and by their position with respect to the face of the excavation. The discontinuous variation of maximum damage with the alignment variation depends in fact on the displacement transmitted by the stiffer blind wall to the façade, which is then subjected to an out of plane deformation. The maximum crack width in this case occurs in intermediate stages of the tunnel excavation, when the tunnel face is located in proximity of the surface building.

7.3 Comparison with Building Risk Assessment

Geodata Engineering (GDE) developed a practical tool to evaluate the potential damage of structures affected by tunnelling excavation (Guglielmetti et al., 2008). The Building Risk Assessment (BRA) procedure takes into account the settlement prediction and the intrinsic vulnerability of the structure, assigning a vulnerability index which adjusts the damage category obtained according to the traditional classification system (Burland and Wroth, 1974). In the BRA, the building assessment includes the evaluation of different aspects such as the structural behaviour, the position and orientation, the aesthetic features, the functionality and the defects of the building (Table 7.2). The vulnerability index is calculated as the sum of the coefficients for the orientation and grouping characteristics, multiplied by a position function. The method distinguishes between short term loading and long term loading. The parameter values are based on engineering judgement of field observation. Data are collected during the Building Condition Survey (BCS) (Guglielmetti et al., 2008). In this section, the results of the numerical study related

Table 7.2: Vulnerability coefficients for position and orientation of the building (Guglielmetti et al., 2008). D is the tunnel diameter, while B , L and x indicate the building dimensions and its distance from the tunnel, as shown in Figure 7.1.

Characteristic		Short term coefficient	Long term coefficient
Orientation	O1. $B/L < 0.5$	5	10
	O2. $0.5 < B/L < 2$	6	6
	O3. $B/L > 2$	10	5
Group effect of buildings	G1. Isolated building $B, L < 2D$	15	15
	G2. Isolated building $B < 2L, L > 2D$	10	10
	G3. Grouped buildings perpendicular to the tunnel axis	7	0
		Multiplying factor	Multiplying factor
Position	P1. $x/D < 1$	1	1
	P2. $1 < x/D < 3$	0.5	0.5
	P3. $x/D > 3$	0	0

to the variations of orientation, grouping and position are compared with the BRA index for short term loading conditions (Table 7.3).

7.3.1 Orientation

The dotted line in Figure 7.15 shows the trend of the vulnerability index (right vertical axis) using the BRA procedure with the variation of the B/L ratio. The curve refers to grouping condition G3 and building position P1. The vulnerability is considered to increase with the increase of B/L ratio, because the building is more exposed to the longitudinal settlement profile developing during the excavation. The numerical curve, which indicates the maximum crack width (left vertical axis), shows a similar trend; a difference is a small decrease in damage between the conditions O1 and O2. This is due to the different geometry of the single structure (a larger B), which makes the O2 grouped building stiffer and reduces the differential settlement as effect of the different soil-structure interaction.

Table 7.3: Results of the numerical analyses in terms of crack width and damage category, besides the BRA index.

Orientation	Grouping	Position	Maximum crack width (mm)		Damage category		BRA index (short term)
			Smooth	Rough	Smooth	Rough	
O1	G1	P1	0.02	0.17	0	1	20.0
O1	G1	P2	0.23	0.44	1	1	10.0
O1	G1	P3	0.02	0.76	0	1	0.0
O1	G2	P1	16.19	10.64	4	3	15.0
O1	G2	P2	13.87	21.68	3	4	7.5
O1	G3	P1	9.91	16.98	3	4	12.0
O2	G1	P1	0.03	0.19	0	1	21.0
O2	G1	P2	3.60	4.28	2	2	10.5
O2	G1	P3	0.18	0.56	1	1	0.0
O2	G3	P1	9.11	19.02	3	4	13.0
O3	G1	P1	0.01	0.06	0	0	25.0
O3	G1	P2	0.03	0.26	0	1	12.5
O3	G1	P3	0.01	0.04	0	0	0.0
O3	G3	P1	10.87	0.49	3	1	17.0
O3	G3	P2	9.57	11.15	3	3	8.5
O3	G3	P3	0.18	3.50	1	2	0.0

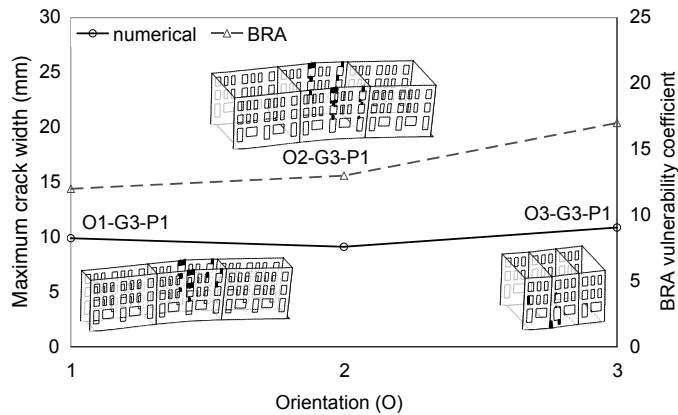


Figure 7.15: Effect of building orientation: comparison between numerical analysis and BRA.

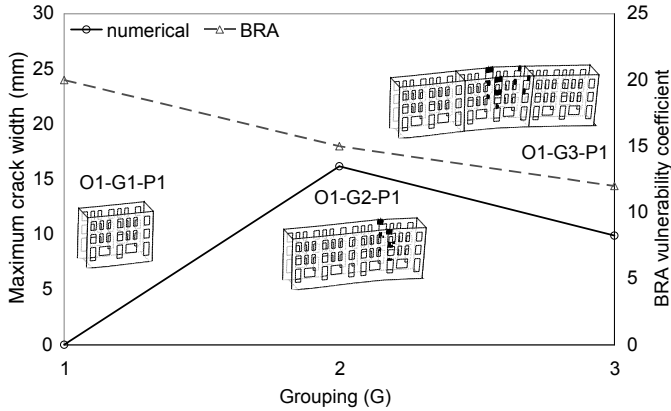


Figure 7.16: Effect of building grouping: comparison between numerical analysis and BRA.

7.3.2 Grouping

The graph in Figure 7.16 shows the situation of a structure with location P1 and orientation O1, when the grouping condition is varied from G1 to G3. The BRA coefficients, extrapolated from empirical measurements, indicate that the grouping effect perpendicular to the tunnel axis tends to decrease the potential damage. The numerical results show that the isolated building in the sagging zone (G1) represents an exception to this trend. The explanation can be found in the type of deformation affecting the building, which is mainly a rigid rotation.

7.3.3 Position

The same distinction between sagging and hogging deformation can be recognized in Figure 7.17, where the effect of the distance between the building and the tunnel is evaluated. Both the numerical and the empirical-based curves show a significant reduction of damage for low values of settlement deflection and distortion (P3); however, the sagging deformation in close proximity to the tunnel again represents a much less vulnerable condition (P1).

All the illustrated curves refer to the smooth interface condition. As can be seen in Table 7.3, allowing for the transmission of horizontal deformations from the ground to the building can significantly affect the structural response. However, field

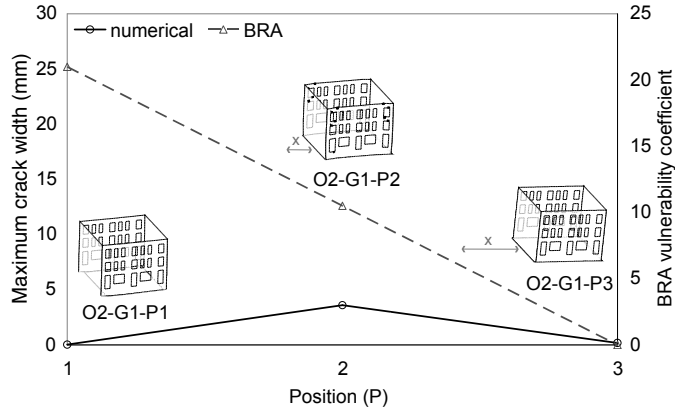


Figure 7.17: Effect of building position: comparison between numerical analysis and BRA.

observations have shown that buildings generally experience small horizontal strains (Burland et al., 2004). For this reason, only the smooth cases are compared with the empirically derived curves.

7.3.4 Global comparison

In Figure 7.18, the correlation between the numerical results and the BRA coefficients is presented for all the performed variations. Also in this case, only the smooth soil-structure interaction is included. Due to the fact that the BRA system does not allow for an explicit distinction between sagging and hogging zone, and considering the previous remarks, the pure sagging cases (isolated buildings G1 in position P1) are marked with a different symbol. Excluding these points, some similar trends can be observed between the numerical analyses and the BRA procedure regarding the effect of orientation, grouping and position on building damage. The results represented by the most dispersed points, generally depend on the specific geometry selection. Since the BRA coefficients are obtained by extrapolation from empirical data, further comparison with the numerical results should focus on the simulation of monitored case studies.

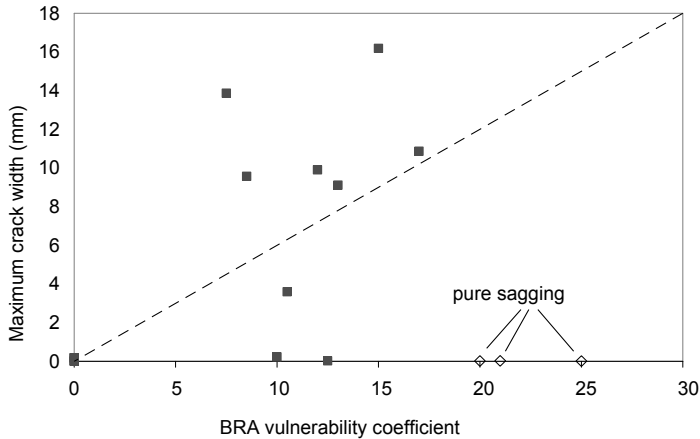


Figure 7.18: Correlation between numerical results and BRA coefficients.

7.4 Conclusions

The proposed 3D modelling approach for the simulation of tunnelling-induced damage to buildings was used to perform a sensitivity study on the effect of several geometrical features on the structural response. The aim was to quantify the influence of four parameters:

- the ratio between the horizontal building dimensions with respect to the tunnel axis direction (orientation O),
- the presence of isolated or grouped buildings (grouping G),
- the distance of the building from the tunnel axis (position P),
- the angle between the main axes of the building plant and the tunnel axis (alignment A).

The use of the 3D coupled model allowed to take into account the following effects:

- the soil-structure interaction, through a non-linear interface connecting the building base with the soil;
- the post-cracking stress redistribution occurring in the masonry, by assuming a smeared crack model for the building material;
- the tunnelling advance, by means of a phased analysis;

- the 3D displacement field with sagging and hogging zones as a consequence of the settlement profiles in both the directions transverse and longitudinal to the tunnel axis;
- the torsional response of the building, as combined effect of the 3D settlement profile and the 3D building model;
- the influence of structural features like openings and transverse walls.

Results showed that the building vulnerability increases with the increase of the façade dimension in the direction transverse to the tunnel axis. The reason is the variation of global stiffness in relation with the settlement profile governing the final damage.

A similar effect occurs when a series of adjacent buildings are connected via common transverse walls. Grouped buildings suffer from more severe damage than short isolated buildings, which tend to tilt more rigidly.

The position parameter affects simultaneously the magnitude and the type of settlement. The damage generally decreases with the increase of distance from the tunnel, due to the reduction of settlement values. Buildings located in the proximity of the tunnel (sagging zone) and characterized by a compact geometry and thus by a stiffer global response represent an exception to this trend.

The 3D model has been useful to evaluate the response of buildings not aligned with the tunnel axis. As a general observation, it can be concluded that the most vulnerable situation corresponds to the alignment of the weakest structural elements, i.e. the façades with openings, with the governing ground deformation. For buildings located far enough from the tunnel, the settlement profile determining the final damage is the one developing in the direction transverse to the tunnel axis; therefore, the most severe damage occurs when the façade is orthogonal to the tunnel axis. In the sagging area, the effect of the transverse and longitudinal components of ground displacements are comparable, and thus it is not possible to recognize a consistent trend in the vulnerability. A major role in this case is also played by the stiff transverse walls, which transmit to the façade an out of plane deformation dependent on the wall inclination with respect to the tunnel face position. This further highlights the importance of simulating the excavation advance.

Analyses with smooth and rough soil-structure interface properties have been performed to investigate the effect of the horizontal displacements transmitted from the soil to the structure. When the building geometry leads to the development of the typical sagging failure mechanism, i.e. a vertical crack arising from the bottom of the façade, the base horizontal strains act as restraint of the final deformation, and the vulnerability is reduced. The opposite situation occurs in hogging area, where the horizontal component tends to worsen the damage pattern. Once again,

compact buildings are exceptions: when located in proximity of the tunnel and falling entirely in the sagging area, they tend to be damaged mainly by the dragging of the transverse walls.

The comparison with classification systems based on field observations showed some common tendency with regards to the influence of the analysed parameters, with the major exception of buildings subjected to a pure sagging mode. The results of the 2D and 3D sensitivity study will be used in the next chapter to derive a vulnerability formulation able to emphasize the weight of the investigated factors.

Settlement vulnerability system

8

Several structural and geometrical features influencing the response of masonry buildings subjected to tunnelling induced settlements have been experimentally and numerically investigated in this research. Once validated by comparison with experimental results and field observations, numerical 2D and 3D models have been proven to offer a deeper insight into the structural vulnerability in relation to the excavation, the building and the soil-structure interaction characteristics. Furthermore, parametric analyses have been performed to extend the empirical data to a wider range of possible scenarios.

In this chapter, the results of the sensitivity study of the structural response to tunnelling are used to set the framework of a comprehensive damage classification model, able to relate the variations of selected structural features with the expected building damage, for a certain level of applied deformation. A damage model based on the numerical results of the present research is proposed. The explicit identification of each parameter with its relative weight allows for a direct estimation of the parameter influence on the global damage, and makes the tool flexible to include further monitoring data or numerical outcomes from different sources.

8.1 Damage model

The selected damage model d depends on a certain number of parameters x_i , collected in an array \mathbf{x} :

$$d = d(\mathbf{x}) \tag{8.1}$$

The damage model is required to fit the data points d_{num} resulting from the parametric analyses performed on the 2D and 3D models in Chapter 5 and Chapter 7, respectively. The approximated solution of the system

$$d(\mathbf{x}) \cong d_{\text{num}}(\mathbf{x}) \quad (8.2)$$

is obtained by minimizing the sum of squares

$$\sum_{f=1}^k (d^f(\mathbf{x}) - d_{\text{num}}^f(\mathbf{x}))^2 \quad (8.3)$$

where k is the total amount of observations, i.e. the number of numerical variations, and where superscript f indicates the individual numerical analyses.

The damage models which have to fit the 2D and 3D numerical results are assumed as:

$$d_{2D}\left(\frac{\Delta}{L}, \bar{\mathbf{x}}\right) = d_{2D,\text{ref}}\left(\frac{\Delta}{L}\right) + \sum_{i=1}^6 a_i \bar{x}_i \quad (8.4)$$

$$d_{3D}(\bar{\mathbf{x}}) = d_{3D,\text{ref}} + \sum_{i=7}^{10} a_i \bar{x}_i \quad (8.5)$$

where $\bar{\mathbf{x}}$ contains the normalized values of the parameters x_i , and $d_{2D,\text{ref}}$ and $d_{3D,\text{ref}}$ are the selected reference values for the 2D and 3D variations, respectively. The 2D and 3D models will address different sets of parameters. The six normalized parameters for the 2D model and the four normalized parameters for the 3D model will be presented in the next two subsections.

The 2D analyses have been carried out by imposing a certain deformation to the interface at the façade base, and therefore the 2D damage model depends on both the deflection ratio Δ/L and the analysed parameters x_i . Conversely, the 3D analyses simulated the tunnel advance for a fixed value of volume loss $V_L = 2\%$, and therefore the 3D damage function does not depend on the applied deformation. Defining the damage model as the sum of the normalized parameters multiplied by coefficients a_i gives a relatively simple expression which has the main advantage of making the relative weight of each parameter explicit. Furthermore, such a formulation is flexible, being open to the modification of any of the accounted parameters, or to the inclusion of additional ones.

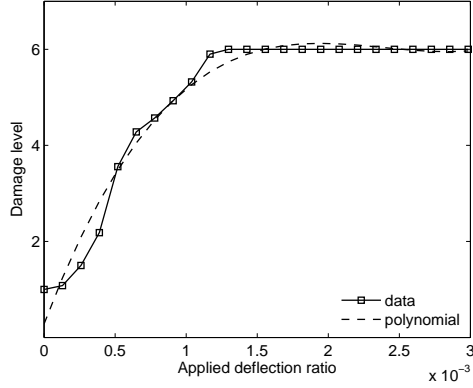


Figure 8.1: Numerical curve and polynomial approximation, reference case.

8.2 2D damage function

For the damage model interpreting the results of the 2D sensitivity study, a third order polynomial is chosen to fit the reference case, which corresponds to the experimentally tested façade:

$$d_{2D,ref} \left(\frac{\Delta}{L} \right) = b_1 + b_2 \left(\frac{\Delta}{L} \right) + b_3 \left(\frac{\Delta}{L} \right)^2 + b_4 \left(\frac{\Delta}{L} \right)^3 \quad (8.6)$$

A preliminary fitting of the numerical results showed that the third is the lowest degree of polynomial that guarantees a good approximation of the numerical curve (Figure 8.1).

The summation $\sum_{i=1}^6 a_i \bar{x}_i$ in Equation (8.4) includes the contribution of six terms; each term takes into account the influence of a different (combination of) parameter, according to the following scheme:

x_1 : percentage of façade openings	$x_1 \in [0, 30\%]$
x_2 : fracture energy of masonry	$x_2 \in [10, 1000 \text{ N/m}]$
x_3 : Young's modulus of masonry	$x_3 \in [1000, 9000 \text{ MPa}]$
x_4 : tensile strength of masonry	$x_4 \in [0.1, 0.9 \text{ MPa}]$
x_5 : normal stiffness of the base interface	$x_5 \in [0.7 \times 10^7, 0.7 \times 10^9 \text{ N/m}^3]$
x_{6s} : shear behaviour of the base interface	$x_{6s} \in \{\text{smooth, rough}\}$
x_{6t} : type of settlement profile	$x_{6t} \in \{\text{sagging, hogging}\}$

The effect of the variation of x_i on the final damage resulting from the numerical simulations is summarized in Figure 8.2. The damage level, which was related to the maximum crack width by means of a step function ranging from 1 to 6 (Figure 4.11a), is now translated into a continuous function of the maximum crack width, as illustrated in Figure 8.3.

The normalized parameters \bar{x}_i are formulated such as to become zero at the reference case and expected to increase for conditions leading to an increase of damage with respect to the reference case. By normalizing the range of each parameter \bar{x}_i to a unit range, the resulting coefficients a_i can directly be interpreted in terms of possible damage level variation. The normalized parameters are defined as:

$$\bar{x}_1 = \frac{x_1 - x_{1\text{ref}}}{30} \quad \bar{x}_1 \in [-1, 0] \quad (8.7)$$

$$\bar{x}_2 = -\frac{x_2 - x_{2\text{ref}}}{990} \quad \bar{x}_2 \in [-1, 0] \quad (8.8)$$

$$\bar{x}_3 = \frac{x_3 - x_{3\text{ref}}}{8000} \quad \bar{x}_3 \in [-1/4, 3/4] \quad (8.9)$$

$$\bar{x}_4 = -\frac{x_4 - x_{4\text{ref}}}{0.8} \quad \bar{x}_4 \in [-1, 0] \quad (8.10)$$

$$\bar{x}_5 = \frac{\log_{10} x_5 - \log_{10} x_{5\text{ref}}}{2} \quad \bar{x}_5 \in [-1, 0] \quad (8.11)$$

$$\bar{x}_6 = 1 - |x_{6s} - x_{6t}|, \quad \bar{x}_6 \in \{0, 1\} \quad (8.12)$$

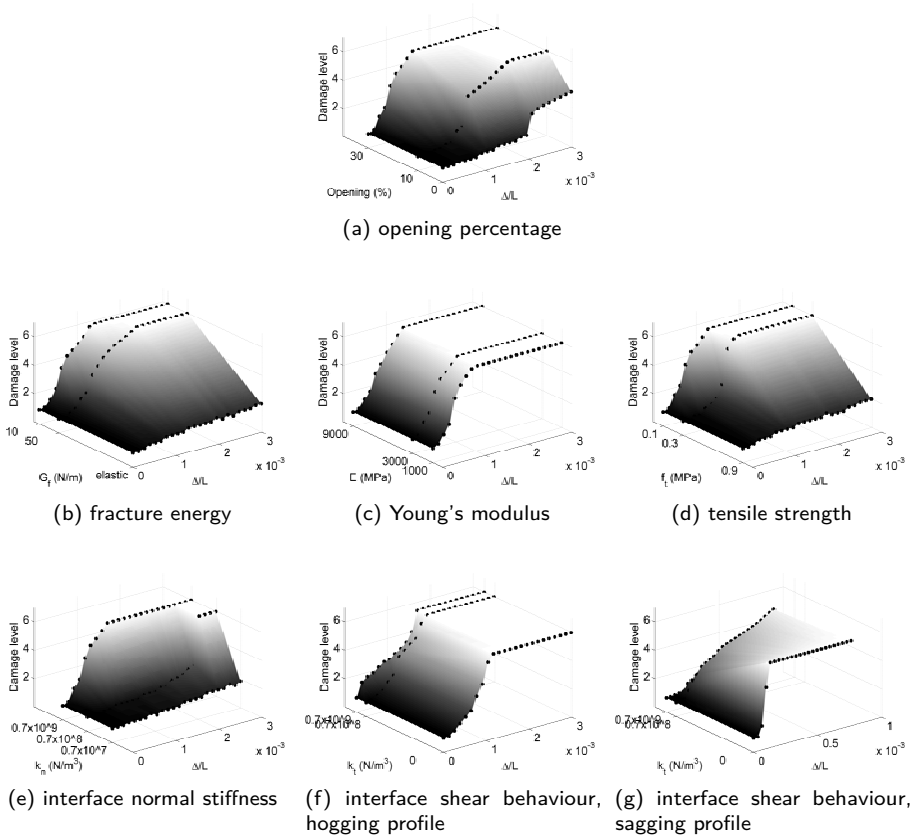


Figure 8.2: Damage level as a function of the applied deflection ratio Δ/L and the parameters included in the 2D numerical simulations.

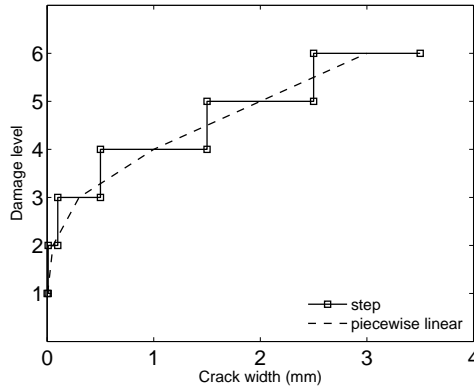


Figure 8.3: Comparison between the step (Figure 4.11a) and the continuous functions relating the maximum crack width with the damage level.

$$\text{where } x_{6s} = \begin{cases} 0 & \text{smooth interface} \\ 1 & \text{rough interface} \end{cases} \quad \text{and} \quad x_{6t} = \begin{cases} 0 & \text{sagging} \\ 1 & \text{hogging} \end{cases}$$

$\bar{x}_{i\text{ref}}$ are equal to the value assumed by each parameter in the reference case. Coefficients and normalized coefficients corresponding to the performed numerical variations are listed in Table 8.1. All the parameters are normalized with respect to the domain of values assumed in the sensitivity study, and described in Section 5.1. These values were selected preliminary to cover a broad range of realistic situations, and therefore the normalization performed at this stage is considered to be sufficiently representative.

Normalized parameters from \bar{x}_1 to \bar{x}_4 are directly related with the parameter values as assumed in the numerical variations (Section 5.1). Due to the units and values selected for the sensitivity analysis of the interface normal stiffness, x_5 can vary over three orders of magnitude; given the uncertainty of this parameter, \bar{x}_5 indicates the order of magnitude by using a logarithmic function (Equation (8.11)). As observed in Section 5.2.4 and Section 5.2.5, the effect of the base interface shear behaviour depends on the applied profile of horizontal deformations, which is determined by the position of the structure with respect to the tunnel (e.g. sagging or hogging area). For this reason, the influence of parameters x_{6s} and x_{6t} is coupled in the \bar{x}_6 formulation. According to Equation (8.12), an increase of damage is expected for the combination of a smooth interface in the sagging zone and a rough

interface in the hogging zone. This formulation interprets a general trend observed by the presented and previous research (Netzel, 2009).

Equation (8.2) can be written in matrix form

$$\begin{bmatrix}
 1 & \frac{\Delta}{L} & \left(\frac{\Delta}{L}\right)^2 & \left(\frac{\Delta}{L}\right)^3 & \bar{x}_{1\text{ref}} & \bar{x}_{2\text{ref}} & \bar{x}_{3\text{ref}} & \bar{x}_{4\text{ref}} & \bar{x}_{5\text{ref}} & \bar{x}_{6\text{ref}} \\
 1 & \frac{\Delta}{L} & \left(\frac{\Delta}{L}\right)^2 & \left(\frac{\Delta}{L}\right)^3 & \bar{x}_{11} & 0 & 0 & 0 & 0 & 0 \\
 1 & \frac{\Delta}{L} & \left(\frac{\Delta}{L}\right)^2 & \left(\frac{\Delta}{L}\right)^3 & \bar{x}_{12} & 0 & 0 & 0 & 0 & 0 \\
 1 & \frac{\Delta}{L} & \left(\frac{\Delta}{L}\right)^2 & \left(\frac{\Delta}{L}\right)^3 & 0 & \bar{x}_{21} & 0 & 0 & 0 & 0 \\
 1 & \frac{\Delta}{L} & \left(\frac{\Delta}{L}\right)^2 & \left(\frac{\Delta}{L}\right)^3 & 0 & \bar{x}_{22} & 0 & 0 & 0 & 0 \\
 1 & \frac{\Delta}{L} & \left(\frac{\Delta}{L}\right)^2 & \left(\frac{\Delta}{L}\right)^3 & 0 & 0 & \bar{x}_{31} & 0 & 0 & 0 \\
 1 & \frac{\Delta}{L} & \left(\frac{\Delta}{L}\right)^2 & \left(\frac{\Delta}{L}\right)^3 & 0 & 0 & \bar{x}_{32} & 0 & 0 & 0 \\
 1 & \frac{\Delta}{L} & \left(\frac{\Delta}{L}\right)^2 & \left(\frac{\Delta}{L}\right)^3 & 0 & 0 & 0 & \bar{x}_{41} & 0 & 0 \\
 1 & \frac{\Delta}{L} & \left(\frac{\Delta}{L}\right)^2 & \left(\frac{\Delta}{L}\right)^3 & 0 & 0 & 0 & \bar{x}_{42} & 0 & 0 \\
 1 & \frac{\Delta}{L} & \left(\frac{\Delta}{L}\right)^2 & \left(\frac{\Delta}{L}\right)^3 & 0 & 0 & 0 & 0 & \bar{x}_{51} & 0 \\
 1 & \frac{\Delta}{L} & \left(\frac{\Delta}{L}\right)^2 & \left(\frac{\Delta}{L}\right)^3 & 0 & 0 & 0 & 0 & \bar{x}_{52} & 0 \\
 1 & \frac{\Delta}{L} & \left(\frac{\Delta}{L}\right)^2 & \left(\frac{\Delta}{L}\right)^3 & 0 & 0 & 0 & 0 & 0 & \bar{x}_{61} \\
 1 & \frac{\Delta}{L} & \left(\frac{\Delta}{L}\right)^2 & \left(\frac{\Delta}{L}\right)^3 & 0 & 0 & 0 & 0 & 0 & \bar{x}_{62} \\
 1 & \frac{\Delta}{L} & \left(\frac{\Delta}{L}\right)^2 & \left(\frac{\Delta}{L}\right)^3 & 0 & 0 & 0 & 0 & 0 & \bar{x}_{63} \\
 \dots & \dots & \dots & \dots & \dots & \dots & \dots & \dots & \dots & \dots \\
 \dots & \dots & \dots & \dots & \dots & \dots & \dots & \dots & \dots & \dots
 \end{bmatrix}
 \begin{bmatrix}
 b_1 \\
 b_2 \\
 b_3 \\
 b_4 \\
 a_1 \\
 a_2 \\
 a_3 \\
 a_4 \\
 a_5 \\
 a_6
 \end{bmatrix}
 =
 \begin{bmatrix}
 d_{\text{ref,num}} \\
 d_{1,\text{num}} \\
 d_{2,\text{num}} \\
 d_{3,\text{num}} \\
 d_{4,\text{num}} \\
 d_{5,\text{num}} \\
 d_{6,\text{num}} \\
 d_{7,\text{num}} \\
 d_{8,\text{num}} \\
 d_{9,\text{num}} \\
 \dots \\
 \dots
 \end{bmatrix}
 \quad (8.13)$$

where \bar{x}_{ij} denotes the value of the normalized parameter \bar{x}_i in the numerical analysis $f = j$. The assumed values are indicated in Table 8.1. The following compact notation is used:

$$\mathbf{A}\mathbf{a} = \mathbf{d}_{\text{num}} \quad (8.14)$$

where \mathbf{A} is the matrix assembling the known coefficients, \mathbf{d}_{num} is the vector containing the results of the numerical variations and \mathbf{a} is the vector of the unknown coefficients. All rows of \mathbf{A} and all elements of \mathbf{d}_{num} are repeated for the progressive 24 values of Δ/L applied in the numerical analyses, leading to the evaluation of 336 observations. The vector of unknown coefficients can be obtained from the (linear) least square fit

$$\mathbf{a} = (\mathbf{A}^T \mathbf{A})^{-1} \mathbf{A}^T \mathbf{d}_{\text{num}} \quad (8.15)$$

The graphs from Figure 8.4 to Figure 8.10 show the comparison between the numerical analysis data and the fitted damage function. Considering the substantial difference in both ranges of analysed variations, the damage model shows an adequate flexibility in predicting the damage level as a function of the applied deformations.

Table 8.1: Parameters and normalized parameters used to derive the damage model from 2D numerical results.

f	x_1 (%)	x_2 (N/m)	x_3 (MPa)	x_4 (MPa)	x_5 (N/m ³)	x_{6s} (-)	x_{6t} (-)	\bar{x}_1 (-)	\bar{x}_2 (-)	\bar{x}_3 (-)	\bar{x}_4 (-)	\bar{x}_5 (-)	\bar{x}_6 (-)
ref	30	10	3000	0.1	0.7×10^9	0	1	0	0	0	0	0	0
1	0	10	3000	0.1	0.7×10^9	0	1	-1.00	0	0	0	0	0
2	10	10	3000	0.1	0.7×10^9	0	1	-0.67	0	0	0	0	0
3	30	50	3000	0.1	0.7×10^9	0	1	0	-0.04	0	0	0	0
4	30	1000	3000	0.1	0.7×10^9	0	1	0	-1.00	0	0	0	0
5	30	10	1000	0.1	0.7×10^9	0	1	0	0	-0.25	0	0	0
6	30	10	9000	0.1	0.7×10^9	0	1	0	0	0.75	0	0	0
7	30	10	3000	0.3	0.7×10^9	0	1	0	0	0	-0.25	0	0
8	30	10	3000	0.9	0.7×10^9	0	1	0	0	0	-1.00	0	0
9	30	10	3000	0.1	0.7×10^7	0	1	0	0	0	0	-1.0	0
10	30	10	3000	0.1	0.7×10^8	0	1	0	0	0	0	-0.5	0
11	30	10	3000	0.1	0.7×10^9	1	1	0	0	0	0	0	1.00
12	30	10	3000	0.1	0.7×10^9	0	0	0	0	0	0	0	1.00
13	30	10	3000	0.1	0.7×10^9	1	0	0	0	0	0	0	0

Approximations appear to deviate when the shape of the numerical curve is particularly steep, i.e. the damage rapidly increases for small increment of applied deformation, due to the brittle behaviour of masonry. This deviation between the numerical analysis and the estimated curves is probably mainly due to the selected shape of the first part of the damage function, which is a third degree polynomial function with linear coefficients b_i . The numerical analysis curves are typically characterised by a steady increase of damage after a longer or shorter latency and before reaching a certain damage level plateau. Alternative damage models, for example a piecewise linear function with three intervals for ranges of Δ/L depending on the parameters x_i , would probably fit better the numerical data (Figure 8.11). However, the used model was intentionally chosen for two principal reasons: the possibility to interpret a_i as relative weight of each parameter on the building response and to directly relate the assumed coefficient range of values with the increase or decrease of expected structural damage (Figure 8.12).

On average, the damage model can give a good approximation of all the selected curves; the only exceptions are represented by the cases of a rough interface, where the damage function tends to overestimate the numerical curves for all the values of applied deformation (Figure 8.9b and Figure 8.10b). The reason is the local discrepancy between the assumed formulation of \bar{x}_6 and the observed interaction of factors x_{6s} and x_{6t} representing the shear behaviour of the base interface and the type of applied settlement, respectively.

Figure 8.12 visualizes the values of the coefficients a_i . The global quantitative evaluation offered by the bar graph is consistent with the results of the numerical

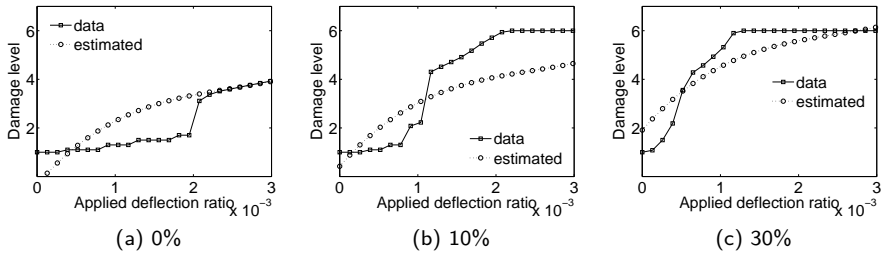


Figure 8.4: Comparison between the observational data and the estimation given by the damage model for the variation of opening percentage.

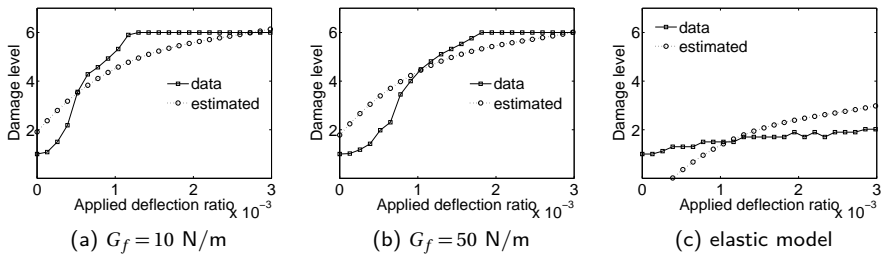


Figure 8.5: Comparison between the observational data and the estimation given by the damage model for the variation of fracture energy.

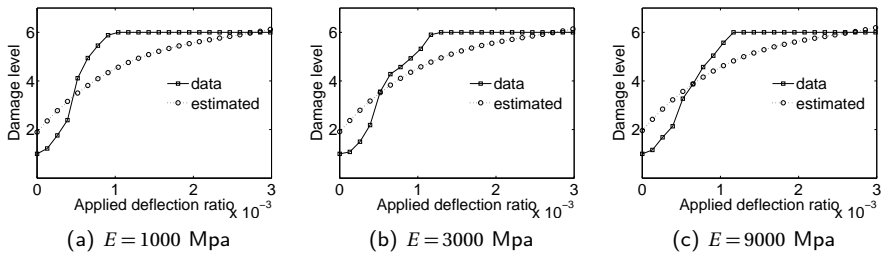


Figure 8.6: Comparison between the observational data and the estimation given by the damage model for the variation of Young's modulus.

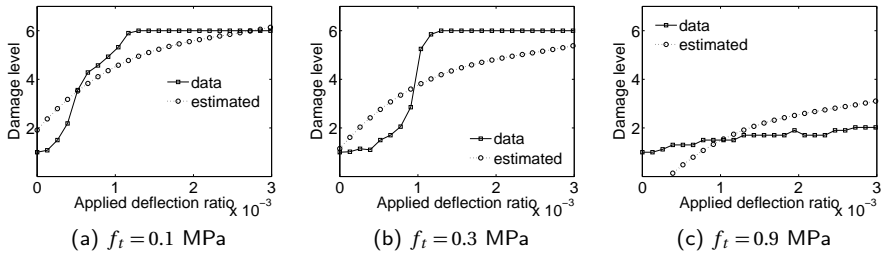


Figure 8.7: Comparison between the observational data and the estimation given by the damage model for the variation of tensile strength.

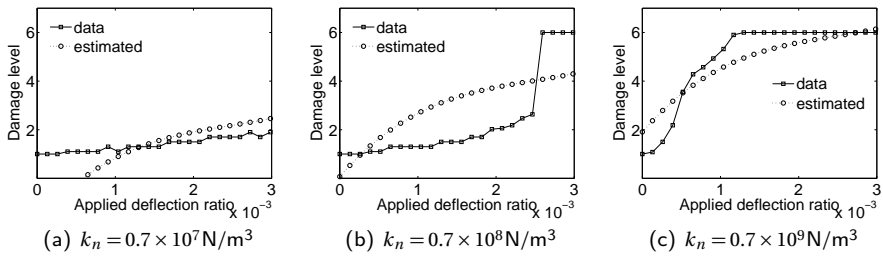


Figure 8.8: Comparison between the observational data and the estimation given by the damage model for the variation of interface normal stiffness.

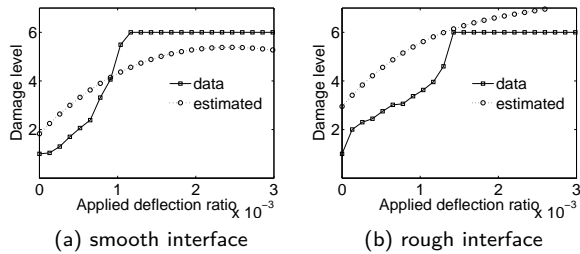


Figure 8.9: Comparison between the observational data and the estimation given by the damage model for the variation of shear normal stiffness in a hogging area.

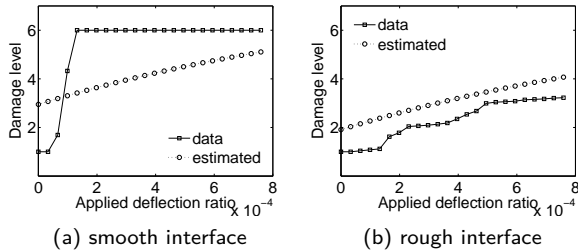


Figure 8.10: Comparison between the observational data and the estimation given by the damage model for the variation of interface normal stiffness in a sagging area.

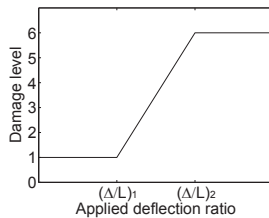


Figure 8.11: Piecewise linear damage function, with deflection ratio values $(\Delta/L)_1$ and $(\Delta/L)_2$ depending on \bar{x} .

study described in Chapter 5. The interface normal stiffness representing the soil-structure interaction and the brittle behaviour of the masonry are the most important parameters governing the settlement-induced structural damage. With reference to the analysed ranges of values, they can vary the final risk assessment by up to four damage levels. These values give an estimation of the impact of neglecting these two fundamental aspects of the structural response in the damage assessment. They also suggest the amount of the reduction of limiting tensile strain values that could be implemented in the current empirical analytical procedure (LTSM) in order to include these effects.

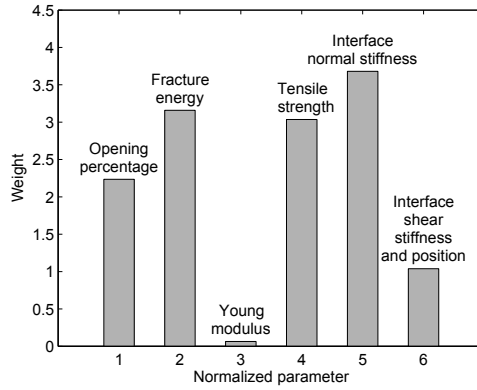


Figure 8.12: Coefficient weights of the 2D damage function, as an indication for a possible variation of damage level.

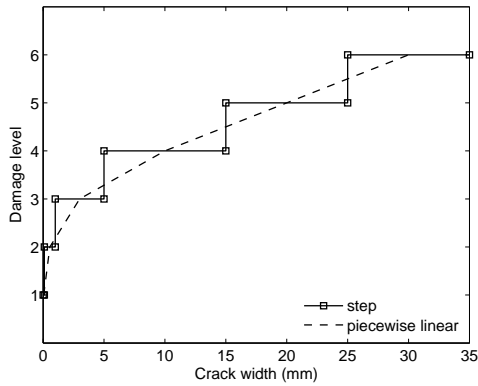


Figure 8.13: Comparison between the step (Figure 4.11a) and the continuous functions relating the maximum crack width with the damage level.

8.3 3D damage function

As mentioned in Section 8.1, all the parametric variations performed on the 3D model simulated the advance of a tunnel excavation leading to the same amount of ground volume loss. Therefore, the reference 3D damage function does not include the dependency on the applied deformation, and it can be simply written as:

$$d_{3D,num} = c_1 \quad (8.16)$$

The normalized parameters \bar{x}_i refer to the building orientation O, grouping G, position P and alignment A, as defined in Section 7.1, and they assume the following values:

$$x_7 = \begin{cases} 1 & B/L < 0.5 & \text{(O1)} \\ 2 & 0.5 < B/L < 2 & \text{(O2)} \\ 3 & B/L > 2 & \text{(O3)} \end{cases} \quad (8.17)$$

$$x_8 = \begin{cases} 1 & \text{isolated building with } B \text{ and } L < 2D & \text{(G1)} \\ 2 & \text{isolated building with } B < 2L \text{ and } L > 2D & \text{(G2)} \\ 3 & \text{grouped building perpendicular to the tunnel axis} & \text{(G3)} \end{cases} \quad (8.18)$$

$$x_9 = \begin{cases} 1 & x/D < 1 & \text{(P1)} \\ 2 & 1 < x/D < 3 & \text{(P2)} \\ 3 & x/D > 3 & \text{(P3)} \end{cases} \quad (8.19)$$

The fourth parameter x_{10} is the angle between the tunnel axis and the transverse walls of the building ($x_{10} \in [0^\circ, 180^\circ]$, Figure 7.6).

As for the 2D case, the step damage function (Figure 4.11a) has been translated into the piecewise linear function shown in Figure 8.13.

Having at disposal more than one analysis set for the orientation, position and alignment variation (Section 7.1), the results were preliminary averaged for these variations, in order to reduce the influence of the arbitrary selection of cases included in the sensitivity study, resulting in a similar weight for the four variations. The average values, which will be used in the least square procedure, are connected by the grey line in Figure 8.14.

The normalized parameters \bar{x}_i are derived following the same criteria used in the 2D procedure, and they are expressed as:

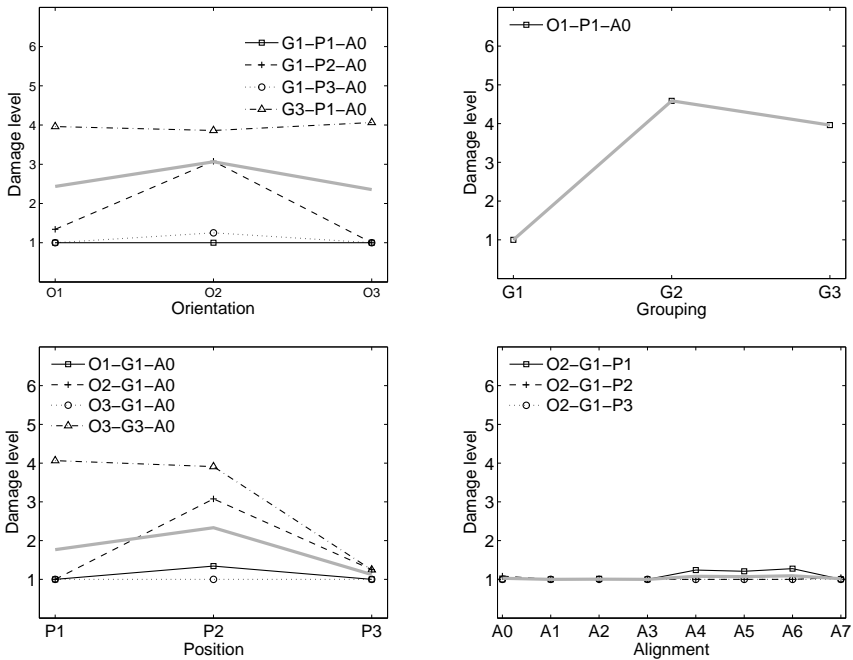


Figure 8.14: Damage level resulting from the 3D sensitivity study and average values used as input for the derivation of the damage model. The grey line connects the average values.

$$\bar{x}_7 = -\frac{x_7 - x_{7ref}}{2} \quad \bar{x}_7 \in \{-1/2, 0, 1/2\} \quad (8.20)$$

$$\bar{x}_8 = \frac{x_8 - x_{8ref}}{2} \quad \bar{x}_8 \in \{0, 1/2, 1\} \quad (8.21)$$

$$\bar{x}_9 = -\frac{x_9 - x_{9ref}}{2} \quad \bar{x}_9 \in \{-1/2, 0, 1/2\} \quad (8.22)$$

$$\bar{x}_{10} = \frac{||x_{10}| - 90| - 90}{90} \quad \bar{x}_{10} \in [-1, 0] \quad (8.23)$$

The definition of \bar{x}_{10} takes into account the observation that in hogging and mixed hogging-sagging the building is more vulnerable when its façades are aligned with the transverse settlement profile, and thus $x_{10} = 0^\circ, 180^\circ$ (Section 7.2.4). The \bar{x}_{10} formulation generalizes this result to the sagging area, where such a trend cannot be deduced, and therefore is expected to lead to a decreased accuracy of the damage function when simulating the alignment variation. The values of x_i and the related \bar{x}_i are listed in Table 8.2. Due to the limited empirical knowledge currently available on the transmission of horizontal displacements, only the results obtained by assuming a smooth interface between the soil and the building have been used to derive the damage model.

Figure 8.15 shows the comparison between the averaged 3D results and the damage model prediction. As for the 2D study, the model is able to interpret the trends of the parameter variations. The accuracy of the prediction is limited by the initial choice of a damage function proportional to possible increase of damage; a parabolic shape would for example follow better the damage level variations as a function of each parameter variation. However, just as for the 2D case, the choice of a multilinear damage function (Equation (8.5)) facilitates the interpretation of the obtained coefficients a_i . The value of a_i indicates possible increases of damage levels by varying the corresponding parameter x_i .

As shown in Figure 8.16, the values of the four coefficients indicate the governing role of the grouping factor, which affects the lateral boundary conditions and the global stiffness of the building in relation to the applied settlement profile. The grouping parameter could induce a variation up to three levels in the final damage assessment; this result is consistent with the numerical outcomes illustrated in Chapter 7.

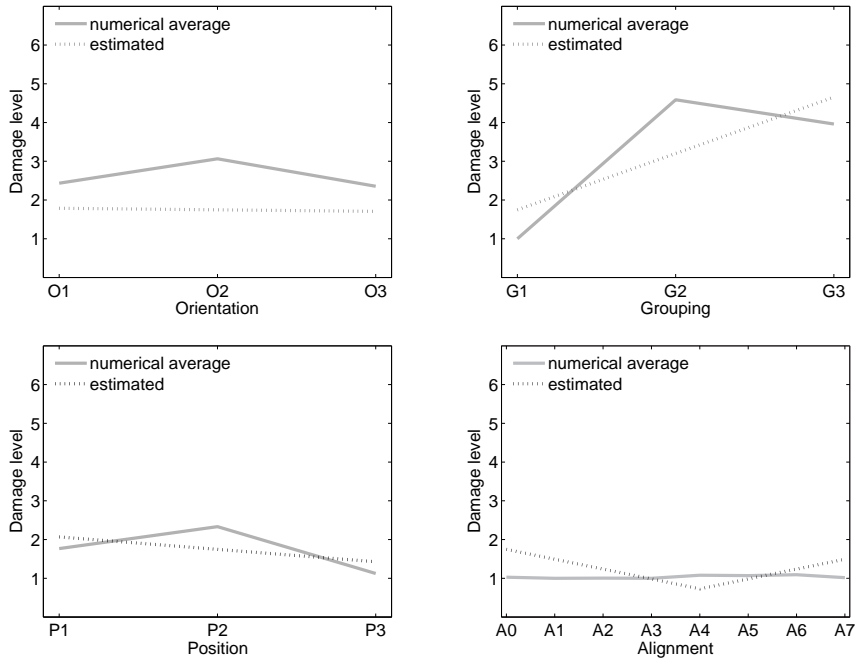


Figure 8.15: Comparison between the observational data and the estimation given by the 3D damage model.

Table 8.2: Parameters and normalized parameters used to derive the damage model from 3D numerical results.

f	x_7 (-)	x_8 (-)	x_9 (-)	x_{10} (-)	\bar{x}_7 (-)	\bar{x}_8 (-)	\bar{x}_9 (-)	\bar{x}_{10} (-)
ref	2.00	1.00	2.00	0	0	0	0	0
1	1.00	1.00	2.00	0	0.50	0	0	0
2	3.00	1.00	2.00	0	-0.50	0	0	0
3	2.00	2.00	2.00	0	0	0.50	0	0
4	2.00	3.00	2.00	0	0	1.00	0	0
5	2.00	1.00	1.00	0	0	0	0.50	0
6	2.00	1.00	3.00	0	0	0	-0.50	0
7	2.00	1.00	2.00	22.50	0	0	0	-0.25
8	2.00	1.00	2.00	45.00	0	0	0	-0.50
9	2.00	1.00	2.00	67.50	0	0	0	-0.75
10	2.00	1.00	2.00	90.00	0	0	0	-1.00
11	2.00	1.00	2.00	112.50	0	0	0	-0.75
12	2.00	1.00	2.00	135.00	0	0	0	-0.50
13	2.00	1.00	2.00	157.00	0	0	0	-0.25
14	2.00	1.00	2.00	180.00	0	0	0	0

The damage model evaluates the alignment as the second most important parameter, while the aspect ratio between the horizontal building dimensions has a very marginal role. However, the orientation and alignment parameters, referring both to the direction of the most vulnerable structural elements with respect to the governing settlement profile, are closely interacting. Given the proposed modelling approach and vulnerability system framework, the numerical analyses could be extended to a more exhaustive investigation of the relation between the two parameters, for example performing the alignment variation for different type of orientation.

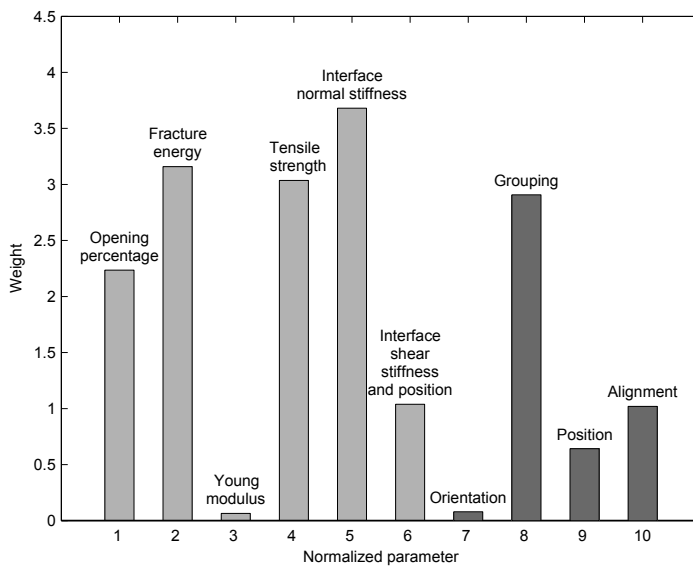


Figure 8.16: Coefficient weights of the 3D damage function as an indication of a possible variation of damage level (dark grey). The coefficients of the 2D damage function have been added for comparison (light grey).

8.4 Conclusion

This chapter proposed a global formulation of the vulnerability of masonry buildings subjected to tunnelling-induced settlements, based on parametric numerical analyses. The analyses were performed on 2D and 3D finite element models validated by comparison with experimental and real-case results. The proposed damage model sets a linear dependency of the parameters evaluated in the sensitivity study with coefficients representing the relative weight of each parameter on the final response. The adopted normalization of parameters has the main advantage of making possible a direct correlation between the selected parameter values and the consequent increase or decrease of the potential structural damage level. This improves the accessibility of the results presented in this thesis.

In this study, limited attention has been spent on possible interaction of the parameters; the model cannot be used for an arbitrary combination of parameters, as this might result in damage levels outside the range [1,6]. However, considering the set of available numerical results, the selection of multi-linear damage functions, i.e. linear in the normalized parameters, is considered adequate to the first definition of an overall vulnerability system.

By incorporating the results of the 2D and 3D parametric analyses, the damage model provides an overall evaluation of the principal factors governing the building response. The damage model outcomes have shown the major influence of the masonry cracking model, the relative stiffness between the soil and the structure, the lateral building constraints and the global stiffness of the building in relation to the governing soil deformation. The proposed damage function makes possible a quantitative assessment of the damage risk variation as defined by the empirical analytical procedure currently used in practice. For example, in case of a masonry façade preliminary classified as subjected to moderate risk of damage, the presence of a large amount of windows can increase the damage category up to two levels, indicating the need for settlement mitigating measurements or building strengthening techniques.

More generally, the results in terms of parameter weights on the structural response can be used to refine the total strain limit values included in the LTSM, according to the building characteristics. Furthermore, due to its flexible formulation, the method represents a growing knowledge system, which would be improved by the inclusion of new input data, e.g. field measurements from actual projects and additional experimental and numerical results.

Conclusions

9

Assessing the potential damage caused by soil subsidence to surface structures is essential for the successful realization of underground projects in urban areas, and remains a challenge, due to the high complexity of the interacting elements. This is especially true for masonry structures, which represent the majority of historical buildings. The damage assessment procedures need to take into account not only the uncertainties about material parameters and state of the constructions, but also their highly non-linear behaviour, characterized by brittle cracking and consequent stress redistribution, and the important effect of soil-structure interaction.

The aim of this thesis was **the development and the validation of an improved modelling approach for the assessment of settlement-induced damage to masonry buildings**. The adopted methodology included experimental testing, real-case numerical modelling, sensitivity studies and the formulation of a structural damage function based on the analysis results. This chapter addresses the main findings, their implications in terms of scientific achievements, the limitations and the possible future research directions.

9.1 Returning to the research questions

In Section 1.2 the principal aim has been decomposed into five sub-questions:

- *What are the most effective indicators to assess the settlement-induced damage?*

In order to set a relation between the differential settlements acting on a building, and the consequent risk of structural damage, the most significant indic-

ators of both the settlement and the damage need to be defined. The damage classification system commonly used in practice relates the settlement-induced building deformations, described as deflection ratio or angular distortion, with the expected number of main cracks and maximum crack width. To integrate the proposed approach with the existing procedure, also the experimental and numerical outcomes of this thesis have been expressed in terms of applied deflection ratio versus resulting maximum crack width, which was successively related to the corresponding level of damage.

- *What are the most suitable numerical approaches to simulate the problem?*

To include the effect of the non-linear behaviour of the building and soil-structure interaction, 2D and 3D modelling approaches have been proposed and validated through comparison with experimental and field data. In both cases, elastic-softening crack models have been assumed to simulate the structural damage. In the 2D semi-coupled model, the assumed soil deformations have been applied to a non-linear interface at the building base, accounting for the soil and foundation stiffness. This approach entails a major reduction of the modelling effort, while it can still address two crucial phenomena: masonry cracking and soil-structure interaction. The 3D coupled model of structure, soil and tunnel has been developed to evaluate the effect on the final damage of the 3D progressive settlement profile and the torsional building response. The coupled model also allows to simulate the reciprocal influence between the surface building and the settlement profile, e.g. the building with its stiffness significantly flattens the settlement profile. The relevance of 3D modelling has been indisputably demonstrated.

- *How to design and perform a laboratory benchmark test to validate the proposed model?*

For the validation of the 2D semi-coupled model, an experimental test has been designed, built and executed on a 1/10th scaled model of a masonry façade. A pre-defined settlement profile was incrementally applied to the façade base, through a rubber interface with calibrated normal stiffness. The façade was subjected to amplified vertical loads to replicate the prototype stress field. Deformations and crack pattern development were accurately monitored throughout the test execution and a series of companion tests were performed on the materials in order to measure their mechanical properties. The comparison between numerical and experimental results has proven the model capability to reproduce, with a high level of accuracy, the crack pattern and the deformation of the tested structure.

- *How can the numerical model evaluate the factors governing the structural response to settlements?*

First, the reliability of the finite element models has been verified by reproducing the laboratory test results (façade test for the 2D semi-coupled model) and the monitoring data of a historic building affected by tunnel excavation (London Mansion House for the 3D coupled model). Then, the models have been used to broaden the investigation to a wider range of possible scenarios. The factors governing the structural response have been evaluated through a series of parametric analyses. In particular, the 2D model has been used to derive information about the effect of openings, material properties, initial damage, initial loading conditions, normal and shear behaviour of the soil-structure interaction and type of settlement profile. The potential of the 3D model has been exploited to include the evaluation of aspect ratio of horizontal building dimensions, connection with adjacent structures, and position and alignment of the building with respect to the excavation. The quantitative assessment in terms of expected damage has shown the substantial effect of soil-structure interaction, brittle masonry cracking and global flexibility of the building with respect to the dominant ground deformations.

- *How to derive an improved classification system from the analysis results?*

The outcomes of the 2D and 3D sensitivity studies have been used to derive an overall damage model which accounts for the building vulnerability as a function of the analysed parameters. The model is based on the principles of the seismic vulnerability assessment. The sensitivity of the structure to be damaged by a given settlement scenario is formulated as the sum of the parametric contributions; each parameter is normalized and multiplied for its relative weight on the final damage. For the analysed ranges of values, the damage level can vary by up to three levels, e.g. from slight to very severe damage. The proposed damage model sets the framework of a damage classification system based on numerical modelling. The system, built on the results derived in this research, is open to the inclusion of new parameters, further monitoring data or extra numerical results from different modelling approaches.

9.2 Scientific contributions

The research contributions offered by this thesis can be summarized as follows:

- *Experimental modelling*: The laboratory test designed to validate the 2D semi-coupled model represents a new benchmark test for the evaluation of masonry deformations and cracking as a consequence of differential settlements. Furthermore, the test provides new experimental data, also for those ranges of large deformation and severe damage where empirical data were lacking.
- *Numerical modelling*: The proposed 2D and 3D finite element models offers a validated tool for the simulation of settlement-induced damage to masonry buildings. As a major advantage, they account for the non-linear behaviour of masonry and soil-structure interaction, which was proven to be essential for the structural response and thus for the damage assessment.
- *Vulnerability assessment*: The damage model interpreting and summarizing the numerical results from the sensitivity study has the potential to be used as an improved procedure for the damage assessment of buildings subjected to soil subsidence. Being based on the same damage definition and indicators from the available empirical-analytical procedures, the proposed model can be integrated with the existent assessment methods.

These research contributions have the following implications:

- *Implications for scientists*: The experimental test, giving accurate measurements of the crack growth in a masonry structure as a function of the applied deformation, can be used to validate new modelling approaches or innovative constitutive laws for quasi-brittle materials.
- *Implications for designers*: The indications, resulting from the numerical analyses, about the main factors governing the building response to excavations, can complement the design criteria for the preliminary assessment currently in use. Decisions on when to step to 2D or 3D modelling can be made on a more solid basis. Furthermore, the developed 2D and 3D finite element models can be used in the further level of assessment.
- *Implications for decision makers*: The framework of the settlement vulnerability system based on numerical results has the potential to be developed as a decision and management tool for the evaluation of the risk associated with underground excavations in urban areas.

9.3 Future research

With reference to the main research contributions, the following subjects are of interest for future investigation:

- *Experimental modelling*: The proposed benchmark test could be supplemented with tests on different scales, geometries, construction material parameters and types of settlement profile. The study of 2D masonry façades could be extended to the simulation of 3D buildings subjected to different settlement profiles in the two main horizontal directions. Furthermore, in order to reproduce in the scaled models the same stress field of the prototype, the use of a geotechnical centrifuge could substitute the application of amplified vertical loads.
- *Field monitoring*: The 2D semi-coupled model has been used to prove the relation between the soil-structure interaction behaviour and the building damage. However, very little information about the normal and shear stiffness of the soil-foundation system is available in literature. Further investigations and field measurements should be conducted to allow the definition of realistic values for the constitutive law of the base interface. Systematic campaigns of material testing should also be performed on masonry samples from existing buildings. Given the high dependency of the damage on the cracking parameters, the availability of local databases of historic construction materials would increase the accuracy of damage predictions.
- *Numerical modelling*: This research focused on a certain number of geometrical, structural and material parameters which were expected to have significant impact on the building response. Also, a limited number of constitutive laws for the modelling of masonry were tested, and simplified assumptions were made on the geotechnical aspects of the problem, e.g. linear model of soil, omission of physical processes related to drained and undrained loading, consolidation and ground water conditions.

Numerical analyses could be extended to different building geometries and structural typologies, e.g. concrete frames, and to the evaluation of the connections between the façade and the transverse walls, and the presence of relatively stiffer horizontal diaphragms. Improved discrete and continuum cracking models, e.g. the sequentially linear analysis, could be applied to the building material in the 3D coupled approach, in order to refine the numerical prediction in terms of crack width. Furthermore, the 3D modelling approach could be generalized to the simulation of deep excavations and other sources of settlements, and include more advanced constitutive laws for the soil.

- *Vulnerability assessment:* The presented damage model sketches the framework of an improved damage classification system which accounts for the relative influence of the numerically modelled parameters. The proposed damage function aims to make the relative weight of each parameter explicit; its relatively simple formulation might be improved to better fit the numerical data, by modifying the relation between the assumed coefficients and the analysed parameters. The global formulation might be also refined by taking into account all possible interactions between the parameters. Results from alternative modelling approaches or experimental and field measurements might be added to the numerical results used as input to improve the damage function.

Bibliography

- J. Alfaiate, A. Gago, and J.R. Almeida. On the numerical analysis of localized damage in masonry structures. In *Proceedings of the 2nd International Conference on Structural and Construction Engineering, System-based Vision for Strategic and Creative Design*, pages 769–774, Rome, Italy, 2003.
- ATC. ATC-13 Earthquake damage evaluation data for California. Applied Technology Council, Federal Emergency Management Agency, 1985.
- P.B. Attewell and J.P. Woodman. Predicting the dynamics of ground settlement and its derivatives caused by tunnelling in soil. *Ground Engineering*, 15(7):13–22, 1982.
- C.E. Augarde. *Numerical modelling of tunnelling processes for assessment of damage to buildings*. PhD thesis, University of Oxford, 1997.
- T. Belytschko, W.K. Liu, and B. Moran. *Nonlinear finite elements for continua and structures*. Wiley, Chichester, 2000.
- D. Benedetti and V. Petrini. On the seismic vulnerability of masonry buildings: proposal of an evaluation procedure. *L'Industria Italiana delle Costruzioni*, 149: 66–78, 1984. (In Italian).
- A. Bernardini, R. Gori, and C. Modena. An application of coupled analytical models and experimental knowledge for seismic vulnerability analyses of masonry buildings. *Engineering Aspects of Earthquake Phenomena*, 3:161–180, 1990.

Bibliography

- L. Bjerrum. Allowable settlement of structures. In *Proceedings of the 3rd European Conference on Soil Mechanics and Foundation Engineering*, pages 135–137, Wiesbaden, 1963.
- A.G. Bloodworth. *Three-dimensional analysis of tunnelling effects on structures to develop design methods*. PhD thesis, University of Oxford, 2002.
- S. Boldrini. Damage assessment of buildings including explicit soil-structure interaction. Master's thesis, Sapienza University of Rome, 2011.
- M. Boonpichetvong, H. Netzel, and J.G. Rots. Numerical analyses of soil-foundation-building interaction due to tunnelling. In E.A. Kwast, K.J. Bakker, W. Broere, and A. Bezuijen, editors, *Proceedings of the 5th International Conference on Geotechnical Aspects of Underground Construction in Soft Ground*. Taylor and Francis, 2006.
- M.D. Boscardin and E.J. Cording. Building response to excavation-induced settlement. *Journal of Geotechnical Engineering*, 115(1):1–21, 1989.
- F. Braga, M. Dolce, and D. Liberatore. A statistical study on damaged buildings and ensuing review of the MSK-76 scale. In *Proceedings of the 7th European Conference on Earthquake Engineering*, Athens, 1982.
- A. Brencich, L. Gambarotta, and S. Lagomarsino. A macroelement approach to the three-dimensional seismic analysis of masonry buildings. In *Proceedings of the 11th European Conference on Earthquake Engineering*, Paris, 1998.
- T. Brettmann and J.M. Duncan. Computer application of CLM lateral load analysis to piles and drilled shafts. *Journal of Geotechnical Engineering*, 122(6):496–498, 1996.
- BSSC. FEMA 178, NEHRP handbook for the seismic evaluation of existing buildings. Building Seismic Safety Council for the Federal Emergency Management Agency, 1992.
- E. Buckingham. On physically similar systems; illustrations of the use of dimensional equations. *The Physical Review*, 4:345–376, 1914.
- H.J. Burd, G.T. Houlsby, C.E. Augarde, and G. Liu. Modelling tunnel-induced settlement of masonry buildings. In *ICE Proceedings: Geotechnical Engineering*, volume 143, pages 17–29, 2000.

-
- J.B. Burland, J.R. Standing, and F.M. Jardine. *Building response to tunnelling: case studies from construction of the Jubilee Line Extension, London*. CIRIA Special Publication Series. Thomas Telford, London, 2001.
- J.B. Burland, R.J. Mair, and R.N. Standing. Ground performance and building response due to tunnelling. In R.J. Jardine, D.M. Potts, and K.G. Higgins, editors, *Conference on Advances in Geotechnical Engineering*, volume 1, pages 291–342. Institution of Civil Engineers, 2004.
- J.P. Burland and C.P. Wroth. Settlement of buildings and associated damage. In *Proceedings of Conference on Settlement of Structures*, pages 611–654, Cambridge, 1974. Pentech Press.
- C. Calderini and S. Lagomarsino. Continuum model for in-plane anisotropic inelastic behavior of masonry. *Journal of Structural Engineering*, 134(2):209–220, 2008.
- G.M. Calvi, R. Pinho, G. Magenes, J.J. Bommer, L.F. Restrepo-Vélez, and H. Crowley. Development of seismic vulnerability assessment methodologies over the past 30 years. *ISET Journal of Earthquake Technology*, 43(3):75–104, 2006.
- M.S. Caspe. Surface settlement adjacent to braced open cuts. *Journal of the Soil Mechanics and Foundations Division*, 92(4):51–59, 1966.
- CEN. EN 1015-11 Methods of test for mortar for masonry - Part 11: determination of flexural and compressive strength of hardened mortar, 2007a.
- CEN. EN 1997-1 Eurocode 7: Geotechnical design - Part 1: General rules, 2007b.
- CNR-GNDT. *Rischio sismico di edifici pubblici. Parte I: aspetti metodologici*. Consiglio Nazionale delle Ricerche, Gruppo Nazionale per la Difesa Dai Terremoti, 1993. (In Italian).
- M.A. Crisfield and J. Wills. Solution strategies and softening materials. *Computer Methods in Applied Mechanics and Engineering*, 66(3):267–289, 1988.
- CUR. C162E Building on soft soil. Dutch Centre for Civil Engineering Research and Codes, 1996.
- CUR. C166 Damwandconstructies. Dutch Centre for Civil Engineering Research and Codes, 2008. (In Dutch).
- CUR-COB. L500 Toetsingsrichtlijn voor het ontwerp van boortunnels voor weg- en railinfrastructuur. Dutch Centre for Civil Engineering Research and Codes and Centre for Underground Construction, 2000. (In Dutch).

Bibliography

- R. de Borst. Computation of post-bifurcation and post-failure behavior of strain-softening solids. *Computers and Structures*, 25(2):211–224, 1987.
- I.A.E. de Vent. *Structural damage in masonry: developing diagnostic decision support*. PhD thesis, Delft University of Technology, 2011.
- M.J. DeJong, M.A.N. Hendriks, and J.G. Rots. Sequentially linear analysis of fracture under non-proportional loading. *Engineering Fracture Mechanics*, 75(18): 5042–5056, 2008.
- M.J. DeJong, B. Belletti, M.A.N. Hendriks, and J.G. Rots. Shell elements for sequentially linear analysis: lateral failure of masonry structures. *Engineering Structures*, 31(7):1382–1392, 2009.
- J. Duncan, L. Evans, and P. Ooi. Lateral load analysis of single piles and drilled shafts. *Journal of Geotechnical Engineering*, 120(6):1018–1033, 1994.
- H.K. Engin, R.B.J. Brinkgreve, Bonnier P.G., and E.G. Septanika. Modelling piled foundation by means of embedded piles. In *Geotechnics of soft soils: focus on ground improvement. Proceedings of the 2nd International Workshop on Geotechnics of Soft Soils*, pages 131–136, Glasgow, 2009. Taylor and Francis.
- R.P. Farrell. *Tunnelling in sands and the response of buildings*. PhD thesis, University of Cambridge, 2010.
- FEMA. HAZUS 99 Earthquake Loss Estimation Methodology, Technical Manual. Federal Emergency Management Agency, 1999.
- J.N. Franzius. *Behaviour of buildings due to tunnel induced subsidence*. PhD thesis, Imperial College, London, 2003.
- J.N. Franzius, D.M. Potts, and J.B. Burland. Twist behaviour of buildings due to tunnel induced ground movement. In E.A. Kwast, K.J. Bakker, W. Broere, and A. Bezuijen, editors, *Proceedings of the 5th International Conference on Geotechnical Aspects of Underground Construction in Soft Ground*, pages 107–113, Amsterdam, 2006. Taylor and Francis.
- W.W. Frischmann, J.E. Hellings, and C. Snowden. Protection of the Mansion House against damage caused by ground movements due to the Docklands Light Railway Extension. In *Proceedings of the Institution of Civil Engineers Geotechnical Engineering*, volume 107, pages 65–76, 1994.

-
- L. Gambarotta and S. Lagomarsino. Damage models for the seismic response of brick masonry shear walls. Part II: the continuum model and its applications. *Earthquake Engineering and Structural Dynamics*, 26(4):441–462, 1997a.
- L. Gambarotta and S. Lagomarsino. Damage models for the seismic response of brick masonry shear walls. Part I: the mortar joint model and its applications. *Earthquake Engineering and Structural Dynamics*, 26(4):423–439, 1997b.
- G. Giardina, A. Marini, M.A.N. Hendriks, J.G. Rots, F. Rizzardini, and E. Giuriani. Experimental analysis of a masonry façade subject to tunnelling-induced settlement. *Engineering Structures*, 45:421–434, 2012.
- S. Giovinazzi and S. Lagomarsino. A macroseismic method for the vulnerability assessment of buildings. In *Proceedings of the 13th World Conference on Earthquake Engineering*, Vancouver, 2004.
- E. Giuriani, A. Marini, P. Riva, S. Sala, and L. Sandrini. Facciate in muratura su archi soggette a cedimenti in fondazione. Technical Report 10, University of Brescia, 2007. (In Italian).
- R. Graça e Costa, J. Alfaiate, D. Dias-da Costa, and L.J. Sluys. A non-iterative approach for the modelling of quasi-brittle materials. In *International Conference on Computational Modeling of Fracture and Failure of Materials and Structures*, Barcelona, 2011.
- G. Grünthal. *EMS-98, European Macroseismic Scale*. European Seismological Commission, Subcommittee on Engineering Seismology, Working Group Macroseismic scales, 1998.
- V. Guglielmetti, P. Grasso, A. Mahtab, and S. Xu, editors. *Mechanized tunnelling in urban areas: design methodology and construction control*. Taylor and Francis, 2008.
- M.A. Gutiérrez. Energy release control for numerical simulations of failure in quasi-brittle solids. *Communications in Numerical Methods in Engineering*, 20(1):19–29, 2004.
- A.F. Hassan and M.A. Sozen. Seismic vulnerability assessment of low-rise buildings in regions with infrequent earthquakes. *ACI Structures Journal*, 94(1):31–39, January 1997.
- M.A.N. Hendriks and J.G. Rots. Sequentially linear versus nonlinear analysis of RC structures. *Engineering Computations*, 30, 2013. (Accepted for publication).

Bibliography

- G.T. Houslyby, H.J. Burd, and C.E. Augarde. Analysis of tunnel-induced settlement damage to surface structures. In *Proceedings of the 12th European Conference on Soil Mechanics and Geotechnical Engineering*, pages 147–152, Amsterdam, 1999.
- IGWR. Richtlijn voor het onderzoeken en beoordelen van bestaande funderingen op houten palen of staal. Ingenieursbureau Gemeentewerken Rotterdam, 2009.
- JBDPA. Standard for seismic capacity assessment of existing reinforced concrete buildings. Japanese Building Disaster Prevention Association, Ministry of Construction, Tokyo, 1990.
- M. Jirásek. Comparative study on finite elements with embedded cracks. *Computer Methods in Applied Mechanics and Engineering*, 188:307–330, 2000.
- C.H. Juang, M. Schuster, C. Ou, and K.K. Phoon. Fully probabilistic framework for evaluating excavation-induced damage potential of adjacent buildings. *Journal of Geotechnical and Geoenvironmental Engineering*, 137(2):130–139, 2011.
- J. Kappen. Three-dimensional numerical analysis of tunnelling induced damage: the influence of masonry building geometry and location. Master's thesis, Delft University of Technology, 2012.
- A.J. Kappos, K.C. Stylianidis, and K. Pitilakis. Development of seismic risk scenarios based on a hybrid method of vulnerability assessment. *Natural Hazards*, 17: 177–192, 1998.
- M. Korff and R.P. Roggeveld. Aanbevelingen voor het ontwerp van bouwkuipen in stedelijke omgeving. Technical Report F530-ER-12-49785, Centre for Underground Construction, 2012. (In Dutch).
- D.F. Laefer, L.T. Hong, A. Erkal, J.H. Long, and E.J. Cording. Manufacturing, assembly, and testing of scaled, historic masonry for one-gravity, pseudo-static, soil-structure experiments. *Construction and Building Materials*, 25(12):4362–4373, 2011.
- S.J. Lee, T.W. Song, Y.S. Lee, Y.H. Song, and J.K. Kim. A case study of damage risk assessment due to the multi-propped deep excavation in deep soft soil. In D. Chan and K.T. Law, editors, *Proceedings of the 4th International Conference on Soft Soil Engineering*, Vancouver, 2007. Taylor and Francis.
- D.J. Lekkerkerker. Sequentially linear analysis of pre-stressed concrete beams. Master's thesis, Delft University of Technology, 2011.

-
- G. Liu. *Numerical modelling of settlement damage to masonry structures caused by tunnelling*. PhD thesis, University of Oxford, 1997.
- F. Lorenzoni. Settlement induced damage modeling of historical buildings: two case studies: Amsterdam and Venice. Master's thesis, University of Padova, 2009.
- P.B. Lourenço. *Computational strategies for masonry structures*. PhD thesis, Delft University of Technology, 1996.
- P.B. Lourenço and J.G. Rots. Multisurface interface model for analysis of masonry structures. *Journal of Engineering Mechanics*, 123(7):660–668, 1997.
- G. Magenes and A. Della Fontana. Simplified non-linear seismic analysis of masonry buildings. *Proceedings of the British Masonry Society*, 8:190–195, 1998.
- R.J. Mair, R.N. Taylor, and A. Bracegirdle. Subsurface settlement profiles above tunnels in clay. *Géotechnique*, 43(43):315–320, 1993.
- R.J. Mair, R.N. Taylor, and J.B. Burland. Prediction of ground movements and assessment of risk of building damage due to bored tunnelling. In R.J. Mair and R.N. Taylor, editors, *Geotechnical Aspects of Underground Construction in Soft Ground. Proceedings of the International Symposium*, pages 713–718, Rotterdam, 1996. Balkema.
- A. Marini, P. Riva, and E. Giuriani. Comportamento sperimentale di una facciata in muratura su archi nell'ipotesi di cedimento differenziale di un pilastro. In *Atti del Convegno Nazionale Sperimentazione su Materiali e Strutture*, Venice, 2006. (In Italian).
- T.J. Massart, R.H.J. Peerlings, and M.G.D. Geers. Mesoscopic modeling of failure and damage-induced anisotropy in brick masonry. *European Journal of Mechanics - A/Solids*, 23(5):719–735, 2004.
- S. Mastrodicasa. *Dissesti statici delle strutture edilizie, diagnosi e consolidamento*. Hoepli, 1993. (In Italian).
- S.V. Medvedev. Seismic intensity scale MSK-76. *Publications of the Institute of Geophysics, Polish Academy of Sciences*, A-6(117):95–102, 1977.
- G.G. Meyerhof. Some recent foundation research and its application to design. *Structural Engineer*, 31:151–167, 1953.

Bibliography

- G.G. Meyerhof. Limit states design in geotechnical engineering. *Structural Safety Journal*, 1:67–71, 1982.
- S.C. Möller. *Tunnel induced settlements and structural forces in linings*. PhD thesis, Stuttgart University, 2006.
- S.C. Möller and P.A. Vermeer. On numerical simulation of tunnel installation. *Tunnelling and Underground Space Technology*, 23(4):461–475, 2008.
- H.D. Netzel. *Building response due to ground movements*. PhD thesis, Delft University of Technology, 2009.
- H.D. Netzel and F.J. Kaalberg. Numerical damage risk assessment studies on adjacent buildings due to TBM-tunnelling in Amsterdam. In *Proceedings of the GeoEng2000 Conference*, Melbourne, 2000.
- NRC. Risk analysis and uncertainty in flood damage reduction studies. Committee on Risk-Based Analysis for Flood Damage Reduction, Water Science and Technology Board, National Research Council, 2000.
- M.P. O'Reilly and B.M. New. Settlement above tunnels in the United Kingdom – their magnitude and prediction. In *Tunnelling 82. Proceedings of the 3rd International Symposium*, pages 173–181, London, 1982. Institution of Mining and Metallurgy.
- R.B. Peck. Deep excavations and tunneling in soft ground. In *Proceedings of the 7th International Conference on Soil Mechanics and Foundation Engineering*, pages 225–290, Mexico City, 1969.
- J.A. Pickhaver, H.J. Burd, and G.T. Houlsby. An equivalent beam method to model masonry buildings in 3D finite element analysis. *Computers and Structures*, 88 (19-20):1049–1063, 2010.
- D.E. Polshin and R.A. Tokar. Maximum allowable non-uniform settlements of structures. In *Proceedings of the 7th International Conference on Soil Mechanics and Foundation Engineering*, volume 1, pages 402–405, London, 1957.
- D.M. Potts and T.I. Addenbrooke. A structure's influence on tunnelling-induced ground movements. *Proceedings of the Institution of Civil Engineers: Geotechnical Engineering*, 125(2):109–125, 1997.
- M.F. Randolph and C.P. Wroth. Analysis of deformation of vertically loaded piles. *Journal of the Geotechnical Engineering Division*, 104:1465–1488, 1978.

- W.J. Rankin. Ground movements resulting from urban tunnelling: prediction and effects. In *Engineering geology of underground movements. Proceedings of the 23rd Annual Conference of the Engineering Group of the Geological Society*, pages 79–92, London, 1988.
- RISK-UE. An advanced approach to earthquake risk scenarios with applications to different european towns. Research Project, European Commission, 2004.
- J.G. Rots. *Structural masonry: an experimental/numerical basis for practical design rules*. CUR Report Series. Balkema, 1997.
- J.G. Rots. Settlement damage predictions for masonry. In L.G.W. Verhoef and F.H. Wittman, editors, *Maintenance and restrengthening of materials and structures – Brick and brickwork. Proceedings of the International Workshop on Urban Heritage and Building Maintenance*, pages 47–62, Freiburg, 2000. Aedificatio.
- J.G. Rots. Sequentially linear continuum model for concrete fracture. In R. de Borst, J. Mazars, G. Pijnaudier-Cabot, and J.G.M. Mier, editors, *Fracture mechanics of concrete structures*, volume 2, pages 831–839, Rotterdam, 2001. Balkema.
- J.G. Rots. Comparative study of crack models. In M.A.N. Hendriks and J.G. Rots, editors, *Proceedings of the 3rd DIANA World Conference, Finite Elements in Civil Engineering Applications*, pages 17–28, Tokyo, 2002. Taylor and Francis.
- J.G. Rots, B. Belletti, and S. Invernizzi. Robust modeling of RC structures with an “event-by-event” strategy. *Engineering Fracture Mechanics*, 75(3–4):590–614, 2008.
- R.K. Rowe, K.Y. Lo, and G.J. Kack. A method of estimating surface settlement above tunnels constructed in soft ground. *Canadian Geotechnical Journal*, 20: 11–22, 1983.
- SBR. Leidraad voor het onderzoek naar de invloed van een grondwaterstands daling op de bebouwing. Stichting Bouwresearch Rotterdam, 1986. (In Dutch).
- SBR. Over het bepalen en bewaken van de kwaliteit van gebouwen. Stichting Bouwresearch Rotterdam, 1998. (In Dutch).
- E. Schultze and A. Horn. Setzungsberechnung. *Grundbautaschenbuch*, 1(5), 1990. (In German).
- A. Singhal and A.S. Kiremidjian. Method for probabilistic evaluation of seismic structural damage. *Journal of Structural Engineering*, 122(12):1459–1467, 1996.

Bibliography

- A.W. Skempton and D.H. MacDonald. The allowable settlements of buildings. *Institute of Civil Engineers*, 5:727–784, 1956.
- M. Son and E.J. Cording. Estimation of building damage due to excavation-induced ground movements. *Journal of Geotechnical and Geoenvironmental Engineering*, 131(2):162–177, 2005.
- M. Son and E.J. Cording. Evaluation of building stiffness for building response analysis to excavation-induced ground movements. *Journal of Geotechnical and Geoenvironmental Engineering*, 133(8):995–1002, 2007.
- SWD. Basisrapport Casco-funderingsonderzoeken Panden in de 19e-eeuwse gordel. Bureau P/A, Stedelijke Woningdienst Amsterdam (SWD), 1998.
- M.J. Tomlinson. *Foundation design and construction*. Pitman Advanced Publishing Program, 4th edition, 1980.
- R. van Abeelen. Modelling of building response to imposed settlements. Master's thesis, Delft University of Technology, 2009.
- A.F. van Tol. Interaction between existing and newly added piles. In L.G.W. Verhoef, editor, *Proceedings of the International Congress on Urban Heritage and Building Maintenance*, pages 103–113, Delft, 1999. Publikatieburo Bouwkunde.
- R.V. Whitman, J.W. Reed, and S.T. Hong. Earthquake damage probability matrices. In *Proceedings of the 5th World Conference on Earthquake Engineering*, volume 2, pages 2531–2540, Rome, 1973.
- A. Yakut. Preliminary seismic performance assessment procedure for existing RC buildings. *Engineering Structures*, 26(10):1447–1461, 2004.
- Y. Yang. Photogrammetric measurement on shear tests of old and new concrete beams. Technical Report No. 25.5-09-07, Faculty of Civil Engineering, Delft University of Technology, 2009.
- A. Zucchini and P.B. Lourenço. A coupled homogenisation damage model for masonry cracking. *Computers and Structures*, 82(11-12):917–929, 2004.

LTSM spreadsheet application



The guidelines described in Section 2.2 have been translated in an excel worksheet, which can be used as a simple and instant tool for the building potential damage assessment. This spreadsheet has been developed in the framework of the Netherlands Knowledge Centre for Underground Construction (COB), Commission F532 (Korff and Roggeveld, 2012).

A.1 User's manual

First, the greenfield displacements are calculated, basing on the user inputs. Three different situations are included: tunnelling-induced ground movements in the transverse and longitudinal direction with respect the tunnel axis, and ground movements due to deep excavation. For the tunnelling-induced ground movements in the transverse direction, the user can fill in the values of the tunnel diameter, the tunnel depth, the depth of the subsurface level where the settlement trough has to be calculated (zero in case of surface settlement trough), the maximum horizontal distance from the tunnel centreline of the considered settlement trough and the desired increment of the settlement trough horizontal coordinate (Figure A.1). If too big or too small values are selected for the last two inputs, a warning message suggests to reduce or increase them (Figure A.2). The settlement curve is calculated basing on the maximum settlement or on the volume loss ratio, depending on the user selection (Figure A.3). The user can also assign the K factor to be used for the calculation of the trough width parameter i_x . The vertical and horizontal displacement curves, automatically derived from the user data, are given as graphical output (Figure A.4). The same approach is adopted for the calculation of the vertical

Appendix A. LTSM spreadsheet application

Tunnel diameter	D =	9.65	m	
Tunnel depth	z ₀ =	19.50	m	
Depth of the subsurface settlement trough below the soil surface	z =	0.00	m	z = 0 in case of surface settlement trough
Max horizontal distance from the tunnel centreline of the considered settlement trough	x _{max} =	22.00	m	e.g. x _{max} = 100 m
Desired increment of the settlement trough horizontal coordinate	dx =	0.10	m	e.g. dx = 1 m

Figure A.1: User input data related to the tunnel, LTSM worksheet.

and horizontal displacements of the ground in the longitudinal direction with respect to the tunnel axis (Figure A.5 and Figure A.6) and for the ground movements due to deep excavation (Figure A.7 and Figure A.8).

In order to derived the settlement-induced deformations and strains of the equivalent beam, the user needs to define the geometry of the building, its distance from the tunnel centreline and its bending and shear stiffness (Figure A.9). In the worksheet, the 1 mm settlement line limitation for the influence area is automatically applied. In case of a long building, this assumption can be neglected by substituting the automatically calculated reduced length L' with the entire building length L . A simple graph of the equivalent beam and the related settlement profile is given as output (Figure A.10).

If the calculated tilt values of the separated hogging and sagging parts and the total structure differ more than 15%, a warning message suggests to reconsider the LTSM assumption of the structure splitting at the settlement curve inflection point (Figure A.11).

According to the LTSM procedure, the building strains are calculated and used to classify the potential building damage (Figure A.12 and Figure A.14). The user has the possibility to include indications about settlement rate and building conditions, which could increase or decrease the damage risk (Figure A.13).

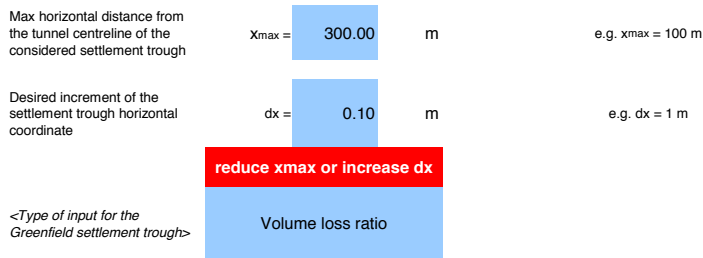


Figure A.2: Warning message related to the required ground displacements curve, LTSM worksheet.

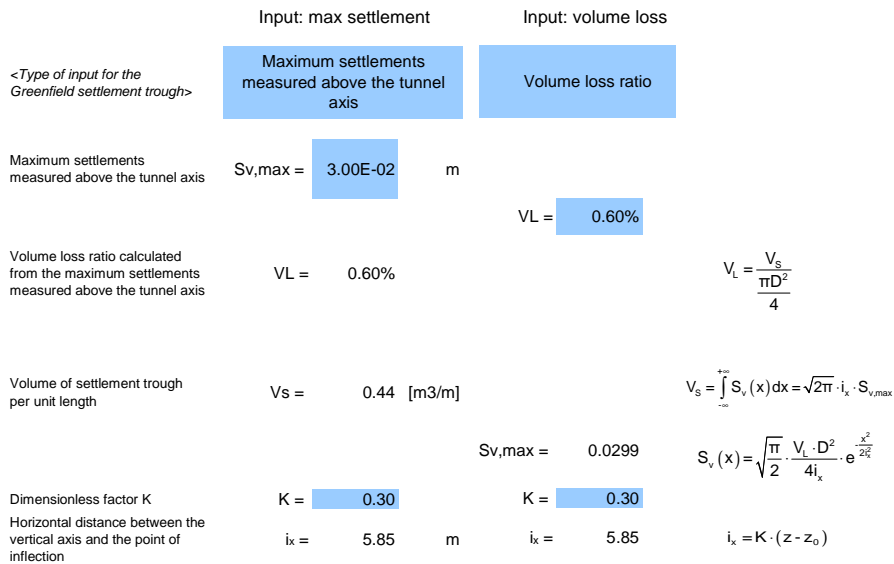


Figure A.3: User input data for tunnelling-induced settlement curve calculation, transverse direction, LTSM worksheet.

Appendix A. LTSM spreadsheet application

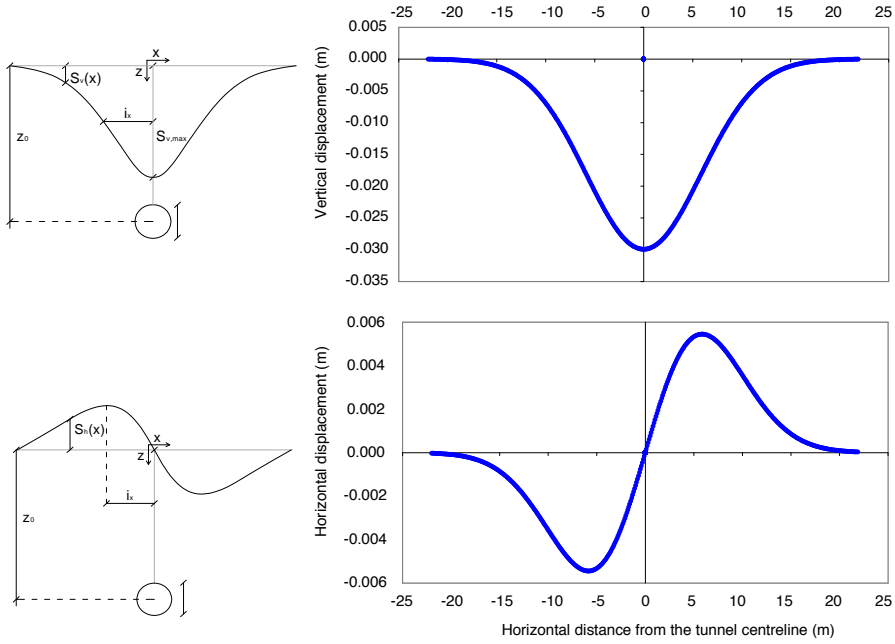


Figure A.4: Graphical output for tunnelling-induced ground displacement curves, transverse direction, LTSM worksheet.

Tunnel diameter	D =	9.65	m	
Tunnel depth	z ₀ =	19.50	m	
Depth of the subsurface settlement trough below the soil surface	z =	0.00	m	z = 0 in case of surface settlement trough
Max longitudinal distance from the tunnel face of the considered settlement trough	y _{max} =	22.00	m	e.g. x _{max} = 100 m
Desired increment of the settlement trough horizontal coordinate	dy =	0.10	m	e.g. dx = 1 m

<Type of input for the Greenfield settlement trough>

Maximum settlements measured above the tunnel axis

Maximum settlements measured above the tunnel axis	S _{v,max} =	3.00E-02	m
Horizontal distance of the considered settlement trough from the tunnel centreline	x =	10.00	m
	S _{v,max(x)} =	0.01	m

Volume loss ratio calculated from the maximum settlements measured above the tunnel axis	VL =	0.60%
--	------	-------

$$V_L = \frac{V_S}{\pi D^2} \cdot 4$$

Volume of settlement trough per unit length	V _s =	0.44 [m ³ /m]
---	------------------	--------------------------

$$V_S = \int_{-x_{max}}^{+x_{max}} S_v(x) dx = \sqrt{2\pi} \cdot i_x \cdot S_{v,max}$$

Dimensionless factor K	K =	0.30
Horizontal distance between the vertical axis and the point of inflection	i _x =	5.85 m

$$i_y = i_x$$

$$i_x = K \cdot (z - z_0)$$

Figure A.5: User input data for tunnelling-induced settlement curve calculation, longitudinal direction, LTSM worksheet.

Appendix A. LTSM spreadsheet application

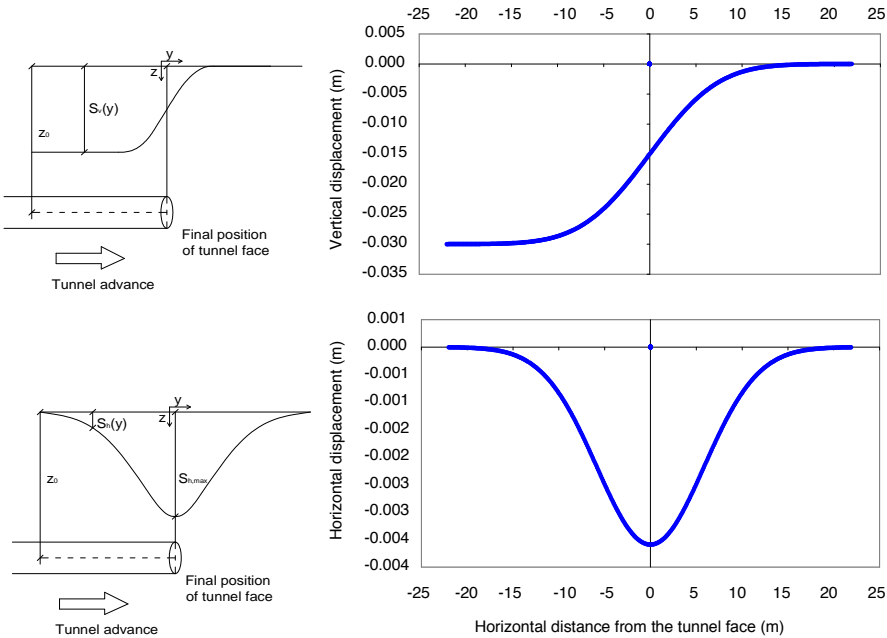


Figure A.6: Graphical output for tunnelling-induced ground displacement curves, transverse direction, LTSM worksheet.

Ratio of horizontal movement to settlement	$\beta =$	0.50		$\beta = 1$ for diaphragm walls $\beta = 0.5$ for sheet pile walls
Max horizontal distance from the wall of the considered settlement trough	$x_{\max} =$	50.00	m	e.g. $x_{\max} = 100$ m
Desired increment of the settlement trough horizontal coordinate	$dx =$	0.50	m	e.g. $dx = 1$ m
<Type of input for the Greenfield settlement trough>	Maximum settlements measured at the wall			
Maximum settlements measured at the wall	$S_{v,wall} =$	5.00E-02	m	$S_v(x) = S_{wall} \cdot e^{\left[0.5 \cdot 0.5 \left(1 + \frac{2x}{W}\right)^2\right]}$ $S_h(x) = -\beta \cdot \left(1 + \frac{2x}{W}\right) \cdot S_v(x)$
Excavation width	$B =$	3.00E+01	m	
<Type of soil>	$\phi > 0$			
	$\Phi =$		degree	
Excavation depth	$H =$	0.00E+00	m	
Influence depth below the excavation	$H_d =$	1.50E+01		
Settlement trough width	$W =$	1.50E+01		$W = (H + H_d) \cdot \tan\left(45 - \frac{\Phi}{2}\right)$
Dimensionless factor K	$K =$	0.50		
Horizontal distance between the vertical axis and the point of inflection	$i_x =$	5.00	m	$i_x = K \cdot (z - z_0)$

Figure A.7: User input data for deep excavation-induced settlement curve calculation, LTSM worksheet.

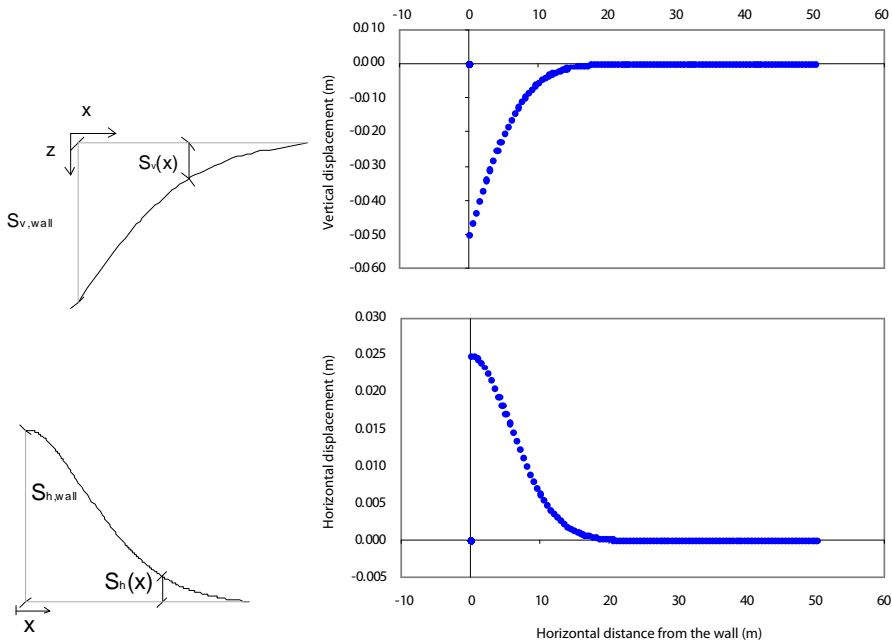


Figure A.8: Graphical output for deep excavation-induced ground displacement curves, transverse direction, LTSM worksheet.

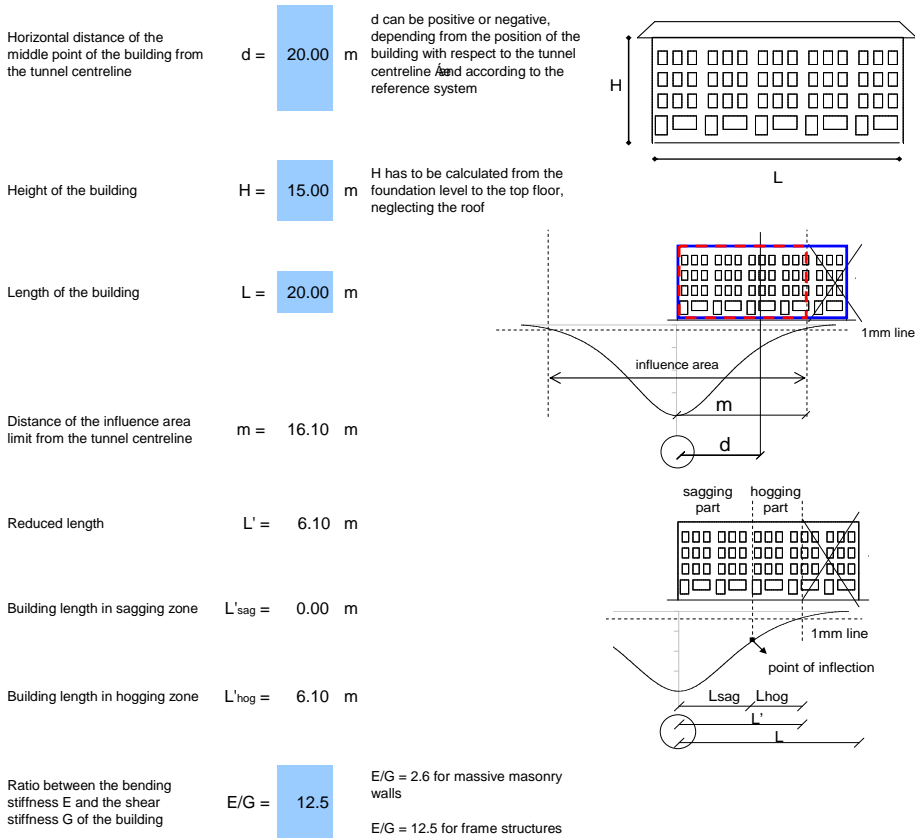


Figure A.9: User input data related to the structure and equivalent beam derivation, LTSM worksheet.

Appendix A. LTSM spreadsheet application

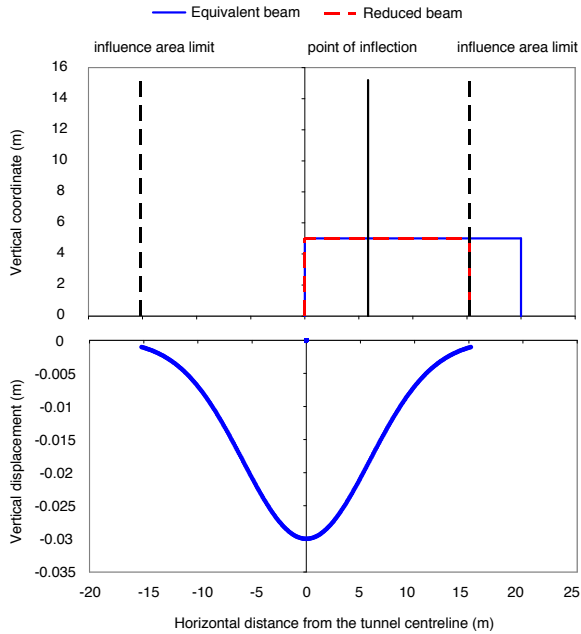


Figure A.10: Graphical output for the equivalent beam geometry and the related settlement profile, LTSM worksheet.

Sagging tilt	$\omega_{\text{sag}} = -0.0002$
Hogging tilt	$\omega_{\text{hog}} = -0.0019$
Total tilt	$\omega_{\text{tot}} = -0.0010$

Tilt verifications	Splitting the building in hogging and sagging zone is NOT ACCEPTABLE	It is suggested to perform an alternative assessment analysis, e.g. FEA
Sagging deflection ratio	$(\Delta/L)_{\text{sag}} = 0.0009$	
Hogging deflection ratio	$(\Delta/L)_{\text{hog}} = 0.0004$	

Figure A.11: Warning message related to the hogging and sagging tilt values, LTSM worksheet.

Maximum bending strain for sagging	$\epsilon_{b,max_sag} = 6.13E-04$	$\epsilon_{b,max} = \left(\frac{\Delta}{L}\right) \cdot \left[\frac{6 \cdot \left(\frac{L}{H}\right)}{\left(\frac{L}{H}\right)^2 + 1.2 \cdot \left(\frac{E}{G}\right)} \right]$
Maximum shear strain for sagging	$\epsilon_{d,max_sag} = 8.87E-04$	$\epsilon_{d,max} = \left(\frac{\Delta}{L}\right) \cdot \left[\frac{3 \cdot \left(\frac{E}{G}\right)}{2 \cdot \left(\frac{L}{H}\right)^2 + 2 \cdot 1.2 \cdot \left(\frac{E}{G}\right)} \right]$
Maximum bending strain for hogging	$\epsilon_{b,max_hog} = 1.53E-04$	$\epsilon_{b,max} = \left(\frac{\Delta}{L}\right) \cdot \left[\frac{3 \cdot \left(\frac{L}{H}\right)}{\frac{1}{4} \cdot \left(\frac{L}{H}\right)^2 + 1.2 \cdot \left(\frac{E}{G}\right)} \right]$
Maximum shear strain for hogging	$\epsilon_{d,max_hog} = 5.10E-04$	$\epsilon_{d,max} = \left(\frac{\Delta}{L}\right) \cdot \left[\frac{3 \cdot \left(\frac{E}{G}\right)}{\frac{1}{2} \cdot \left(\frac{L}{H}\right)^2 + 2 \cdot 1.2 \cdot \left(\frac{E}{G}\right)} \right]$
Horizontal tensile strain	$\epsilon_h = 3.04E-04$	$\epsilon_h = \frac{\delta L}{L}$
Maximum bending strain	$\epsilon_{b,max} = 6.13E-04$	
Maximum shear strain	$\epsilon_{d,max} = 8.87E-04$	
Total bending strain	$\epsilon_{bt} = 9.17E-04$	$\epsilon_{bt} = \epsilon_{b,max} + \epsilon_h$
Total shear strain	$\epsilon_{dt} = 1.05E-03$	$\epsilon_{dt} = \frac{\epsilon_h}{2} + \sqrt{\left(\frac{\epsilon_h}{2}\right)^2 + \epsilon_d^2}$
Total tensile strain	$\epsilon_t = 1.05E-03$	

Figure A.12: Building strain output, LTSM worksheet.

Settlement rate	Long term settlements
Building conditions	Poor building conditions

Figure A.13: Additional user input data, LTSM worksheet.

Appendix A. LTSM spreadsheet application

Category of damage	Damage class	Limiting tensile strain levels (min) (max)		Approximate crack width [mm]	Description of typical damage and ease of repair
Aesthetic damage	Negligible	0.000%	0.040%	up to 0,1mm	Hairline cracks of less than about 0,1mm width.
	Very slight	0.040%	0.060%	up to 1mm	Fine cracks which can easily be treated during normal decoration. Perhaps isolated slight fracturing in building. Cracks in external brickwork visible on close inspection.
	Slight	0.060%	0.120%	up to 5mm	Cracks easily filled. Redecoration probably required. Several slight fractures showing inside of building. Cracks are visible externally and some repainting may be required externally to ensure water tightness. Doors and windows may stick slightly.
Functional damage, affecting serviceability	Moderate	0.120%	0.240%	5 to 15mm or a number of cracks > 3 mm	The cracks require some opening up and can be patched by a mason. Recurrent cracks can be masked by suitable linings. Repainting of external brickwork and possibly a small amount of brickwork to be replaced. Doors and windows sticking. Service pipes may fracture. Weather-tightness often impaired.
	Severe	0.240%		15 to 25mm , but also depends on number of cracks	Extensive repair work involving breaking out and replacing sections of walls, especially over doors and windows. Windows and door frames distorted, floors sloping noticeably. Walls leaning or bulging noticeably, some loss of bearing in beams. Service pipes disrupted.
Structural damage affecting stability	Very severe			Usually >25mm, but depends on number of cracks	This requires a major repair involving partial or complete rebuilding. Beams loose bearing, walls lean badly and require shoring. Windows broken with distortion. Danger of instability.

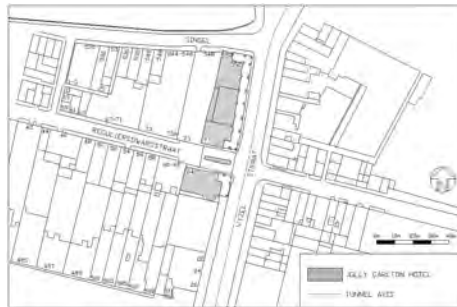
Figure A.14: Damage classification, LTSM worksheet.

A.2 Examples

The LTSM procedure as implemented in the spreadsheet has been applied to a building subjected to tunnelling. The Jolly Carlton Hotel in Amsterdam is a concrete frame building with a masonry facade (Figure A.15a). The damage assessment is performed on the transverse and longitudinal section with respect to the tunnel axis (Figure A.15b). In the next pictures (Figure A.16 - Figure A.25), the results related to the consecutive steps of the LTSM applied to the Jolly Carlton Hotel, for the transverse and longitudinal considered sections, are presented.



(a) Jolly Carlton Hotel, Amsterdam



(b) building location with respect to the tunnel

Figure A.15: Case study (Lorenzoni, 2009).

Appendix A. LTSM spreadsheet application

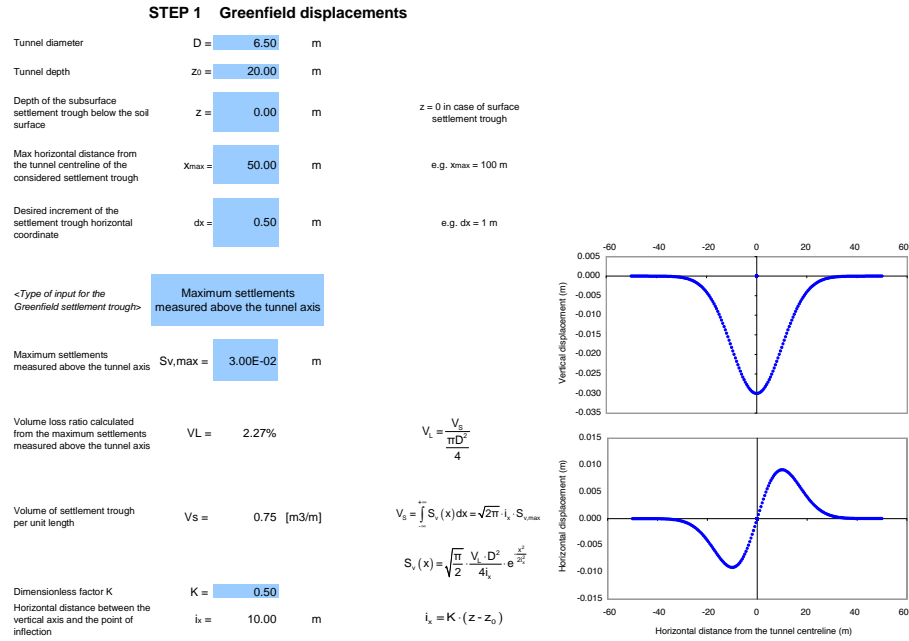


Figure A.16: User input data and graphical output related to tunnelling-induced ground displacement curves, transverse direction, Jolly Carlton Hotel case study.

STEP 2-3 Building deformations

Horizontal distance of the middle point of the building from the tunnel centreline	$d =$	19.00	m	d can be positive or negative, depending from the position of the building with respect to the tunnel centreline and according to the reference system
Height of the building	$H =$	30.00	m	H has to be calculated from the foundation level to the top floor, neglecting the roof
Length of the building	$L =$	18.00	m	
Distance of the influence area limit from the tunnel centreline	$m =$	26.00	m	
Reduced length	$L' =$	16.00	m	
Building length in sagging zone	$L'_{sag} =$	0.00	m	
Building length in hogging zone	$L'_{hog} =$	16.00	m	
Ratio between the bending stiffness E and the shear stiffness G of the building	$E/G =$	12.5		$E/G = 2.6$ for massive masonry walls $E/G = 12.5$ for frame structures
Sagging tilt	$\omega_{sag} =$	0.0000		
Hogging tilt	$\omega_{hog} =$	-0.0012		
Total tilt	$\omega_{tot} =$	-0.0012		
Tilt verifications	Splitting the building in hogging and sagging zone is acceptable			
Sagging deflection ratio	$(\Delta/L)_{sag} =$	0.0000		
Hogging deflection ratio	$(\Delta/L)_{hog} =$	0.0003		

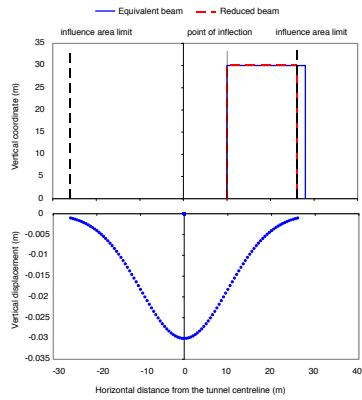


Figure A.17: User input data related to the building and equivalent beam geometry output, transverse direction, Jolly Carlton Hotel case study.

Appendix A. LTSM spreadsheet application

STEP 4 Building strains

Maximum bending strain for sagging	$\epsilon_{b,max_sag} = 0.00E+00$	$\epsilon_{b,max} = \left(\frac{\Delta}{L}\right) \left[\frac{6 \left(\frac{L}{H}\right)}{\left[\left(\frac{L}{H}\right)^2 + 1.2 \left(\frac{E}{G}\right)\right]} \right]$
Maximum shear strain for sagging	$\epsilon_{d,max_sag} = 0.00E+00$	$\epsilon_{d,max} = \left(\frac{\Delta}{L}\right) \left[\frac{3 \left(\frac{E}{G}\right)}{2 \left(\frac{L}{H}\right)^2 + 2 \cdot 1.2 \left(\frac{E}{G}\right)} \right]$
Maximum bending strain for hogging	$\epsilon_{b,max_hog} = 3.15E-05$	$\epsilon_{b,max} = \left(\frac{\Delta}{L}\right) \left[\frac{3 \left(\frac{L}{H}\right)}{\left[\frac{1}{4} \left(\frac{L}{H}\right)^2 + 1.2 \left(\frac{E}{G}\right)\right]} \right]$
Maximum shear strain for hogging	$\epsilon_{d,max_hog} = 3.69E-04$	$\epsilon_{d,max} = \left(\frac{\Delta}{L}\right) \left[\frac{3 \left(\frac{E}{G}\right)}{\left[\frac{1}{2} \left(\frac{L}{H}\right)^2 + 2 \cdot 1.2 \left(\frac{E}{G}\right)\right]} \right]$
Horizontal tensile strain	$\epsilon_h = 4.84E-04$	$\epsilon_h = \frac{\delta L}{L}$
Maximum bending strain	$\epsilon_{b,max} = 3.15E-05$	
Maximum shear strain	$\epsilon_{d,max} = 3.69E-04$	
Total bending strain	$\epsilon_{bt} = 5.15E-04$	$\epsilon_{bt} = \epsilon_{b,max} + \epsilon_h$
Total shear strain	$\epsilon_{dt} = 6.84E-04$	$\epsilon_{dt} = \frac{\epsilon_{d,max}}{2} + \sqrt{\left(\frac{\epsilon_{d,max}}{2}\right)^2 + \epsilon_h^2}$
Total tensile strain	$\epsilon_t = 6.84E-04$	

Figure A.18: Building strain output, transverse direction, Jolly Carlton Hotel case study.

Settlement rate	Short term settlements
Building conditions	Good building conditions

Figure A.19: Additional user input data, Jolly Carlton Hotel case study.

STEP 5-6 Damage level

Category of damage	Damage class	Limiting tensile strain levels (min) (max)		Approximate crack width [mm]	Description of typical damage and ease of repair
Aesthetic damage	Negligible	0.000%	0.050%	up to 0,1mm	Hairline cracks of less than about 0,1mm width.
	Very slight	0.050%	0.075%	up to 1mm	Fine cracks which can easily be treated during normal decoration. Perhaps isolated slight fracturing in building. Cracks in external brickwork visible on close inspection.
	Slight	0.075%	0.150%	up to 5mm	Cracks easily filled. Redecoration probably required. Several slight fractures showing inside of building. Cracks are visible externally and some repainting may be required externally to ensure water tightness. Doors and windows may stick slightly.
Functional damage, affecting serviceability	Moderate	0.150%	0.300%	5 to 15mm or a number of cracks > 3 mm	The cracks require some opening up and can be patched by a mason. Recurrent cracks can be masked by suitable linings. Repainting of external brickwork and possibly a small amount of brickwork to be replaced. Doors and windows sticking. Service pipes may fracture. Weather-tightness often impaired.
	Severe	0.300%		15 to 25mm , but also depends on number of cracks	Extensive repair work involving breaking out and replacing sections of walls, especially over doors and windows. Windows and door frames distorted, floors sloping noticeably. Walls leaning or bulging noticeably, some loss of bearing in beams. Service pipes disrupted.
Structural damage affecting stability	Very severe			Usually >25mm, but depends on number of cracks	This requires a major repair involving partial or complete rebuilding. Beams loose bearing, walls lean badly and require shoring. Windows broken with distortion. Danger of instability.

Figure A.20: Damage classification, transverse direction, Jolly Carlton Hotel case study.

Appendix A. LTSM spreadsheet application

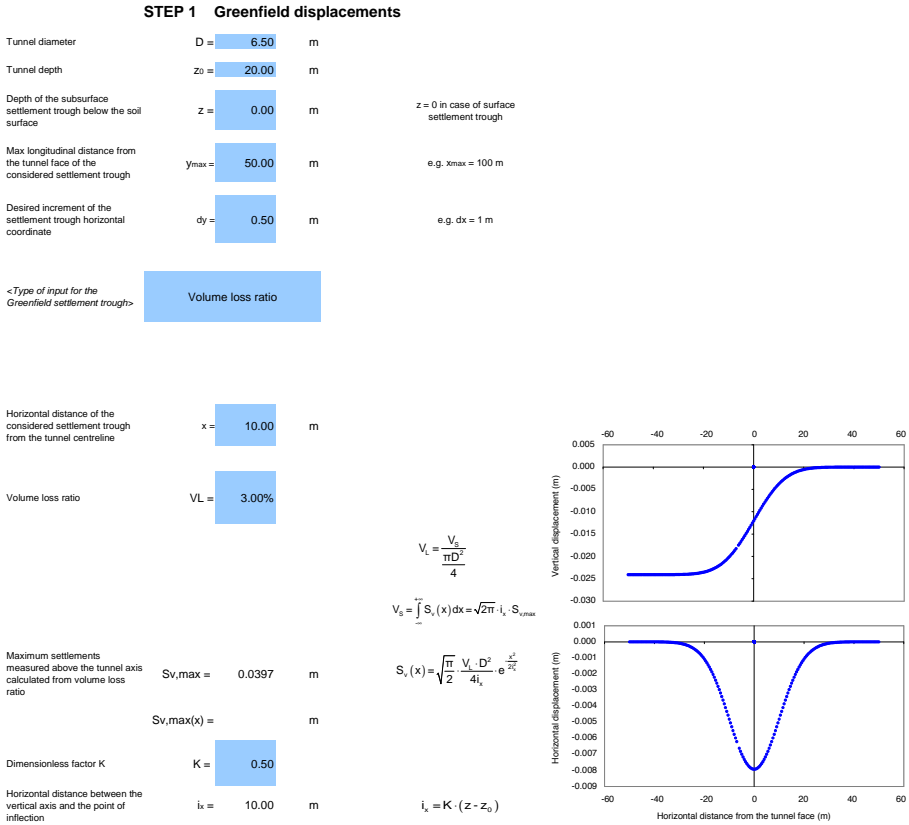


Figure A.21: User input data and graphical output related to tunnelling-induced ground displacement curves, longitudinal direction, Jolly Carlton Hotel case study.

STEP 2-3 Building deformations

Horizontal distance of the middle point of the building from the tunnel face	$d =$	1.00	m	<small>d can be positive or negative, depending from the position of the building with respect to the tunnel face and according to the reference system in Fig.1</small>
Height of the building	$H =$	30.00	m	<small>H has to be calculated from the foundation level to the top floor, neglecting the roof</small>
Length of the building	$L =$	50.00	m	
Distance of the influence area limit from the tunnel centrelime	$m =$	17.00	m	
Reduced length	$L' =$	41.00	m	
Building length in sagging zone	$L'_{sag} =$	26.00	m	
Building length in hogging zone	$L'_{hog} =$	15.00	m	
Ratio between the bending stiffness E and the shear stiffness G of the building	$E/G =$	6		<small>E/G = 2.6 for massive masonry walls E/G = 12.5 for frame structures</small>
Sagging tilt	$\alpha_{sag} =$	0.0005		
Hogging tilt	$\alpha_{hog} =$	0.0006		
Total tilt	$\alpha_{tot} =$	0.0006		
Tilt verifications	Splitting the building in hogging and sagging zone is acceptable			
Sagging deflection ratio	$(\Delta/L)_{sag} =$	0.0004		
Hogging deflection ratio	$(\Delta/L)_{hog} =$	0.0001		

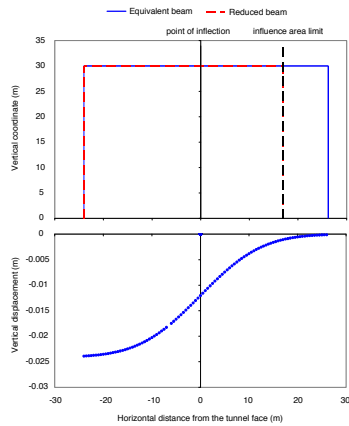


Figure A.22: User input data related to the building and equivalent beam geometry output, longitudinal direction, Jolly Carlton Hotel case study.

Appendix A. LTSM spreadsheet application

STEP 4 Building strains

Maximum bending strain for sagging	$\epsilon_{b,max_sag} = 2.82E-04$	$\epsilon_{b,max} = \left(\frac{\Delta}{L}\right) \cdot \left[\frac{6 \left(\frac{L}{H}\right)}{\left(\frac{L}{H}\right)^2 + 1.2 \left(\frac{E}{G}\right)} \right]$
Maximum shear strain for sagging	$\epsilon_{d,max_sag} = 4.87E-04$	$\epsilon_{d,max} = \left(\frac{\Delta}{L}\right) \cdot \left[\frac{3 \left(\frac{E}{G}\right)}{2 \left(\frac{L}{H}\right)^2 + 2.1.2 \left(\frac{E}{G}\right)} \right]$
Maximum bending strain for hogging	$\epsilon_{b,max_hog} = 2.05E-05$	$\epsilon_{b,max} = \left(\frac{\Delta}{L}\right) \cdot \left[\frac{3 \left(\frac{L}{H}\right)}{\frac{1}{4} \left(\frac{L}{H}\right)^2 + 1.2 \left(\frac{E}{G}\right)} \right]$
Maximum shear strain for hogging	$\epsilon_{d,max_hog} = 1.23E-04$	$\epsilon_{d,max} = \left(\frac{\Delta}{L}\right) \cdot \left[\frac{3 \left(\frac{E}{G}\right)}{\frac{1}{2} \left(\frac{L}{H}\right)^2 + 2.1.2 \left(\frac{E}{G}\right)} \right]$
Horizontal tensile strain	$\epsilon_h = 3.47E-05$	$\epsilon_h = \frac{\delta L}{L}$
Maximum bending strain	$\epsilon_{b,max} = 2.82E-04$	
Maximum shear strain	$\epsilon_{d,max} = 4.87E-04$	
Total bending strain	$\epsilon_{bt} = 3.16E-04$	$\epsilon_{bt} = \epsilon_{b,max} + \epsilon_h$
Total shear strain	$\epsilon_{dt} = 5.05E-04$	$\epsilon_{dt} = \frac{\epsilon_{b,max}}{2} + \sqrt{\left(\frac{\epsilon_{b,max}}{2}\right)^2 + \epsilon_d^2}$
Total tensile strain	$\epsilon_t = 5.05E-04$	

Figure A.23: Building strain output, longitudinal direction, Jolly Carlton Hotel case study.

Settlement rate	Short term settlements
Building conditions	Good building conditions

Figure A.24: Additional user input data, Jolly Carlton Hotel case study.

STEP 5-6 Damage level

Category of damage	Damage class	Limiting tensile strain levels (min) (max)		Approximate crack width [mm]	Description of typical damage and ease of repair
Aesthetic damage	Negligible	0.000%	0.050%	up to 0,1mm	Hairline cracks of less than about 0,1mm width.
	Very slight	0.050%	0.075%	up to 1mm	Fine cracks which can easily be treated during normal decoration. Perhaps isolated slight fracturing in building. Cracks in external brickwork visible on close inspection.
	Slight	0.075%	0.150%	up to 5mm	Cracks easily filled. Redecoration probably required. Several slight fractures showing inside of building. Cracks are visible externally and some repainting may be required externally to ensure water tightness. Doors and windows may stick slightly.
Functional damage, affecting serviceability	Moderate	0.150%	0.300%	5 to 15mm or a number of cracks > 3 mm	The cracks require some opening up and can be patched by a mason. Recurrent cracks can be masked by suitable linings. Repainting of external brickwork and possibly a small amount of brickwork to be replaced. Doors and windows sticking. Service pipes may fracture. Weather-tightness often impaired.
	Severe	0.300%		15 to 25mm , but also depends on number of cracks	Extensive repair work involving breaking out and replacing sections of walls, especially over doors and windows. Windows and door frames distorted, floors sloping noticeably. Walls leaning or bulging noticeably, some loss of bearing in beams. Service pipe disrupted.
Structural damage affecting stability	Very severe			Usually >25mm, but depends on number of cracks	This requires a major repair involving partial or complete rebuilding. Beams loose bearing, walls lean badly and require shoring. Windows broken with distortion. Danger of instability.

Figure A.25: Damage classification, longitudinal direction, Jolly Carlton Hotel case study.

Experimental analysis of a masonry façade: measured displacements



.1 .2 .3 .4 .5 .6 .7 .8 .9 .10 .11 .12 .13 .14 .15 .16 .17 .18 .19 .20 .21 .22 .23 .24 .25 .26 .27 .28
 .29 .30 .31 .32 .33 .34 .35 .36 .37 .38 .39 .40 .41 .42 .43 .44 .45 .46 .47 .48 .49 .50 .51 .52 .53 .54 .55 .56
 .57 .58 .59 .60 .61 .62 .63 .64 .65 .66 .67
 .68 .69 .70 .71 .72 .73 .74 .75 .76 .77 .78
 .79 .80 .81 .82 .83 .84 .85 .86 .87 .88 .89
 .90 .91 .92 .93 .94 .95 .96 .97 .98 .99 .100
 .101 .102 .103 .104 .105 .106 .107 .108 .109 .110 .111 .112 .113 .114 .115 .116 .117 .118 .119 .120 .121 .122 .123 .124 .125 .126 .127 .128
 .129 .130 .131 .132 .133 .134 .135 .136 .137 .138 .139 .140 .141 .142 .143 .144 .145 .146 .147 .148 .149 .150 .151 .152 .153 .154 .155 .156
 .157 .158 .159 .160 .161 .162 .163 .164 .165 .166 .167 .168 .169 .170 .171
 .172 .173 .174 .175 .176 .177 .178 .179 .180 .181 .182 .183 .184
 .185 .186 .187 .188 .189 .190 .191 .192 .193 .194 .195 .196 .197
 .198 .199 .200 .201 .202 .203 .204 .205 .206 .207 .208 .209 .210
 .211 .212 .213 .214 .215 .216 .217 .218 .219 .220 .221 .222 .223
 .224 .225 .226 .227 .228 .229 .230 .231 .232 .233 .234 .235 .236 .237 .238 .239 .240 .241 .242 .243 .244 .245 .246 .247 .248 .249 .250 .251
 .252 .253 .254 .255 .256 .257 .258 .259 .260 .261 .262 .263 .264 .265 .266 .267 .268 .269 .270 .271 .272 .273 .274 .275 .276 .277 .278 .279
 .280 .281 .282 .283 .284 .285 .286 .287 .288
 .289 .290 .291 .292 .293 .294 .295 .296 .297
 .298 .299 .300 .301 .302 .303 .304 .305 .306
 .307 .308 .309 .310 .311 .312 .313 .314 .315
 .316 .317 .318 .319 .320 .321 .322 .323 .324
 .325 .326 .327 .328 .329 .330 .331 .332 .333 .334 .335 .336 .337 .338 .339 .340 .341 .342 .343 .344 .345 .346 .347
 .348 .349 .350 .351 .352 .353 .354 .355 .356 .357 .358 .359 .360 .361 .362 .363 .364 .365 .366 .367 .368 .369 .370
 .371 .372 .373 .374 .375 .376 .377 .378 .379 .380 .381 .382 .383 .384 .385 .386 .387 .388 .389 .390 .391 .392 .393 .394 .395 .396 .397 .398
 .399 .400 .401 .402 .403 .404 .405 .406 .407 .408 .409 .410 .411 .412 .413 .414 .415 .416 .417 .418 .419 .420 .421 .422 .423 .424 .425 .426

Figure B.1: Numbering of the photogrammetric markers.

Marker	0 mm		Coordinate	X	Y
	dx (mm)	dy (mm)			
Marker	2.5 mm		Coordinate	X	Y
	dx (mm)	dy (mm)			
Marker	5 mm		Coordinate	X	Y
	dx (mm)	dy (mm)			
Marker	7.5 mm		Coordinate	X	Y
	dx (mm)	dy (mm)			
Marker	10 mm		Coordinate	X	Y
	dx (mm)	dy (mm)			

Appendix B. Experimental analysis of a masonry façade: measured displacements

The influence of the initial adjustment of the load application system was removed from the measurements. Initial coordinates were extrapolated from the coordinates at step 1 (0.5 mm of applied displacement) by using the relative displacement between step 1 and step 2 (1 mm of applied displacement).

Results of the 3D sensitivity study

C

Appendix C. Results of the 3D sensitivity study

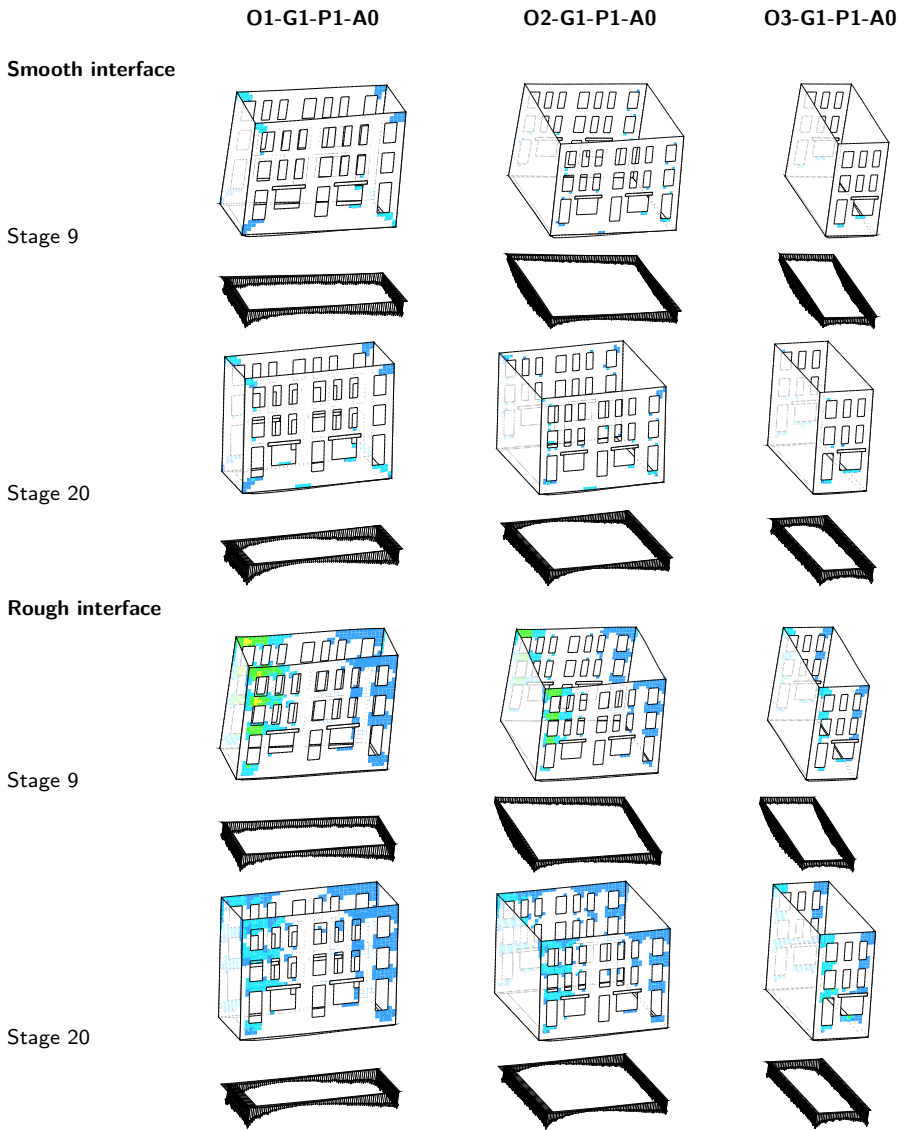


Figure C.1: Crack strain distribution, deformed configuration and soil-structure interface normal stresses: orientation variation for the case G1-P1-A0.

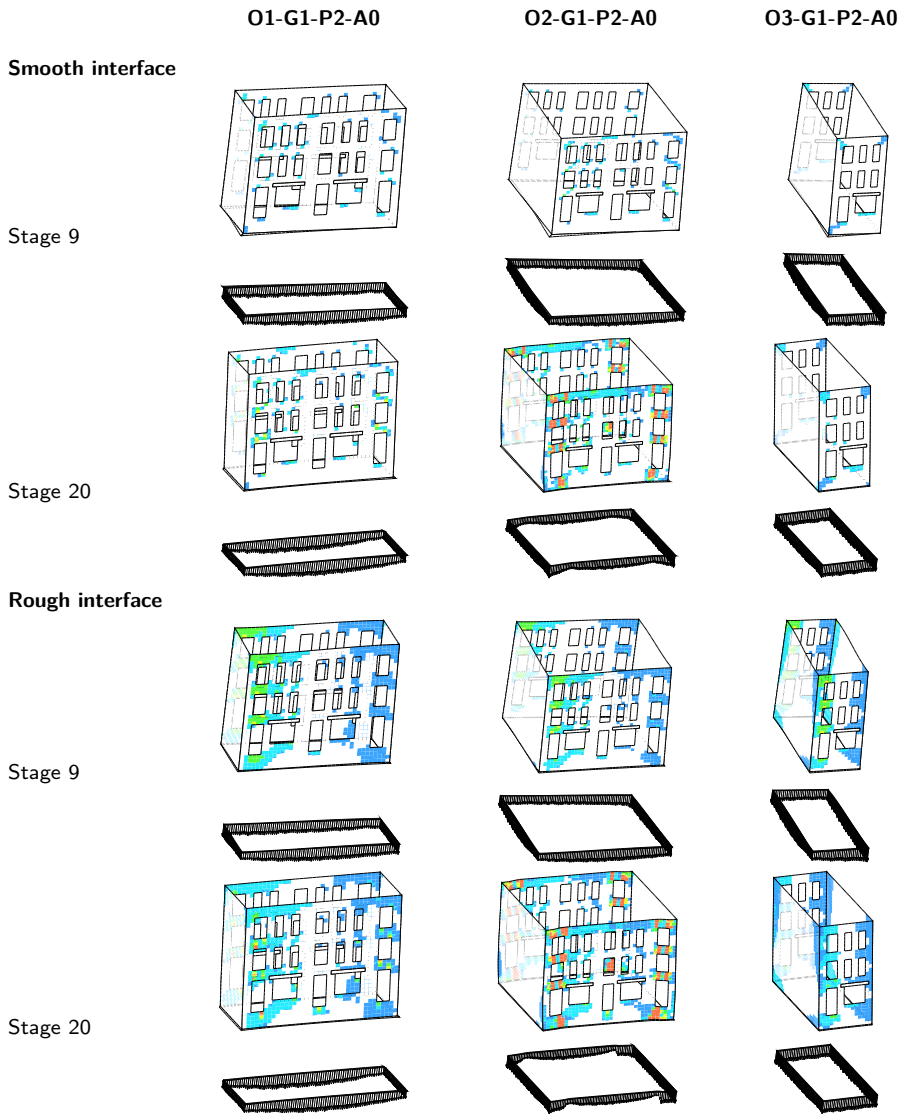


Figure C.2: Crack strain distribution, deformed configuration and soil-structure interface normal stresses: orientation variation for the case G1-P2-A0.

Appendix C. Results of the 3D sensitivity study

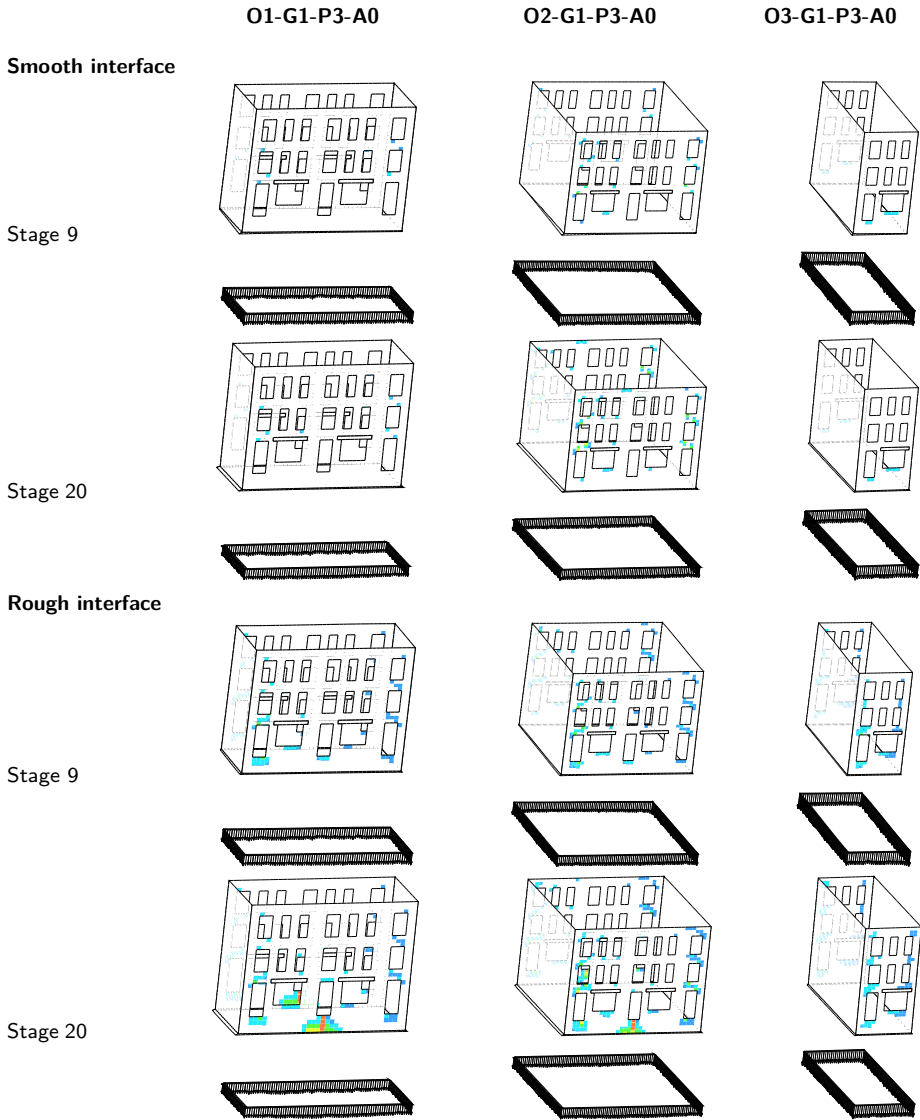


Figure C.3: Crack strain distribution, deformed configuration and soil-structure interface normal stresses: orientation variation for the case G1-P3-A0.

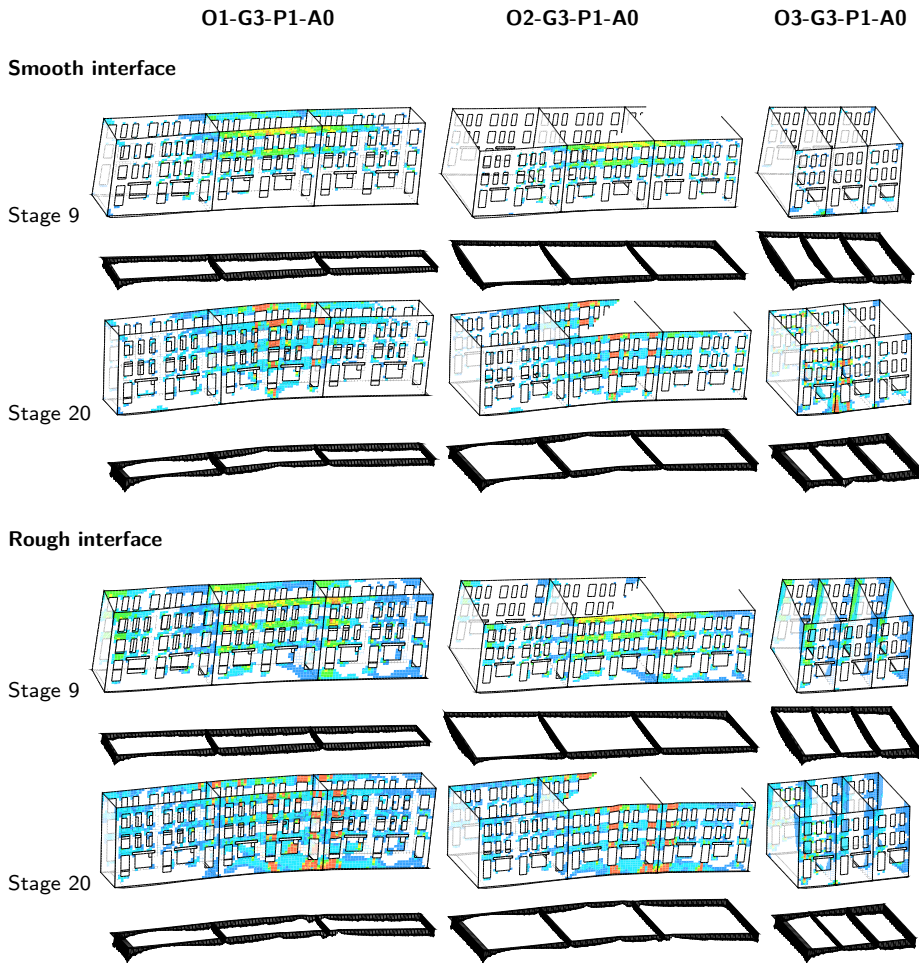


Figure C.4: Crack strain distribution, deformed configuration and soil-structure interface normal stresses: orientation variation for the case G3-P1-A0.

Appendix C. Results of the 3D sensitivity study

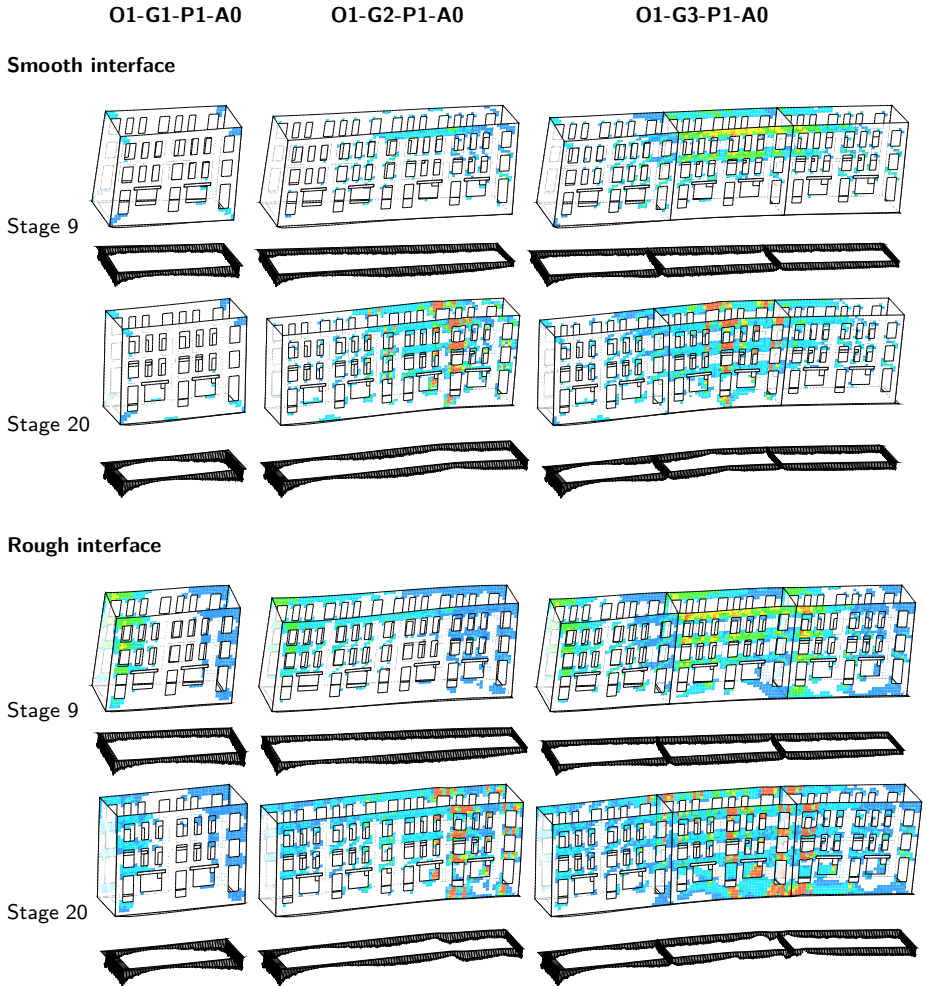


Figure C.5: Crack strain distribution, deformed configuration and soil-structure interface normal stresses: grouping variation for the case O1-P1-A0.

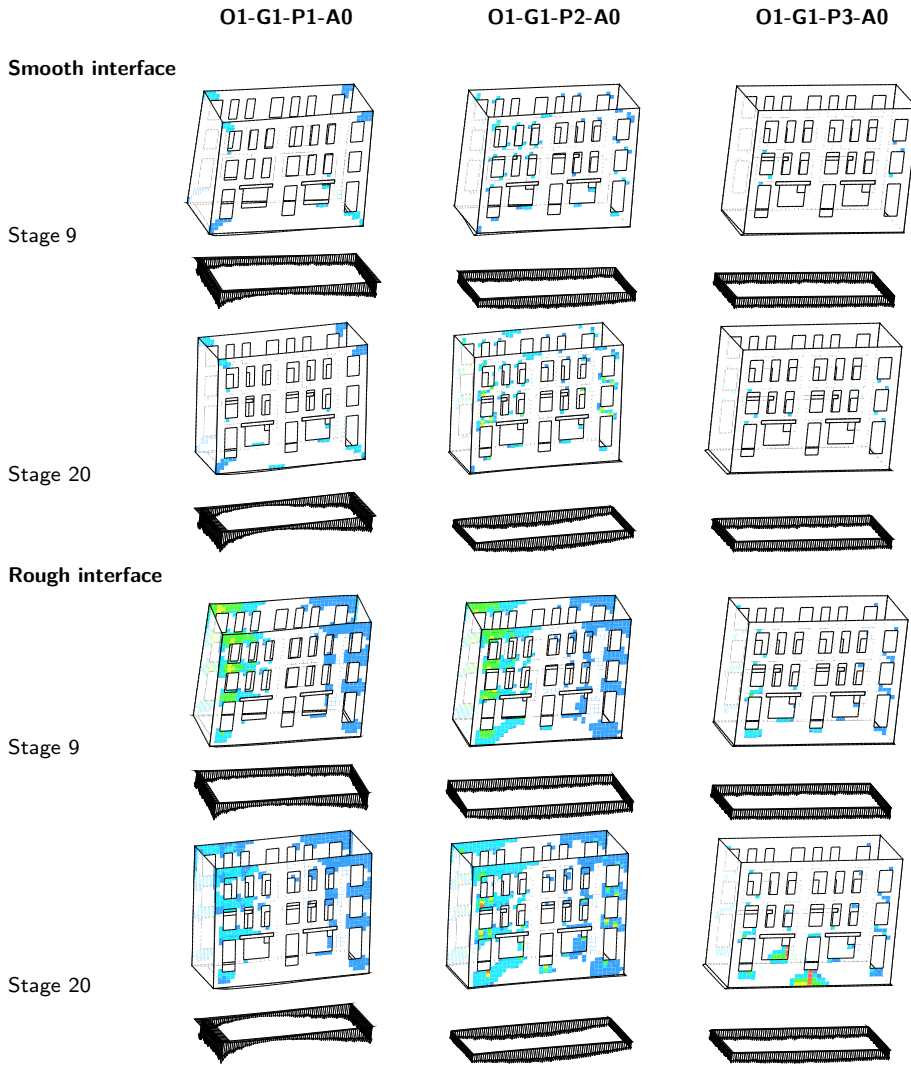


Figure C.6: Crack strain distribution, deformed configuration and soil-structure interface normal stresses: position variation for the case O1-G1-A0.

Appendix C. Results of the 3D sensitivity study

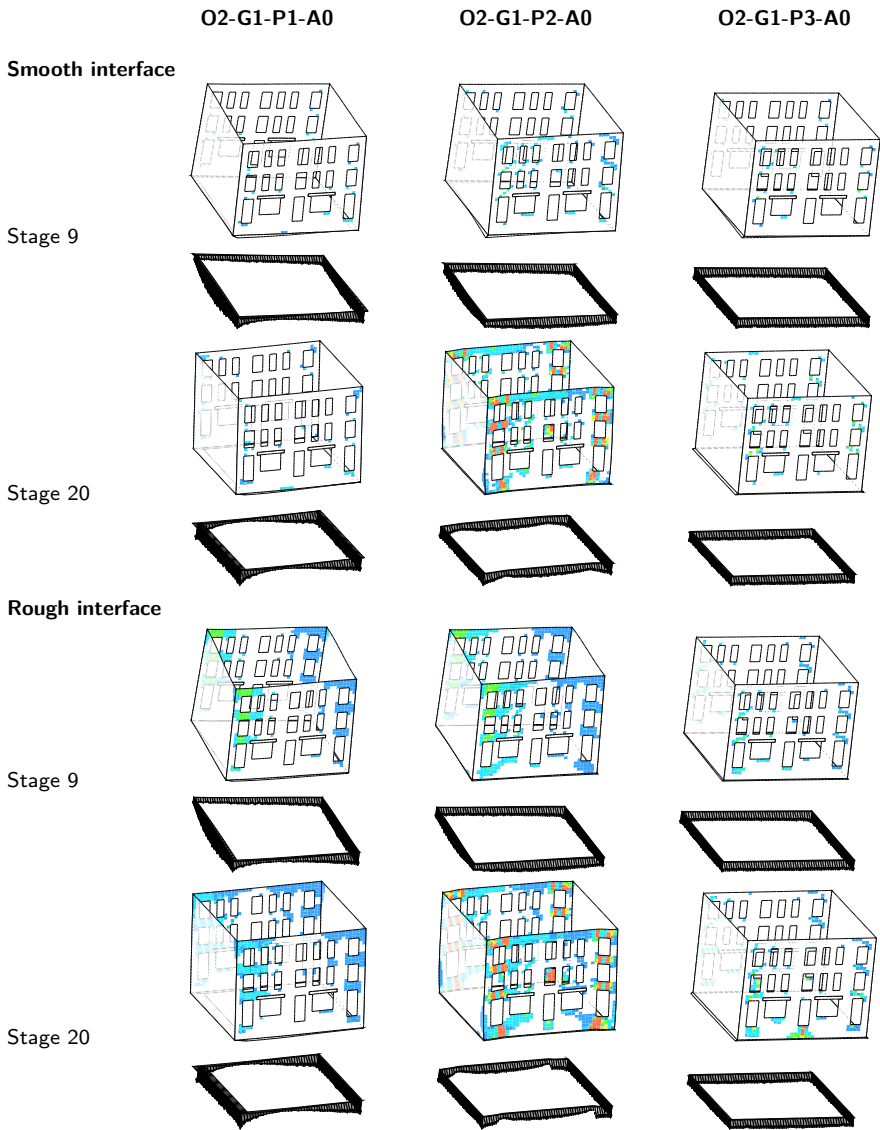


Figure C.7: Crack strain distribution, deformed configuration and soil-structure interface normal stresses: position variation for the case O2-G1-A0.

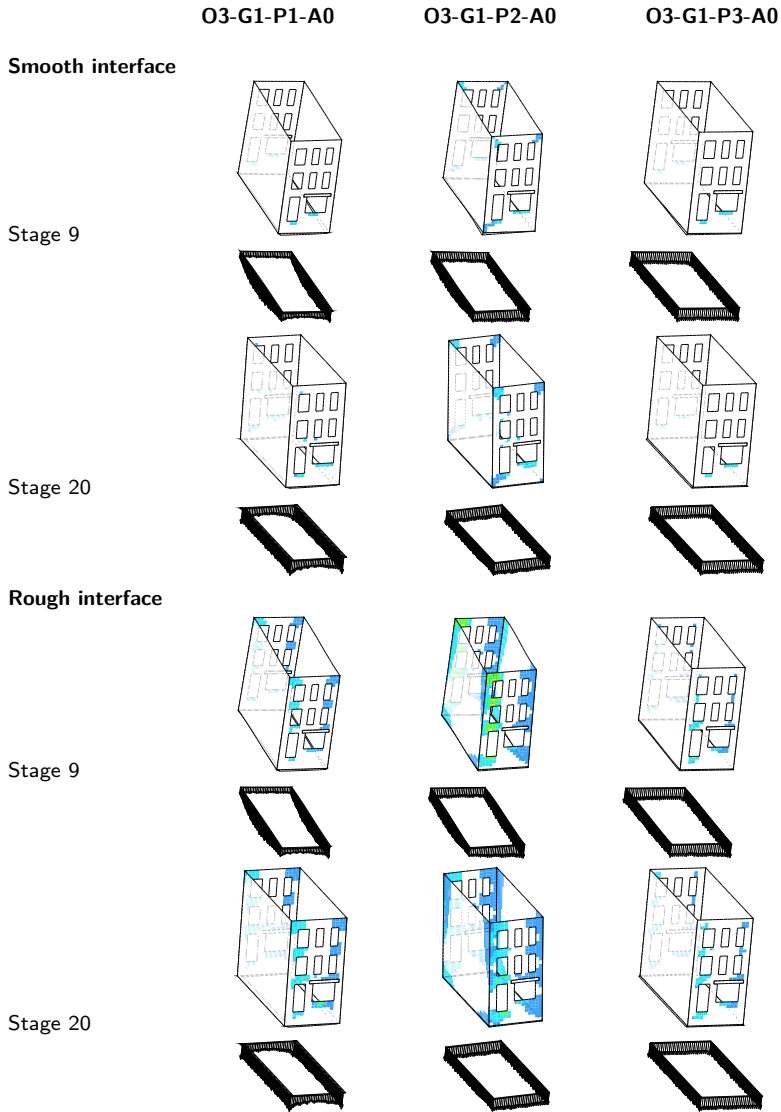


Figure C.8: Crack strain distribution, deformed configuration and soil-structure interface normal stresses: position variation for the case O3-G1-A0.

Appendix C. Results of the 3D sensitivity study

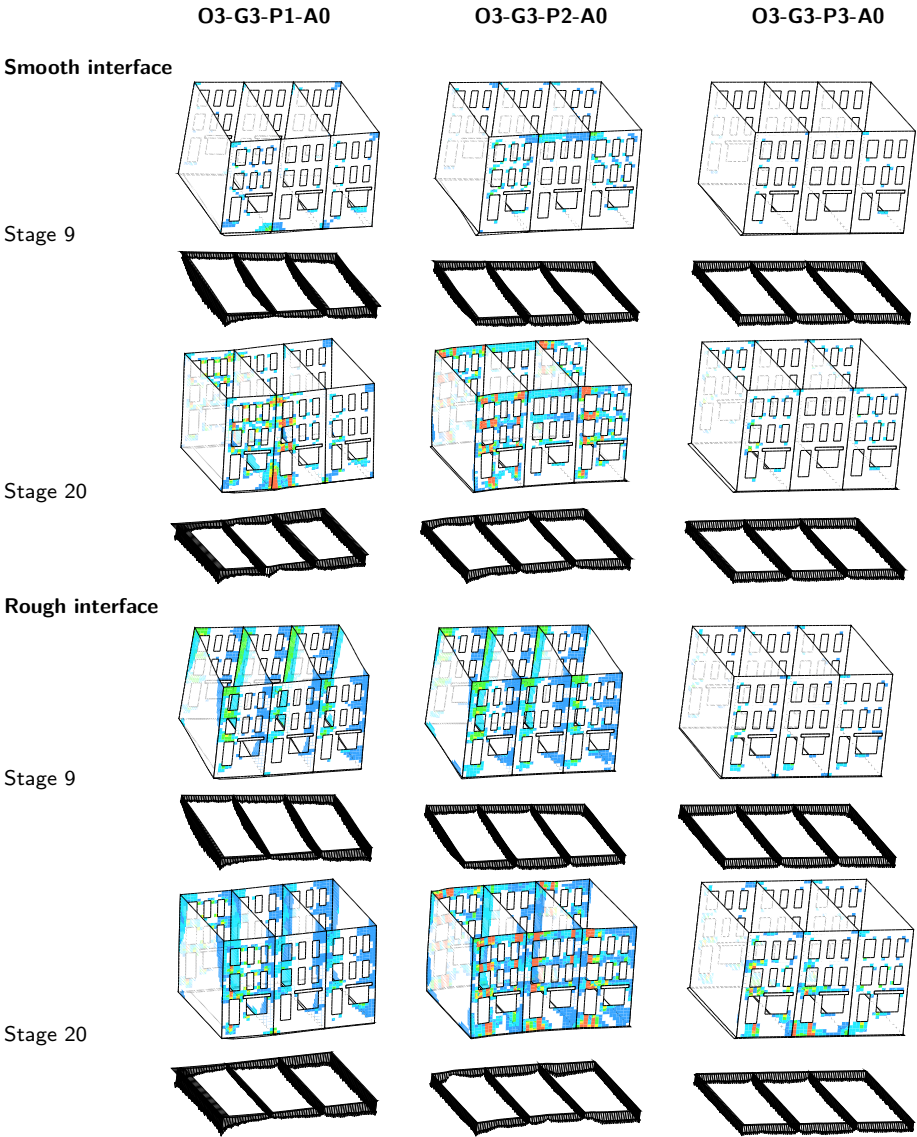


Figure C.9: Crack strain distribution, deformed configuration and soil-structure interface normal stresses: position variation for the case O3-G3-A0.

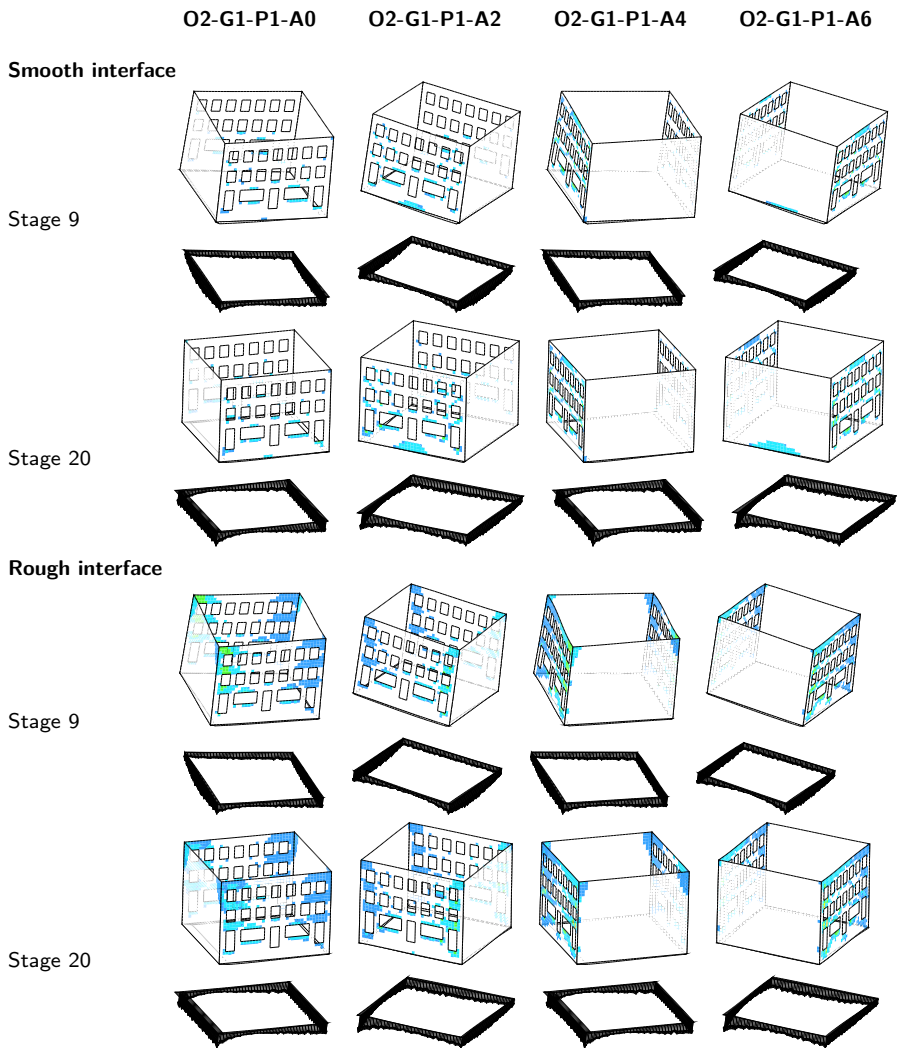


Figure C.10: Crack strain distribution, deformed configuration and soil-structure interface normal stresses: alignment variation for the case O2-G1-P1.

Appendix C. Results of the 3D sensitivity study

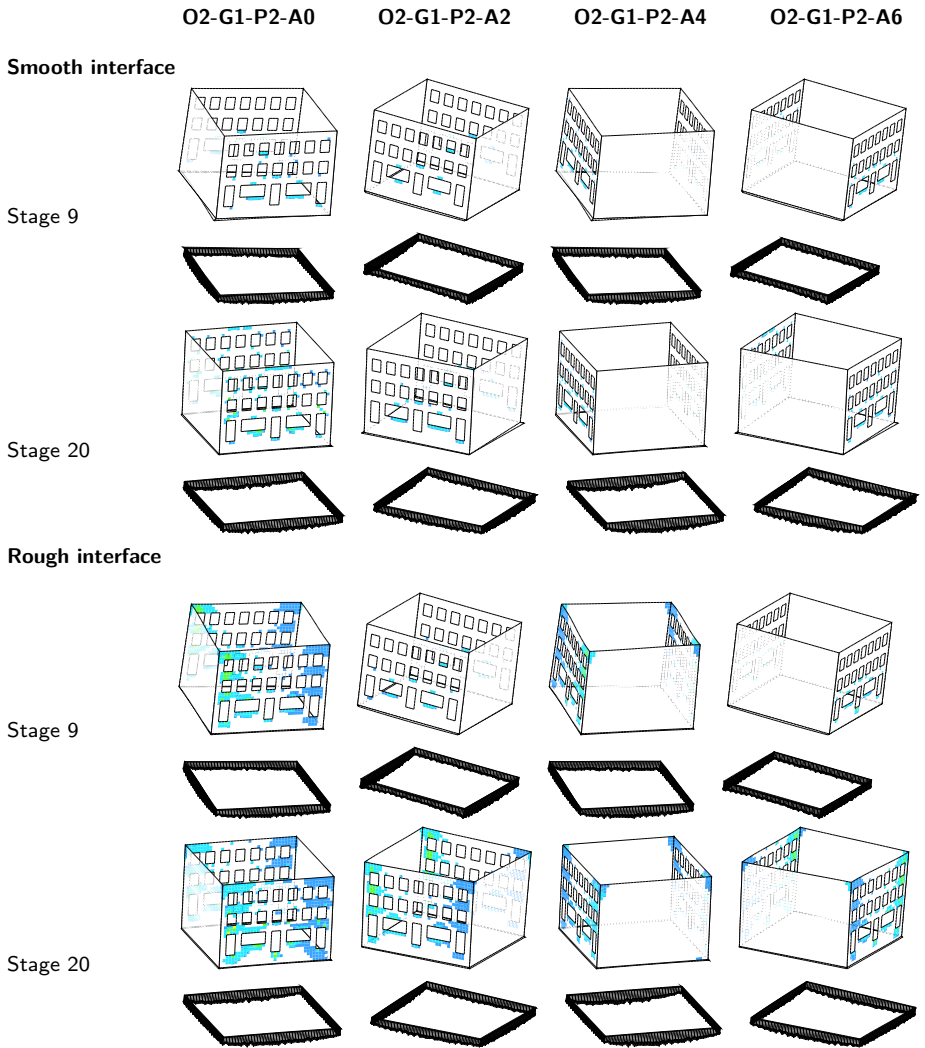


Figure C.11: Crack strain distribution, deformed configuration and soil-structure interface normal stresses: alignment variation for the case O2-G1-P2.

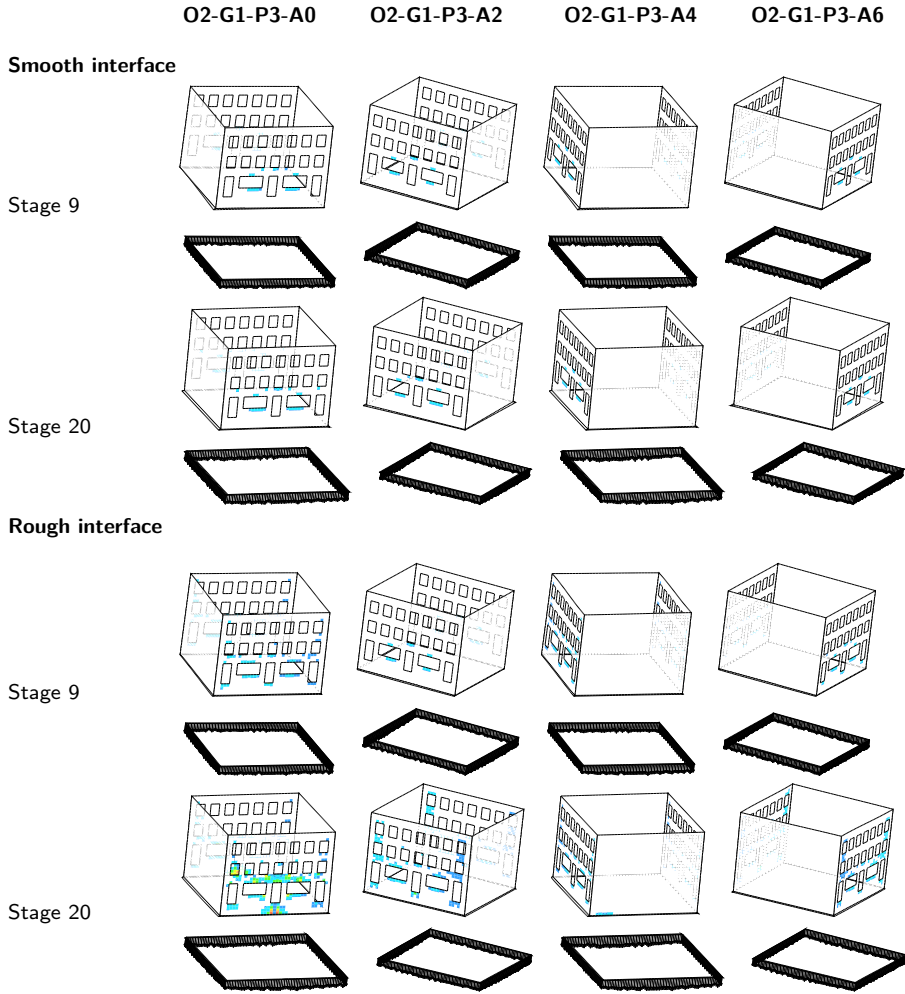


Figure C.12: Crack strain distribution, deformed configuration and soil-structure interface normal stresses: alignment variation for the case O2-G1-P3.

Acknowledgements

I want to express my gratitude to Prof. Jan Rots and Prof. Max Hendriks: working under their supervision has been a privilege from both the scientific and personal points of view. They gave me constant guidance and the freedom to find my own way, sometimes trusting me more than I trusted myself.

Part of this work has been carried out for the COB commission F532. Financial support of Delft Cluster and Centre for Underground Construction is gratefully acknowledged. I could have not done the laboratory experiment without the precious help of Prof. Alessandra Marini, a mentor and a friend. I am also grateful to Prof. Paolo Riva, Prof. Paulo Lourenço, Prof. Rob van Hees, Prof. Dirk Martens and Prof. Johan Bosch for their helpful comments and the inspiring discussions.

I am indebted to Anne van de Graaf, Arthur Slobbe and Rita Esposito, for sharing work, trouble, chocolate and chatting, and to Ilse de Vent, for her friendship and patient feedback on my work. I am thankful to Yuguang Yang, Sara Boldrini, Fabio Rizzardini and Jori Kappen for their contribution to this thesis, and I extend my acknowledgements to all master's students with whom I had the fortune to work: I learnt a lot from them.

Many other people walked with me this adventure: my deepest gratitude goes to the old Italian friends, who never let me go, and to all the new fellow-travellers, who brought magic in my life in the most unexpected ways. A special thought is dedicated to Jennifer, with whom I shared the first of many Dutch coffees.

I am thankful to João, for being Home, and to my parents, for their unconditional love. Grazie.

Giorgia Gardina

Acknowledgements

Curriculum Vitae

- June 14, 1981 Born in Peschiera del Garda, Italy, as Giorgia Giardina
- 2001 – 2006 Degree in Environmental Engineering
University of Brescia
- July – Dec. 2007 Research Assistant
Department of Civil Engineering, Land and Environment
University of Brescia
- 2008 – 2011 PhD candidate
Department of Structural Mechanics
Delft University of Technology
- 2012 – Present Researcher
Department of Structural Mechanics
Delft University of Technology